XXXIV OSTIV CONGRESS

28 July - 3 August 2018
Hosín, Czech Republic

Congress Program and Proceedings

Die Deutsche Bibliothek – CIP Einheitsaufnahme

Die Deutsche Nationalbibliothek verzeichnet diese Publikation in der Deutschen Nationalbibliografie; detaillierte bibliografische Daten sind im Internet unter http://dnb.d-nb.de abrufbar.

Rolf Radespiel, Alexander Barklage, Tim Landa (Eds.)

XXXIV OSTIV Congress – Congress Program and Proceedings

ISBN 978-3-947623-07-5

Publisher of OSTIV Conference Proceedings:
TU Braunschweig – Niedersächsisches Forschungszentrum für Luftfahrt
Hermann-Blenk-Straße 27 • 38108 Braunschweig
Tel: 0531-391-9822 • Fax: 0531-391-9804
Mail: nfl@tu-braunschweig.de
Internet: www.tu-braunschweig.de/nfl

NFL
am Campus Forschungsflughafen

Reis Dijital Baskı Sistemleri Sanayi ve Ticaret Limited Şirketi
Davutpaşa V.D.:7340058478
Litros Yolu 2. Matbaacılar Sitesi 1 BD 20
Topkapı, Istanbul, Turkey
Tel: +90212 5015957/61-61
Internet: http://www.reisdijital.com/

Abstract

The XXXIV Congress of the International Scientific and Technical Organisation for Gliding (OSTIV) is held at the site of the 35th FAI World Gliding Championships in the 18m-, 20m-, and Open Class, in Hosín, Czech Republic, from 28 July - 3 August, 2018. OSTIV Congresses address all scientific and technical aspects of soaring flight. The Congress 2018 features presentations from 10 countries worldwide. These contributions describe new knowledge in the meteorological fields of atmospheric convection and atmospheric waves. The presentations on sailplane technologies comprise the areas of sailplane design and performance, aerodynamics, aeroelasticity, loads, and propulsion, whereas further contributions cover various aspects of training and safety. The present Congress Proceedings lead the participants through the full-week program, and they make extended abstracts of the presentations accessible to the public.

Welcome to the OSTIV Congress 2018 in Czech Republic. Every two years the Congress offers new information and latest research results in soaring and sailplane technology to scientists and engineers from all over the world. The meeting presents unique opportunities for scientific exchange and coordination of future activities.

This year the Congress is hosted by the Czech Aero Club, along with the 35th FAI World Gliding Championships, in Hosín, Czech Republic. We are thankful that the OSTIV Congress can take place in a well equipped hall near the club house at Hosín Airfield.

We thank our industrial sponsors, Alexander Schleicher Segelflugzeugbau, HpH Sailplanes, Jonker Sailplanes, and Schempp-Hirth Flugzeugbau, who made it possible for us to offer free access to the Congress and give special support to participating students.

The Call for Abstracts issued by OSTIV generated response by engineers and scientists from 10 countries worldwide. The received extended abstracts were reviewed, and they are published in this proceeding booklet. We believe that an excellent program has been generated this way. For their efforts in recruiting high-quality contributions we acknowledge the members of the Program Committee:

Zafer Aslan, Turkey	Götz Bramesfeld, Canada	Michael Greiner, Germany
Mark Maughmer, USA	Judah Milgram, USA	Ian Oldaker, Canada
Lukáš Popelka, Czech Republic	Rolf Radespiel, Germany	Gerard Robertson, New Zealand

Preparing the Congress took endless hours of work by the Organizing Team, consisting of Lukáš Popelka Czech Republic, Rolf Radespiel, Germany and Britta Schlenker, Germany. We are very thankful for their efforts. Our thanks also go to Alexander Barklage and Tim Landa of Technische Universität Braunschweig for booklet editing. We would like to thank Nabi Sarıbaş and Doğan Bayraklı of Istanbul Aydın University for booklet printing.

The OSTIV Congress is the perfect setting to bestow the OSTIV Plaque, OSTIV Prize 2017 and the OSTIV Best Student Paper Awards. We look forward to the Opening Ceremony and the Congress Closing Dinner for presenting the Award Winners.

We wish all Congress participants an exciting and rewarding week in Hosín.

Prof. Rolf Radespiel — OSTIV President

Prof. Mark Maughmer — OSTIV Vice President

OSTIV acknowledges support provided by

HpH sailplanes
AS
JONKER SAILPLANES
SCHEMPP-HIRTH
35th FAI WORLD GLIDING CHAMPIONSHIPS 2018 HOSÍN | CZECH REPUBLIC
ISTANBUL AYDIN UNIVERSITY
Technische Universität Braunschweig

Welcome to Hosín for the XXXIV OSTIV Congress

Hosín is a village in the South Bohemian Region of the Czech Republic with a population of 750, famous explicitly for local sport-aviation airfield. Hosín lies about 7 km north of České Budějovice, a statutory city in the Czech Republic. It is the largest city in the South Bohemian Region and its political capital. České Budějovice is the seat of the University of South Bohemia, and the Academy of Sciences with a population of almost 100,000. It is located in the valley of the Vltava River.

České Budějovice, established in 1265, has long been known for the beer brewed there since the 13th century. The old town preserves architecture from the Gothic, Renaissance, Baroque, and 19th century periods. The Museum of South Bohemia holds a large collection of historic books, coins, weapons and other cultural articles.

The OSTIV Excursion – HpH sailplane manufacturer and Kutná Hora town Wed 1st August 2018

OSTIV delegates are invited to join in on this interesting tour to the facilities of Congress' main Sponsor.

HpH Ltd. is a company long established in the aviation industry. Having been involved with initial construction of the Diamond Dimona, Katana, and more recently the mighty EB29, HpH has gained reputation for its engineering, build quality and attention to detail. In 1997, the HpH company succeeded in gaining the technology and production documentation for the original Glasflügel 304. Production started in 1997 with an updated version of the Glasflügel 304, the HpH 304CZ, which proved successful both with customers and in competitions. After that, HpH produced the HpH304C Wasp, an affordable FAI Standard Class version of the 304CZ.

HpH has used this knowledge, design & manufacturing know-how to produce a highly competitive sailplane with the »all-new« HpH Shark series. As the Shark is a refreshing alternative to the established competition, HpH has already shipped over 70 Shark gliders to customers worldwide.

A new entry into FAI double-seater 20m-class has also been developed. This involved extensive aerodynamic studies and wind-tunnel testing, building on the experience gained in the Shark family. PW-series airfoils, plus a wing area of 15.38m^2, yielding an aspect ratio of 26.5 deliver performance, and advanced manufacturing techniques provide wing-loadings as low as 36kg/m^2. An optimally curved wing leading edge and elliptical tailplane deliver a unique silhouette.

Photos Petr Kolmann

The town of Kutná Hora has been historically competing with Czech capital, Prague, over many centuries, economically, culturally, and politically. The town premises began in 1142 with the settlement of Sedlec Abbey, the first Cistercian monastery in Bohemia. By 1260, German miners mined for silver in the mountain region, which they named Kuttenberg, being the part of the monastery property. The earliest traces of silver have been found dating back to the 10th century, when Bohemia already had been in the crossroads of long-distance trade for many centuries. Silver dinars have been discovered belonging to the period between 982–995.

Kutná Hora and the neighboring town of Sedlec are a UNESCO World Heritage Site. Among the most important buildings in the area are the Gothic jewel, five-naved St. Barbara's Church, construction begun in 1388, and the

neighboring Italian Courtyard (Vlašský dvůr), former a royal residence, which was built at the end of the 13th century.

Delegates and friends of OSTIV are invited to join in on this tour. Cost will be specified at Congress registration.

Departs: Hosín airfield; meet 8.15am at OSTIV Hangar for a strict 8:30am departure.

OSTIV Congress Dinner @ Podhrad Hotel **Friday 3rd August 2018**

After the fascination of a solid week of technical presentations, all OSTIV Speakers, Delegates, family and friends of OSTIV are invited to enjoy a relaxed and friendly dinner together at the Hotel Podhrad, address Nám. Čsl. armády 30.

This venue offer an excellent gastronomy in the beautiful and calm environment of the town of Hluboká nad Vltavou. The hotel is located just below the famous picturesque Tudor-style Hluboká chateau, which is the dominant landmark of the whole town.

A balanced menu of Czech specialties is served from 7:30 pm.

Please advise attendance and numbers at Registration desk when you register.

OSTIV Congress, 28 July - 3 August 2018

Hosín, Czech Republic

	Saturday, 28 July 2018
	Hosín - LKHS airfield
17:30 - 18:30	Opening Ceremony and Presentation of OSTIV-Awards 2018

	Hosín - LKHS, OSTIV Hangar
15:00 - 18:00	registration
	Monday, 30 July 2018
	Hosín - LKHS, OSTIV Hangar
08:00 - 08:45	registration
	Sailplane Loads
	Chair: Loek Boermans
08:45 - 09:15	LIFETIME CALCULATIONS FOR GLIDERS ON THE BASIS OF DIFFERENT LOAD SPECTRA. C. Kensche, Stuttgart, Germany.
09:15 - 09:45	APPLICATION OF AEROELASTIC TAILORING FOR GUST ENERGY EXTRACTION. M. Melville, G. Bramesfeld, A. Kolaeiy, H. Alighanbari, Toronto, Canada.
09:45 - 11:00	coffee break
	Aerodynamic Prediction
	Chair: Mark Maughmer
11:00 - 11:30	CIRCLING CALCULATIONS FOR PREDESIGN OF SAILPLANES. J. Himisch, K. Rhode-Brandenburger, Braunschweig, Germany.
11:30 - 12:00	AIRFOIL MAXIMUM LIFT COEFFICIENT ASSESSMENT FOR PRELIMINARY DESIGN PURPOSES AND OPTIMIZATION. L. Popelka, D. Šimurda, V. Skála, M. Matějka, M. Schmirler, Prague, Czech Republic.
12:00 - 12:30	TRANSITION PREDICTION RESULTS FOR NLF(1)-0416 AIRFOIL AND SICKLE WING. M. Kruse, F. Munoz, R. Radespiel, Braunschweig, Germany.
12:30 - 14:00	lunch break / registration
	Aerodynamic Drag
	Chair: Rolf Radespiel
14:00 - 14:30	PREDICTION OF INSECT CONTAMINATION ON AIRFOIL BY USING CFD METHODS. V. Běták, Prague, Czech Republic.
14:30 - 15:00	DETERMINATION OF NOSE WHEEL DRAG AND PERFORMANCE INCREASE BY A RETRACTABLE NOSE GEAR. J. Condé-Wolter , J. Frey, Dresden, Germany.
15:00 - 15:30	coffee break
	Atmospheric Waves - 1
	Chair: Edward Hindman
15:30 - 16:00	SOARING INTO THE STRATOSPHERE. D. Etling, Hannover, Germany.
16:00 - 16:30	DFS 582 - HIGH-ALTITUDE RESEARCH GLIDER PROJECT 1958-1964. H.-L. Meyer, Braunschweig, Germany.
	Evening
20:00 - 21:00	OSTIV General Conference

	Tuesday, 31 July 2018
	Hosín - LKHS, OSTIV Hangar
08:30 - 08:45	registration
	Aeroelasticity
	Chair: Fritz Kießling
08:45 - 09:15	HOW TO PERFORM FLIGHT VIBRATION TESTING BASED ON OPERATIONAL MODAL ANALYSIS? J. Schwochow, Göttingen, Germany.
09:15 - 09:45	STUDY OF CLOSE GROUND PROXIMITY ON A FLEXIBLE WING. Z. Pátek, R. Kulhánek, Prague, Czech Republic.
09:45 - 11:00	coffee break
	Performance
	Chair: Götz Bramesfeld
11:00 - 11:30	OPTIMIZED HIGH-SPEED PERFORMANCE OF RC GLIDERS BY DYNAMIC SOARING. G. Sachs, B. Grüter, München, Germany.
11:30 - 12:00	TRAVEL PERFORMANCE OF ENGINELESS UAV BY DYNAMIC SOARING. G. Sachs, B. Grüter, München, Germany.
12:00 - 13:30	lunch break
	Atmosheric Waves - 2
	Chair: Zafer Aslan
13:30 - 14:00	EXPLORING GRAVITY WAVES IN THE PYRENEES BY GROUND BASED OBSERVATIONS, IN-FLIGHT MEASUREMENTS, AND MODEL ANALYSIS. E. Mascus, M. Sistach, M. Soler, A. Ultsch, C. Maul , Frankfurt, Germany.
14:00 - 14:30	CATSKILL MOUNTAIN WAVE PROJECT: EXPLORATION, MAPPING, AND FORECASTING OF WAVE CONDITIONS IN SOUTHERN NEW YORK. D. Sazhin, P. Chidekel, J. Bird New York, USA.
14:30 - 15:00	coffee break
	Atmospheric Convection - 1
	Chair: Dieter Etling
15:00 - 15:30	STRUCTURES OF THE BOUNDARY LAYER - SOME BOUNDARY LAYER THERMO-DYNAMICS. C. Lindemann, Berlin, Germany.
15:30 - 16:00	EFFECTS OF HIGH EVAPORATION, TEMPERATURE AND HUMIDITY ON SOARING IN AND NEAR VICINITY OF ISPARTA, TURKEY. F. Dökmen, A. Tokgözlü, Z. Aslan, TURKEY.
16:00 - 16:30	URBAN HEAT ISLAND; IN ANKARA-İZMIR-KARAPINAR (TURKEY). K. Yasdiman , A. Tokgozlu, E. T. Özdemir, Z. Aslan, Istanbul, Turkey.
	Hosín - LKHS, OSTIV Hangar
	Evening Session
	Chair: Rolf Radespiel
20:00 - 21:00	ON THE HISTORY OF FLUTTER PREDICTION AND PREVENTION. F. Kießling, Germany.

	Wednesday, 1 August 2018
	Departing Hosín - LKHS, Carpark
08:15 - 20:30	**Excursion to Kutná Hora**
	HpH Ltd., Manufacturer of HPH sailplanes, and historic city of Kutná Hora. Tickets sold at registration desk of OSTIV Congress

	Thursday, 2 August 2018
	Hosín - LKHS, OSTIV Hangar
	Safety - 1
	Chair: Patrick Pauwels
08:45 - 09:15	SAFETY AS AN ADDITIONAL SUBJECT IN PILOT TRAINING. A. Ultsch, Marburg, Germany.
09:15 - 09:45	TIME TO ESCAPE! A SURVEY OF TIME REQUIRED FOR GLIDER PILOTS TO ESCAPE A GROUND BASED COCKPIT SIMULATOR. S. Smith, Melbourne, Australia.
09:45 - 11:00	coffee break
	Sailplane Propulsion
	Chair: Lukas Popelka
11:00 - 11:30	SAILPLANE WING INTEGRATED WITH A MOTOR-PROPELLER SYSTEM. J. Pytka, E. Gnapowski, A. Rypulak, P. Kasprzak, J. Pytka , Lublin, Poland.
11:30 - 12:00	SAFETY MANAGEMENT OF BATTERY ELECTRIC PROPULSION IN GLIDERS. R. Klein, Mosbach, Germany.
12:00 - 12:30	PUSHER-FLAP OR COANDAJET. G. Koppenwallner, Göttingen, Germany.
12:30 - 14:00	lunch break
	Safety – 2
	Chair: Alfred Ultsch
14:00 - 14:30	GLIDING TRAINING IN THE EU – PAST & FUTURE. P. Pauwels, Belgium.
14:30 - 15:00	FATAL ACCIDENT RATES INVOLVING SPINNING FOR SELECTED SINGLE-SEAT GLIDERS. M. Stimson, S. Smith, Melbourne, Australia.
15:00 - 15:30	A STATIC LINE SYSTEM DESIGNED TO BE RETROFITTED TO TYPICAL EMERGENCY PARACHUTES FOR USE BY GLIDER PILOTS:- BUYING THE PILOT TIME IN A CRITICAL SITUATION. S.Smith, Melbourne, Australia.
15:30 - 16:00	coffee break
	Atmosheric Waves - 3
	Chair: Rick Millane
16:00 - 16:30	VALIDATING MOUNTAIN-WAVE UPDRAFT SPEEDS PREDICTIONS FROM THE HIGH-RESOLUTION, RAPID-REFRESH (HRRR) NUMERICAL WEATHER PREDICTION (NWP) MODEL. E. Hindman, New York, USA.
16:30 - 17:00	LEE WAVES WITHOUT MOUNTAINS EXTENSIVE WAVE INDUCED CLOUD STREETS OVER GERMANY ON 14TH APRIL 2015. J. West, Germany.
17:00 - 17:30	ONGOING DEVELOPMENTS IN MOUNTAIN WAVE FORECASTING AT THE HUNGARIAN METEOROLOGICAL SERVICE. P. Salavec, Budapest, Hungary.
	Hosín - LKHS, OSTIV Hangar
	Evening Session
	Chair: Lukas Popelka
20:00 - 21:30	ON THE WAY TO GLIDE RATIO 100:1. L. Boermans, Delft, The Netherlands.

	Friday, 3 August 2018
	Hosín - LKHS, OSTIV Hangar
	Sailplane Design - 1
	Chair: Mark Maughmer
08:45 - 09:15	AN ULTRA-LONG ENDURANCE SOLAR-POWERED UNMANNED AIRPLANE. B. Bissonnette, T. Krebs, M. Melville G. Bramesfeld, Toronto, Canada.
09:15 - 09:45	DILEMMA RESOLVED: AIRBRAKES TAMED. M. Greiner, G. Bangga, Stuttgart, Germany.
09:45 - 11:00	coffee break
	Sailplane Design - 2
	Chair: Rolf Radespiel
11:00 - 11:30	AIRFOIL OPTIMIZATION WITH CST-PARAMETERIZATION FOR (UN-)CONVENTIONAL DEMANDS. J. Achleitner, K. Rhode-Brandenburger, M. Hornung München, Germany.
11:30 - 12:00	MODERN SAILPLANE WING DESIGN. M. Maughmer, University Park, PE, USA.
12:00 - 13:30	lunch break
	Atmospheric Convection - 2
	Chair: Edward Hindman
13:30 - 14:00	FINE STRUCTURE OF THERMALS IN ARID CLIMATE: RESULTS OF GLIDER-BASED IN FLIGHT MEASUREMENTS. A. Ultsch, C. Maul, Marburg, Germany.
14:00 - 14:30	MEASUREMENT RESULTS FROM WARM AIR THERMALS OVER THE NAMIBIAN STEPPE. A. Kiessling, Weil der Stadt, Germany.
14:30 - 15:00	MODELLING BOUNDED RATIONALITY AND RISK STRATEGY IN THERMAL SOARING. J. Bird, D. Sazhin, J. Langelaan, University Park, Pennsylvania, USA.
	Podhrad Hotel, Hluboká nad Vltavou, Nám. Čsl. armády 30
19:00	**Congress Closing Dinner**

Lifetime calculations for gliders on the basis of different load spectra

Christoph Kensche
Stuttgart, christophkensche@aol.com

Abstract: Five service life spectra for sailplanes are compared quantitatively using s-n curves representative for GFRP-shear web and CFRP-spar cap material of a wing. The damage accumulation is carried out according to the Palmgren-Miner rule. The damage or lifetime, respectively, is calculated for different maximum design values for the shear web and the spar cap.

***Keywords*:** Lifetime, service life spectrum, fatigue, s-n curve, Palmgren-Miner rule

Introduction

Commonly the life load spectra for sailplanes are presented in form of a cumulative frequency plot. This is a very descriptive and well proven method to compare different spectra qualitatively. However, an objective comparison is only possible by means of a quantification of the fatigue damage. This is done the first time for sailplanes, and the results will be demonstrated in the paper. For the calculations a program was used which was developed at DLR [1]. It uses the Markov-matrices which are the base of the spectra, typical s-n curves of shear web and spar cap material in the wing as well as the widely applied linear Palmgren-Miner rule for the damage accumulation.

Service life spectra for gliders

Five glider-spectra are compared:

- The Kossira-Reinke spectrum without aerobatic flights,
- The Kossira-Reinke spectrum with 12.5 % aerobatic flights,
- The KoSMOS-spectrum. This spectrum is based on the Kossira-Reinke-spectra considering also motor flight. It is recognized as standard by OSTIV for possible certification tests at sailplanes and available on request by the German LBA.
- The Franzmeyer block-program which was used before KoSMOS was established and which still can be used for certification of sailplanes.
- A block-program derived from the Australian Dorning-spectrum [2,3]. This spectrum was used e.g. to perform a well-described full-scale fatigue test with a GFRP-Janus wing.

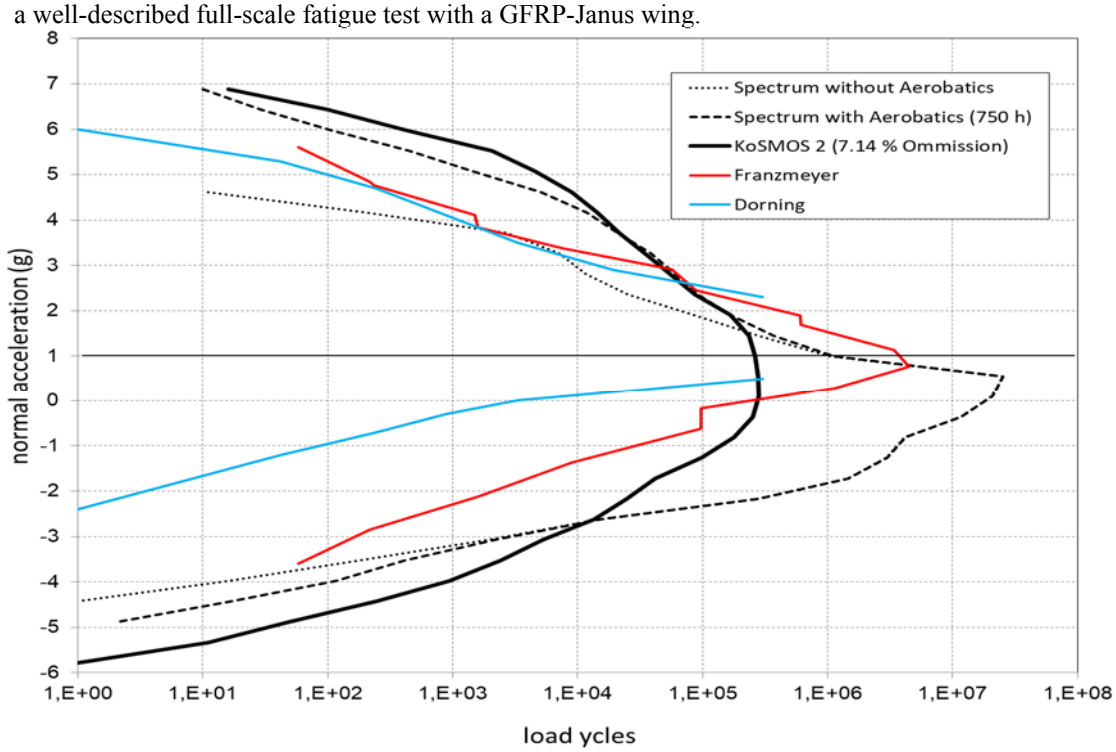

Figure 1: Cumulative frequency plot of the five glider load spectra for 6.000 h

With exception of the Franzmeyer-program which was developed on theoretical assumptions about the level and number of the loads, the other spectra are based on flights of several hundred flight hours each. Figure 1 shows the above mentioned spectra in form of a cumulative frequency plot. The flight time for all of them is extrapolated to a 6.000 h life cycle.

Damage calculation and results

For preparation of the individual damage calculations all loads were ordered in classes ranging from 1 to 32 according e.g. to the description in [4]. The classes can be referred to either the g-loads or the strains in the wing material measured or calculated. Since the design values may differ for different gliders the calculations were performed accordingly, e.g. for the GFRP-shear webs between about 0.3 and 0.6 % maximum strain in the 45° fibres, shown in Figure 2. The comparison valid for the mean values of the respective s-n curve shows the maximum damaging effects of the KoSMOS-standard as could be expected. However, it is interesting that the Franzmeyer-spectrum seems to damage the gliders even more than the Kossira-Reinke spectrum with aerobatics, and is thus conservative enough for certification of sailplanes as admitted. This is, however, not identifiable in the cumulative frequency plot. With respect to the Dorning block program, the damage rate is significantly lower than those of the other spectra. This is surprising, since the Dorning spectrum represents the upper envelope of different Australian glider flight data including cross country and aerobatic flights, and it was interpreted to be harder than flight data established in Europe [2]. The reason for this behaviour is not yet clear and has still to be investigated.

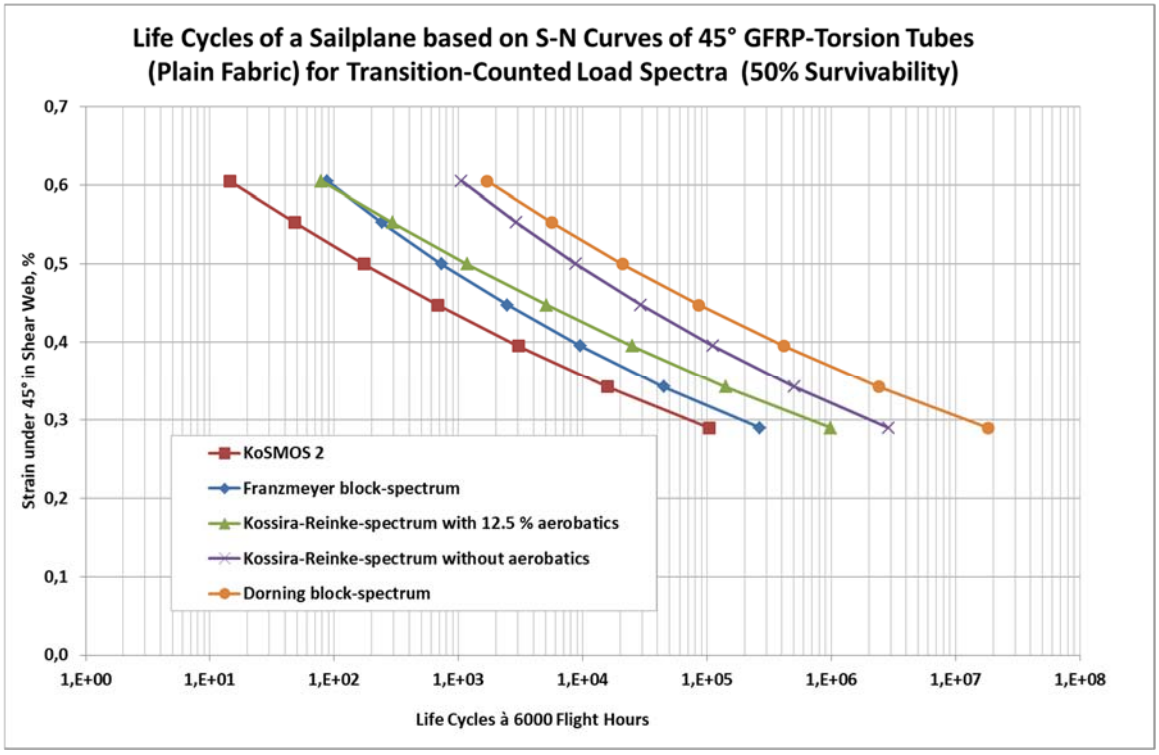

Figure 2: Damage calculation of the service life spectra with respect to different maximum strains in the 45°-fibres of the shear web

References

[1]Ch.W. Kensche, *Lifetime of GFRP in a shear web and in the cap of a sailplane wing spar*, XXVI OSTIV-Congress, Bayreuth, Germany, 6 to 13 August 1999

[2]J.M. Ritchie, A.O.Payne, N. Mileshkin, *Fatigue Life Assessment of the IS28B2 Sailplane*, Technical Soaring, Volume 19, No.2, 1995

[3]C.A. Patching, L.A. Wood, *Further Fatigue Testing of a Glass Fiber Reinforced Plastic Glider Wing*, Technical Soaring, Volume 22, No.1, 1998

[4]H. Kossira, *Determination of load spectra and their application for keeping the operational life proof of sporting airplanes*, ICAS-Proc. 8/1982, ICAS-82-2.8.2, page 1330-1338

Application of Aeroelastic Tailoring for Gust Energy Extraction

Michael Melville[1], Götz Bramesfeld, Amir Kolaei[1], Hekmat Alighanbari[1]
[1]*Ryerson Unviersity, Department of Aerospace Engineering, Toronto, Canada, michael.melville@ryerson.ca*

Abstract: The harvesting of energy from gusts has been a research interest for several years, boasting significant possible performance gains for low-speed aircraft. Several active control methods for gust energy extraction exist with today's technology; however, these active control methods can be complicated and expensive. Passive methods can prove to be more reliable and cost effective. Aeroelastic tailoring is used as a passive approach for improving gust energy extraction in order to reduce the overall drag of a wing. Performance increases as a result of shifting the chordwise location of the elastic axis, as well as its orientation were observed using a tightly coupled fluid-structure interaction model; both cases provided approximately 7.5% drag reductions while the latter showed additional improvements of 0.25%.

***Keywords*:** Aeroelasticity, unsteady aerodynamics, fluid-structure interaction.

Introduction

In the early aircraft design stages, it is very common to use low-fidelity analysis tools to predict aerodynamic performance. These analysis tools provide sufficient accuracy with a low computational cost, allowing rapid analysis of multiple design configurations. A major concern in the design of both small Unmanned Aerial Vehicles (UAVs) and high performance sailplanes is the ability to extract energy from their environment in order to improve their performance. Several designs utilize active control methods to facilitate such energy extractions, such as those described in Refs. 1-3. Passive methods, however, can be more attractive due to their often simpler nature. One common passive method of energy extraction is through the use of aeroelastic tailoring. Aeroelastic tailoring provides of means of modifying the coupling between aerodynamic and elastic loads to control the response of the aircraft. This paper presents a fluid-structure interaction model that is suitable to explore the aerodynamic performance effects of aeroelastic tailoring of low-speed aircraft wings in order to improve the energy extraction from gusts.

Methodology

A tightly coupled fluid-structure interaction model was used for performance predictions. The aerodynamics was modeled using the potential flow method of Bramesfeld and Maughmer [4]. The aerodynamic model was then coupled to an explicit finite difference method used by Ironside et al. [5] to predict the structural dynamic response. The coupling procedure for the FSI model is illustrated in Figure 1. Induced velocities as a result of elastic deformations are updated every time step, providing a better prediction of the transient response. An unsteady aerodynamic model was also implemented to capture the time changing aerodynamic forces when encountering a gust. The unsteady method utilizes an unsteady formulation of the Kutta-Joukowsky theorem; this approach was first used with the current aerodynamic model by Cole [6] and was adapted for this research.

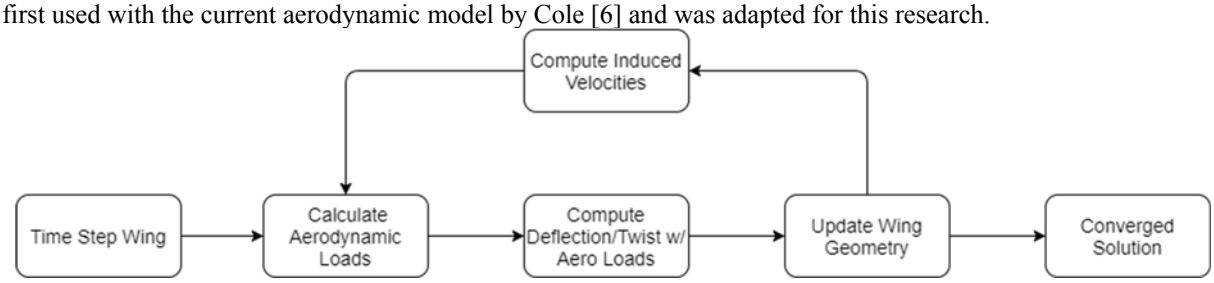

Figure 1. Coupling procedure for FSI model

The energy extracted from a gust is typically attributed to a drag reduction, as discussed by Melville [7]**.** As such, a means of comparing cases using this drag reduction was developed. Using a time integration of the profile drag coefficient through the gust field, normalized by a reference drag coefficient, an efficiency term was derived, as shown in Eq. (1). This term can be thought of as the efficiency that the elastic wing extracts energy from the flow field, in comparison to the steady state conditions.

$$\eta_{gust} = -\frac{1}{T}\int_0^T \frac{(C_D) - (C_D)_{ref}}{(C_D)_{ref}}\,dt \tag{1}$$

Further discussion on this term can be found in Ref. 7.

Results

The case study follows that of Ref. 8, seeking to investigate the effects of the elastic axis location on the gust energy extraction capabilities of an elastic wing. In practice, the elastic axis location can be modified relatively simply through the use of composite materials; changing the cross sectional properties in the wing structure changes the shear flow through the structure, and thus the elastic axis location [9]. A theoretical wing geometry, outlined in Table 1, was used for this case study. Constant stiffness and mass properties were used for simplicity; in practice, these properties would be constantly changing across the span, however, a constant distribution allows for the focus to solely fall on the elastic axis location.

Table 1. Specifications for theoretical wing

Geometry		Flight Conditions		Structural Properties	
Span (m)	*32*	*Airspeed (m/s)*	*30*	*Bending Stiffness (Nm^2)*	*750,000*
Chord (m)	*1*	*Density (kg/m^3)*	*1.225*	*Torsional Stiffness (Nm^2)*	*750,000*
Airfoil	*NACA2412*	*Angle of Attack (deg)*	*-0.5*	*Linear Mass (kg/m)*	*5.0*
				Mass Moment of Inertia (kgm)	*2.0*
				Mass Axis Location	*0.2c*

The elastic axis location and orientation was allowed to vary between each of the cases. The gust profile for the case study was a 1-cosine gust with a 4 m/s amplitude and 6 m length; the freestream velocity was set to 50 m/s at sea level conditions. The aerodynamic model used 10 spanwise and 6 chordwise elements to adequately resolve the time dependent loads; these were determined from a panel density study shown in Ref. 7.

The first set of cases kept a constant elastic axis distribution across the span, shifting its location from 0.5c to 0.2c chord locations. The results of this study are shown in Figure 2. The elastic axis locations investigated include configurations where static instability may be of concern as well as cases of unconditional static and dynamic stability. The drag reductions of each configuration were compared, providing trends in configurations that can best exploit the gust to reduce the drag on the wing.

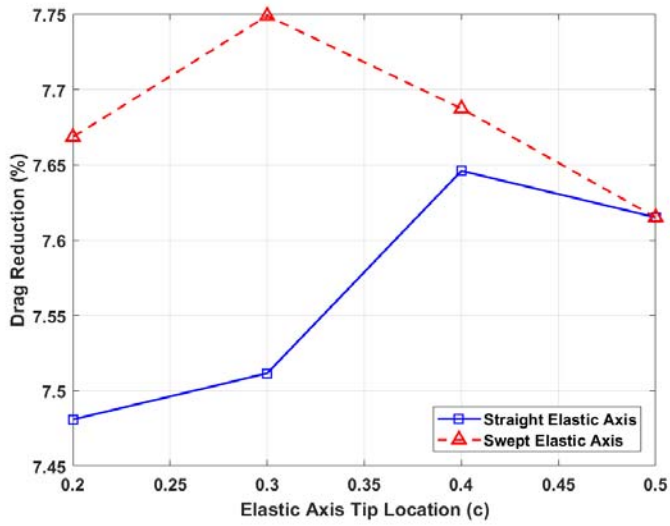

Figure 2. Overall drag reduction in response to 4 m/s 1-cosine gust as a function of elastic axis tip location and shape.

Across all the presented cases, the drag on the elastic wing, through the duration of the gust, was reduced by over 7.5%. Moving the elastic axis forward, towards the aerodynamic center, showed a further increase in the energy extracted from the gust. However, a point exists at which the energy extracted from the gust decreased from the previous case. Between an elastic axis location of 0.4c and 0.3c, the energy extracted was reduced by approximately 0.15%. Similar research conducted by Mai [10] concluded that bending deformations play a significant role in the energy harvest; additionally, it was noted that the increased downward twist created from moving the elastic axis towards the aerodynamic center is also beneficial. The benefits of an increased downward twist created from moving the elastic axis forward in these cases were outweighed by the reduced tip deflection, thus resulting in slightly less energy being harvested from the gust.

The second case study looked at the effect of adding sweep to the elastic axis. The results are also shown in Figure 2, together with the already discussed results of the wing with an unswept elastic axis. The results for the swept configuration are plotted versus the tip location of the elastic axis. The following case study investigated the effect of adding a linear variation to the elastic axis location. For each case, the elastic axis was held fixed at the root at 0.5c; the location at the tip was allowed to vary between 0.5c and 0.2c, thus altering the coupling between elastic

and aerodynamic forces across the span. The resulting drag reductions from this case study are compared to those found from the straight elastic axis.

A marked improvement in performance was noted when adding sweep to the elastic axis. All cases showed similar performance when compared to their steady state configuration; nearly a 7.75% reduction in drag was noted across all configurations. Comparing the results of the straight and swept configurations, adding sweep to the elastic axis provided additional performance gains between 0.05-0.25%. For example, moving the tip location of the elastic axis to 0.3c showed a nearly 0.25% gain over the straight case. Adding sweep to the elastic axis is a more realistic approach since this can be achieved through tapering of the internal structure and careful placement of fibers. Shifting the entire elastic across the whole span is more difficult, and based on the study shown here, does not provide as good performance gains. The further forward the elastic axis is swept, a greater performance increase over both the rigid wing and straight elastic axis case is seen.

The same gust profile was used on a rigid wing configuration, which showed very minimal energy harvesting (<1% drag reductions). The addition of elastic deformations, thus, has a significant effect on the energy harvesting capabilities of the wing, which is in line with trends shown by Mai [10].

The presented results show energy gains that are within a reasonable margin of those presented in other research, such as those in Ref. 10. Drag reductions from similar gust profiles of approximately 10% were observed; this research modelled the entire aircraft while the current study only investigates the effects on the wing. These changes likely contribute to some of the discrepancies in results. However, the comparison indicates that the presented results are within the correct range.

While the case studies indicate significant performance gains are possible, one must be wary of the possibility of static instability. With the elastic axis further aft, wing divergence can be a concern; however, by sweeping the elastic axis towards the aerodynamic center, as was done for the second case study, this reduces the likelihood of such instabilities occurring. The forward sweeping of the elastic axis, can, however, lead to undesirable reductions in aileron effectiveness. In the most extreme case, the elastic axis at the tip is forward of the aerodynamic center (0.2c); in this configuration, increases in lift cause a downward twisting of the wing. Thus, the increase in lift from deflecting the aileron may be negated by the lift reduction from the wing twisting downward, causing a loss in roll control. The above results are a reference for trends in improving gust energy extractions, while keeping in mind the possibility of the aforementioned static instabilities.

Conclusions

An aeroelastic model was presented to investigate the effects of aeroelastic tailoring on gust energy retrieval. The results from the model demonstrated performance gains through aeroelastic tailoring are possible; the addition of flexibility provided drag reductions of approximately 7.5%. Changing the orientation of the elastic axis provided further improvements of 0.25%. While these may seem like minimal gains, such techniques used on long endurance aircraft, such as high performance sailplanes, can mean the difference between winning and losing competition. Aeroelastic tailoring provides a means for passively extracting these performance gains, with little to no weight penalties.

The efficiency of the model makes it attractive for use in early design stages; computation time required for a single gust case on a desktop computer with a 3.5 GHz processor is approximately 8-9 hours. Higher fidelity methods such as coupled CFD-CSD approaches require significantly more computational power, in the order of 36-48 hours [12], in addition to the pre-processing time required for mesh generation and refinement. In comparison to similar coupled UVLM approaches, the presented method requires fewer elements to achieve a similar force resolution, especially for induced drag computations and provides improved numerical robustness. Highly non-planar wakes as a result of elastic deformations and gust encounters can also be modelled with reasonable accuracy.

References

[1]Allen, M. J. and Lin, V., "Guidance and Control of an Autonomous Soaring Vehicle with Flight Test Results," *45th AIAA Aerospace Sciences Meeting and Exhibit*, 2007.

[2]Bruni, C., Gibert, J., Frulla, G., Cestino, E., and Marzocca, P., "Energy harvesting from aeroelastic vibrations induced by discrete gust loads," *Journal of Intelligent Material Systems and Structures*, Vol. 28, No. 1, 2017, pp. 47-62.

[3]Langelaan, J. W., "Gust Energy Extraction for Mini and Micro Uninhabited Aerial Vehicles," *Journal of Guidance, Control, and Dynamics*, Vol. 32, No. 2, 2009, pp. 464-473.

[4]Bramesfeld, G. and Maughmer, M. D., "Relaxed-wake Vortex-Lattice Method Using Distributed Vorticity Elements," *Journal of Aircraft*, Vol. 45, No. 2, 2008, pp. 560-568.

[5]Ironside, D., Bramesfeld, G., and Schwochow, J., "Modeling of Wing Drag Reductions Due to Structural Dynamics in Atmospheric Gusts," *28th AIAA Applied Aerodynamics Conference*, 2010.

[6]Cole, J. A., *A Higher-Order Free-Wake Method for Propeller-Wing Systems*, Ph.D. thesis, Pennsylvania State University, 2016.

[7]Melville, M., *Modeling of Gust Energy Extractions through Aeroelastic Tailoring*, Master's thesis, Ryerson University, 2018.

[8]Melville, M., Kolaei, A., Bramesfeld, G., and Alighanbari, H., "An Efficient Model for Aeroelastic Tailoring of Aircraft Wings Under Gust Loads," *2018 AIAA Aerospace Sciences Meeting*, 2018.

[9]Hibbeler, R. C., *Mechanics of Materials*, Pearson, 10th ed., 2014.
[10]Mai, H. U., "The Effect of Aeroelasticity Upon Energy Retrieval of a Sailplane Penetrating a Gust," *XIXth Congress of OSTIV*, 1985.
[11]Bramesfeld, G., Ironside, D. J., and Schwochow, J., "Simplified modeling of wing-drag reduction due to structural dynamics and atmospheric gusts," *Collection of Technical Papers - AIAA Applied Aerodynamics Conference*, 2008.
[12]Combes, T. P., Malik, A. S., Bramesfeld, G., and McQuilling, M. W., "Efficient Fluid-Structure Interaction Method for Conceptual Design of Flexible, Fixed-Wing Micro-Air-Vehicle Wings," *AIAA Journal*, Vol. 53, No. 6, 2015, pp. 1442{1454.

Circling calculations for predesign of sailplanes

Jan Himisch[1], Kai Rohde-Brandenburger[2]
[1]*DLR, Institute of Aerodynamics and Flow Technology, Braunschweig, Germany, jan.himisch@dlr.de*
[2]*DLR, Institute of Aerodynamics and Flow Technology, Braunschweig, Germany, kai.rohde-brandenburger@dlr.de*

Abstract: The predesign of sailplanes is mostly based on the calculated polars for straight flight. The tool chain used at DLR for optimizing sailplanes in straight flight is well validated and includes the whole plane with all tailplanes and trim-surfaces.The tool-chain was modified to allow the same calculation in circling mode with the modification of the velocities on each wing due to circling.The intended conference article will cover the results of the validation, which are based on measurements performed with the Discus-2c DLR, as well as the results of optimization illustrating the potential future benefits of such an optimization process.

***Keywords*:** predesign, sailplane, low speed aerodynamics.

Introduction

The "Discus-2C DLR" is used as research plane at the German Aerospace Center. The flight performance measurements over the last 60 years led to high quality alculation methods. The fast calculation of straight flight polars of sailplanes can be done more and more exact and therefor can be used for optimization calculations for new designs, leading to actual high performance sailplanes like the Ventus 3 or the Arcus.
The calculation of circling polars were not used in optimization calculations in the past. The tool chain used at the DLR is well validated from measured straight flight polars, but no circling polars are given for validating the circling polar calculation.
For this reason, the Discus-2C DLR was modified with Rudder-Sensors and an experimental autopilot system, used for flying nearly static circles with constant bank angle and constant velocity. The measured values will be used for validating the trim calculation in circling flight, but also for validating the sink speed calculation while circling. Even the spanwise lift distribution is measured with the calibrated strain gauges and can be used for validating.

Discus-2C DLR

The Discus-2C DLR was modified with many sensors. The Five-Hole-Probe at the Nose-Boom is used for determining the Angle of Attack and the SideSlipAngle, and also for stagnation and static pressure. A big motor box from the Ventus M in the fuselage can be used for mounting measurement equipment. In the structure of the Wings, the fuselage and the tail 46 strain gauges were implemented while construction. In the fuselage and the wings, high performance rudder sensors were mounted as near as possible to the Rudders. The actuators in the fuselage are able to actuate the horizontal and the ailerons.

Figure 1. Discus-2C DLR in flight

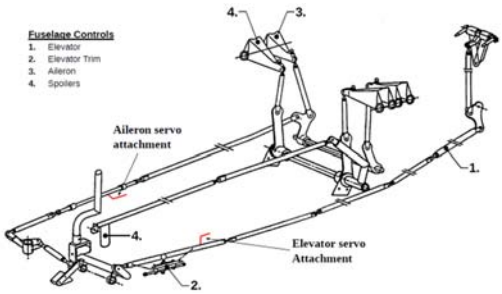

Figure 2. Fuselage Controls with actuator mounting points

Circling flight Polars

While in circling flight, a lot of parameters differ from steady flight calculations. Due to the circling and the needed bank angle, the freestream velocity is not equal over the wing. The needed Lift increases due to higher g-loads, resulting in higher wingloading. If an updraft speed of the thermal is taken into account, the updraft velocity changes the freestream velocity distribution too.

The basic parameters are calculated by formula from [1] and [2]:

$n_{z'} = \frac{1}{\cos\varphi}$; $A_{z'} = m * g * n_{z'}$; $V_K = \sqrt{\frac{2*m*g}{\rho*S*C_L\cos\varphi}}$ $R_g = \frac{V_K^2}{g*\tan\varphi}$

$\Omega = \frac{s*\cos\varphi}{R_g}$ $\eta = \frac{y}{s}$

For calculating the freestream distribution, the work from [1] was taken into account.
The local stream velocity differs from the flight speed with the spanwise coordinate. The local stream velocity are calculated for each axis.

$$u_e(\eta_v) = V_K * (1 - \Omega * \eta_v) * \cos\beta_g$$
$$v_e(\eta_v) = V_K * (1 - \Omega * \eta_v) * \beta_g * \cos\varphi$$
$$w_e(\eta_v) = -V_K * (1 - \Omega * \eta_v) * \beta_g * \sin\varphi$$

The local stream velocities are added to the stream velocity on each panel in the LiftingLine Programm.

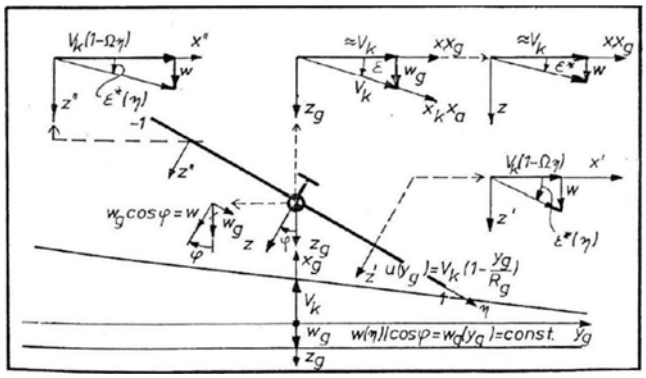

Figure 3. Velocity components in circling flight with sinkspeed from [1]

With this difference in local velocities LiftingLine is calculating “a straight flight polar with local circling flight velocities”. Those values have to be recalculated into the normal coordinate system in accordance with [2].

Calculation method

As allready demostrated in previous publications[3], a LiftingLine[4] based prozess chain can be used to predict the performance of new glider-designs. This design chain is additionally using a polar interpolastion method to account for friction based drag determind with Xfoil based on the sections.
Up to now the design chain was limited to straight forward flight. In recent years the current LiftinLine Version has been extended to allow the simulation of a circling wing.

Results

The paper will contain the comaprisson between the measured flight performances with the simulated ones in order to validate the process chain. This will contain the attemp to compare the measured and the simulated sinking speeds and the trim states.

References

[1] Müller, B.; Inst. f. Aerodynamik, 1982: Entwurfsstudie f. ein Segelflugzeug mit Flächenklappen, DFVLR
[2] Thomas, F.; 1993: Fundamentals of Sailplane Design, College Park Press
[3] Himisch,J.; Rhode-Brandenburger,K.; “The influence of target function selection on the optimization of winglets for the glider SB14, using and developing a Lifting-Line based program-chain”, OSTIV-Congress 2014
[4] Karl-Heinz Horstmann, Ein Mehrfachtraglinienverfah- ren und seine Verwendung für Entwurf und Nach- rechnung nichtplanarer Flügelanordnungen, DFVLR Forschungsbericht 87-51

Airfoil maximum lift coefficient assessment for preliminary design purposes and optimization

Lukáš Popelka[1], David Šimurda[2], Vladislav Skála[2], Milan Matějka[2], Michal Schmirler[1], Francisco Urbano Garcia[1]

[1] *Center of Advanced Aerospace Technology, Czech Technical University in Prague, Czech Republic, l.popelka@fs.cvut.cz*

[2] *Institute of Thermomechanics, Academy of Sciences of the Czech Republic, Prague*

Abstract: Preliminary sailplane design requires solid input on maximum lift airfoil coefficient. Current approach relies on extrapolation of wind-tunnel data, which was considered excessively overestimating with respect to Reynolds number. New study presents analysis of the wind-tunnel data for selected typical sailplane airfoils. In a range, where published data are missing, new experiments were performed. A universal correlation of cLmax as function Reynolds number is created. Theoretical/numerical methods do not provide required accuracy for high angles of attack in relation to cLmax. This creates an issue for the optimization purposes. Therefore, a study to relate cLmax to airfoil geometry is carried out.

***Keywords*:** airfoil maximum lift coefficient; wind-tunnel testing; parametric design laminar-flow high-performance aircraft.

Introduction

Development of laminar-flow high-performance aircraft requires solid aerodynamic data inputs at all stages of the design. Whereas crescent wing planform is becoming a new canonic form, airfoils retain their vast room for tailoring (optimization) for the given purpose (target function).

Historically, airfoil families were developed and thoroughly tested. This coverage of optimization space enables first rational selection of the wing section. Implementing highest scoring airfoil as first design iteration for optimization is suggested (e.g. [1]). The other approach, preferred by design offices, is to leverage a proven (typically proprietary) legacy airfoil. These options are studied for the entire aerodynamic conceptual design (CDR).

Given the Certification Specification constraints, Target Function objectives and Crew perception, maximum lift coefficient value is of paramount importance. Absolute value comparison at design point is executed, whereas function of the Reynolds number shall be captured to enable optimization of the wing design (variation of wing area in given wingspan-restricted classes yield chord changes).

Typically, aerodynamic design evolves into preliminary phase (PDR) with a brand-new airfoil design. Inevitably, value of cLmax ratio vs. reference airfoil and cLmax=f(Re) capture drives main conclusions for both CDR and PDR.

Analysis of published data

As mentioned, an extensive published data are available on the NACA 6-series family, Wortmann and Althaus airfoils and other, as tested in well-known and proven wind-tunnels, e.g. TDT (NASA Langley), LWK and MWK (Uni Stuttgart), LSL (Uni Delft). These are supplemented by particular testing of NACA 6A airfoils in the Czech Republic in Aerospace and Test Research Institute (ARTI, Czech VZLU abbreviation used more frequently). These were part of extensive wind-tunnel testing for the Czech L-13 sailplane, in the wind-tunnel D = 3m. It followed an ideal scheme: airfoil(s)-wing-sailplane with empennage.

Full list of test data references is available in [4] and [5]. Fig. 1 presents selection of airfoils that were subject to studies in the abovementioned facilities. Data are plotted as a function of the Reynolds number. It enables to draw a first conclusion, that extrapolation from a small Re-range may lead to significantly misleading results. Unfortunately, to authors knowledge, this is a fairly common mistake nowadays, spanning from student projects even down to design offices.

Common trends can be identified, with two apparent exceptions, these being Wortmann designs FX66-S-196V1 and FX66-17AII-182 (cLmax increases with Re decreased). First was tested at LSL, while the latter at TDT. Outlined integral characteristics behavior is attributed to laminar boundary layer separation driving the flow at high angles of attack.

For sake of simplicity, this article deals only with turbulent separation affected airfoils at their cLmax, with respect to Reynolds number influence.

On a local level, i.e. for each particular airfoil, it is possible to formulate a mathematic correlation of cLmax=f(Re). Further discussion is followed in fulltext of the Technical Soaring Journal.

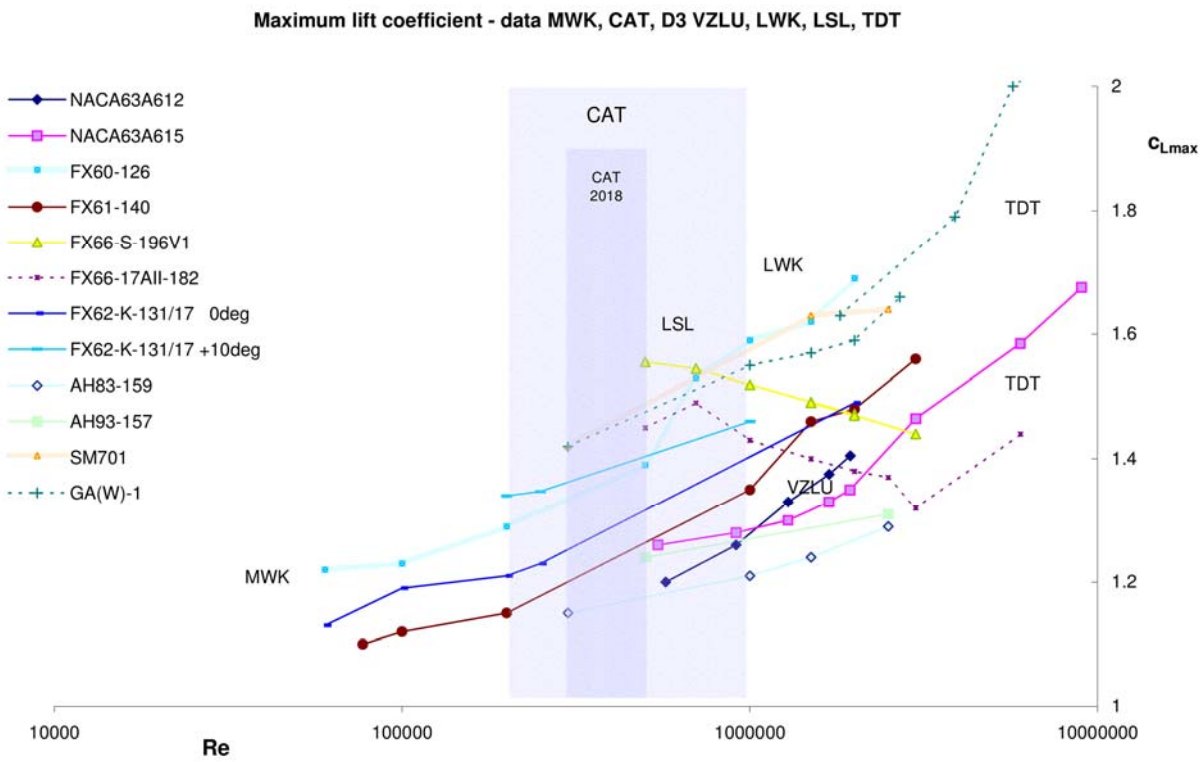

Fig. 1 Maximum lift coefficient for set of reference airfoils, whole range of available Reynolds numbers in the CAT wind-tunnel and range of currently presented data (2018)

Additional wind-tunnel testing

An analysis of the published data, summarized in Fig. 1 showed that there is a vacant data area between Re = $2 \cdot 10^5$ and $5 \cdot 10^5$. A decision has been made to bridge this interval by an additional testing.

The closed-circuit, closed test section, research wind-tunnel (CAT) of the Institute of Thermomechanics Academy of Sciences CR, [2] was equipped by new MP1 test section of dimensions 865 x 485 x 900mm3, being designed and validated for airfoil and wing-body investigations [3], Fig. 2.

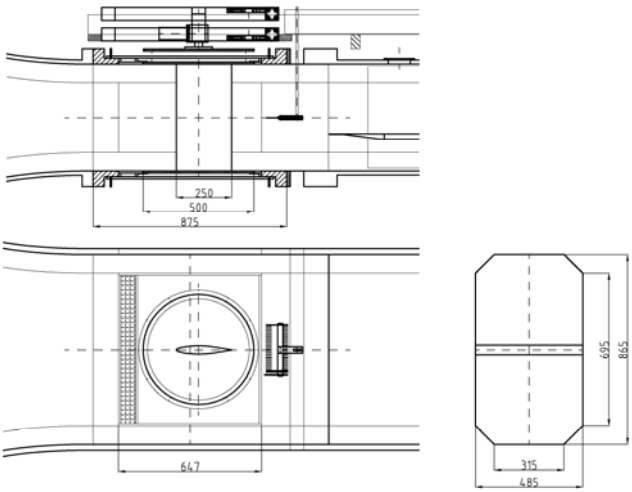

Fig. 2 Airfoil test section MP1 of the CAT wind-tunnel

MP1 layout is given in Fig. 2. Circular end plates provide an attachment for both types of models, Fig 3. They are 500 mm in diameter and are flush with the wind-tunnel walls. The turntables are electrically driven to enable angle of attack changes for the model. The airfoil is mounted so the center of rotation of the circular plates is at 40% of the model chord. The same fraction is preserved for the wing-body model, with respect to wing chord. Air gaps at the tunnel walls are sealed by labyrinth arrangement. Mean flow velocity in the test section is set by pressure difference on wind-tunnel contraction, measured by Omega pressure transducer PX653-02D5V, range 2”. PSI Model 9010 pressure scanner, with 16 individual inputs, is used for data reading from tested model. Secondary option employing a 32-channel Scanivalve device was develop in order to expedite the test process. Airfoil lift

coefficient is evaluated via static pressure distribution along walls of the test section. Drag coefficient is measured using wake pressure rake, operated by electrically driven 2-axis traversing system. LabVIEW software is used for data acquisition.

Fig 3 Airfoil integration into the MP1 test section (PW09-145K17)

Relation between airfoil lift coefficient cL and integral pressure coefficient cW, yielded from static pressure distribution on test section walls, Fig. 4, has been established by measurements on four configurations of NACA63A421 airfoil equipped by static pressure taps. 2nd order polynomial fit was used for cL / cW = f(α). Evaluated uncertainty of 1.02% was considered adequate for ongoing research of active and passive flow control. Pressure rake with 40 individual total head tubes of outer diameter 1.2mm, spaced 5.5mm provides data for momentum analysis in the airfoil wake. Longitudinal static pressure gradient is used for correction on a reference dynamic pressure.

Following wind-tunnel models were carefully produced along with MP1 assembly: FX66-S-196V1, AH83-159 and SM701 with model chord c = 250mm. Set of reference airfoils was further extended by GA(W)-1 airfoil of c = 300mm, NACA63A615, FX60-126, FX62-K-131, FX66-S-196V1 and AH93-157 of c = 400mm.

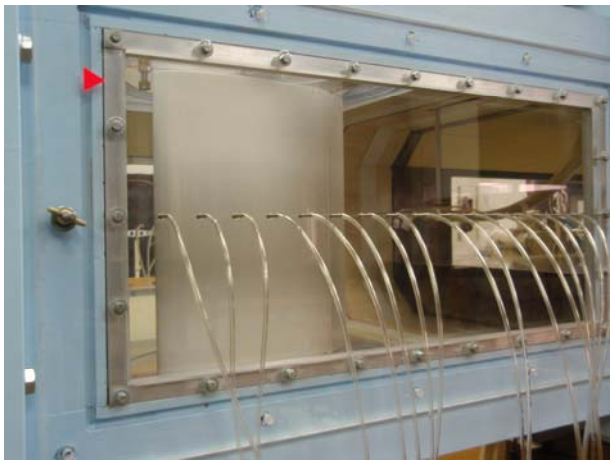

Fig 3 Static pressure sensing on test section walls

Results

General overview of maximum lift coefficient properties was provided, based on published references, supplemented by own testing. Focus has been put on single-element (unflapped) airfoils.

Described starting line enabled to draw a correlation between airfoil geometry and corresponding cLmax. Actual idea has been devised by Nonweiler (1956, 1955), quoted in classical text [6], in a graphical form. Herein presented formula (1), valid for Re = $1 \cdot 10^6$ enables sought input for CDR and PDR-type aerodynamic reviews, involving reference, legacy and new airfoils. Evaluation of calculated *(reg)* vs. measured value *(exp)* ratio is in line with formulation of optimization tasks:

$$c_{L_{max}} = Ay_1 + B$$

$$A = at^2 + bt + c$$
$$B = dt + e, \qquad (1)$$
$$a = 1.828 \cdot 10^3,\ b = -8.121 \cdot 10^2,\ c = 1.050 \cdot 10^2,\ d = 6.462,\ e = -7.236 \cdot 10^{-1},$$
$$f_{cLmax} = \frac{c_{Lmax\ j}}{c_{Lmax\ ref}}$$
$$f_{cLmax\ exp}/f_{cLmax\ reg} = 0.994 \pm 0.018$$

t is defined as airfoil thickness, while y1 is a coordinate in x = 0.05·c. Both scalars [t; y1] are normalized by airfoil chord c. Correlation of airfoil nose geometry with cLmax is provided incl. accuracy range.
Stuttgart profil catalogues I and II, [7]&[8] in total 24 airfoils, single-element, cambered type, spanning from FX61-184 to AH95-160 were used to provide required sought input data.
Flapped airfoils, even at zero flap deflection were ruled out from the statistics, due to typical lift curve behavior (experiencing so called plateau before angle of attack α reaches cLmax).
Besides pure fit, there is a physical background to [t; y1] scalars, since both are good measures of a suction peak, driving boundary layer separation at cLmax.

Acknowledgement
Development of data acquisition methodologies has been supported by the ESIF, EU Operational Programme Research, Development and Education, and from the Center of Advanced Aerospace Technology (CZ.02.1.01/0.0/0.0/16_019/0000826), Faculty of Mechanical Engineering, Czech Technical University in Prague.

References
[1] Popelka, L.: Aerodynamic Optimization of Airfoils. Dissertation, Prague: Czech Technical University in Prague, 2006, 166p.
[2] Píchal, M.: Aerodynamický tunel 0.485 x 0.865 m^2 se široce měnitelným pásmem turbulence. Research Report Z 91/59, Praha: Československá akademie věd, Ústav pro výzkum strojů, 1959. 38p. English: Wind-tunnel 0.485 x 0.865 m2 designed with adjustable outer stream turbulence. Czechoslovak Academy of Sciences.
[3] Popelka, L.: Wind Tunnel Test Section for Airfoils and Bodies, Research Programme Feasibility Studies. Conference Topical Problems of Fluid Dynamics 2008. Prague: Institute of Thermomechanics AS CR, v. v. i.
[4] Thomas, F.: Fundamentals of Sailplane Design. 3rd Ed. College Park Press, 1999. 274 p. ISBN 0-9669553-0-7
[5] Popelka, L., Matějka, M., Šimurda, D, Součková, N.: Evaluation of Wind-Tunnel Test Section for Airfoils and Bodies. Conference Topical Problems of Fluid Dynamics 2011. Prague: Institute of Thermomechanics AS CR, v. v. i.
[6] Schlichting, H., Truckenbrodt, E., Ramm, H.: Aerodynamics of the Airplane. 1st Ed. N.Y.: McGraw-Hill, 1979. 526 s. ISBN 0-07-055341-6
[7] Althaus, D., Wortmann, F.X.: Stuttgarter Profilkatalog I
1st Ed. Braunschweig: Vieweg & Sohn Verlagsgesellschaft, 1981. 319 p. ISBN 3-528-08464-2
[8] Althaus, D.: Niedriggeschwindigkeitsprofile
1st Ed. Braunschweig: Vieweg & Sohn Verlagsgesellschaft, 1996. 592 s. ISBN 3-528-03820-9

Transition Prediction Results for NLF(1)-0416 Airfoil and Sickle Wing

Martin Kruse[1], Federico Muñoz[2], Rolf Radespiel[2]
[1]*DLR, Institute of Aerodynamics and Flow Technology, Braunschweig, Germany*
[2]*Technische Universität Braunschweig, Institute of Fluid Mechanics, Germany, r.radespiel@tu-bs.de*

Abstract: In this paper, results for two of the validation test cases of the AIAA SciTech 2018 Special Session "CFD Transition Modeling and Predictive Capabilities" are presented. The well-known Somers NLF(1)-0416 airfoil is chosen as a 2D-test case. The capability of transition prediction in highly three-dimensional flows is demonstrated on the Sickle Wing Model test case. Simulation results are obtained from RANS flow solver with an iteratively coupled transition prediction scheme. Boundary layer stability is calculated by means of local linear stability theory (LST) and the transition location is estimated by a 2-N-factor method. The results are compared to given experimental data.

***Keywords*:** 3D boundary layers, boundary layer transition, stability anaylsis.

Introduction

For the development of laminar-flow high-performance aircraft it is necessary to have reliable numerical methods that allow predicting where and how laminar-turbulent boundary layer (BL) transition occurs. Methods based on local linear stability theory (LST) and the e^N-method are still widely employed. Founded on the parallel flow assumption, local stability methods neglect effects of stream- and spanwise boundary layer variations and boundary-layer curvature [1]. While streamwise variations of the boundary layer may be present in airfoil flows, spanwise gradients can be found in regions of wing fuselage interaction, at connections between wing sections with different sweep and taper, and around intersections of wing and winglet. The present work aims at assessing the present capabilities in predicting boundary layer transition for well established 2D and 3D test cases.

Methodology

In the present work, DLR's RANS Solver TAU with iteratively coupled transition prediction [2] is employed. The prediction of transition locations is based on evaluation of the local stability of boundary layer profiles extracted directly from the RANS flow solution. For this purpose, the linear stability solver lilo is used to calculate the spatial growth rates of modal disturbances of Tollmien-Schlichting and cross flow instability type. The transition location is predicted at the point where one of the amplitude ratios of investigated modes reaches a threshold value of e^N. Distinction between TS and CF modes is made by employing a 2-N factor transition criterion. The critical values N_{TS}, N_{CF} are of empirical nature and must be prescribed by the user. The local amplitude ratio of a mode is obtained from integration of spatial growth rates along the group velocity trajectory. For 2D subsonic flow, the group velocity trajectory is aligned with the surface contour. For 3D flow, the group velocity trajectory is approximated here by the direction of the streamlines at the edge of the boundary layer. Numerically, this approach is efficient, since the linear stability ODEs are solved along a discrete number of lines, instead of solving the spatial eigenvalue problem. For each external streamline a transition point is calculated. Connecting the discrete transition points by a polyline and projection to the contour gives a closed transition front, required by the CFD solver. A flow diagram of the coupling process is shown in Figure 1. The inclusion of the outer iterative loop allows the numerical solution to capture the effect that boundary layer transition has on the local and global RANS flow field. For details of technical implementation of the TAU-Code's transition module please refer to [2]. A wide range of application examples of the method can be found in [3].

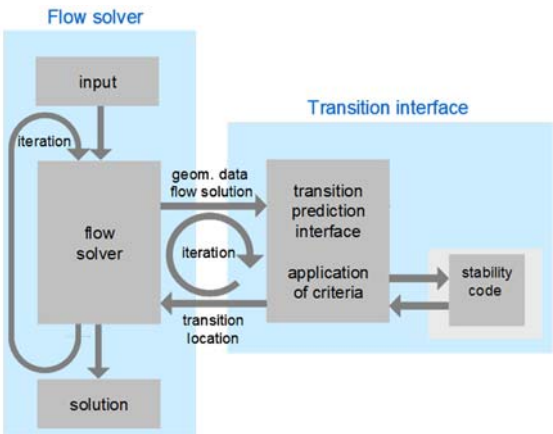

Figure 1 Coupled Transition Prediction

Results

NLR(1)-0416 airfoil. The NLF(1)-0416 airfoil is a classic validation case for 2D flow transition. Designated to general aviation purposes, the natural laminar flow airfoil has a design c_l=0.4 and a maximum relative thickness ratio t/c=0.16 in combination with favorable stall characteristics. Results from extensive wind tunnel testing are summarized in the report of Somers [4]. Case 3 of the AIAA Special Session "CFD Transition Modeling and

Predictive Capabilities" refers to the experimental results obtained at Re=4.5E6, M=0.1 and T=300K. The free-stream turbulence intensity is given as Tu=0.15%. According to the correlation of Mack this turbulence level relates to a critical N-Factor for TS instability of NTScr=7.2. The numerical results given below have been carefully scrutinized for their numerical accuracy [5]. They are grid-coverged to about plotting accuracy.

The transition prediction method is validated against experimental data for various angles of attack of the NLF(1)-0416 airfoil.

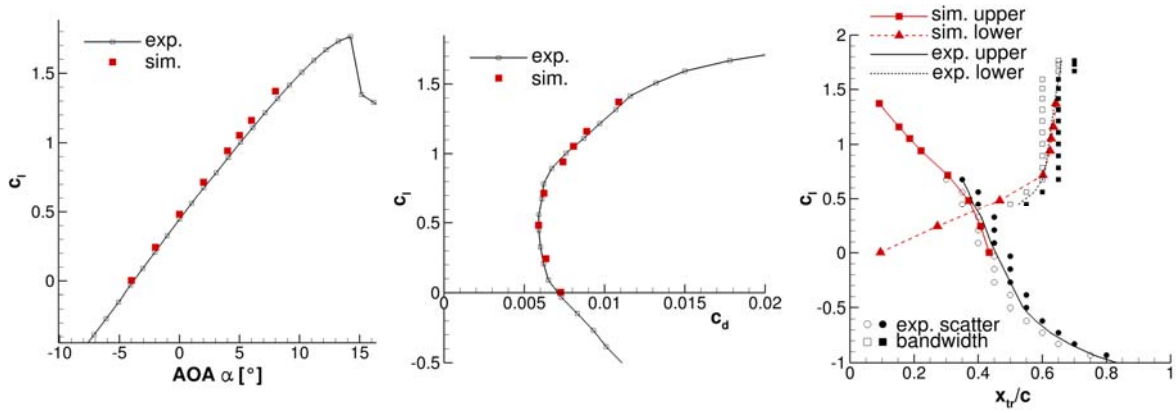

a) lift coefficient over AOA **b) drag polar** **c) lift coefficient over transition location**

Figure 2 Comparison of simulation results with free transition and experimental data [4]

In Figure 2 the results from simulation with transition prediction are plotted against the experimental data of Somers. The experimental lift slope (Figure 2a) is well matched, although the c_l obtained from simulations shows a slight over prediction of lift, increasing with AOA. As shown in Figure 2b, the drag polar shows an excellent agreement of experimental and numerical results. The laminar bucket is predicted almost exactly. Finally, the predicted transition locations are compared to the measurement in Figure 2c. All predicted transition locations lie in the bandwidth of Somers measurements.

Sickle Wing. The Sickle Wing model of TU Braunschweig is a versatile validation experiment to study swept wing transition. The model is characterized by its spanwise sweep variation over three segments. Depending on Reynolds number and angle of attack, the model covers a wide range of transition scenarios, including Tollmien Schlichting-, cross-flow- and mixed mode transition. Near the kinks, locally strong spanwise gradients are induced by the change of sweep angle. Here, rapid changes in the experimental transition location are observed. The highly three dimensional base flow in these regions is a challenge for current transition prediction methods, especially for those relying on the local parallel flow assumption.

The transition experiments with the Sickle wing referred to in this section were conducted in September 2015. The model was tested in DNW-NWB wind tunnel. Figure 3 shows the model installed on a rotational floor inside the closed-wall test section (3.25m x 2.80m x 8.0m). This low-speed facility offers favorable conditions for experiments with natural transition. The given nominal turbulence intensity is Tu_x = 0.053% at 60m/s. Critical N-factors for this tunnel were given by [6] . Infrared thermography (IRT) was employed to detect flow transition in the experiments. This imaging method measures radiation intensity emitted from the models surface. As flow transition from laminar to turbulent causes a distinct increase in convective heat flux, the transition location can be detected as long as a small difference of flow and surface temperature exist. The advantage of IRT is that it is non-intrusive and delivers surface data of high spatial resolution. The Sickle Wing model has been optimized for transition detection by means of infrared thermography. The surface coating is low reflective and possesses a high emission coefficient. A rms surface roughness of 1.47µm was measured. To enhance contrast of thermal imaging, the model features an internal electrical heating. Further, the model is equipped with 108 pressure taps. The pressure taps are aligned in three rows at the center of each sweep segment (see Figure 4). For a comprehensive description of the wind tunnel model see Petzold [7]. Techniques of IR-image acquisition and processing as well as transition line extraction are described in [6].

The numerical simulation of the 'Sickle Wing' experiment required significant effort for mesh generation, as nozzle and wind tunnel walls were included in the simulation. A structured mesh of 440x400x162 points served for resolving the 3D boundary layer flow of the sickle wing. In total, the grid consists of 45million grid nodes, of which 28.5 million nodes are spend for the boundary layer mesh around the model. This explains why computational costs for such simulation are higher than for standard RANS calculations.

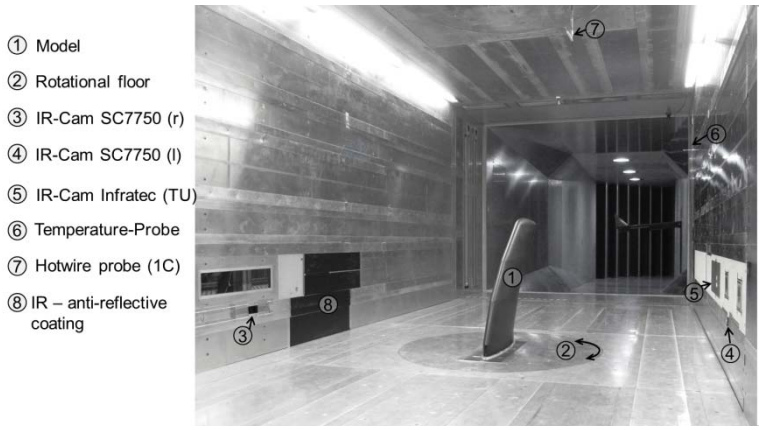

Figure 3 Experimental set-up in the closed test section of NWB

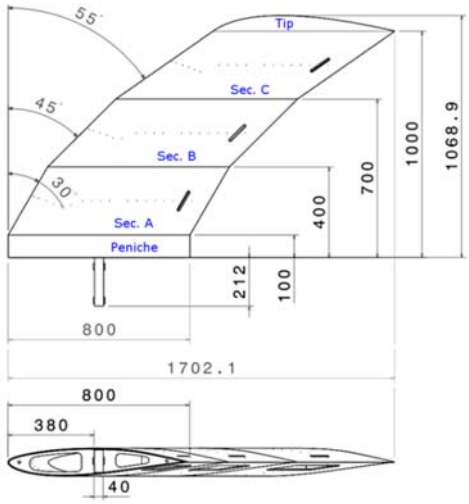

Figure 4 Sketch of the Sickle Wing model. All dimensions in mm.

For this validation test case with fully 3D boundary layers, transition prediction by means of LST and e^N is applied along external streamlines. For this purpose, 90-100 external streamline starting points were prescribed along the span on both sides of the surface. A 2-N factor transition criterion is evaluated for TS and CF instabilities. Based on the experimental results published in [6], the critical N-factors for transition prediction of this wind tunnel experiment are chosen as N_{TScrit} =11.0 and N_{CFcrit} =7.6. No interaction model is employed, i.e. transition is either caused by TS or by CF instability. Ref. [5] presents more details of the computational setup. The comparison of calculated pressure coefficients with experimental data displays a high level of agreement, as Figure 5 shows. As the consistency of numerical and experimental surface pressure distributions is a basic requirement for the correct prediction of the boundary layer, the numerical effort taken is justified.

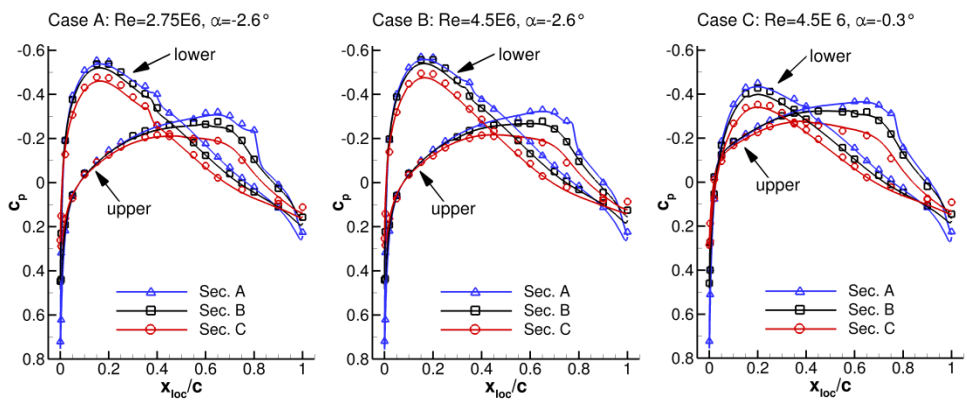

Figure 5 Comparison of c_p distributions for Sickle Wing test cases. Solid lines denote CFD results; symbols denote measurement data

The predicted transition locations were compared with the experimental transition locations obtained from infrared thermography. Overlay images of experimental and numerical transition locations are used for the presentation and discussion. The results show that for the majority of cases a very good prediction of the location of flow transition is achieved. In regions with pure TS type transition or transition by laminar separation bubbles, the accuracy of the prediction is highest. The prediction of cross flow type is fairly good in many cases. Figures 6-7 display samples of the comparison, which include the effects of changing the Reynolds number. A closer examination of the cases where the prediction of cross flow transition does not match the experimental data reveals that the sign of the spatial deviation w.r.t. to the experimental transition line is dependent to the side of the wing model. It appears that the difference in surface curvature of the model affects the growth of CF modes. This effect is not captured by the LST method employed [5].

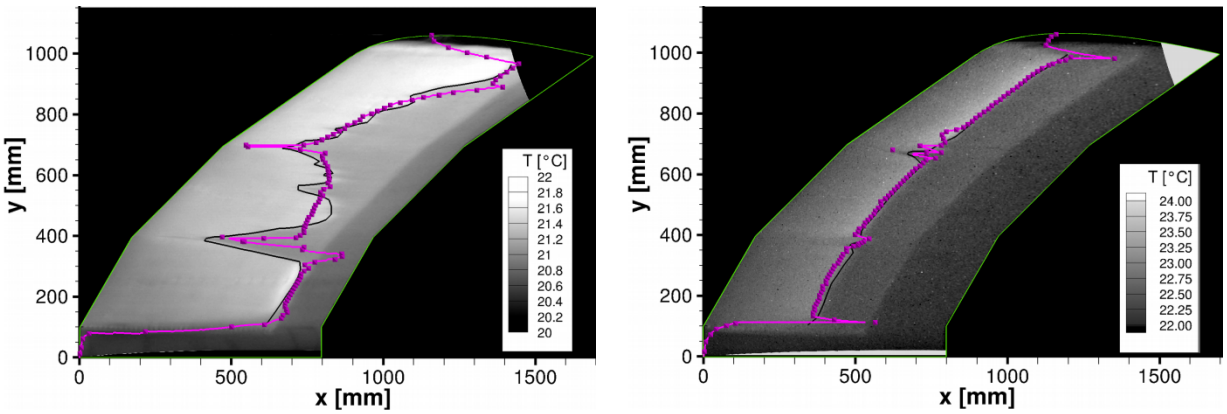

Figure 6 IR-image with extracted experimental transition line (black) and predicted transition line (pink) for α =-2.6°, Re=2.75·10^6, left: upper surface, right: lower surface

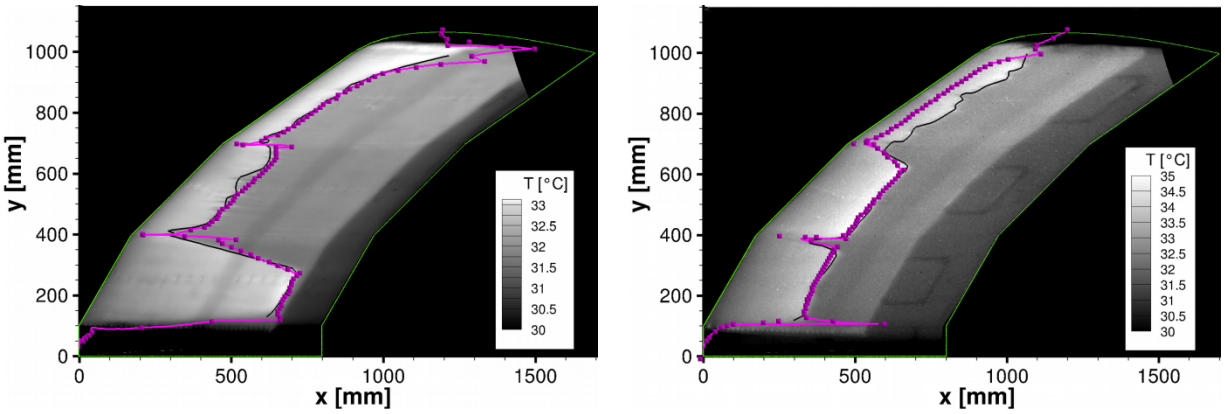

Figure 7 IR-image with extracted experimental transition line (black) and predicted transition line (pink) for α =-2.6°, Re=4.5·10^6, left: upper surface, right: lower surface

In the regions of sweep changeover of wing segments, strong spanwise pressure gradients are imposed. Here, the assumption of local parallel flow underlying linear stability theory is clearly violated. But even in these regions the transition prediction method captures the right trends and appropriately predicts the increase of cross flow towards the kinks. Only at very close distance to the kink regions, the predictive quality reduces or the transition model fails. As other types of flow instability may trigger transition to turbulence near the kink regions, the employed transition model is likely to be unsuited for reliable transition predictions in these local areas.

References

[1]Reed, H. L., Saric, W., Arnal, D., 1996: Linear Stability Theory applied to Boundary Layers, Ann. Rev. Fluid. Mech., 281, pp 389-428.

[2]Krimmelbein, N. and Radespiel, R., 2009: Transition prediction for three-dimensional flows using parallel computation. Computers & Fluids 38, pp 121–136.

[3]Krimmelbein, N., and Krumbein, A., 2011: Automatic Transition Prediction for Three-Dimensional Configurations with Focus on Industrial Application, Journal of Aircraft, Vol. 48, No. 6, pp. 1878–1887. doi:10.2514/1.C031230

[4]Somers, D. , 1981: Design and experimental results for a natural laminar flow airfoil for general aviation applications. NASA-TP-1861, L-14117.

[5]Kruse, M., Munoz, F., Radespiel, R. 2018: Transition Prediction Results for Sickle Wing and NLF(1)-0416 Test Cases, AIAA-2018-0537.

[6]Kruse, M., Küpper, A., Petzold, R., Munoz, F., 2018: Determination of the Critical Cross Flow N-factor for the Low-Speed Wind Tunnel Braunschweig (DNW-NWB). In: Dillmann A. et al. (eds) New Results in Numerical and Experimental Fluid Mechanics XI. Notes on Numerical Fluid Mechanics and Multidisciplinary Design, vol 136. Springer, Cham, Switzerland, pp. 251-261. ISBN 978-3-319-64518-6, DOI https://doi.org/10.1007/978-3-319-64519-3_23

[7]Petzold, R., Radespiel, R., 2015: Transition on a wing with spanwise varying crossflow and linear stability analysis, AIAA Journal, Vol. 53, pp. 321-335.

Prediction of insect contamination on airfoil by using CFD methods

Vojtech Betak[1]
[1]*Czech Aerospace Research Centre, Department of Engines, Czech Republic, betak@vzlu.cz*

Abstract: Presented work is focused on prediction of insect contamination on airfoil by using Computational Fluid Dynamics (CFD) methods. This work is based on the previous project focused on the development of a robust algorithm for particle tracking (rain droplets) and estimate place of impact on complex geometry (aircraft). Results of these simulations were used to estimate critical place on aircraft structures where critical places for an ice accretion are. The developed algorithm was also used to simulate soiling of road vehicles. The soiling problem is closely connected with aircraft industry too. Especially in the case of modern gliders which are using a wing with laminar profiles. Any kind of the profile contamination leads to a transition from laminar to turbulent flow which has a negative impact on glider performance. Most of the codes (e.g. NASA – LEWICE, ...) was built on particle tracking by using a Lagrangian method which is simple and fast. Evaluation of results for 2D simulation is very simple but in case of complex 3D geometry and turbulent flow is evaluation more difficult. Therefore the system of ordinary differential equations (ODE) equation describing tracking of Lagrangian particles was reformulated into the system of partial differential equations (PDE) similar to the work presented by McGill University. This system of PDE is easy to implement into modern CFD codes based on finite volume or finite element methods.
Results obtained from the implementation of an algorithm for the Eulerian approach for particle tracking into open-source CFD package OpenFOAM and simulations of Drosophila impact on 2D airfoil are shown in this paper. There are selected two flight regimes (cruise, climb) characterized by different Reynolds number and angle of attack. Results obtained from these simulations help to calibrate and validate modern laminar-turbulent transition model.

***Keywords*:** CFD, airfoil insection, Euler-Euler equation

Introduction

For many problems in fluid mechanics, it's necessary to solve a motion of particles or their concentration in the bounded domain. These problems are e.g. a flow of steam with evaporation or condensation, combustion of fuel, soiling or water-management of vehicles. These problems are usually solved by solvers which used Navier-Stokes equations for description of fluid flow and the particles are described by Lagrangian equations. This is necessary in some cases when we need to solve e.g. evaporation and combustion of fuel spray where the mass of droplet is time-dependent. In the case of vehicle soiling, the mass of particles is not changing in time. Therefore is easy to apply the Eulerian approach which is similar to Navier-Stokes equations. This approach was implemented into OpenFOAM in previous work [1] and was compared with the Lagrangian approach and applied on monitoring of water droplets impact on airplane surface to determine critical points for ice accretion.
In this work is developed algorithm applied to a problem of profile leading edge contamination by insect Drophilas which affect the performance of modern glider. The contamination of leading edge leads to transforming of the fluid regime from laminar to turbulent which leads to drag increase and reduce performance parameters. Results of these simulations are possible to use for calibration of laminar-turbulent transition model and study the effect of contamination level on performance parameters in a design phase.

Governing equations

In this case is used model of inviscid turbulent flow which is described by following system of equations

$$\frac{\partial u_i}{\partial x_i} = 0, \tag{1}$$

$$\frac{\partial u_i}{\partial t} + \frac{\partial u_i u_j}{\partial x_j} = \frac{-\partial \tilde{p}}{\partial x_i} + \frac{\partial}{\partial x_j}\left(\nu \frac{\partial u_i}{\partial x_j}\right) - \overline{u_i' u_j'} \tag{2}$$

where u_i is part of velocity vector U, $\tilde{p}$is kinematic pressure, $\nu$is kinematic viscosity and $\overline{u_i' u_j'}$is a part o Reynolds stress tensor which is modeled by EARSM turbulent model derived by Hellsten [4].

$$\frac{\partial k}{\partial t} + \frac{\partial k u_j}{\partial x_j} = P_k - \beta^* k\omega + \frac{\partial}{\partial x_j}\left[(\nu + \nu_t \sigma_k)\frac{\partial k}{\partial x_j}\right], \tag{3}$$

$$\frac{\partial \omega}{\partial t} + \frac{\partial \omega u_j}{\partial x_j} = \gamma \frac{\omega}{k} P_k - \beta \omega^2 + \frac{\partial}{\partial x_j}\left[(\nu + \nu_t \sigma_\omega)\frac{\partial \omega}{\partial x_j}\right] + \frac{\sigma_d}{\omega} max\left(\frac{\partial k}{\partial x_j}\frac{\partial \omega}{\partial x_j}, 0\right) \text{and} \tag{4}$$

$$\overline{u_i{}'u_j{}'} = \frac{\partial}{\partial x_j}(\nu_t \frac{\partial u_i}{\partial x_j}) + \frac{2}{3}k\delta_{ij} + a_{ij}^{(ex)}k. \tag{5}$$

This turbulence model is based on $k - \omega SST$ where $k$is kinetic energy of turbulence, $\omega$is specific speed of dissipation, $\nu_t$is turbulent viscosity and $a_{ij}^{(ex)}$is part of turbulent anisotrophy tensor. Definition if all model functions and constant is possible to find [4].
Movement of droplets is described by following system of partial differential equations which is similar to Navier-Stokes equations.

$$\frac{\partial \alpha}{\partial t} + \frac{\partial \alpha v_i}{\partial x_i} = 0, \tag{6}$$

$$\frac{\partial v_i}{\partial t} + \frac{\partial (v_i v_j)}{x_j} = (1 - \frac{\rho}{\rho_D})g_i - \frac{3}{4}\frac{c_d}{d}\frac{\rho}{\rho_D}|V - U|(v_i - u_i) \tag{7}$$

where αrepresent concentration of particles, $v_i$is part of particle velocity vector V, $\rho, \rho_D$is density of air and liquid, $g_i$is part of gravity vector, $d$is droplet diameter and $c_d = c_d(\mathrm{Re})$is drag coefficient of sphere based on local Reynolds number which is computed by following equation which is described in [3].

$$c_d = [\frac{1}{(\varphi_1+\varphi_2)^{-1}+\varphi_3^{-1}} + \varphi_4]^{\frac{1}{10}}, \tag{8}$$

$$\varphi_1 = (\frac{24}{\%_K})^{10} + (\frac{21}{\%_K^{0,67}})^{10} + (\frac{4}{\%_K^{0,33}})^{10} + (0,4)^{10}, \varphi_2 = \frac{1}{(0,148\cdot\%_K^{0,11})^{-10}+0,5^{-10}}$$
$$\varphi_3 = (\frac{1,57\cdot 10^8}{\%_K^{1,625}})^{10} \text{and } \varphi_4 = \frac{1}{(1,67\cdot 10^{-17}\%_K^{2,63})^{-10}+0,2^{-10}}. \tag{9}$$

Equations (6) and (7) have to be completed by boundary conditions. On inlet is prescribed fixed value and on outlet is prescribed zero gradient for particles concentration and velocity. On profile is prescribed mixed boundary condition. If the particles are hitting the profile then is used zero gradient. Otherwise is prescribed fixed value. In the case of velocity is used value which is corresponding to free stream value and for concentration is used 0.

Results

In previous work [1] was shown that both approaches provide similar results as is shown in figure 1. Here is shown comparison of droplets trajectories achieved by Lagrangian and Eulerian approach.

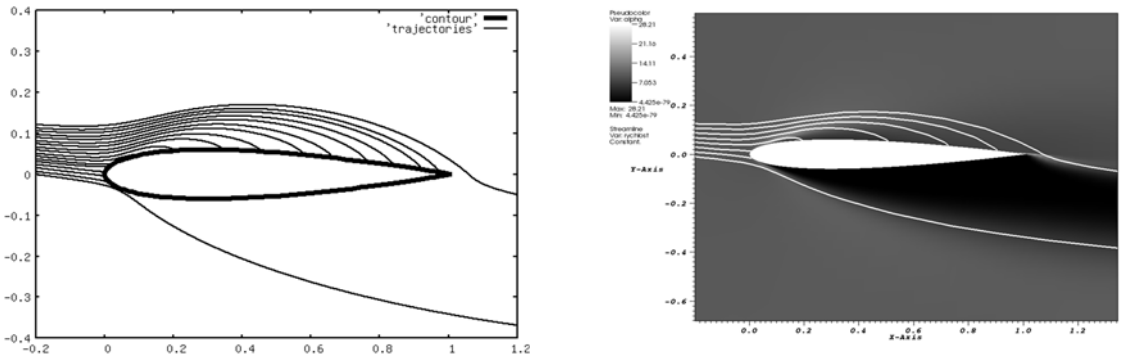

a) Lagrangian model **b) Eulerian model**

Figure 1. Comparison of droplets trajectories between Lagrangian and Eulerian model

For study of leading edge contamination was chosen a profile FX-60-126 which is used e.g. on glider ASW 19 and two regimes of flight. The first one is characterized by Reynolds number 1.41e6 and angle of attack 5° and the second one is characterized Reynolds number 2.21e6 and angle of attack -1.25°. Drophilas are replaced by sphere with diameter 2 mm and density 230 kg/m^3.
In figure 2 is shown an example of results achieved by simulation. There is possible to see concentration of insect close to the profile and comparison between streamlines and insect trajectories. The insect trajectories are hitting leading edge while the streamlines trace the shape of surface.

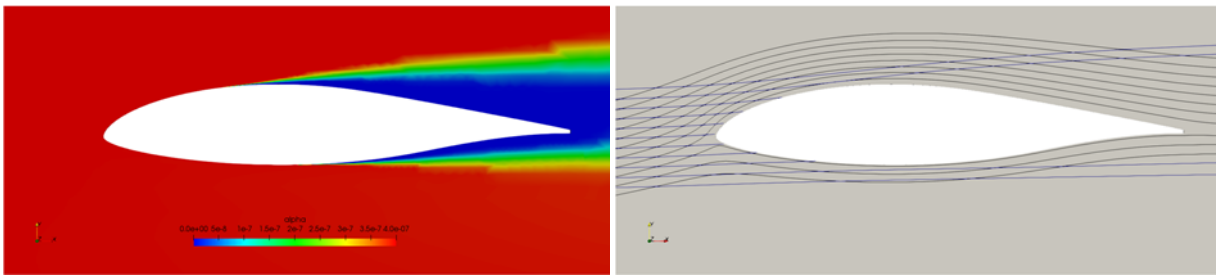

a) insect concentration close to the profile **b) comparison of streamlines and insect trajectories**

Figure 2. Example of result

The of insect hitting on profile is determined by following formula

$$m = \alpha v_i n_i, \tag{10}$$

where n_i is surface normal. In figure 3 is shown the concentration of insect hitting on leading edge obtained by numerical simulation and comparison with experimental data [5]. There is possible to see differences between experimental and numerical data. The main difference is in affected area. The experimental data predicts affected area aroudn 10% of chord length while the numerical simulation predicts more then 30% of chord length. The observed differences may be caused by replacement of Drophilas bodies by spheres with constant mass and used numerical schemes.

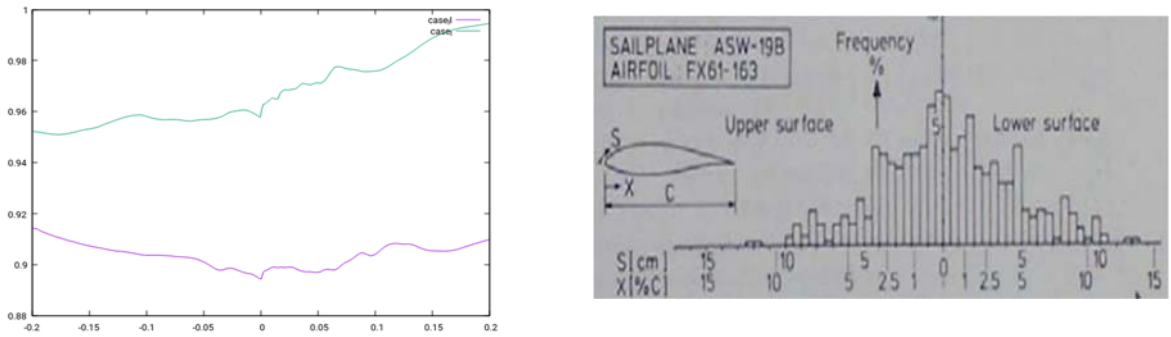

a) numerical data **b) experimental data [5]**

Figure 3. Contamination of leading edge by insect

Conclusion

In this paper was presented a method for determining contamination leading edge by the insect. This method is based on algorithms which predict the impact of droplets on the surface. The insect is replaced by spheres of similar size and weight. This can lead to the observed differences between experimental and numerical results.
The results obtained by the simulations can serve to calibrate of the modern RANS transition models where the roughness caused by the insect is an important production source of turbulence. These models will enable to describe the effect of turbulence on the plane profile and a better predict their performance characteristics.
Future work will be focused into an immprovement of model which described insect and their properties and into an improvement of numerical performance and stability.

References

[1]Betak, V. Furst, J., 2009: Comparison of two different approaches to simulate of droplets trajectories, Topical problems of fluid mechanics
[2]Habashi, W., 2009: Pacing In- flight Icing Simulation, Montreal, Quebec, Canada
[3]Almedeij, J., 2007: Drag coefficient of flow around sphere: Matching asymptotically the wide trend, Science.
[4]Hellsten, A., 2004: New Two-Equation Turbulence Model for Aerodynamics Applications, Espoo, Finland.
[5]Boermans, L.M.M., Selen, H. J. V.: Design and tests of airfoils for sailplanes with an application to the ASW-19b, Delft University of Technology, Netherlands

Determination of nose wheel drag and performance increase by a retractable nose gear

Jan Condé-Wolter[1], Jürgen Frey[1]
[1]*Technical University Dresden, Department of Experimental Aerodynamics*

Abstract: The drag of different nose wheel configurations has been determined in wind tunnel experiments using a full-scale model by far wake pressure distributions. Results have been validated in free flight experiments. Drag polars have been calculated out of this data on the base of a Schempp-Hirth Duo-Discus XL.

***Keywords*:** gear, nose wheel, drag-reduction, free flight experiments, wind tunnel experiments

Introduction

The Akaflieg Dresden is currently building a twin seater glider, the D-B 11. During the design process different landing gear configurations have been evaluated and a fixed front gear was chosen due to the positive effects in terms of safety and usability as a training plane. Because of the growing electrification in planes the retraction of wheels becomes easier viable. Hence the additional drag of fixed nose-wheels was evaluated to quantify a possible increase of flight performance. Different configurations such as no nose-wheel (like the ASG-32), a fixed front-wheel (Duo-Discus XL), extracted and retracted nose wheel and an aerodynamic fairing for a fixed nose wheel were tested.

Methodology

A full-scale mockup of the D-B11-fuselage from the nose to the middle of the tail boom was used as a wind tunnel model. A center wing section with endplates was added to reproduce the upstream effect of the lift correctly.
The model included a retractable main gear with gear doors, so it was possible to measure the main gear drag as well. Different nose-wheel configurations could be attached to the fuselage, by this the following configuration could be tested: no nose-wheel (e.g. ASG-32), a fixed front-wheel (e.g. Duo-Discus XL), extracted and retracted nose wheel with doors and an aerodynamic fairing for a fixed nose wheel.
The contribution of the landing gear configuration to the parasite drag has been determined from the loss of total pressure in the far wake of the gear. Therefore a traversed pitot tube measured the total pressure at 1110 equidistant points of the size 15x15mm. This area of the size 435x540mm covered the whole affected far wake of the main and nose gear. The additional drag of the different configurations could be determined by the differential consideration. This approach of measuring total pressure loss in the wake was already used to determine drag of wing fences and aileron covers [1].
All experiments were carried out in the same flight mode with standard mass of 600kg (two pilots, no ballast) at 180kph. In this mode the wing produces a lift coefficient of C_L=0.25 which represents the lower end of the laminar bucket. The pressure distribution of the wing was checked at 25 pressure taps, and a realistic flow was shown by oil visualisation.

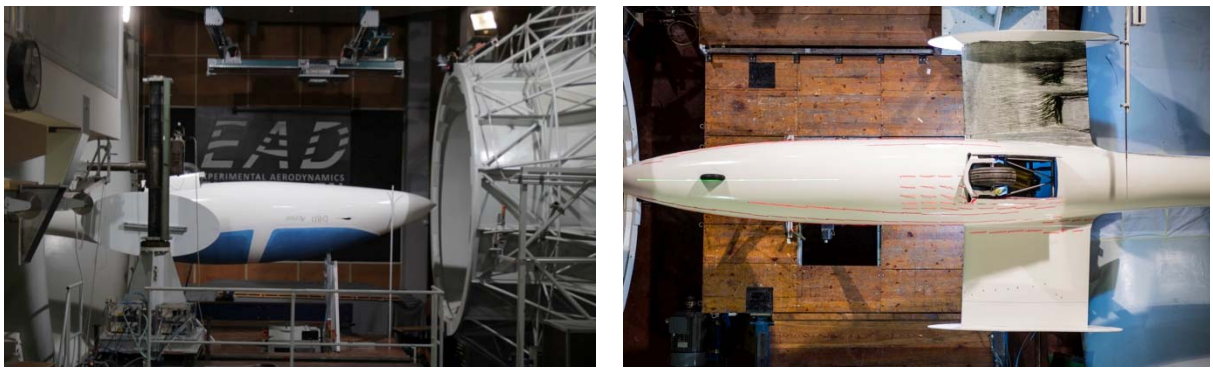

Figure 2: Side view (left) and top view (right) of the wind tunnel experiment assembly, nozzle diameter: 3m; traversed pitot tube visible behind the main gear

For the free flight experiments the B-12, a twin-seater prototype of the Akaflieg Berlin, was used and equipped with up to three nose wheel dummies. One nose wheel was placed on a centered position underneath the fuselage. Two additional ones were placed on both sides close to the canopy. Therefore the effect of the nose wheel was multiplied and quantifiable above the measurement noise. This approach has already been used in other free flight experiments to measure the drag of small structural details e.g. aileron fences [2].

Static and total pressure were measured and logged with a data recording system provided by the DLR to determine altitude and airspeed. In each flight a static glide path was flown at 180kph for 3 to 5 minutes. By the loss of altitude during this time the glide ratio could be calculated. In 7 flights 14 of those static sections were logged with no, one and three nose-gears.
From the collected data and the lift to drag ratio the additional drag of a fixed nose-gear could be calculated and compared to the results of the wind tunnel experiments.

Wind tunnel Results

In Figure 2 are the total pressure distributions in the far wake of the three most differing configurations shown. Without a main or nose wheel the fuselage has a smooth undistorted surface, therefore a boundary layer is visible. The fixed nose-wheel is a dull-body and creates a system of horseshoe vortices. These vortices lead to the two separated areas of lower pressure. In addition the dull body is followed by a backwater area and a turbulent wedge, which increases the form and friction drag.
The pressure distribution of the extracted main gear shows a large backwater area and its shape is formed by a complex system of vortices around the gear and wheel.

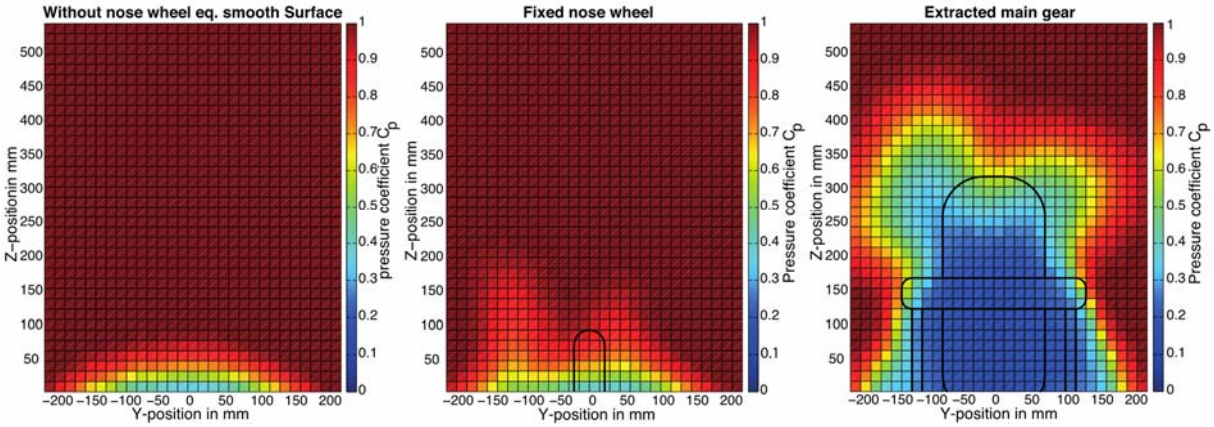

Figure 3: Pressure distribution 1000mm behind main gear with different configurations. left: no gears, smooth fuselage surface; middle: fixed nose wheel; right: extracted main gear

The local pressure coefficient represents in an incompressible flow the ratio of local speed to the inflow velocity to the square. The loss of velocity represents a loss of impulse from which drag coefficients can be calculated. By an integration of the pressure distribution over the whole area, the total drag of each configuration can be determined. Since the D-B 11 is designed with a fixed nose-wheel, this configuration was used as a basis to determine the drag increase or decrease of each other configuration.
Based on the glide performance of the Duo-Discus XL and the drag counts of each configuration, polars have been calculated delivering changes in L/D for respective flight conditions. The Duo-Discus XL was suitable because of its fixed nose-wheel, and the same MTOW, airfoil and wing design as the D-B 11.
In Figure 3 you can see the flight performances of a normal Duo-Discus XL and the calculated ones without a nose-wheel and with an extracted main gear. It shows that the effect of a drag increase and decrease effect a large speed range from the best L/D to the end of laminar bucket (approx. 180km/h, C_L=<0.25). The differences in descent rate are at slow speeds imperceptible and even with its cubic growth the effect of a removed nose wheel is within the scale of centimeters per second. But the effect on the L/D is significant, in the speed range from 100kph to 200kph the L/D improves at least by 0.5 points, between 120kph and 180kph the increase is above 0.85 points.

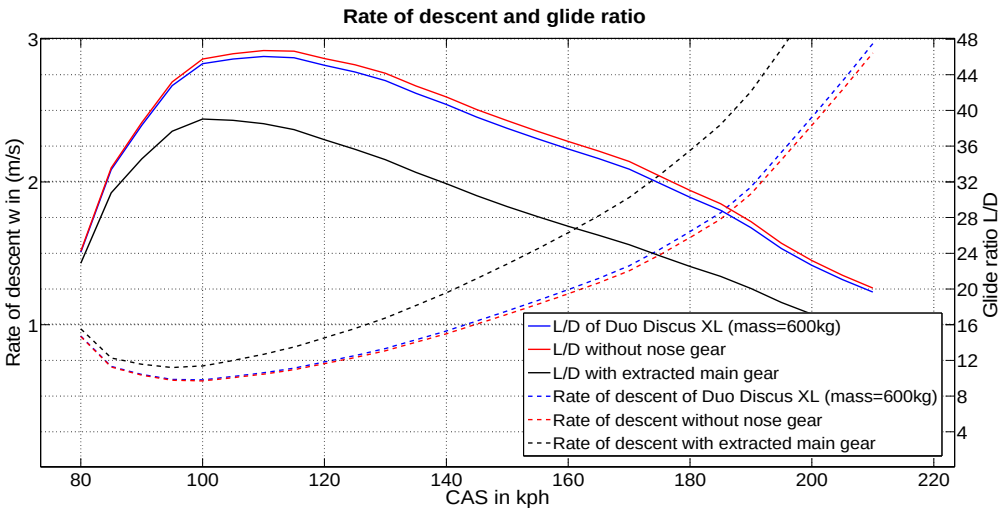

Figure 4: rate of descent and glide ratio with and without nose wheel and with extracted main gear

In Table 1 is the drag increase and decrease of all other configurations compared to a fixed nose-wheel shown, in addition to this the maximum change in L/D is shown.

Table 1: Wind tunnel results from different configurations

Configuration	Change in Drag (drag counts)	Change in L/D
Fixed nose wheel		Max. 46
No nose wheel	-2.256	+0.85
Retracted nose wheel (with door gaps)	-1.813	+0.71
Extracted nose wheel with doors	+1.392	-0.16
With aerodynamic fairing	-0.804	+0.3
With extracted main gear	+31.02	-9.4

The positive effect on the flight performance of a retracted nose gear is lower than a configuration without a nose gear due to laminar-turbulent transition at the door gaps, which causes an increased friction coefficient. The extracted nose wheel is worse than a fixed nose wheel because of the wheel bay and the doors. An aerodynamic fairing, even with a comparatively poor surface quality, lowers the drag of the fixed gear of more than a third.

Free flight results

In the free flight experiments the glide ratio was directly measured by the loss of altitude and the test duration, which result in an averaged descent rate. However the test procedure is affected by many factors like the speed variation, control inputs and atmospheric movement of the local air. Therefore sections with the most static or symmetric velocity distribution were chosen out of the 5 minute long experiments. This is necessary because the descent rate is proportional to the cubic of the flight speed. Therefore even little changes in airspeed have a large impact on the loss of altitude. The experiments were carried out right after sunrise to keep atmospheric effects small. With those methods pretty consistent results could be achieved, which are shown in Table 2.

Table 2: Free flight results

Configuration	Averaged descent rate w in m/s		Averaged L/D	
Without nose wheel	2.35	**Difference**:	20.98	**Difference**
With one nose wheel	2.45	+0.098	20.07	-0.92
With three nose wheels	2.59	+0.238 +0.079 per wheel	19.12	-1.87 -0.62 per wheel

In all flight tests the nose wheel showed a significant reduction of aerodynamic performances. The impact of three nose wheels is a bit smaller then three times the effect of one nose wheel.

Comparison and Summary

The calculated drag count for a single nose wheel out of the arithmetically averaged free flight data is 4.15 drag counts, which is 85% higher than the wind tunnel results (2.25 drag counts). The free flight experiments predict a

performance increase without a fixed nose wheel of 1.65 points of L/D, which is shown in the calculated flight performances of both experiments in Figure 4.

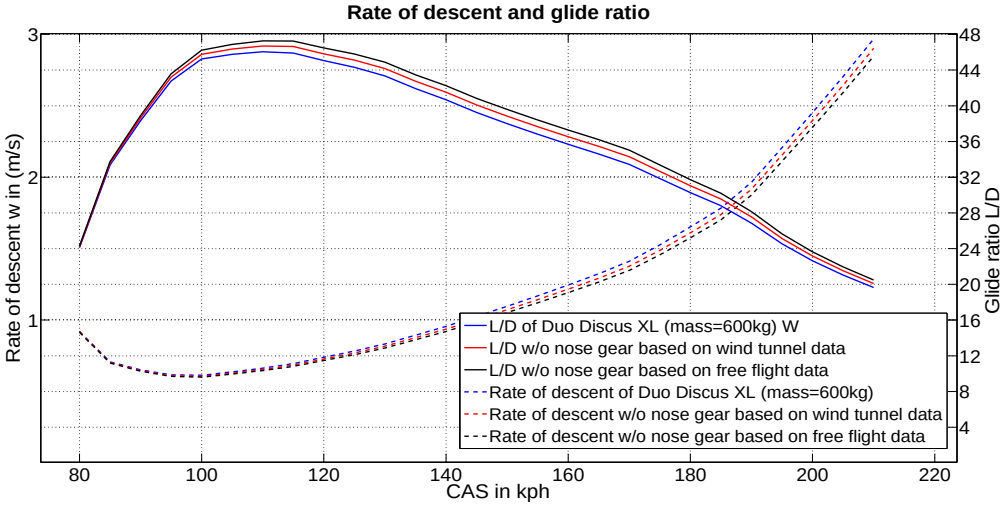

Figure 5: Calculated Flight performances of a Duo-Discus XL with and without nose wheel based on wind tunnel and free flight results

Both experimental approaches show a significant effect on glide performance by removing or retracting of a nose wheel. The wind tunnel results can be assumed as conservative due to the pressure distribution was measured at the beginning of the tail boom and not behind the plane. Therefore higher friction drag does not take the whole plane in account. In addition to this, effects like wind tunnel blockage, which can't be neglected due to the model size, have an undetermined effect on the results.

The scale of the impact of atmospheric movement in free flight results is undeterminable without a reference plane, but all results vary in a small range. Therefore it can be assumed that the exact performance increase of configuration without or retracted nose wheel resides within the range of both methods.

These results implemented in a cross-country flight simulation with a climbing fraction of 33% come to the conclusion that the overall flight time is reduced by at least 2.5% by the retraction of a nose wheel.

References

[1]Frey, J., 2013: Wind Tunnel Measurements on Details of Laminar Wings, Technical Soaring Vol.39 No.2.

[2] Pätzold, F.: Messungen von Detailwiderständen an Segelflugzeugen zu den IDAFLIEG-Sommertreffen 2007 und 2008, Idaflieg -Berichtsheft Nr. 35, 2009

Soaring into the Stratosphere

Dieter Etling
Leibniz University Hannover, Institut for Meteorology and Climatology, Germany, etling@muk.uni-hannover.de

Abstract: Soaring at altitudes above the tropopause is only possible by using updraughts of mountain waves which penetrate into the atmospheric layer above, called the *stratosphere*. Here we present some atmospheric conditions under which mountain waves can be expected in heights above 10 km or more. As special case the meteorological situation during the new altitude record of Perlan 2 will be discussed.

***Keywords*:** mountain waves, stratosphere, Perlan.

Introduction

On 3 September, 2017, a new altitude record for soaring flight was achieved by the special glider PERLAN 2 . Pilots Jim Payne and Morgan Sandercock reached the altitude of 52,172 feet (15,902 meter) after take off from El Calafate in Southern Argentinia. They exceeded the former record by Einar Enevoldson and Steve Fosset from the year 2006 by 1445 feet (540 meter). Both record flights were achieved by using the updraughts in the mountain wave system of the Southern Andes. Here we will explain the meteorological conditions under which mountain waves can propagate into these heights in the middle stratosphere, far above the weather systems of the troposphere. In light of these conditions, the recent altitude record flight by PERLAN 2 will be analysed from the meteorological point of view.

Mountain waves propagating into the Stratosphere

The stratosphere is the atmospheric layer above the tropopause, which marks the upper extent of the troposphere. The tropopause is located between about 8 and 12 km asl depending on latitude and season. As there are no convective clouds in the stratosphere supporting updraughts for soaring flight, the only possible source for strong vertical motions are gravity waves. When induced by mountains, theses waves are well known for soaring flight in the lowest 2-8 km of the atmosphere (e.g. Etling, 2013; Palmer, 2004). But gravity waves are also quite common in the stratosphere (e.g. Fritts et al., 2016; Kaifler et al., 2015). In order to find mountain waves also above the tropopause, which marks the jump in the vertical temperature gradient (see Figure 1), some special conditions are necessary. These are mainly tied to the horizontal wind speed. The wind direction should not change very much with height and the wind speed should increase with height also above the tropopause (see Figure 1). The reason for this condition might be explained simplified as follows. Gravity waves propagating trough the tropopause will be usually weakened due to stronger stratification in the stratosphere. But if the wind speed is increasing with height, the waves can extract energy from the wind and their amplitudes will increase .

Now one has to ask, where such increase of wind speed with height can be found. Figure 2 shows the vertical cross section of the mean zonal wind speed for the months June-August from pole to pole and from the surface up to pressure level 1 hPa (about 50 km). In the troposphere (below about 100 hPa), westerly winds dominate in both hemispheres. In the stratosphere however, easterly winds are prevailing in the northern hemisphere, just in opposite direction as the winds below. Hence in this situation, mountain waves can not prentrate into the stratosphere and soaring flight will not be possible in theses heights. In the Southern Hemisphere, zonal winds in the stratosphere are also from the west like in the troposphere below. But a continuous increase in wind speed from the surface up to the middle stratosphere can be observed only at the most southern latitudes, between about 50° S and 90° S (as indicated by the vertical line in Figure 2). In this area, the westerly winds in the stratosphere are called “Polar Night Jet”. Hence the wind conditions for mountain waves penetrating into the middle stratosphere are favorable in these geographical latitudes. This is the reason, why the last two altitude records for soaring flight have been achieved in the mountain wave system of the Southern Andes. A similar distribution of the zonal wind with westerlies up to the stratosphere is found Northern Hemisphere for the northern winter (December-February), but with a weaker Polar Night Jet than in the southern winter.

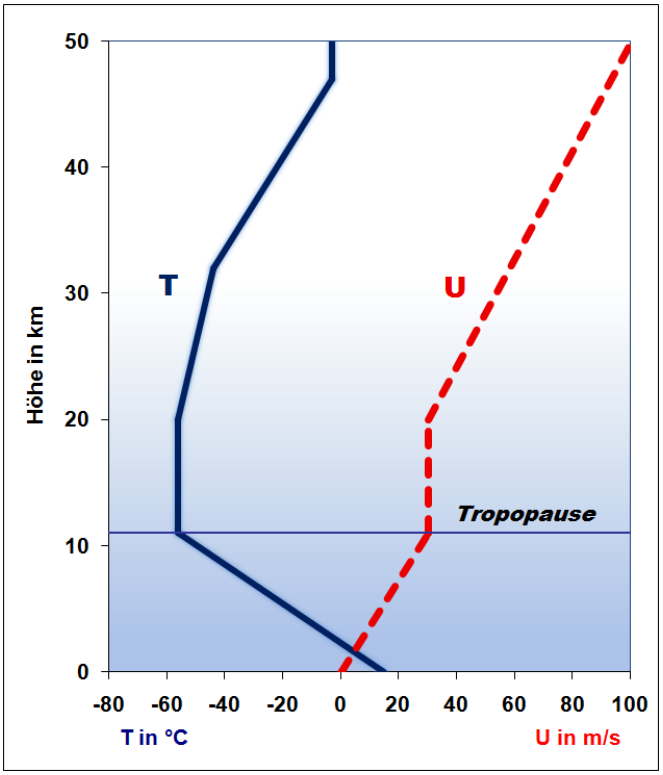

Figure 1: Typical temperature (T) and wind (U) profiles favorable for mountain wave propagation into the stratosphere.

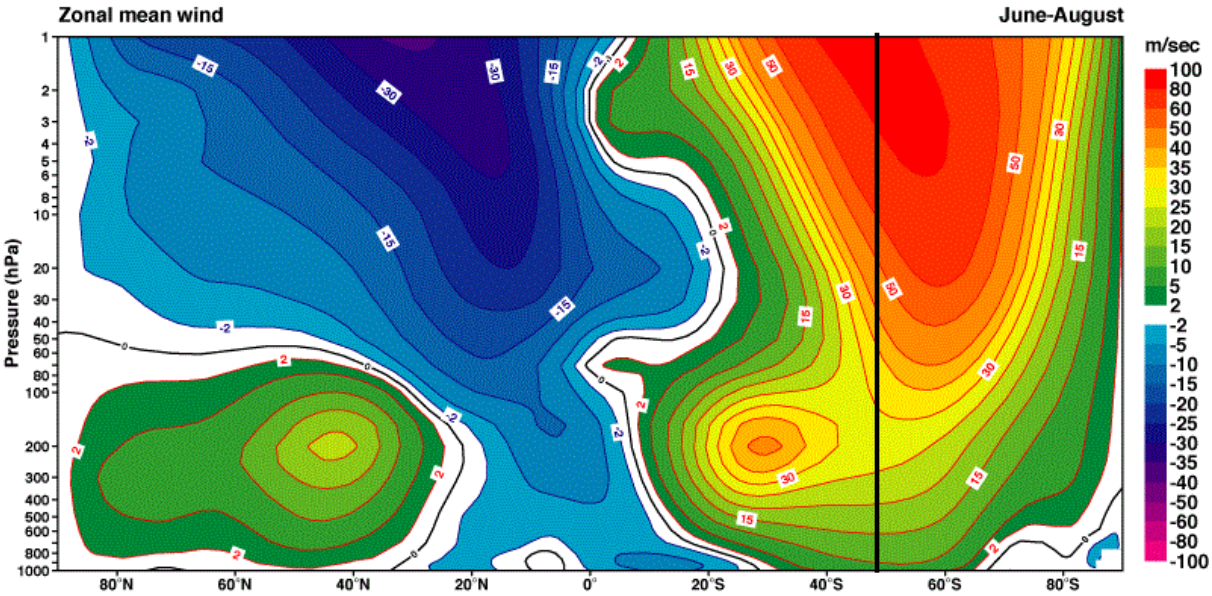

Figure 2: Mean zonal wind (in m/s). Altitude-height cross section for the months June-August. Positive values: westerly winds, negative values: easterly winds. Credit: ECMWF.

Meteorological conditions during the altitude record of PERLAN 2

On September 3, 2017, the new altitude record for soaring flight (52,172 feet, 15,902 meter) was achieved by the special glider PERLAN 2 by using the updraughts of the mountain wave system of the Southern Andes, starting from El Calafate, located at 50°21' S, 72°16' W. The details of the record flight can be found in the OLC under https://www.onlinecontest.org/olc-2.0/gliding/flightinfo.html?dsId=6116604. For characterizing the air mass in this area on this day, the radiosonde ascent from the Falkland Islands is shown in Figure 3. The tropopause is located at about 9 km height at this date. The wind direction (see wind barbs) is more or less from west at all heights and the wind speed is increasing continuously from about 35 knots at 1 km to 125 knots at 25 km height. Hence the wind conditions for mountain waves reaching the stratosphere were quite favorable on this date. But with this information only, the existence of mountain waves in the middle stratosphere can not be guaranteed. Therefore, the results from numerical weather prediction models have to be consulted. These models can simulate mountain waves directly if their horizontal resolution is fine enough (say less than 4 km).

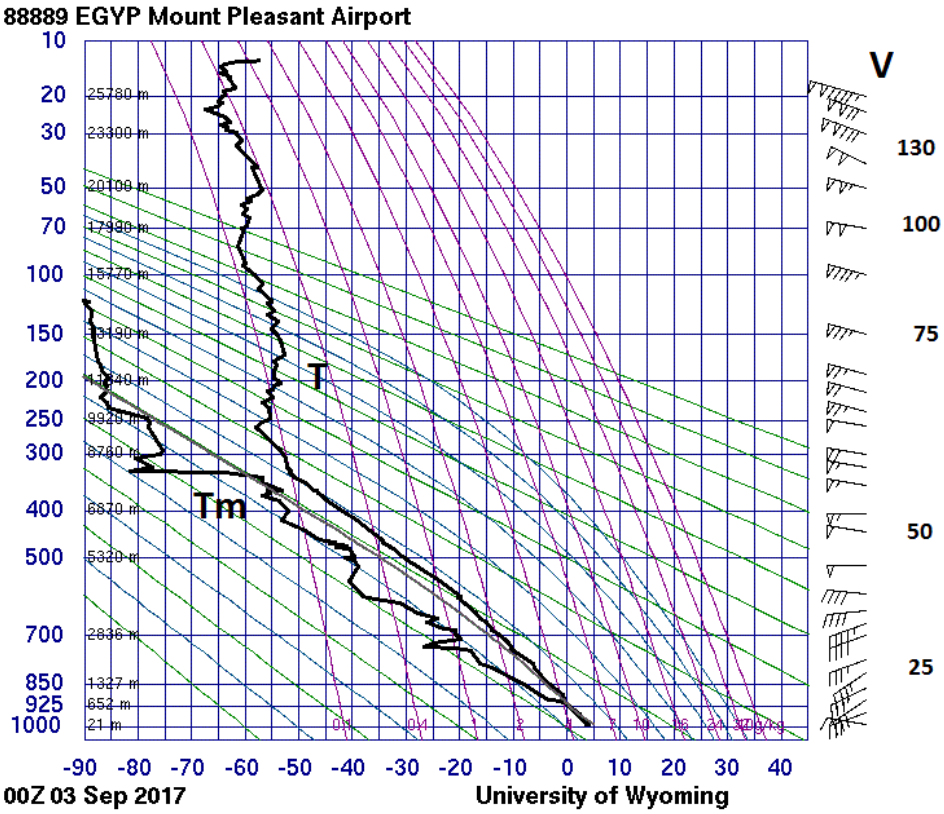

Figure 3: Radiosonde ascend at the Falkland Islands from 03 September 2017, 00UTC. T: temperature, Tm: moist temperature, V: wind speed. Credit: University of Wyoming.

For the PERLAN project, mountain wave forecasts are provided by the company WeatherExtreme Ltd. by using the well known Weather and Research Forecast model WRF. One of the wave forecasts for the day of the altitude record flight is shown in Figure 4. In this west-east cross section at the latitude of 50° S, the vertical wave velocities (updraughts and downdraughts) in the lee wave system of the Andes are shown. One can observe some weaker waves in the troposphere (below 9 km) and some stronger waves in the stratosphere (around 15 km). The location of PERLAN 2 at the altitude record is indicated by a dot.

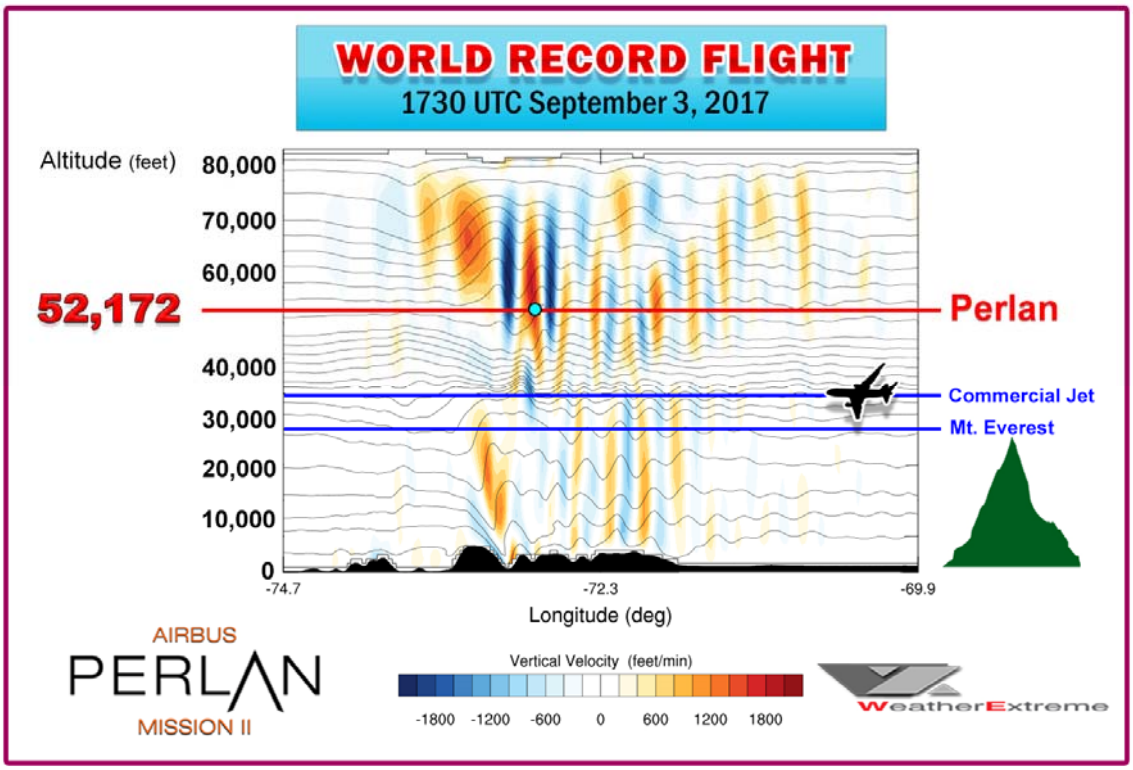

Figure 4: Wave forecast for 03 September 2017 as obtained from the WRF model. West-East cross section at 50° S. Vertical velocity in ft/min, red: upward, blue: downward. Credit: WeatherExtreme Ltd.

Conclusions

Soaring into the stratosphere is possible by using the updraughts of mountain waves penetrating up to heights of 12 km and more. Suitable meteorological conditions for stratospheric mountain waves can be found in the region of the "Polar Night Jet", which is observed during the hemispheric winter between about 50° and the pole. The recent soaring altitude record of nearly 16 km by PERLAN 2 has been achieved in the mountain wave system of the Southern Andes in September 2017. The ultimate goal of the *Perlan project* however is to reach the altitude of 90,000 ft (about 27 km) by soaring flight, far above of most powered aircrafts. But also this is possible from the meteorological point of view, as mountain waves can exist even in these heights and beyond (see e.g. Fritts et al., 2016 or Kaifler et al., 2015).

References

Etling, D., 2013: Atmospheric gravity waves and soaring flight. 118 pp, freely available under: https://www.schwerewelle.de/literatur/dieter-etling-atmospheric-gravitywaves-and-soaring-flight

Fritts, C. and several coauthors, 2016: The Deep Propagating Gravity Wave Experiment (DEEPWAVE): An Airborne and Ground-Based Exploration of Gravity Wave Propagation and Effects from Their Sources throughout the Lower and Middle Atmosphere. Bull. Amer. Meteor. Soc. **https://doi.org/10.1175/BAMS-D-14-00269.1**

Kaifler, B. and several coauthors, 2015: Influences of source conditions on mountain wave penetration into the stratosphere and mesosphere. Geophysical Research Letters. **https://doi.org/10.1002/2015GL066465**

Palmer, M., 2004: Practical wave flying. Bob Wanders Soaring Books and Supplies, Minneapolis, USA, 80 pp.

Information about the altitude record flight of PERLAN 2 and on the Perlan project can be found under www.perlanproject.org and www.airbusgroup.com/perlan .

DFS 582 - High-Altitude Research Glider Project 1958-1964

H.-L. Meyer, *Braunschweig, Germany*

Abstract: The DFS 582 was a project of the DFS (Deutsche Forschungsanstalt für Segelflug) in the 1960'th for a jet-powered high-altitude research glider. Investigation of jet streams, basic meteorological research, measurement of radioactivity, ozone concentration, gamma rays, application as relay station, production of areal photographs and boundary layer control were planned. Two almost complete all-metal-airframes were built before the project was cancelled in 1966 prior to a first flight.

***Keywords*:** Historic powered Glider, High Altitude Glider

Introduction

The DFS 582 development was financed by a contract of the german ministry of traffic in order to be operated as a platform for research and measurements at high altitude. Primary missions should be survey of jet streams to better understand the phenomena. The strong winds, specially above the north atlantic, where important for planning the routings for airliners between Europe and the USA, to avoid turbulent areas, strong headwinds und to use tailwinds. Furthermore basic meteorological research, measurement of radioactivity, ozone concentration, gamma rays, application as relay station, production of areal photographs and even boundary layer control at wing test sections by blowing pressurized air were planned applications. Some members of the development crew had experience from war-time designs, for example the high altitude glider DFS 228.

Project Characteristics and History

Design started in 1958, different layouts and versions were investigated.

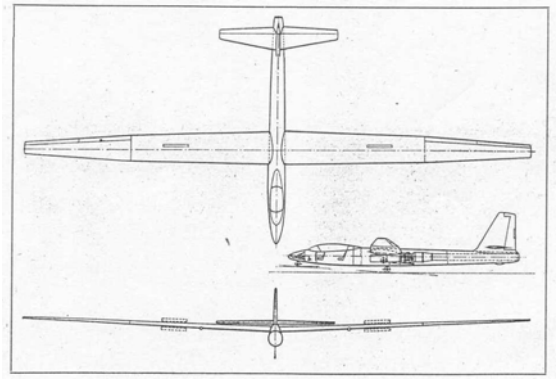

Figure 1. Final version of the DFS 582

The DFS 582 was designed as an all metal construction with a constant laminar wing section NACA 643 – 618. Different combinations of material and construction methods were tested. Finally, the airframe structure was a monocoque design with aluminum plates and sandwich-material of aluminum foil.

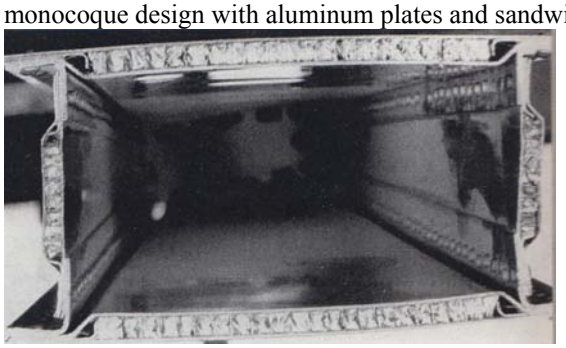

Figure 2. Wing Test Section

The glued honeycomb skin and flanges of the DFS 582 wing were lightweight and assured the high accurate surface as required for the laminar airfoil.
Each wing could be separated in an outer and inner part, connected by many tractor-screws.

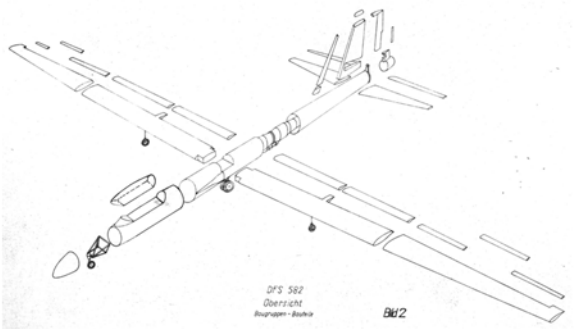

Figure 3. Structural Parts

The fuselage was constructed in three main parts and could be disassembled for maintenance, specially at the engine, and for installation work.

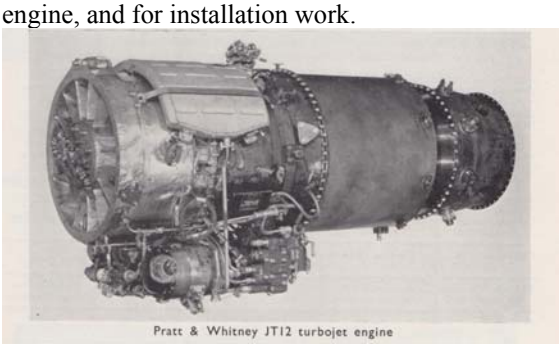

Figure 4. Jet-Engine Pratt&Whitney JT12-6A

The engine type was flown in several business-class and trainer aircraft types.
Some technical data of project DFS 582:
Wing span 30 m, wing area 45,6 m^2, max. T/O-mass 3.400-3.800 kg, wing loadind 75-85 kg/m^2, Engine P&W JT12-6A, T/O-thrust 1360 kp (initially Armstrong-Siddely „Viper“,T/O-thrust 1.135 kp), V_{min} 85-100 km/h, M_{max} 0,6, V_{max} 550-600 km/h, operating altitude 14-16 km, range ~2.000 km with a scientific payload of ~100 kg.

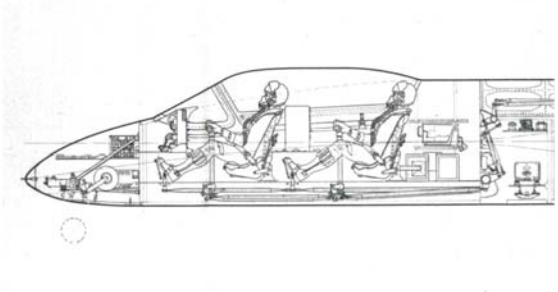

Figure 5. The pressurized Cockpit Section

With running engine the cockpit was pressurized by bleed-air from the compressor stage through a heat exchanger. Without engine, cabin pressurizing was achieved by vaporized oxygen from the liquid oxygen bottles. At an aircraft altitude of 15-16 km, cabin pressure was as at an altitude of about 7,5 km.
The only existing hardware of the DFS 582 is a wind tunnel model with a span of 3 meter, the two almost complete airframes were stored and disappeared later.

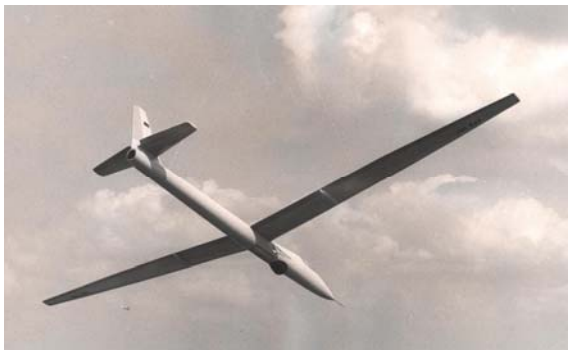

Figure 6. Wind Tunnel Model of the DFS 582
Due to financial constraints, the completion of the jet-driven high-altitude research airplane DFS 582 was cancelled in 1966.

References

-DVL-Nachrichten, Heft 23, Februar 1964
-Fotos, Zeichnungen, Berichte aus dem DLR-Archiv Göttingen, z.B. DFS-582 Kurzbeschreibung vom Nov. 1963
-Jugendzeitschrift „hobby“, 1960
-Lommel/Geheimprojekte der DFS

How to perform Flight Vibration Testing based on Operational Modal Analysis?

Jan Schwochow
DLR, Institute of Aeroelasticity, Göttingen, Germany, jan.schwochow@dlr.de

Abstract: Flutter is a dynamic instability caused by the interaction of the structural dynamics of the aircraft and unsteady aerodynamic forces. It occurs when one of the elastic modes of the airframe tends to negative damping above a critical speed. Prediction and flutter clearance are important problems in the design, testing and type-certification of sailplanes. From a practical point of view, Flight Vibration Testing (FVT) needs to be performed whenever a new sailplane is built or an existing type is modified.
The application of Operational Modal Analysis (OMA) methods may provide improvements to identify modal parameters of multiple modes in one step without knowing the type of external excitation. If the identification is repeated for increasing flight velocities, it is possible to find the aeroelastic damping trends and to extrapolate to the stability boundary. The application of OMA needs a broadband excitation spectrum, which result from impulsive control kicks or continuing random excitation like gusts and turbulence in the atmosphere. To demonstrate the performance of the proposed method measured time histories are post-processed to identify all relevant mode shapes with natural frequencies and damping rates of the flying sailplane. Requirements for test equipment, software and the procedure to perform the FVT are summarized..

***Keywords*:** Aeroelasticity, flight vibration test, operational modal analysis.

Introduction

Flutter is a dynamic instability caused by the interaction of the structural dynamics of the glider airframe with control system and unsteady aerodynamic forces induced by the oscillation of the airframe. Depending on the phase lag the resulting forces can amplify the vibration levels above a critical flutter speed. Most flutter problems involve two or more of the following types of vibration modes: bending and torsion of fixed surfaces, rotation and/or torsion of control surfaces and rotation of tabs. Flutter occurs when the aerodynamic damping due to motions in one vibration mode such as wing bending is balanced by the lift due to the angle of attack in another vibration mode such as wing torsion. The primary causes of flutter are as follows:

- Insufficient torsional stiffnesses with center of gravity locations of spanwise sections substantially behind the quarter chords on wings, stabilizers and fins.
- Control surfaces with center of gravity locations of spanwise sections behind the hinge lines and inadequate rigidities in the control systems.
- T-tails which produce unstable coupling between fin torsion and stabilizer yaw with fin bending and stabilizer roll.
- Rotational flexibilities at the roots of all movable horizontal tails which substantially lower the torsional frequencies.

Flutter prediction and flutter clearance are important problems in the design, testing and certification of glider aircrafts. From a practical point of view, the aeroelastic stability must be checked in the flight vibration test (FVT). It needs to be performed whenever a new aircraft is built or an existing aircraft is modified. The procedure of demonstrating that the aircraft is free from flutter in the specified range of velocities and altitudes is called flight envelope clearance. Here, the test pilot tries to excite the glider with impulsive manual control stick jerks and rudder kicks. It is common praxis, that a sufficient decaying response oscillation is evaluated by the judgement of the experienced pilot based on his impression during flight. More reliable methods based on instrumented flutter testing are desirable to reduce remaining risks during test flights.
As a prerequisite for the FVT, it is required to measure the modal parameters of the glider airframe comprising natural frequencies, damping ratios and mode shapes without the impact of aerodynamic forces in the so-called ground vibration test (GVT). The modal parameters are used to obtain the vibration mode shapes, the natural frequencies and structural damping of the airframe for use in the prediction of flutter problems in the rational flutter analysis. It is desirable to have in-flight measurements to compare and calibrate the analysis results, particular for the damping estimates. More sophisticated methods for FVT consist of estimating frequencies and damping ratios of the dynamic pressure dependent aeroelastic modes against the flight speed. The flutter speed is mainly determined by extrapolation of the damping at subcritical speeds. Since damping characteristics often change abruptly near the flutter boundary, it is necessary to evaluate them up to speeds which are very close to the stability boundary. An overview of the methods used in the FVT can be found in [1].
Output-only or operational modal analysis (OMA) techniques have become available in the last years [2] to extract the modal parameters from the dynamic response to operational (ambient) forces, e.g. in flight. Consequently, they deliver a linear (modal) model of the structure around the real working point of operation. The unmeasured,

ambient forces are usually modelled as stochastic quantities with unknown parameters but with known behavior, e.g., as white noise time series with zero mean and unknown covariance. The application of OMA may provide improvements to identify modal parameters of multiple modes in one step from measured acceleration response in flight. If the measurement is repeated for increasing flight velocities, it is possible to find the flutter damping trends and to extrapolate to the stability boundary. In OMA all modal parameters are to be determined without knowing the excitation forces. Therefore it is normally assumed that spectral densities of these forces are all flat. It is not essential to satisfy that assumption for the actual physical forces because these acting on the structure can be thought as created by a linear filter loaded by white noise. In this case white noise system input is added with the properties of a linear filter to the system that is going to be identified. Thus the actual physical forces do not need to be white noise or have a flat spectrum, which means that the ambient turbulence in the atmosphere, represented by e.g. the von Karman spectrum [3], might be sufficient to excite glider in the gusty air with thermals (see Figure 1). For demonstration of the performance capabilities, the presented OMA procedure is applied to the recorded in-flight vibration signals of an instrumented FVT.

Figure 2 shows the club-class glider airframe response measured with tri-axial accelerometers during flight at a speed of V=150km/h in 1300m altitude, which was tried to be constant for 120 seconds. Five span-wise wing stations and the vertical tail were instrumented with MEMS sensors of type ADXL 326 [5]. It provides analog electrical output signals, which are low-pass filtered with cut-off frequency of 50Hz to avoid aliasing effects. The 8x3 signals were recorded and digitized with National Instruments compactDAQ hardware [6], which allows simultaneous acquisition of all channels at high sample rates. The aircraft was excited by random impulsive pilot control jerks and rudder kicks and the thermal turbulence, as well.

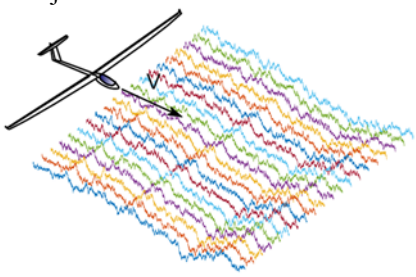

Figure 1. Glider flying in gusty atmosphere

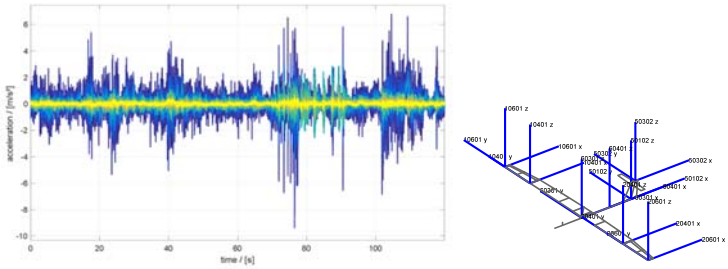

Figure 2. Acceleration response measured in flight at constant flight speed

Methodology

The general modelling procedure numerically linearizes the full nonlinear aeroelastic model represented by the flying glider about the operating point, which comprises current flight speed, flight altitude and trimmed condition including static deformation due to the lifting forces. The linearization routines can be used to develop both a first- and a second-order linearized representation. The complete nonlinear aeroelastic equations of motion can be written as follows:

$$\left[M\left(\{q\},\{u\},t\right)\right]\{\ddot{q}\}+\left\{f\left(\{q\},\{\dot{q}\},\{u\},t\right)\right\}=0 \tag{1}$$

where $[M]$ is the mass matrix, $\{f\}$ is the nonlinear forcing function vector, $\{q\}$ is the vector of displacements, $\{u\}$ is the vector of control inputs, and t is time. Numerically, linearization perturbs all system variables about their respective operating point values. The displacement, velocity, and acceleration perturbation vectors are replaced with the first-order state vector and state derivative vector, in order to determine the first-order representation of the linear time-invariant (LTI)-system:

$$\{x\}=\begin{Bmatrix}\Delta q\\ \Delta\dot{q}\end{Bmatrix},\quad \{\dot{x}\}=\begin{Bmatrix}\Delta\dot{q}\\ \Delta\ddot{q}\end{Bmatrix}\quad\Rightarrow\quad \begin{matrix}\{\dot{x}\}=[A_c]\{x\}+[B_c]\{\Delta u\}\\ \{y\}=[C]\{x\}+[D]\{\Delta u\}\end{matrix} \tag{2}$$

In [4] the full derivation of the aeroelastic state-space modelling is presented, where the vibration-induced aerodynamic forces scaled by the dynamic pressure are introduced. If the measurement sampling step Δt is fixed, the continuous state-space model in Eq. (2) can be discretized in time, where k is the index for the time steps. While the inputs $\{u\}_k$ are unknown, the outputs $\{y\}_k$ can be measured e.g. with accelerometers installed at adequate positions on the airframe. The LTI-system of Eq. (2) can now be converted from continuous-time to discrete-time domain by introducing the matrix exponential:

$$\begin{matrix}\{x\}_{k+1}=[A]\{x\}_k+\{w\},\quad with\quad [A]=e^{[A_c](\Delta t)}\\ \{y\}_k=[C]\{x\}_k+\{v\}\end{matrix}\ . \tag{3}$$

The unknown input terms $\{v\}$ and $\{w\}$ are assumed to be of stochastic type with discrete white noise nature and an expected value equal to zero. For application of the data-driven SSI, first the recorded output data samples plotted in Figure 2 are gathered in a so-called Hankel-matrix:

$$[Y]=\begin{bmatrix}[Y_p]\\[Y_f]\end{bmatrix}=\begin{bmatrix}\{y\}_1 & \{y\}_2 & \{y\}_3 & \cdots & \{y\}_{N-2q}\\ \vdots & \vdots & \vdots & \ddots & \vdots\\ \{y\}_{2q} & \{y\}_{2q+1} & \{y\}_{2q+2} & \cdots & \{y\}_N\end{bmatrix} \tag{4}$$

Each $\{y\}_k$ contains all accelerations at one certain point in time. The first subset with subscript p expresses the past information and f expresses the future. The subscript q expresses the number of time increments to be used in the analysis, which needs to be pre-selected by the user. N represents the total number of acquired samples. Now, the linear projection from past to future must be represented by the discrete LTI-system in Eq. (3) to be identified. The first step is the orthogonal-triangular decomposition (QR-decomposition) of the Hankel-matrix. Then, the so-called system observability matrix is approximated by singular value decomposition (SVD) of the covariance submatrix between past and future. The dominating part determines the rank of the subspace representing the relevant dynamic system response, while the insignificant part contains the measurement noise. The observability matrix is truncated at the user-selected model order:

$$\begin{bmatrix}[Y_p]\\[Y_f]\end{bmatrix}=\begin{bmatrix}[L_{11}] & 0\\ [L_{21}] & [L_{22}]\end{bmatrix}\begin{bmatrix}[Q_1]\\[Q_2]\end{bmatrix} \Rightarrow [L_{21}]=\begin{bmatrix}[U_1] & [U_2]\end{bmatrix}\begin{bmatrix}[S_1] & \\ & [S_2]\end{bmatrix}\begin{bmatrix}[V_1]^T\\[V_2]^T\end{bmatrix} \Rightarrow [O]=[U_1][S_1]^{1/2} \tag{5}$$

The system matrix $[A]$ is now calculated via least-squares solution, while the output matrix $[C]$ is the first block row of the observability matrix:

$$[A]=[O_1]^{\dagger}[O_2],[O_1]=\begin{bmatrix}[C]\\ [C][A]\\ \vdots\\ [C][A]^{p-1}\end{bmatrix},[O_2]=\begin{bmatrix}[C][A]\\ [C][A]^2\\ \vdots\\ [C][A]^{p}\end{bmatrix}. \tag{6}$$

The modal parameters of the system are found by performing eigenvalue decomposition of the identified system matrix $[A]$ from Eq. (6). This leads to the discrete-time system poles μ_i with corresponding eigenvectors $\{\psi\}_i$. The damped natural frequencies and damping ratios are calculated from the re-transferred continuous-time system poles:

$$f_i=\frac{\mathrm{Im}(\lambda_i)}{2\pi},\quad \zeta_i=-\frac{\mathrm{Re}(\lambda_i)}{|\lambda_i|},\quad with\quad \lambda_i=\frac{\ln(\mu_i)}{\Delta t},\qquad \{\phi\}_i=[C]\{\psi\}_i \tag{7}$$

All applied mathematical functions - QR-decomposition, SVD-decomposition and eigenvalue-decomposition - are standard matrix algebra routines, which are available from most mathematical software libraries. An introduction in signal processing and vibration analysis is given in [7], which is accompanied by a software toolbox for the free mathematical software GNU/Octave [8].

Results

The acceleration response data from flight test plotted in Figure 3 are analyzed with the presented OMA method above. The number of time increments in Eq. (4) is chosen to 12, while the model order in Eq. (5) – the number of singular values representing the orthogonal subspace of the Hankel matrix – is set to 120. Table 1 contains the 17 identified natural frequencies and dampings calculated via Eq. (7). Two of the identified mode shapes are plotted in Figure 3. Mode 2 is the fundamental bending of the glider wing at frequency 2.45Hz. The aeroelastic damping is high with 20.5%, which results from the motion-induced aerodynamic forces acting as damping force for heave motion. Usually the structural damping values of a glider airframe measured in the GVT are all below 2%. The second mode is symmetrical fuselage bending at 10.74Hz. As can be seen from Table 1 the presented algorithm is able to identify mode shapes with natural frequencies up to 30Hz with comparable high damping rates. Generally, this range covers the symmetric and antisymmetric wing torsion modes of glider airframes, which are most important to be monitored in the flutter analysis.

No.	Name	freq. Hz	damp. %
1	rigid-body heave	0.75	62.88
2	sym. 1st wing bending	2.45	20.50
3	anti. fuselage against wing	4.00	8.54
4	sym. in-plane wing bending	4.69	13.21
5	anti. 1st wing bending	6.24	6.47
6	anti. htp roll	7.30	9.04
7	sym. 2nd wing bending	8.89	9.13
8	sym. fuselage bending	10.74	5.17
9	sym. in-plane bending	11.78	2.83
10	anti. horizontal tail bending	12.56	5.53
11	anti. 2nd wing bending	15.73	4.26
12	anti. in-plane bending	17.58	5.57
13	sym. 3rd wing bending	18.71	4.25
14	sym. 2nd fuselage bending	21.84	4.54
15	anti. in-plane bending	22.96	2.88
16	sym. in-plane bending	26.45	3.18
17	anti. wing torsion	28.93	4.27

Table1. OMA-identified frequencies and dampings

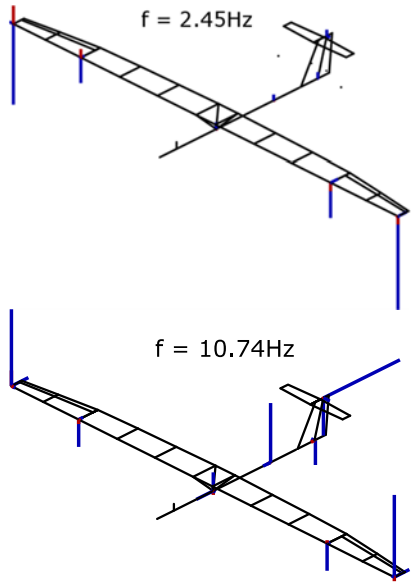

Figure 3. OMA-identified mode shapes

Conclusion

The application of OMA methods to evaluate flight vibration acceleration response data is presented, which needs unknown random excitation of the glider in flight by random pilot control inputs and atmospheric turbulence. The advantage of OMA may provide improvements to identify modal parameters of multiple modes in one step which is infeasible by manual pilot monitoring during flight testing. If the identification process is repeated for increasing flight velocities, the aeroelastic damping trends can be evaluated, extrapolated towards the flutter stability boundary and compared to the rational analysis.

References

[1] Meijer, J.J. Introduction to Flight Test Engineering - Aeroelasticity. RTO AGARDograph 300 Vol.14 (2005).
[2] Brincker, R. Some Elements of Operational Modal Analysis, Shock and Vibration, vol. 2014, Article ID 325839, 11 pages, (2014). doi:10.1155/2014/325839
[3] Hoblit, F. M. Gust Loads on Aircraft: Concepts and Applications. Washington, DC: American institute of Aeronautics and Astronautics, Inc. (1988). ISBN 0930403452.
[4] Schwochow, J., Jelicic, G. Automatic Operational Modal Analysis for Aeroelastic Applications. 6th International Operational Modal Analysis Conference IOMAC, 12-14 May, Gijón, Spain (2015).
[5] www.adafruit.com/product/1018 .
[6] www.ni.com/en-us/shop/pc-based-measurement-and-control-system.html .
[7] Brandt, A. Noise and Vibration Analysis: Signal Analysis and Experimental Procedures, Wiley and Sons., (2011).
[8] https://www.gnu.org/software/octave/.

Study of close ground proximity on a flexible wing

Zdeněk Pátek[1], Robert Kulhánek[1]
[1]*VZLU Czech Aerospace Research Centre, Aerodynamics department, Czech Republic* patek@vzlu.cz

Abstract: The coupling of the aerodynamic forces and the elastic deformation of a generic wing approaching to the ground and its consequences are studied. Static aero-elastic phenomena are modelled in a coupled manner. The aerodynamic characteristics of the wing respecting the deformation of the wing caused by the aerodynamic loads and the gravitational force with respect to the wing flexibility are computed using a relatively simple method suitable for the wings of the higher aspect ratios. The presented study is focused on the very close proximity of a wing to the ground as it is the case during a sailplane take-off run. The study was initiated by the problems encountered during sailplane take-off where the touch of the wingtip with the ground during the take-off run is not uncommon.

***Keywords*:** Ground effect, Aeroelasticity

Introduction

A touch of the wingtip with the ground during the initial stages of a take-off run is not uncommon event during a sailplane take-off. Potentially dangerous situation can develop as its consequence; if the pilot does not manage to elevate the wingtip quickly while the ground speed is continually increasing. Especially with a centre-of-gravity tow-hook when the sailplane is not directionally supported by a towing plane, abortion of the take-off after several seconds of attempts of no effect can be a reasonable safe solution. Reasons why the pilot has difficulty elevating the wingtip at certain conditions seem to originate from complex interactions of many factors, depending not only on the sailplane itself. The presented study is focused on the part of the influencing factors, namely on the interaction of the aerodynamic forces, the gravitational forces and the flexibility of a wing.

Computional model

Wing aerodynamic model

The aerodynamic forces are modelled by means of numerical lifting line theory where a wing is discretized in a system of N horseshoe vortices. The bound part of the vortices lies on the wing lifting line. The applied theory is fully described by Phillips and Snyder[1] with minor modifications to include ground effect. The fundamental forces equilibrium is described in eq.1 where ρ is the density, Γ_i is the circulation of ith vortex, $\vec{v}_j$ is the induced velocity vector from j^{th} vortex, V_∞ is the airspeed, $\overrightarrow{dl_i}$ is the vector of the bound part of ith vortex, dA_i is the area of the portion of the wing represented by i^{th} vortex, C_{Li} is the local lift coefficient, ΔC_{Li} is the change of the section lift characteristics caused by ground proximity. The airspeed is always set to maintain the equilibrium of the lift and the gravitational forces. The Reynold number effects on aerodynamic characteristic are neglected.

$$\rho\Gamma_i\left|\left(\overrightarrow{V_\infty}+\sum_{j=1}^{N}\vec{v}_j\right)\times\overrightarrow{dl_i}\right| = \frac{1}{2}\rho V_\infty^2(C_{Li}+\Delta C_{Li})dA_i \qquad eq.1$$

Ground proximity

Two effects are included in the ground proximity modelling. The first one is the attenuation of the influence of the wingtip vortices. It is modelled by the well-known mirror image approach mentioned for example by McCormick[2]. The principal idea is to have the wing lift distribution which satisfies the condition of zero flow through the ground. This is achieved by positioning of the second wing to the computational model; the wing is created as a mirror image of the first wing about the ground plane. The second effect is related to the 2D airfoil section characteristics; the computational and experimental study of this effect was performed by Pátek et al.[3]. Two illustrative examples of a velocity field from CFD computations are presented in Fig. 1. The increased velocity under the airfoil at low angles of attack is clearly seen in the bottom part of the image, a change of the character of the flowfield under the airfoil to a flow typical for a nozzle is accompanied by a change of the aerodynamic forces. The change of the lift coefficient ΔC_L is a function of the angle of attack and the height over ground, an example is presented in Fig. 2. In the proposed model the local angle of attack is a function of circulation distribution on the wing $\Gamma(t)$.

$$\Delta C_L = \Delta C_L(\Gamma(t), h) \qquad eq.2$$

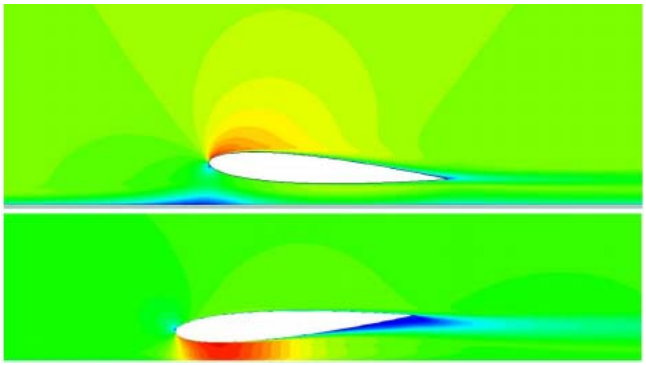

Fig. 1 Velocity field around the symmetrical airfoil section in ground proximity

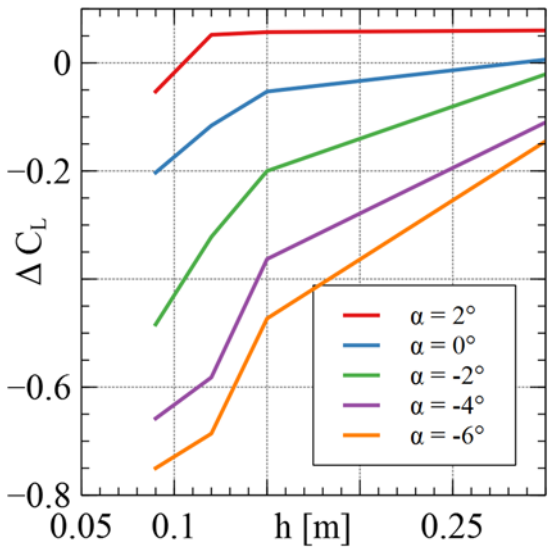

Fig. 2 Effect of ground proximity on lift characteristics of the airfoil section.

Structural model and coupling

The torsional and bending deformations of the wing are taken into account. Simple cantilever beam model based on the Maxwell-Mohr method is used to determine the wing torsional twist Φ and the angle of rotation Θ along the spanwise. The deformation increments are determined as follows.

$$\Delta\Phi = C^{\Phi\Phi}M^{y} \qquad eq.3$$

$$\Delta\Theta = C^{\Theta y}F + C^{\Theta\Theta}M^{x} \qquad eq.4$$

where $C^{\Phi\Phi}$, $C^{\Theta y}$, $C^{\Theta\Theta}$ are the matrices of flexibility coefficients, F is the force load vector and M^{y} and M^{x} are the moments load vectors of torsional and bending moments respectively, the details are discussed in literature[4,5]. Coupling is implemented in the following steps.

1. The aerodynamic forces are computed from the initial shape by solving system of N simultaneous nonlinear equations 1 and 2.
2. The distribution of the torsional twist ΔΦ and the angle rotation ΔΘ along the span are computed from the eq. 3 and 4.
3. The new set of the aerodynamic forces is computed for the new deformed wing shape.
4. If the new ΔΦ and ΔΘ are lower than certain limit, then it is assumed that the algorithm found the final equilibrium shape.
5.

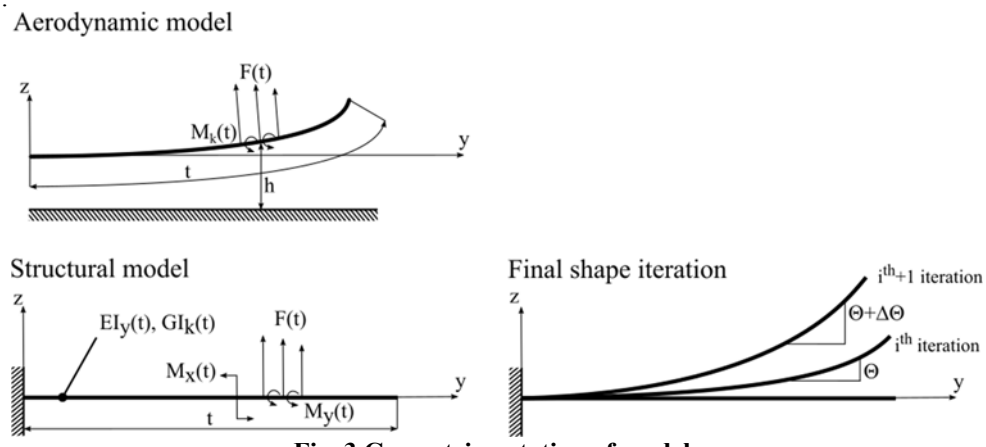

Fig. 3 Geometric notation of models

Results

The wing is of 18 m span and 12 m^2 area. The torsional and bending elasticities of the wing are similar to a typical advanced wing based on carbon fibre structure, its elastic axis is situated behind the line of the aerodynamic focuses. The mass of the left and right wings together is 150 kg, with the water ballast 350 kg, the position of the line of local centres of gravity depends on the amount of water in the ballast tanks that are positioned in the front inner part of the wing. Aerodynamic characteristics of the wing are calculated for three versions of the wing

structure: the absolutely rigid wing, the wing flexible in the torsion and rigid in the bending and the wing flexible both in the torsion and in the bending. The results (Fig. 4) leads to the conclusion that the influence of the torsional flexibility on C_L is much more pronounced than the influence of the bending flexibility and that the influence of the flexibility increases with the diminution of the lift coefficient. The influence of the water in the ballast tanks is also perceptible.

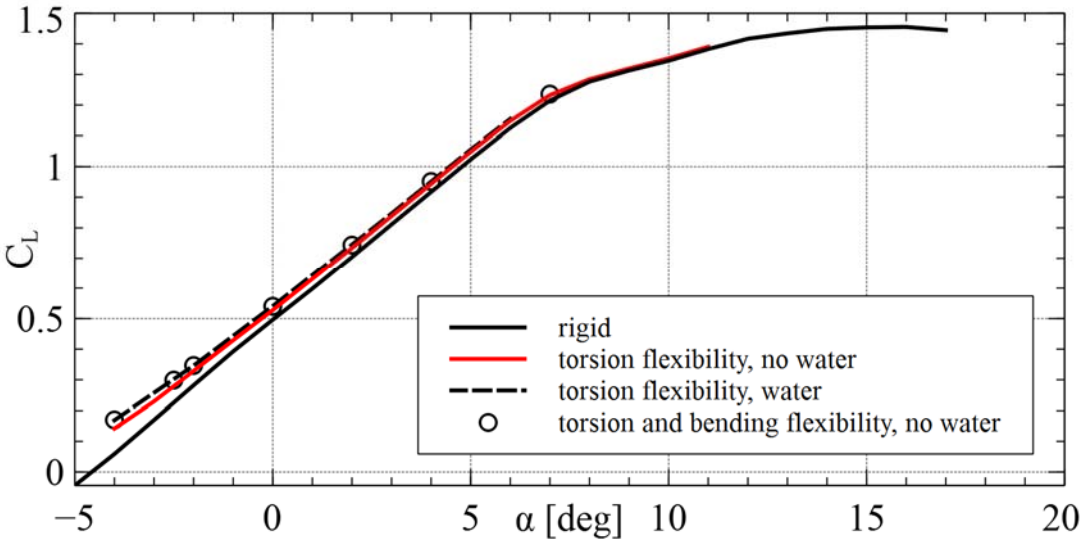

Fig. 4 Lift curves

The importance of the torsional flexibility is illustrated in Fig. 5 and 6. The lift distribution along the span is highly influenced by the torsion of the wing with the very distinctive increase of the angle of incidence and the lift coefficient towards the wingtip. The redistribution of the lift together with the bending flexibility causes distinctive bending of the wing even in the case of the load factor equal to 1 (Fig. 7).

In the very close proximity to the ground, the airfoil is sucked towards the ground as mentioned above. This phenomenon together with the flexibility of the outer part of the wing complicates the situation with the wingtip touching the ground at low-speed when aerodynamic control surfaces are less effective. The presented typical example describes a generic sailplane during take-off with bank angle of 5 deg. The results of the computations show that the combination of the aerodynamic sucking force and the wing flexibility causes aerodynamic moment about the longitudinal axis of the order of 0.01 (Fig. 8) at small angles of attack (that correspond to the initial stages of the take-off run). For comparison, the similar rolling moment coefficient is created by the deflection of the flaperons of 3 deg in the free flight. Together with aerodynamic moment, the moment of the gravity force at the bank angle takes effect which necessitates additional deflection of the flaperons to counter it. If the situation is further made difficult by yawing moment caused by the friction of the wingtip on the ground, the low authority of the rudder at low speed and use of a centre-of-gravity tow-hook, the initial stage of the take-off could become precarious.

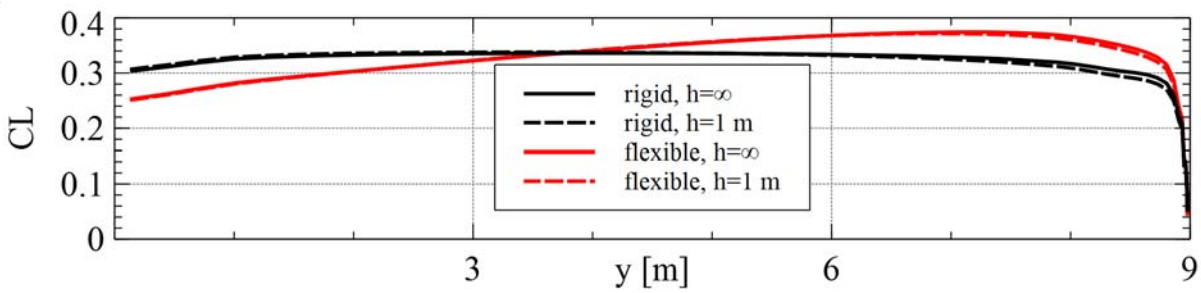

Fig. 5 Lift distribution along the wingspan, C_{Lwing} = 0.33.

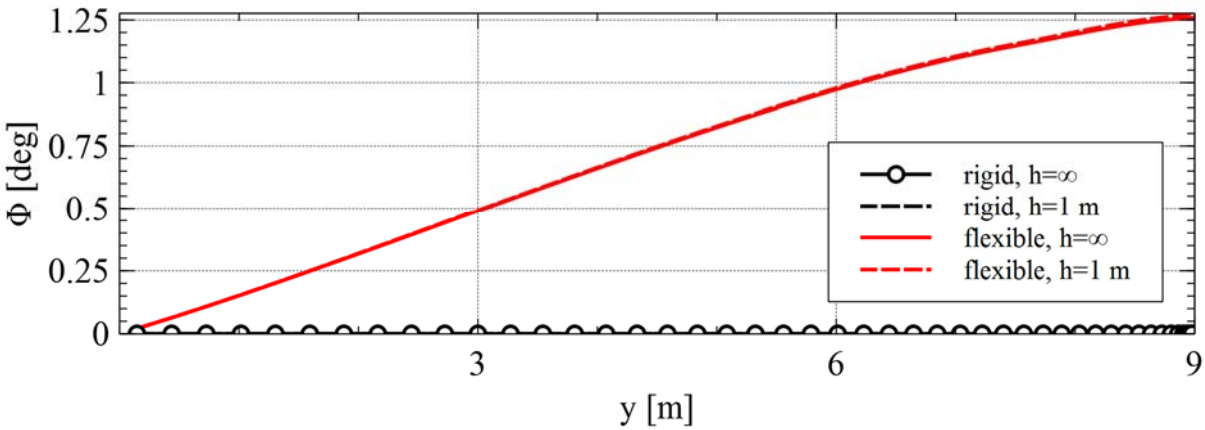

Fig. 6 Torsional deformation along the wingspan, C_{Lwing} = 0.33

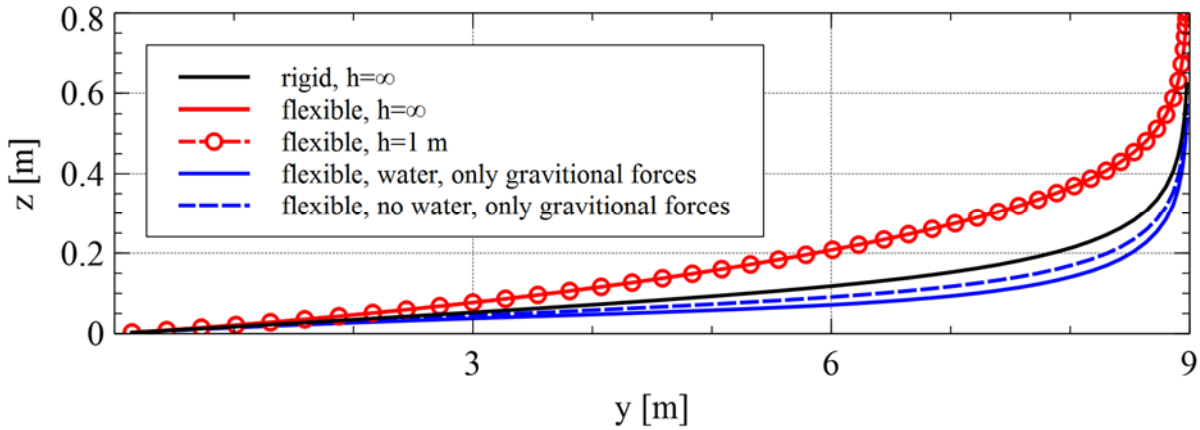

Fig. 7. Bending deformation along the wingspan, C_{Lwing} = 0.33

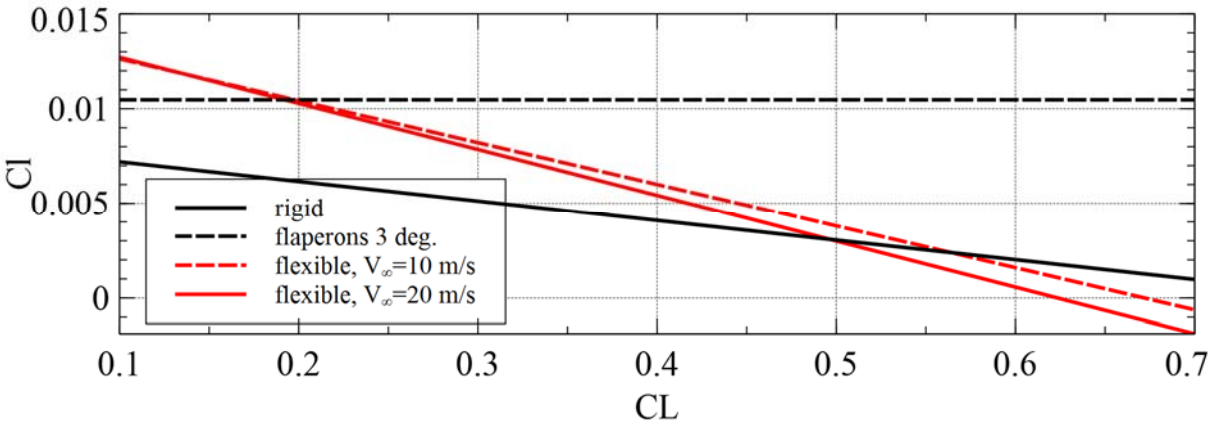

Fig. 8. Aerodynamic moment Cl about longitudinal axis

References

[1]Phillips, W. F., & Snyder, D. O., Modern adaptation of Prandtl's classic lifting-line theory. Journal of Aircraft, Vol. 37 (2000), No. 4, pp. 662-670

[2]McCormick, B. W., Aerodynamics, Aeronautics, and Flight Mechanics, 1st ed. Wiley, New York, 1979, pp. 419–424

[3]Pátek, Z., Vrchota, P., & Červinka, J., Experimental and computational study of ground effect on airfoil section. 30th Congress of the International Council of the Aeronautical Science in Daejeon, Korea, September 25-30, 2016. ICAS2016_0122, ICAS 2016 Congress Proceedings, ISBN: 978-3-932182-85-3

[4]Slavík, S., Aeroelasticita leteckých konstrukcí. Vydavatelství ČVUT, Praha 1997, ISBN: 80-01-01415-0

[5]Bisplinghoff R. L., Ashley H., Halfman R. L., Aeroelasticity. Dover Publications, Mineola 1996, ISBN 978-0486691893

Optimized High-Speed Performance of RC Gliders by Dynamic Soaring

Gottfried Sachs, Benedikt Grüter
Technische Universität München, Institute of Flight System Dynamics, Germany, sachs@tum.de

Abstract: High-speed dynamic soaring of radio controlled gliders at ridges is dealt with. Appropriate flight mechanics and wind modellings are developed for describing the motion of a glider in the wind scenario involving a thin shear layer in the leeward region of ridges. It is shown how gliders can extract the maximum of energy from the moving air in such a wind scenario in order to achieve the highest speed that is possible with dynamic soaring. For constructing results on maximum-speed dynamic soaring, an efficient optimization method which is capable of dealing with the complex dynamics problem is used.

***Keywords*:** High-speed soaring, shear wind, energy gain from wind.

Introduction

Dynamic soaring is a flight mode by which energy can be extracted from horizontal wind so that non-powered flight is possible [1]. For continually performing dynamic soaring, it is necessary that the horizontal wind changes with altitude, yielding what is termed shear wind. There is a unique shear wind scenario in the leeward side of sharp-crested ridges where a thin layer separates the wind blowing over the ridge from a zone of still air below the layer. Such shear winds are utilized by radio controlled (RC) gliders for dynamic soaring [2, 3]. By exploiting the difference in the velocity of the two adjacent air masses, dynamic soaring enables extremely high speeds. This has led to ever-growing speed records over the past years to reach now a value as high as 232 m/s [4]. The purpose of the present paper is to show with the use of mathematical optimization how gliders can extract the maximum of energy from the wind in order to achieve the highest speed that is possible with dynamic soaring in thin shear-wind layers at ridges.

Vehicle Dynamics and Optimal Control Problem

The modelling developed for the dynamic soaring problem under consideration is graphically addressed in Figure 1 which presents the wind scenario before and behind a ridge and a dynamic soaring trajectory suitable for extracting energy from the wind. The wind scenario shows a thin shear layer in the leeward region of the ridge which separates a zone of no wind from a zone with wind. The dynamic soaring trajectory consists of an inclined closed loop where the shear layer is traversed upwards in the climb phase and downwards in the descent phase.

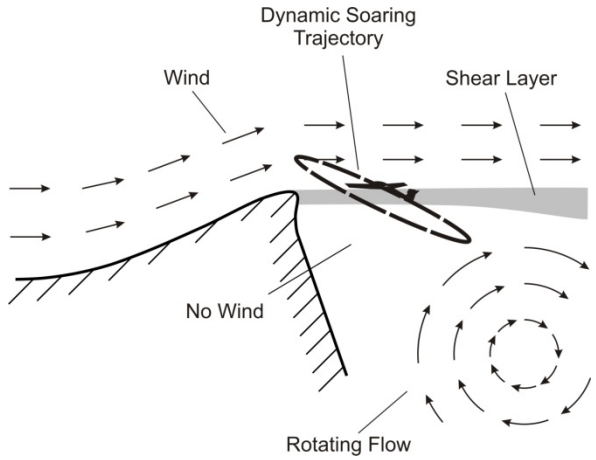

Figure 1. Dynamic soaring at ridge

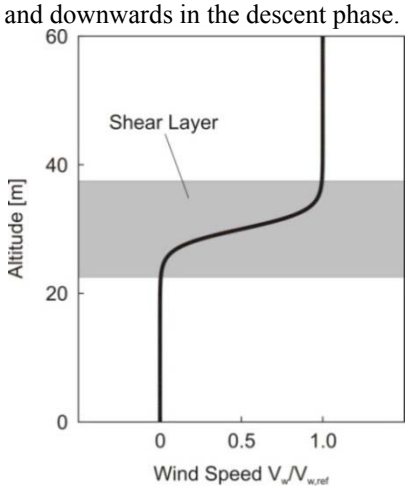

Figure 2. Modelling of shear layer

For describing the motion of the glider, a point mass dynamics model is used. Thus, the following relations hold for the equations of motion with regard to an inertial reference system

$$\begin{aligned} \dot{u}_i &= -a_{u1} D/m - a_{u2} L/m \\ \dot{v}_i &= -a_{v1} D/m - a_{v2} L/m \\ \dot{w}_i &= -a_{w1} D/m - a_{w2} L/m + g \\ \dot{x}_i &= u_i, \ \dot{y}_i = v_i, \ \dot{h} = -w_i \end{aligned} \tag{1}$$

where the coefficients $a_{u1,2}$, $a_{v1,2}$ and $a_{w1,2}$ are abbreviations of relations between the aerodynamic force components and the associated axes [5]. The aerodynamic forces, lift L and drag D, can be expressed as

$$L = C_L(\rho/2)V_a^2 S$$
$$D = C_D(\rho/2)V_a^2 S \tag{2}$$

The aerodynamic forces are dependent on the airspeed vector $\mathbf{V}_a$, while the motion of the glider is described by the inertial speed vector $\mathbf{V}_{inert} = (u_i, v_i, w_i)^T$. These speed vectors are related to each other by the following expression

$$\mathbf{V}_a = \mathbf{V}_{inert} - \mathbf{V}_w \tag{3a}$$

With the use of $\mathbf{V}_w = (-V_w, 0, 0)^T$, Eq. (3a) can be rewritten as

$$\mathbf{V}_a = (u_i + V_w, v_i, w_i)^T \tag{3b}$$

where

$$V_a = \sqrt{(u_i + V_w)^2 + v_i^2 + w_i^2} \tag{3c}$$

Modelling of the glider used in the optimization of dynamic soaring is referenced to data of existing vehicles, yielding for the maximum lift-to-drag ratio $(L/D)_{\max} = 37.5$, the wing area $S = 0.51\,\mathrm{m}^2$ and the mass $m = 15.96\,\mathrm{kg}$. Modelling of the wind scenario including the shear layer which is important for the energy gain is according to the pictorial presentation in Figure 2 where $V_{w,ref}$ refers to the free stream wind speed above the shear layer. The transitions from the shear layer to the zero wind and the full wind zones are modelled in terms of gradual junctions.

The optimization problem is to determine the closed-loop trajectory that shows the highest speed achievable with dynamic soaring. For this purpose, the performance criterion is specified as

$$J(\mathbf{x}) = V_{inert} \tag{4}$$

With reference to this performance criterion, the optimal control problem can be formulated as to determine the optimal control history

$$\mathbf{u}^*(t) = [C_L^*(t), \mu^*(t)]^T \tag{5a}$$

resulting in the optimal state history

$$\mathbf{x}^*(t) = [u_i^*(t), v_i^*(t), w_i^*(t), x^*(t), x^*(t), y^*(t), h^*(t)]^T \tag{5b}$$

subject to the equations of motion according to Eq. (1)

$$\dot{\mathbf{x}}(t) = \mathbf{f}(\mathbf{x}(t), \mathbf{u}(t)) \tag{5c}$$

and subject to periodic boundary conditions

$$\mathbf{x}(t_{cyc}) = \mathbf{x}(0) \tag{5c}$$

such that the objective function $J(\mathbf{x})$ is maximized.

The optimal control problem is solved by applying a full discretization on the time grid $\bar{\mathbf{t}}$ resulting in the discretized states $\bar{\mathbf{x}}$ and controls $\bar{\mathbf{u}}$ using a trapezoidal collocation scheme. The dynamic constraints given by the equations of motion are replaced by a set of defect equations

$$\mathbf{c}(\bar{\mathbf{x}}, \bar{\mathbf{u}}, \bar{\mathbf{t}}) = \bar{x}_{k+1} - \bar{x}_k - \frac{\bar{t}_{k+1} - \bar{t}_k}{2}\left[\mathbf{f}(\bar{x}_{k+1}, \bar{u}_{k+1}) + \mathbf{f}(\bar{x}_k, \bar{u}_k)\right] = \mathbf{0} \tag{6}$$

at every point on the discretized time grid. This transcription of the optimal control problem is automatically performed utilizing the direct optimal control tool FALCON.m [6]. The resulting large parametric optimization problem which includes all discretized states, controls and parameters contained in the optimization vector is solved efficiently employing readily available software, e.g. the interior point solver IPOPT.

FALCON.m is a free optimal control tool developed at the Institute of Flight System Dynamics of the Technische Universität München. It provides a MATLAB class library in order to set-up, solve and analyze optimal control problems using numerical optimization methods. The code is optimized for usability and performance and enables the solution of high-complexity optimal control problems.

Results

Results on optimizing dynamic soaring with the goal of maximizing the speed are presented in Figure 3 which provides a perspective view of the maximum-speed trajectory and its relationship with the wind scenario. The maximum-speed trajectory consists of four flight phases which are characteristic for dynamic soaring, yielding:

1) windward climb with traversing the shear layer upwards
2) upper curve from wind- to leeward
3) leeward descent with traversing the shear layer downwards
4) lower turn from lee- to windward

A main result is the maximum speed which is obtained as $V_{inert,\max} = 239.2$ m/s. Furthermore, the trajectory point is of importance where $V_{inert,\max}$ occurs in the course of the dynamic soaring cycle. This point which is indicated in Figure 3 is in a trajectory section within the shear layer. Thus, it is not at the lowest trajectory point,

but well above. Additionally, it is remarkable that $V_{inert,\max}$ is many times higher than the free stream wind speed which is supposed to be $V_{w,ref} = 20$ m/s , manifesting in the ratio $V_{inert,\max} / V_{w,ref} = 12$.

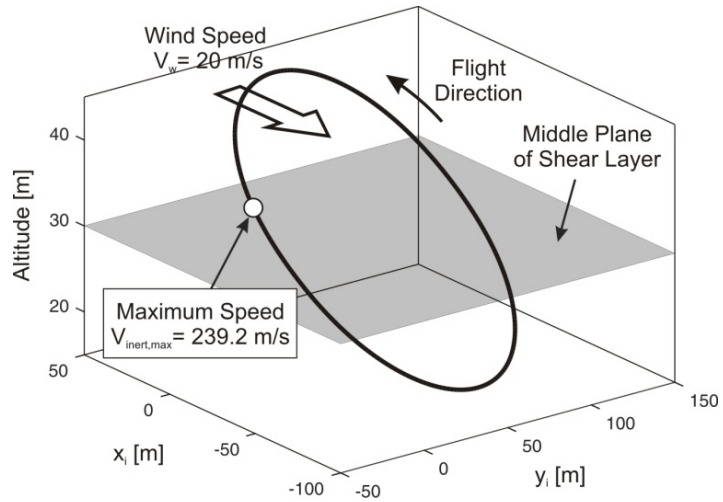

Figure 3. Maximum-speed dynamic soaring cycle

The behaviour of the altitude and the speed, h and V_{inert} , and the relationship between these quantities are graphically described in more detail in Figures 4 and 5. According to the cycle character of the trajectory, the altitude and speed time histories show a corresponding behaviour. The cyclic behaviour of h is around the wind shear layer and appears to be rather symmetrical as regards the variation about the average (with the zero altitude reference the same as in Figure 2). The speed is at a high level throughout the dynamic soring cycle to reach the maximum speed $V_{inert,\max}$ at the beginning and end of the presented cycle. The cyclic behaviour of V_{inert} appears to be less symmetrical around the average.

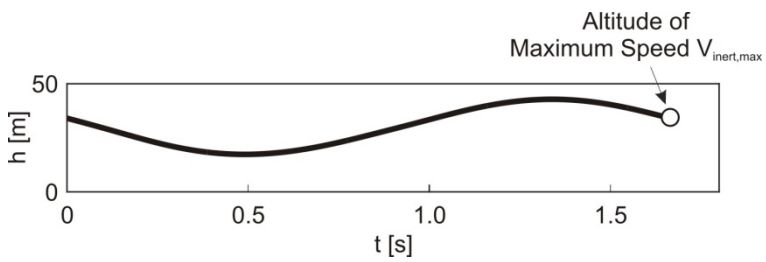

Figure 4. Altitude time history of maximum-speed dynamic soaring cycle

Further to Figure 4, the altitude is indicated at which the maximum speed, $V_{inert,\max}$, is reached. This is a point that is above the middle of the altitude range traversed during the dynamic soaring loop. Thus, it differs considerably from the lowest altitude point.

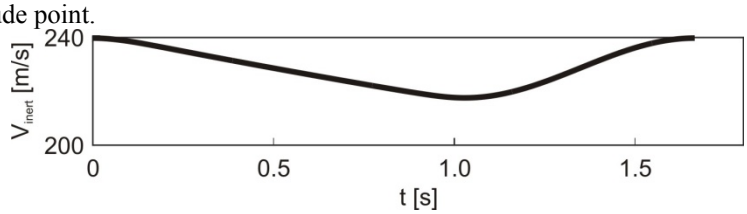

Figure 5. Inertial speed time history of maximum-speed dynamic soaring cycle

The flight path angle, γ, is presented in Figure 6 to provide an insight into the inclination of the dynamic soaring cycle relative to the horizontal wind. The data show that γ stays within a range of about $\pm 12.5\,\text{deg}$. This suggests that the inclination is of moderate size.

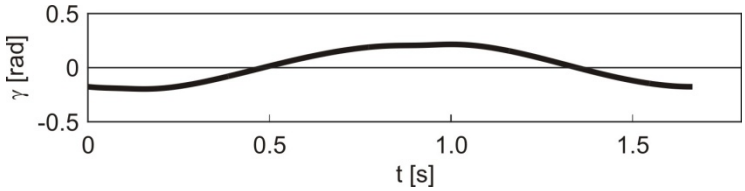

Figure 6. Flight path angle time history of maximum-speed dynamic soaring cycle

The time histories of the controls which are the lift coefficient and the lift vector bank angle, C_L and μ, are presented in Fig. 7. There are considerable changes of C_L in the course of the dynamic soaring cycle where the lowest values occur in about the middle of the windward climb phase (Figure 6). The bank angle shows a low level in the lower curve in terms of comparatively small negative values where the glider changes the flight direction from lee- to windward. In the upper curve, a considerable increase in the bank attitude in terms of larger negative values occurs.

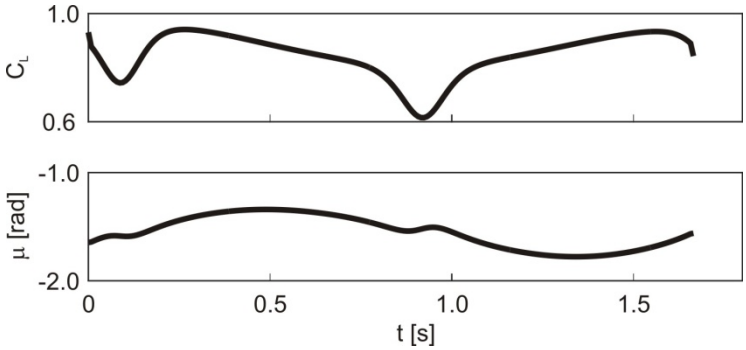

Figure 7. Controls time histories of maximum-speed dynamic soaring cycle

References

[1]Idrac, P., 1932: Experimentelle Untersuchungen über den Segelflug mitten im Fluggebiet großer segelnder Vögel (Geier, Albatros usw.) – Ihre Anwendung auf den Segelflug des Menschen. München und Berlin: Verlag von R. Oldenbourg.
[2]Richardson, P.L., 2012: High-Speed Dynamic Soaring. R/C Soaring Digest, Vol. 29, No. 4, pp. 36-49.
[3]Sachs, G., Mayrhofer, M., 2001: Shear Wind Strength Required for Dynamic Soaring at Ridges, Technical Soaring, Vol. 25, No. 4, pp. 209-215.
[4]Lisenby; S., 2017: Dynamic Soaring, Big Techday 10, June 2nd, 2017, Technology Consulting, München.
[5]Sachs, G., 2005: Minimum shear wind strength required for dynamic soaring of albatrosses. Ibis 147, pp. 1-10.
[6]Rieck, M., Bittner, M., Grüter, B., and Diepolder, J., 2016: FALCON.m − User Guide, Institute of Flight System Dynamics, Technische Universität München.

Travel Performance of Engineless UAV by Dynamic Soaring

Gottfried Sachs, Benedikt Grüter
Technische Universität München, Institute of Flight System Dynamics, Germany, sachs@tum.de

Abstract: The travel performance in terms of the maximum travel speed that can be achieved in non-powered flight using dynamic soaring is dealt with. A flight mechanics model is developed for describing soaring in a horizontal wind field that involves altitude dependent wind speeds. It is shown using this model that dynamic soaring is a flight technique that provides the possibility of engineless travelling by gaining energy form the wind. An efficient optimization method is applid for determining the maximum travel speed.

***Keywords*:** Travelling speed, non-powered flight, shear wind.

Introduction

For travelling and covering large distances, an aerial vehicle needs to have a propulsive force in order to compensate for the drag. The energy source for generating a propulsive force is usually an engine that generates the necessary thrust. Vehicles without an engine can gain energy required for travelling from the wind by an appropriate flight technique. In the case of a shear wind where the horizontal wind varies with altitude, the energy for generating a propulsive force can be gained by a flight mode termed dynamic soaring [1]. The fact that energy can be extracted from a shear wind by dynamic soaring for enabling non-powered fight was first observed with birds. This possibility has stimulated research interest in using shear winds as an energy source for technical applications. Evidence for this are biologically inspired research and development activities directed at utilizing the dynamic soaring mode of albatrosses for aerial vehicles [2 - 5].

Dynamic Soaring Mode Adequate for Travelling

There are two modes of dynamic soaring that may be regarded as basic types of this kind of flight. These modes are graphically addressed in Figures 1 and 2 which show the corresponding flight paths and shear wind scenario. The dynamic soaring mode presented in Figure 1 is S-shaped and may be termed as bend type. The other mode of which two variants are presented in Figure 2 is O-shaped and may be characterized as oval or spiral type. This mode involves a reversal in the flight direction in the course of the dynamic soaring cycle where the flight directions at the end and beginning of a cycle are opposite to each other at the left variant in Figure 2 while they are the same at the right variant.

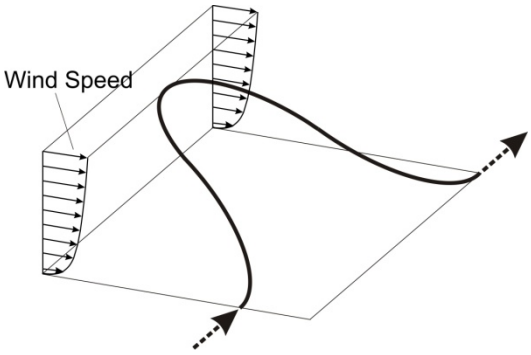

Figure 1. Dynamic soaring cycle (bend mode)

The forms of the two dynamic soaring modes suggest that the bend mode is more suited for an efficient travel performance than the oval mode. The oval mode is an option for flight tasks such as searching, loitering, surveillance applications, etc. Thus, the bend mode is considered an appropriate candidate for achieving an efficient travel performance of engineless UAV using dynamic soaring so that it will be dealt with in the following. The presented cycles involve four flight phases which can be considered as characteristic elements of dynamic soaring, yielding

Phase 1: windward climb
Phase 2: upper curve from windward to leeward flight direction
Phase 3: leeward descent
Phase 4: lower curve from leeward to windward flight direction

At the end of the cycle, the energy state is considered to be the same as at the beginning. This kind of dynamic soaring cycle may be termed energy-neutral. Because of this energy-neutral property, the dynamic soaring cycle can be continually repeated. Thus, dynamic soaring is a flight mode that enables a cruise type flight in order to cover large distances at no energy cost.

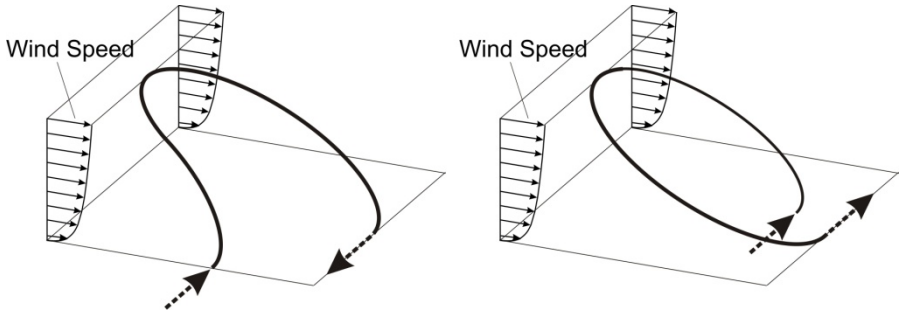

Figure 2. Dynamic soaring cycle (oval mode)

Vehicle Dynamics and Optimal Control Problem

For describing the motion of an aerial vehicle or a bird performing dynamic soaring, a point mass dynamics model can be used. Thus for the equations of motion with regard to an inertial reference system

$$\begin{aligned} \dot{u}_i &= -a_{u1}D/m - a_{u2}L/m \\ \dot{v}_i &= -a_{v1}D/m - a_{v2}L/m \\ \dot{w}_i &= -a_{w1}D/m - a_{w2}L/m + g \\ \dot{x}_i &= u_i,\ \dot{y}_i = v_i,\ \dot{h} = -w_i \end{aligned} \tag{1}$$

where the coefficients $a_{u1,2}$, $a_{v1,2}$ and $a_{w1,2}$ are abbreviations of relations between the aerodynamic force components and the associated axes [6]. The aerodynamic forces, lift L and drag D, can be expressed as

$$\begin{aligned} L &= C_L(\rho/2)V_a^2 S \\ D &= C_D(\rho/2)V_a^2 S \end{aligned} \tag{2}$$

The aerodynamic forces are dependent on the airspeed vector $\mathbf{V}_a$, while the motion of the glider is described by the inertial speed vector $\mathbf{V}_{inert} = (u_i, v_i, w_i)^T$. These speed vectors are related to each other by the following expression

$$\mathbf{V}_a = \mathbf{V}_{inert} - \mathbf{V}_w \tag{3a}$$

With the use of $\mathbf{V}_w = (-V_w, 0, 0)^T$, Eq. (3a) can be rewritten as

$$\mathbf{V}_a = (u_i + V_w, v_i, w_i)^T \tag{3b}$$

where

$$V_a = \sqrt{(u_i + V_w)^2 + v_i^2 + w_i^2} \tag{3c}$$

As a representative case typical for travelling by means of dynamic soaring, the flapless flight of an albatross is dealt with. This case can also serve for dynamic soaring of engineless aerial vehicles since there are similarities in regard to the soaring aerodynamic configuration which plays a main role for the travelling performance achievable with dynamic soaring. Concerning data used for describing aerodynamics, size and mass properties, reference is made to [6].

The maximum travel speed is considered a measure for the achievable travel performance. Therefore, maximizing the travel speed was subject of an optimization treatment, with the goal of determining the highest travel speed achievable with dynamic soaring. For this purpose, the direct optimal control tool FALCON.m was used which was developed at the Institute of Flight System Dynamics of the Technische Universität München [7]. It provides a MATLAB class library in order to set-up, solve and analyse optimal control problems using numerical optimization methods. The code is optimized for usability and performance and enables the solution of high-complexity optimal control problems.

Results

To provide an insight into dynamic soaring characteristics for achieving a high travel performance, properties of state and control variables are dealt with. For this purpose, a low and a high wind speed case are considered as representative examples and details of the state and control behaviour are examined.

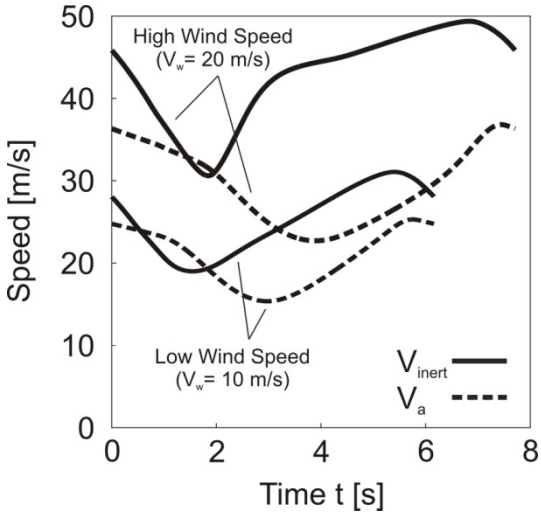

Figure 3. Speeds during optimized dynamic soaring cycle of maximum travel performance

The speed behaviour in the two wind speed cases is presented in Figure 3 where the time histories of the inertial speed, V_{inert}, and the airspeed, V_a, are plotted for the time period of a dynamic soaring cycle. The high wind speed case shows a considerably higher level in both V_{inert} and V_a compared to the low wind speed case. As a common feature, there are rather large variations of V_{inert} and V_a in the course of the cycle. A decrease in each of V_{inert} and V_a takes place in the first part of the cycle, followed by an increase thereafter. The increase of V_{inert} is indicative for the increase in the kinetic energy state and corresponds with an energy gain from the wind. Furthermore, V_{inert} is larger than V_a in both wind speed cases (apart from a small time segment) where the difference between V_{inert} and V_a is more pronounced in the high wind speed case.

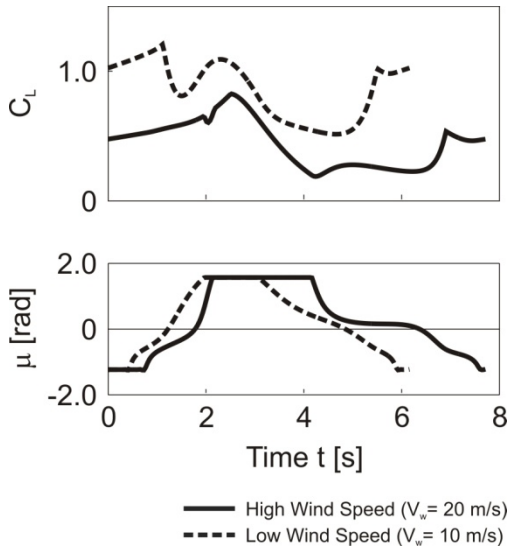

Figure 4. Controls during optimized dynamic soaring cycle of maximum travel performance

The controls behaviour is presented in Figure 4 where the time histories of the lift coefficient, C_L, and the bank angle, μ, during a dynamic soaring cycle are shown. The lift coefficient which involves considerable changes in the course of the cycle is higher in the low wind speed case compared to the high wind speed case. This indicates a correspondence with the airspeed behaviour examined before. Despite of the difference in the magnitude of C_L in both wind speed cases, there is some similarity in the form of the C_L curves. The bank angle which also shows considerable changes during a dynamic soaring cycle is of comparable magnitude in both wind speed cases.

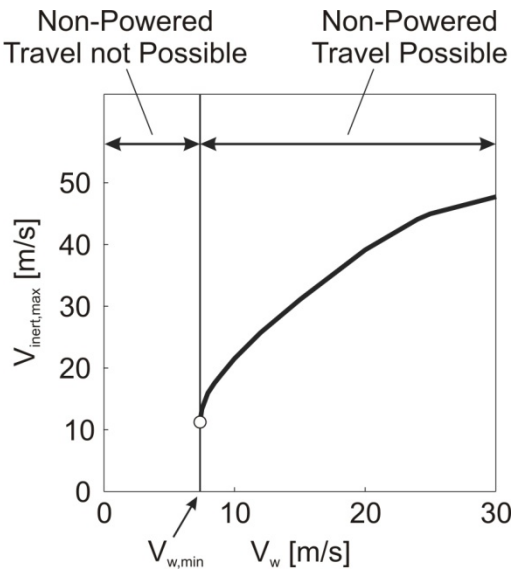

Figure 5. Maximum travel speed achievable with dynamic soaring

The wind speed plays a major role for the travel performance achievable in non-powered flight. Accordingly, the effect of the wind speed on the maximum travel speed was determined and, as a summarizing outcome, results on this topic are presented in the following.

In Figure 5, the maximum travel speed in terms of the maximum average cycle speed, denoted by $V_{inert,\max}$, is depicted dependent on the wind speed V_w. The $V_{inert,\max}$ curve shows the wind speed range where non-powered travelling is possible. The curve begins at a definite wind speed, denoted by $V_{w,\min}$, below which the wind is not strong enough for non-powered travelling. This is because $V_{w,\min}$ is the minimum wind speed required for dynamic soaring. Already at $V_{w,\min}$, however, the maximum travel speed $V_{inert,\max}$ shows a considerable level. From that value on, $V_{inert,\max}$ continually increases with the wind speed. Comparing travel and wind speeds, the maximum travel speed is about twice the wind speed.

References

[1]Cone, C. D., Jr., 1964: A Mathematical Analysis of the Dynamic Soaring Flight of the Albatross with Ecological Interpretations. Virginia Institute of Marine Science, Gloucester Point, Virginia, Special Scientific Report·No. 50.

[2]Liu, D.-N., Hou, Z.-X., Guo, Z., Yang, X.-X. and Gao, X.-Z., 2017: Bio-inspired energy-harvesting mechanisms and patterns of dynamic soaring. Bioinspir. Biomim. 12, 016014.

[3]Deittert, M., Richards, A., Toomer, C.A., Pipe, A., 2009: Engineless Unmanned Aerial Vehicle Propulsion by Dynamic Soaring. Journal of Guidance, Control, and Dynamics, Vol. 32, pp. 1446-1457.

[4]Langelaan, J.W., Roy, N., 2009: Enabling New Missions for Small Robotic Aircraft. Science, Vol. 326, pp. 1642-1644.

[5]NASA – http://www.max3dmodels.com/vdo/NASA-Albatross-Dynamic-Soaring-Open-Ocean-Persistent-Platform-UAV-Concept/F4zEaYl01Uw.html, 2010.

[6]Sachs, G., 2005: Minimum shear wind strength required for dynamic soaring of albatrosses. Ibis 147, pp. 1-10.

[7]Rieck, M., Bittner, M., Grüter, B., and Diepolder, J., 2016: FALCON.m − User Guide, Institute of Flight System Dynamics, Technische Universität München.

Exploring gravity waves in the Pyrenees by ground based observations, in-flight measurements, and model analysis

Elena L. Mascus[1,2,5], Mireia Udina Sistach[1], Maria Rosa Soler[1], Alfred Ultsch[3,5] and Christof Maul[4,5]

1 Departament d'Astronomia i Meteorologia, Universitat de Barcelona, Barcelona, Spain
2 Institute of Atmospheric and Environmental Sciences, Goethe University Frankfurt, Frankfurt, Germany
3 Data Bionics, Philipps University Marburg, Marburg, Germany,
4 Institute of Physical and Theoretical Chemistry, Technische Universität Braunschweig, Braunschweig, Germany
5 Akademische Fliegergruppe (Akaflieg) Frankfurt, Frankfurt, Germany

Abstract: We report preliminary results obtained both during a long term campaign to study mountain gravity waves and orographic precipitation (GWOP 17) and for glider based in-flight data monitoring. The field campaign took place from October 2016 to April 2017 in the higher Segre valley in the southern part of the Pyrénées. Among the monitored data are horizontal wind, vertical wind profiles, temperature and humidity profiles, and turbulence parameters. Observational data have been screened for the occurrence of gravity waves in order to identify relevant atmospheric parameters indicating trapped lee-wave mountain events. Selected events have been analyzed using the Weather Research and Forecasting (WRF) Model. A serious limitation of ground based instrumentation is its limited observation range. Thus, we have explored the possibility to complement ground based observation by in-flight measurements using sailplanes equipped with state of the art miniaturized measurement equipment in accordance with the space and energy available. With the advent of small yet very powerful single-board computers and a large number of low cost, yet powerful and reasonably accurate sensors it has become feasible to build a data logger for gathering meteorological and flight data for mountain wave research. The potential of glider-based in-flight meteorological monitoring is highlighted for a wave event in the Cerdanya valley in the spring of 2015.

***Keywords*:** mountain waves, model analysis, in-flight measurements

Introduction

This study consists of preliminary results obtained during a long term field campaign "La Cerdanya 17" studying mountain gravity waves and orographic precipitation (GWOP17) and during the "Akaflieg Frankfurt Wave Research Camp" for glider based in-flight data monitoring (Akaflieg Frankfurt). One part of the data gained through the campaign was examined within the framework of a bachelor thesis at the Goethe-Universität Frankfurt (Mascus, 2018).

The field campaign

The scope of the campaign was to improve the knowledge of mountain waves and associated processes: rotors and subrotors, turbulence and boundary layer separation, to study the dynamics and microphysics of the precipitation processes influenced by orographic effects, with emphasis on heavy precipitation events, and to analyze the interaction of gravity waves with cloud structures and its influence on precipitation. The campaign was part of the joint project "Atmount" (Meteo France, Meteo Catalunya, Universitat de Barcelona, University of Portsmouth, University of the Balearic Islands) and took place from October 2016 to April 2017 in the southern part of the Pyrenees.

Ground based instrumentation such as a lidar, UHF radar, microwave radiometer, wind profiler, ceilometer, and disdrometer was located at or in the direct vicinity of La Cerdanya aerodrome, and a large number of temperature and humidity sensors were distributed all over the valley. In addition, radiosonde and tethered balloon measurements were carried out. Among the monitored data are horizontal wind, vertical wind profiles, temperature and humidity profiles, and turbulence parameters.

Model evaluation, Bachelor Thesis

The thesis aims at validating the performance of WRF Weather Research and Forecasting Model regarding wind speed and direction, vertical velocity and wave length by comparing the 24h model output to measurements obtained during the campaign (surface stations, wind profiler) and to in-flight data of glider flights in the Cerdanya valley on April 6, 2017. Each simulation was performed for the grid point of the according measurement device.

a) Ground based measurements

Horizontal wind component

Fig. (1) compares the simulated (blue line) wind direction (above) and the 10-m wind speed (below) to the measurements (green line) of the surface station Tosa d'Alp (2478m): the simulated wind directions coincide very well with the observed values, whereas the model tends to exaggerate the horizontal wind speed during the first half of the day.

The general overestimation of the wind speed is a known weakness of models using the linear theory. According to (Nappo, 2012) "the linear theory predicts unrealistically strong winds" and corresponding to (Udina et al., 2017) the overestimation might also be caused through the smoothed topography the model uses and could be solved by refining the terrestrial data.). Another reason may be error propagation through initialization: The model was initialized 48 hours before the analyzed day, which could lead to serious divergences between simulation and measurements.

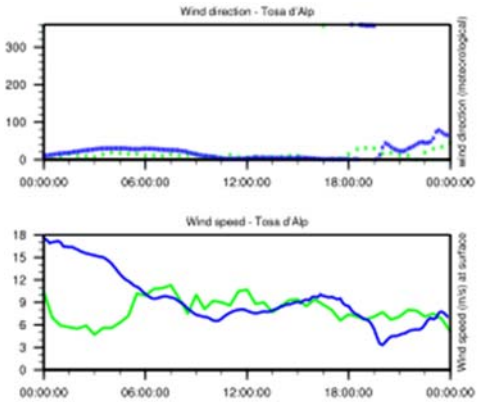

Figure 1: Measurements of the automatic weather station (green) compared to model output (blue) for April 6, 2017.

Vertical wind component

Figure (2) illustrates the comparison in a height against time plot of the vertical wind component measured (left) by the wind profiler and the according simulation (right) calculated by WRF.

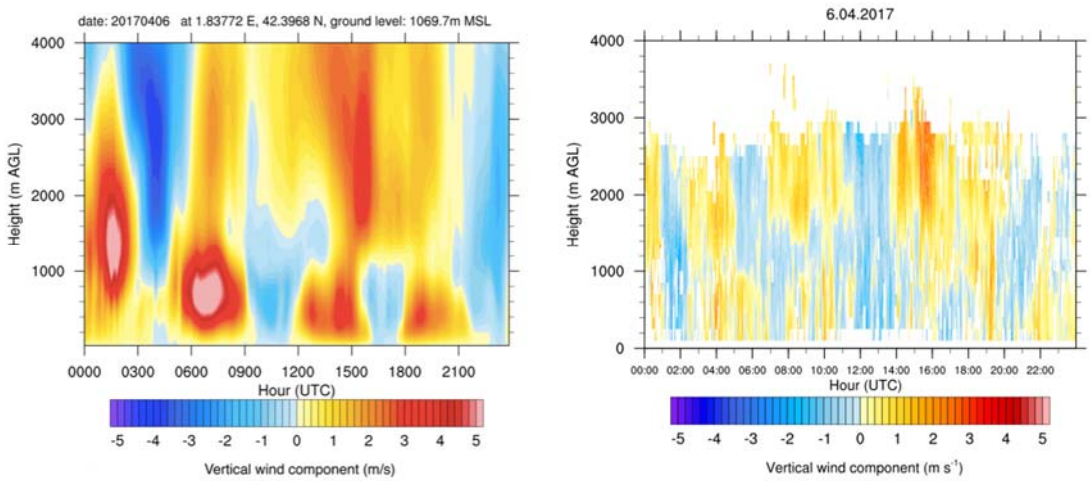

Figure 2: Comparison of the measured (left) and simulated (right) vertical velocity during 24h up to 4 km AMSL.

Wave typical updrafts and downdrafts appear in the measurements as well as in the model simulation. As a direct consequence of the overestimated horizontal wind speed (see Fig. 1), the model exaggerates again: the vertical speed reaches values of more than 5 m/s whereas the measurements are below.

The simulation and the measurements agree very well in exhibiting a time oscillating behavior of the vertical wind speed meaning that the wavelength varies such that ascent and descent are interchanging their position above the UHF wind profiler. The decreasing wavelength and the alternating location of up- and downdraft above the UHF might be caused by the continuously decreasing horizontal wind speed throughout April 6, 2017.

b) Flight data

Wavelength

To further evaluate the performance of the WRF model regarding the wavelength, the model output was compared with wave flights of glider pilots flown on the analyzed day.

The location of one updraft used to climb was inserted as a green point into the model output: Fig. (3, right) depicts a horizontal plane section indicating the vertical wind component and the horizontal wind in 4000 m MSL and Fig. (3, left) shows a cross section along the black line in Fig. (2, right) in the wind direction through the area of ascent.

At the time and altitude the glider starts ascending, the model output yields very good results: the modeled updraft is located within the glider's climb. In addition, during the whole period of climb these locations are in good agreement.

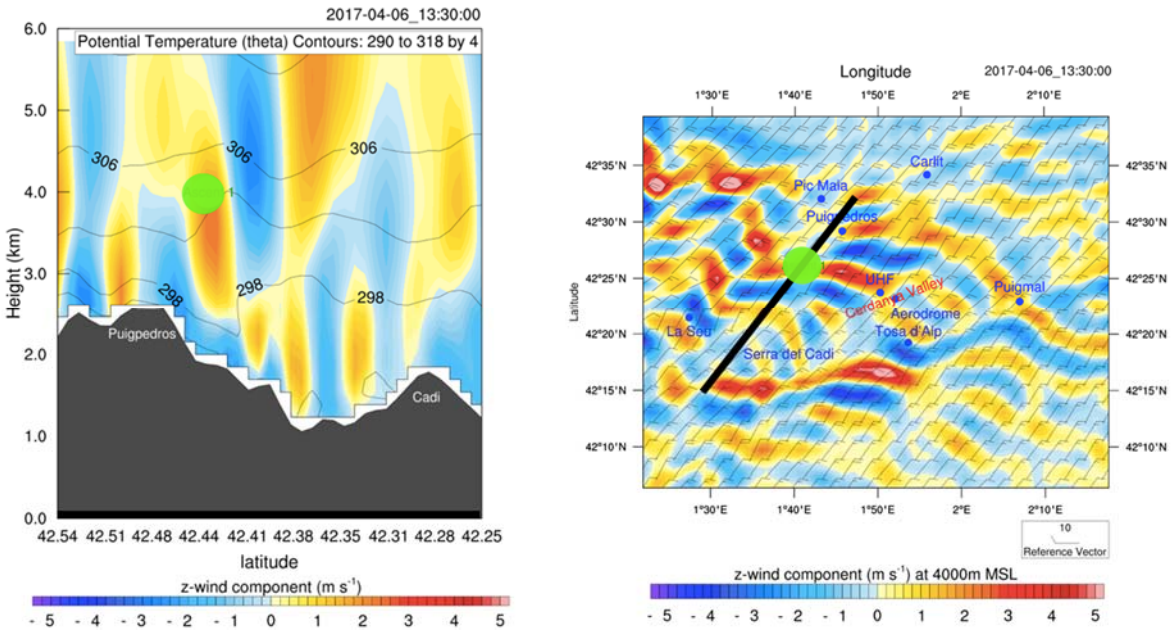

Figure 3: Left: Cross section along the black line in the right figure in wind direction through the area of ascent of the glider (green point) at the beginning of the climb period (1330 UTC). Shown are vertical velocity (m/s, shaded), potential temperature (K, grey contour lines), and the underlying terrain (shaded grey). The isentropes and the vertical velocity are in phase-shift of 90. Right: Horizontal plane section in 4000 m indicating vertical velocity (m/s, shaded) and the horizontal wind (wind barbs) over the Cerdanya valley. The area of updraft used by the glider is marked with a green point. The black line corresponds to the cross section shown in the left panel.

In conclusion, the model yields excellent result in higher altitudes, especially when regarding the wavelength. The different model performances in different heights may arise from model limitations in lower heights, where the linear theory is less applicable and many gravity wave characteristics are beyond a linear analysis (Nappo, 2012).

In-flight measurements, Akaflieg Frankfurt Wave Research Camp

Measurement devices

For research purposes the academic flight group of the Goethe University Frankfurt (Akaflieg Frankfurt) equipped their sailplanes during the Akaflieg Frankfurt Wave Research Camp with an open glide computer developed by Henrik Hoeth which is a state of the art miniaturized measurement device meeting space and energy requirements of sailplanes. It consists of a powerful all-in-one computer (Raspberry Pi) and several low cost, very small but powerful and reasonably accurate sensors: static and dynamic air pressure, high resolution GPS, air temperature, humidity, 3-axis gyroscope, 3-axis accelerometer, 3-axis digital magnetic compass and a real time clock.

First results

As an illustrative example the determination of vertical air speed from glider flight data is shown in Fig. 4. Shown are the net vertical speed of the air u^{net} (green line) against time as derived from the gross vertical speed u^{gross} (black line) of the glider, its polar vertical sink u^{polar} (red line) due to the glider's air speed, and the dynamically induced vertical motion u^{stick} (blue line) due to the glider's acceleration. Potential temperature has reliably been

measured as well (data not shown). Additionally, different wave flight modes (climb mode, speed mode) can easily be identified.

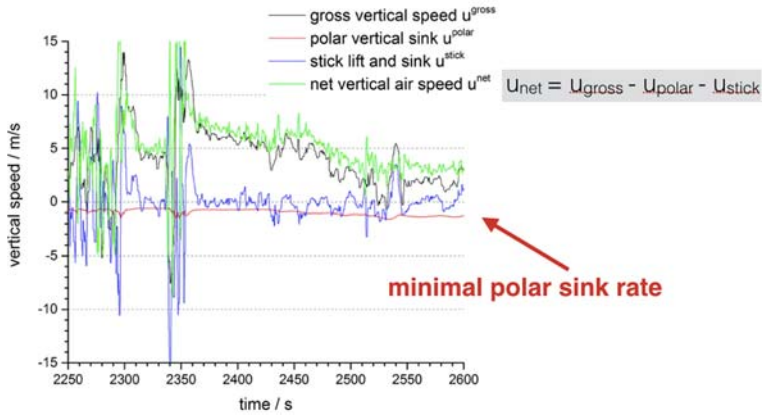

Figure 4: Vertical speeds (black: gross vertical speed of the glider, red: polar vertical sink of the glider, blue: dynamically induced vertical motion of the glider, green: net vertical speed of the air) as derived from open glide computer data

Fig.(4) shows a flight period where the pilot intends on climbing (wave climb): he keeps the sink rate of the sailplane as small as possible (red line) to benefit from the meteorological lift (green line), that in this area and at this time was throughout positive. Dynamical effects accounting for air speed corrections and reactions on turbulences are given by the blue line. In this flight mode the gross vertical speed is similar to the meteorological lift because dynamical lift or sink and the polar sink are small.

Conclusion

We have demonstrated that mountain wave research requires numerical modeling as well as in-situ measurements. Our results suggest that ground based observations should be complemented by in-situ measurements by aircraft. The model performance at larger altitudes is expected to be much better than close to the ground, where turbulence and non-linear effects become more important.

For obvious safety reasons and logistical difficulties, until now in-flight measurements, especially of rotors, are fairly rare. Nevertheless, they have a tremendous potential. We suggest therefore to promote the equipment of sailplanes, which frequently fly in mountain waves, with low cost, small and reasonably accurate measurement devices available today.

References

Mascus, E.L., 2018, Mountain Waves Over The Pyrenees - Analysis of a case study during the campaign La Cerdanya 2017 using numerical simulations and meteorological observations, B.Sc. Thesis, Goethe-Universität Frankfurt

Nappo, C. J., 2012. An introduction to atmospheric gravity waves. Academic Press.

Udina, M., Soler, M. R., Sol, O., 2017. A modeling study of a trapped lee-wave event over the pyrenees. Monthly Weather Review 145 (1), 7596

Ultsch, A., Curtius, J., Maul, C., 2016. Data Mining for Atmospheric Gravity Waves (LeeWaves), Technical Soaring 40, 25 (2016)

Catskill Mountain Wave Project: Exploration, Mapping, and Forecasting of Wave Conditions in Southern New York

Daniel Sazhin[1] Philip Chidekel[2] John J Bird[3]

Submitted 31 May 2018 for presentation at the Scientific Sessions of the XXXIV OSTIV Congress, Hozin, Czech Republic, 28 July – 3 August 2018 (submitted to 'best student paper' contest)

Abstract: Four high-altitude flights conducted in four months in the vicinity of the Catskill Mountains have demonstrated that strong wave conditions are both common and predictable in southern New York. While waves in this area have allowed several high altitude flights in the past, no one has systematically analyzed the weather conditions and the topography that creates them. We demonstrated that through the use of Skysight and other meteorological tools, wave conditions can be forecasted and predictably exploited in southern New York. We discovered that waves also occur during southwest and west winds. Through an analysis of the Skysight archive, we estimated that there were nine days between September 24th, 2017 and February 7th, 2018 that were especially conducive for wave operations. With ten glider clubs within a three-hour drive of these mountains and within visual distance of New York City, these developments can open high-altitude flying to many soaring pilots.

Introduction

Several pilots have documented high climbs, and it was local knowledge that the Catskill Mountains can generate good wave conditions. This is unsurprising as Slide Mountain is a prominent peak at 1277 meters tall. The first documented wave flight out of Wurtsboro was by Louis B. Feireabend on April 2nd 1949 in a TG-2, who topped out at 2400 meters (Feierabend, 1965). In 1959, Martin Beck completed the first wave Gold "C" altitude leg east of the Mississippi river, climbing up to 3860 meters (Beck, 1958). Subsequently, multiple Gold climbs have been achieved out of Wurtsboro airport, with the common wisdom that post-frontal days can generate favorable weather conditions for wave soaring. In 2002, Ward Hindman et al. documented a climb to 5400 meters (Hindman et al., 2004). In 2014, Warren Cramer found widespread wave up to 3800 meters on a northerly wind (Cramer, 2014). Furthermore, Daniel Zelek also achieved two successful wave climbs, to 5000 meters (Zelek, October 19th, 2014) and 5400 meters respectively (Zelek, October 26th, 2014). However, wave flights tended to be sporadic and successful climbs were generally found somewhat accidentally. In late 2017, the authors endeavored to *forecast, explore, and map* the Catskill wave. Thanks to recent advances in wave forecasting and through a deliberate analysis of topography and weather, we completed four high wave climbs triggered by Slide Mountain and have reason to assert that there are many more such favorable soaring conditions.

Methodology

Prior to attempting a wave climb on a given day, we developed a forecast of the wave conditions. The following day, the first author completed a high climb and noted which topographical features set up the wave and any notable challenges. Following each flight, we reviewed the flight log and calibrated our future predictions. Our meteorological analysis consisted of: 1) Skysight: Monitoring for days with lift stronger than two meters per second at 3000 meters at 11am local time in the vicinity of Slide Mountain. 2) Synoptic analysis, reviewing the airmass' suitability for safe wave operations. 3) Sounding analysis to forecast maximum altitude through the vertical profile of natural wavelength (Durran, 2003).

Forecasting Background

Wave conditions are fairly regular in the eastern United States, however most of this wave is limited in depth and propagates downstream rather than vertically. In order to achieve a high climb in Catskill wave, the correct balance between wind velocity and static stability must exist; otherwise, the wave will be trapped. A review of the logs from Catskill wave flights since 2014 has defined a conventional synoptic regime under which vertically propagating wave is favored (Lindsay et. al., 1976):

[1] *New York University ds5498@nyu.edu*

[2] *Pennsylvania State University philchdkl@psu.edu*

[3] *Pennsylvania State University jjbird@psu.edu*

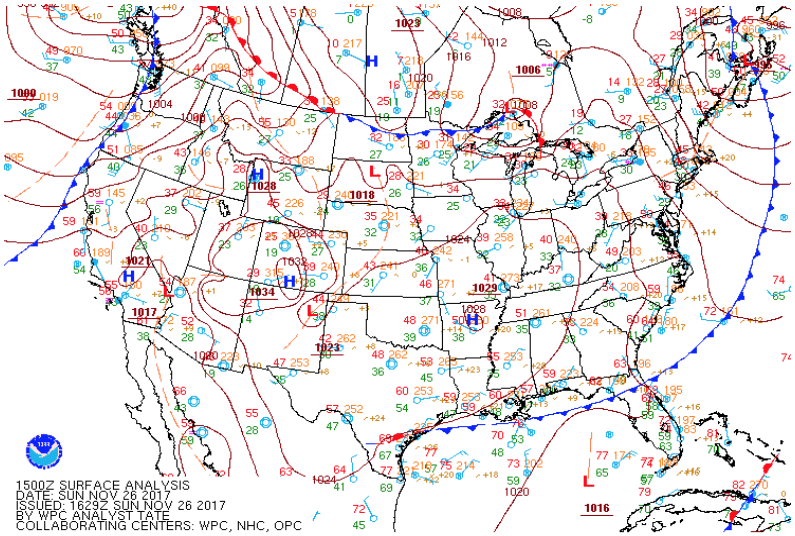

Figure 1: Surface analysis from 2017-11-26. This surface analysis is consistent with the observed synoptic regime for high wave flights.

1. The soaring site is located in northeastern quadrant of building surface high pressure *(see figure 1)*.
2. The soaring site is located on the upstream side of a sharp, 500mb trough; and thus, centered within the axis of strongest 700mb subsidence.
3. The soaring site is located under the exit region of a 300mb jet stream.

Under these conditions, northwest winds (roughly perpendicular to the Catskill escarpment) are established at the surface by building high pressure, and are maintained throughout the column by the orientation of the upper-level trough.

The location of the soaring site under the exit region of the jet stream allows for a gradual increase of mean wind speed with altitude, eventually reaching a "blunt, broad maximum" (OSTIV, 1993) at jet stream level. This is preferable to the "sharp" wind profiles commonly observed with the core of the jet stream directly overhead, which can trap the wave. However, the relationship between jet stream dynamics and the strength of the wave remains unclear.

In concert with the favorable wind profile, this set of conditions provides a temperature structure conducive to high wave. Under the observed regime, the 500mb trough axis is located downstream of the soaring site, which places the Catskill Mountains under a zone favoring upper level convergence and strong subsidence. Indeed, North American Regional Reanalysis (NARR) output for the wave days analyzed in this report reveals a pattern: the soaring site is consistently located under a local maximum in 700mb subsidence. This is important for two apparent reasons. Synoptic-scale subsidence contributes a layer of stability close to the topography in which the wave can be initiated, and correlates with a sufficiently dry mid-troposphere for safe, VFR climbs.

In addition to the successes provided by conventional northwesterly days, evidence suggests prefrontal arrangements with southwesterly flow contain favorable stability and wind profiles, and have great potential for future climbs. However, these types of days must be pursued with extreme caution. In the northeastern United States, strong southwest flow usually corresponds with warm advection and overrunning precipitation, so the frequency of prefrontal days with safe wave conditions remains to be determined.

Skysight Review

We also reviewed the Skysight archive from 2017-09-24 to 2018-02-07 to estimate how frequently good wave conditions occur. The conditions were broadly assessed at 11am, with parameters including two meters per second or stronger lift at 3000 meters and dewpoint/temperature spread more than five degrees Celsius above the boundary layer. Our review revealed 32 days with wave lift, however most were unsuitable due to excessive cloud cover. The final results suggest that nine days were likely suitable for wave operations: 2018-02-05, 2018-01-27, 2018-01-20, 2017-11-29, 2017-11-26, 2017-11-21, 2017-11-17, 2017-10-19, and 2017-10-13. This shows that once wave season begins in mid-autumn, it is plausible to find good wave soaring conditions approximately twice each month.

Results

The Catskill Mountains in the wave area form three distinct escarpments, that roughly approximate the shape of a right angle. As such, the positioning of the mountains will set up a wave in any wind direction as long as there is a conducive upper air profile. Conditions that allow for useful exploitation of the wave near Peakamoose Mountain during 330-360 degrees winds, Cornell Mountain during 270-330 degrees and Slide Mountain 220-270 Degrees. Northeast and south winds tend to be unsuitable for wave flying due to excessive moisture and the excessive distance from safe landing sites. However, it is not out of the question that special conditions may occur that may allow an even wider range of wind directions to be tested.

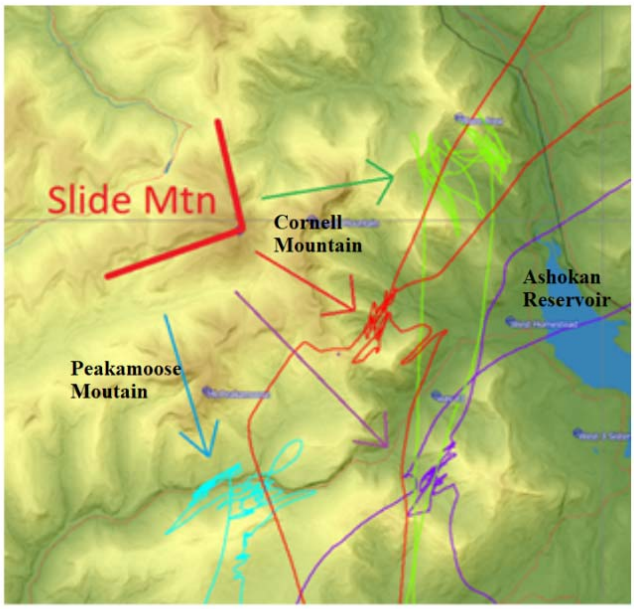

Figure 2: Areas where wave was explored.

The first author conducted four wave flights to between 5347 and 5477 meters. The limiting factor to climbing higher was due to controlled airspace.

Three flights were conducted in post-frontal conditions: 2017-11-17 (blue), 2017-11-26 (purple), and 2018-02-05 (red) (see figure 2). These flights indicated that Slide Mountain was the most likely topographic feature that triggered the wave with wind directions between 340 and 300 degrees. When the wind direction is northerly, the wave is more likely to set up on the east-west escarpment and subsequent secondary and tertiary waves would form over Ellenville and Wurtsboro. When the wind is more westerly, the waves will form more off the north-south escarpment, with waves forming closer to the Ashokan reservoir.

One flight (2018-01-27) was conducted in pre-frontal conditions, with a 240-degree wind direction (see green flight track in figure 2). This flight demonstrated for the first time in this area that southwest winds can generate strong and consistent wave lift. The biggest challenge of such days is that they require towing well downwind of Wurtsboro Airport, which precludes any possibility of returning unless wave lift is encountered.

There are several notable challenges to using wave lift from the Catskills. The first is that like many wave areas, there are few safe places to land near the mountains. An extensive field search by Richard Kaleta and Roman Micholowski has mitigated this risk and their findings can be found on a local knowledge crowdsourcing tool (The Ridge Map). Next, the primary wave forms between 25 and 50 kilometers from Wurtsboro Airport. The closest viable airport to the best wave areas is Ellenville Airport, which would save up to 30 kilometers of tow. Another challenge is the lack of an oxygen refill station in this area. This makes it difficult to refill oxygen bottles, which will become essential if pilots conduct extensive wave operations. Furthermore, our research revealed that many wave days have excessive moisture for safe operations. Pilots must be wary to fully interpret the weather forecasts to make sure that soaring the wave can be done safely. Lastly, due to the lack of a wave window, pilots are precluded from climbing above 5486 meters into Class A airspace. This makes it impossible to currently earn a Diamond Climb from a direct aerotow to the primary wave. The first author is working with Boston Center to develop a letter of agreement that would allow for pilots to operate in controlled airspace.

In summary, the Catskill Mountain Wave project has definitively demonstrated that high altitude climbs are both predictable and attainable in southern New York. With ten soaring clubs within three hours' driving distance, Wurtsboro and Ellenville are among the most accessible wave sites in the United States. We hope that this research will be the starting point of extensive wave operations in this area. Furthermore, we hope that future pilots will explore other escarpments and wave areas in this region. Future possibilities also include wave cross-country soaring by connecting to waves triggered by the northern Catskill, Berkshire, Green and Adirondack Mountains.

References

Beck, M. R. (1958, November/December). Wurtsboro Wave to Gold C Altitude. Soaring, 17-21.

Cramer, W. (2014, March 05). Retrieved from https://www.onlinecontest.org/olc-2.0/gliding/flightinfo.html?flightId=-828184133

Durran, D. R. (2003). Lee Waves and Mountain Waves. In Encyclopedia of atmospheric sciences (pp. 1161–1169).

Feierabend, L. B. (1965, January). Gold C Altitude at Wurtsboro. Soaring, 18-19.

Hindman, E. E., et al. (October 2004). An Unusually High Summertime Wave Flight. Technical Soaring, 28(4), 7-23. Retrieved from http://journals.sfu.ca/ts/index.php/ts/article/view/228/212

Lindsay, C. V., & Lacy, S. J. (1976). Soaring Meteorology For Forecasters. Silver Springs, MD: Office of Meteorological Operations, Weather Analysis and Prediction Division. Organization Scientifique et Technique International du Vol a Voile. (1993). Handbook of Meteorological Forecasting for Soaring Flight (No.495).

The Ridge Map. (n.d.). Retrieved from

https://www.google.com/maps/d/u/0/edit?mid=1LHFN5CNHKPlPYfwpVFSCiwyZbvU&ll=40.97628367552031,-75.05381849350073&z=13
Zelek, D. (2014, October 19). Retrieved from https://onlinecontest.org/olc-2.0/gliding/flightinfo.html?flightId=844542953
Zelek, D. (2014, October 26). Retrieved from https://onlinecontest.org/olc-2.0/gliding/flightinfo.html?flightId=1477206496

(Flight logs accessed with the permission of their respective pilots.)

Structures of the Boundary Layer
Some Boundary Layer Thermo-Dynamics

Carsten Lindemann
Freie Universität Berlin, Institute for Space Sciences

Abstract: Regular structures of the boundary layer especially for use of glider pilots will be presented. There will be an extended definition of thermal waves. Cloud or thermal streets will be described as a very normal state of the thermal driven lower atmosphere as a result of minimizing frictional forces. Some information will be given on mountain waves in special to extend the knowledge about the lower criteria of their existence.

Keywords: Thermal Waves, Cloud Streets, Mountain Waves

Effects of High Evaporation, Temperature and Humidity on Soaring in and near vicinity of Isparta, Turkey

Funda **DÖKMEN**[1], Ahmet **TOKGÖZLÜ**[2], Zafer **ASLAN**[3]

[1]Kocaeli University, Food and Agricultural Vocational School, Campus of Arslanbey, 41285, Kartepe, Kocaeli-Turkey, *E-mail: f_dokmen@hotmail.com & funda.dokmen@kocaeli.edu.tr*

[2] Süleyman Demirel University, Science and Literature Faculty, Isparta, Turkey
[3] Istanbul Aydın University, Faculty of Engineering, 34295, Istanbul, Turkey

Abstract: Generally, temperate climate conditions have been observed in Isparta. There is more precipitation in winter than summer in the region. Climate classification of the region is Csa according to Köppen-Geiger. Annual average temperature is 11.9 ^{0}C. Annual average precipitation is 537 mm. August is more drought month in a year with amount of 9 mm of rainfall. More precipitation is recorded in December with the average of 85 mm in a year. Air temperature range is between – 17 ^{0}C and +37 ^{0}C. Where evaporation initiates above from the soil surface, the degree of shading of the crop canopy and the amount of available water at the surface are other factors that affect the evaporation process. Rain, irrigation and upward water transportation in a soil from a shallow water surface result in increasing of soil wetness.Turkey is among the countries under the risk group in terms of the potential effects of high evaporation, temperature and humidity based on climatic conditions. Generally, the most important changes in increasing summer temperatures have been observed in Isparta, Turkey. This paper presents a study of the high evaporation, temperature and humidity in the study area and role of climatological conditions and combined effects on soaring. Long term analyses of these variables and their role on study area were discussed by using climatological data.

Key-words: Soaring, out-landing, drought, farming, global warming, plant cover.

Introduction

Evapotranspiration as a major component of the water balance has been identified as a key factor in hydrological modelling and a wealth of methods have been developed for its calculation.[1-2-3] In general; the term potential evaporation and potential evapotranspiration are to be differentiated. The first one is a measure for the demand, which is solely meteorologically driven under the assumption of unlimited water supply. Especially for irrigation scheduling, this definition was further specified to refer to a reference surface consisting of a hypothetical grass with specific characteristics, termed reference crop evapotranspiration.[4-5]

Evapotranspiration varies regionally and seasonally; during a drought it varies according to weather and wind conditions. The more important factors include net solar radiation, surface area of open bodies of water, wind speed, density and type of vegetative cover, availability of soil moisture, root depth, reflective land-surface characteristics, and season of year.[6]

Turkey is located in a semi-arid region, where the average annual rainfall is 643 mm. The significant differences between regions that are observed worldwide in terms of the amount and distribution of precipitation have also been observed in our country. Some regions record up to 3000 mm rainfall, while others do not exceed 250 mm. In Isparta region-Turkey, the annual rainfall is generally less than 537 mm. This value is lower that average annual anifall rate all over Turkey. Frequently disordered, unpredictable storms have been observed.Therefore, especially during periods of crop cultivation, plants do not provide enough water for their vegetal grow in terms of the desired amount of water. As a direct cause of global warming, forest fires, drought and desertification, and ecological degradation, will affect our water resources in particular, as well as our other natural resources. These factors play a geat role on soaring activities and flight plants.

Methodology

The various equations of potential evapotranspiration show great differences in magnitude.It is difficult to assess which method is the physically most reasonable to be applied.

Potential evaporation or **potential evapotranspiration (PET)** is defined as the amount of evaporation that would occur if a sufficient water source were available. If the actual evapotranspiration is considered the net result of atmospheric demand for moisture from a surface and the ability of the surface to supply moisture, then PET is a measure of the demand side. Surface and air temperatures, insulation, and wind all affect this. A dry land is a place where annual potential evaporation exceeds annual precipitation.

Thornthwaite equation (1948),[7]

$$PET = 1.6\left(\frac{L}{12}\right)\left(\frac{N}{30}\right)\left(\frac{10T_a}{I}\right)^{a} \quad (1)$$

Where,

PET is the estimated potential evaporation (mm/month)

T_a is the average daily temperature (degrees Celsius; if this is negative, use 0) of the month being calculated

N is the number of days in the month being calculated

L is the average day length (hours) of the month being calculated

$$a = (6.75 \times 10^{-7})I^3 - (7.71 \times 10^{-5})I^2 + (1.792 \times 10^{-2})I + 0.49239 \quad (2)$$

$$I = \sum_{i=1}^{12}\left(\frac{T_{ai}}{5}\right)^{1.514} \quad (3)$$

Where, α is…… and I is a heat index which depends on the 12 monthly mean temperatures T_{ai}.[7] Somewhat modified forms of this equation appear in later publications (1955 and 1957) by Thornthwaite and Mather.[8]

Results

There was too much evaporation in this semi-arid agricultural area (Fig.1). When there are high levels of evaporation, plants live in stressful conditions. High evaporation was measured in the between 1970 and 2017 water year for the agricultural drought. There is gradually an increasing trend.

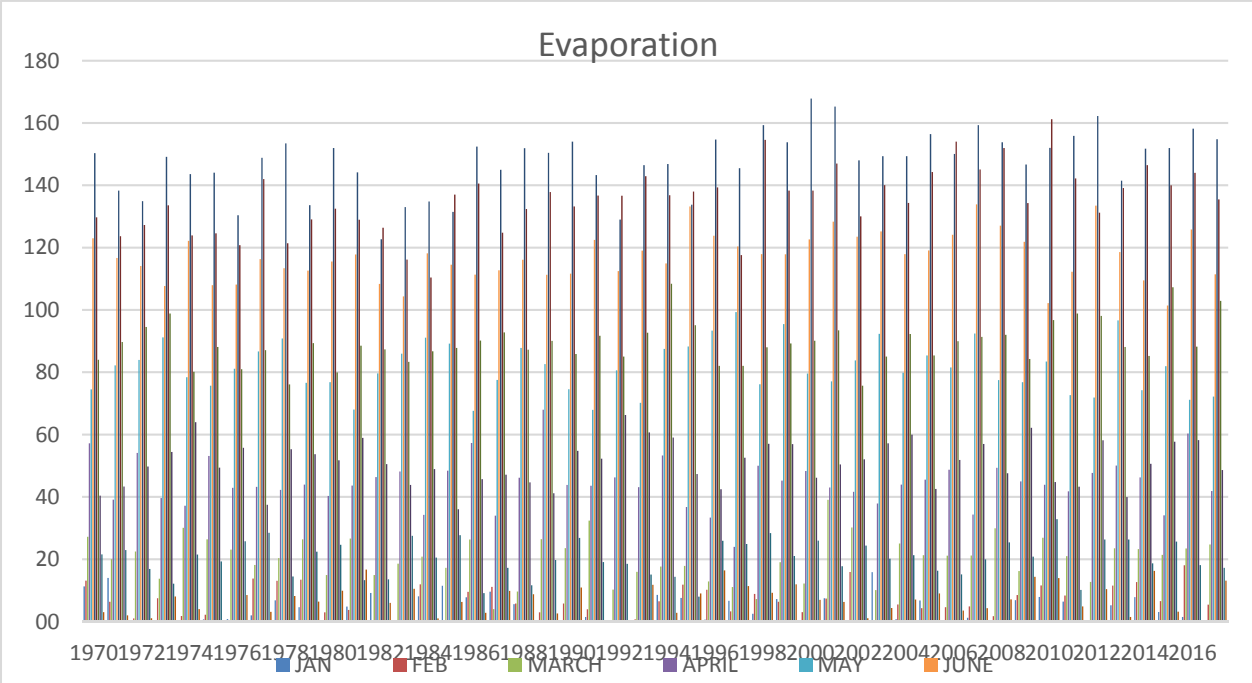

Figure.1. Long-term evaporation data in Isparta, (Turkey)

In this study area, the monthly temperature increased during the spring and summer months. There were high temperatures for rain-fed conditions (Fig. 2). Figure 3 shows that long-term rainfall data in Isparta of Turkey.

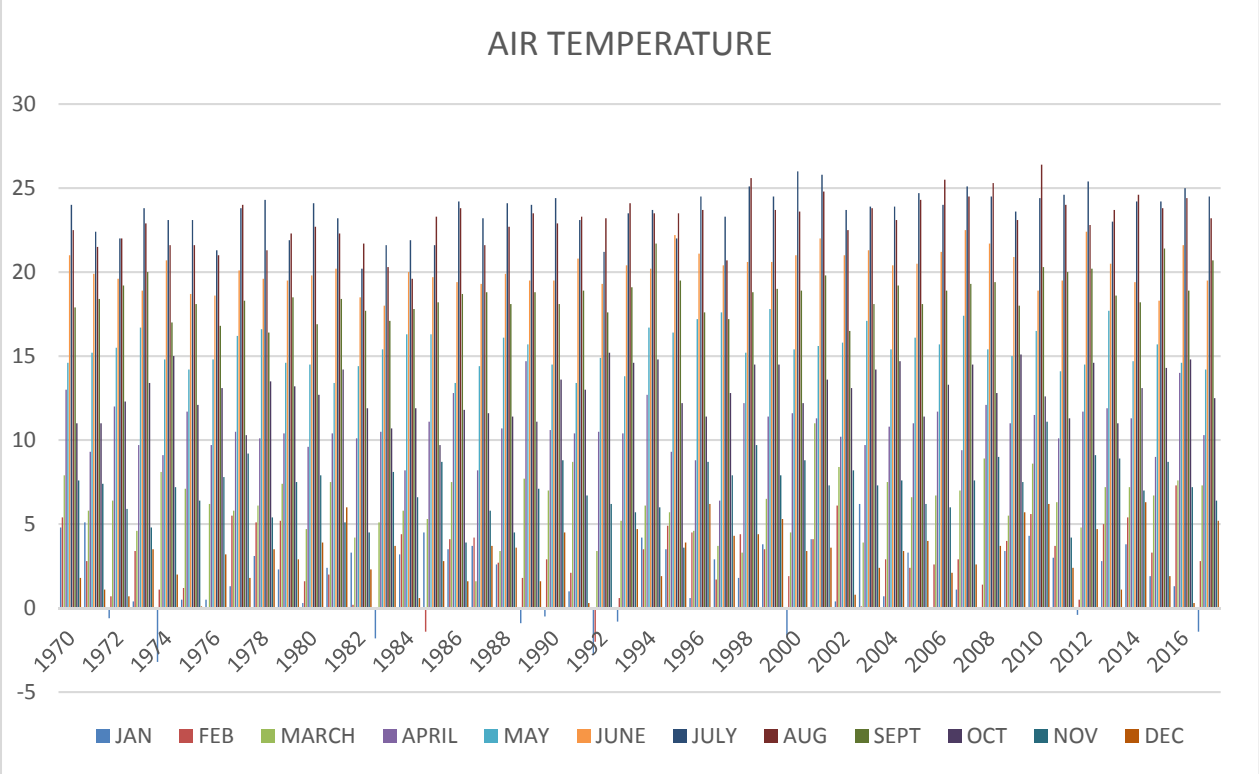

Figure.2. Long-term temperature data in Isparta of Turkey

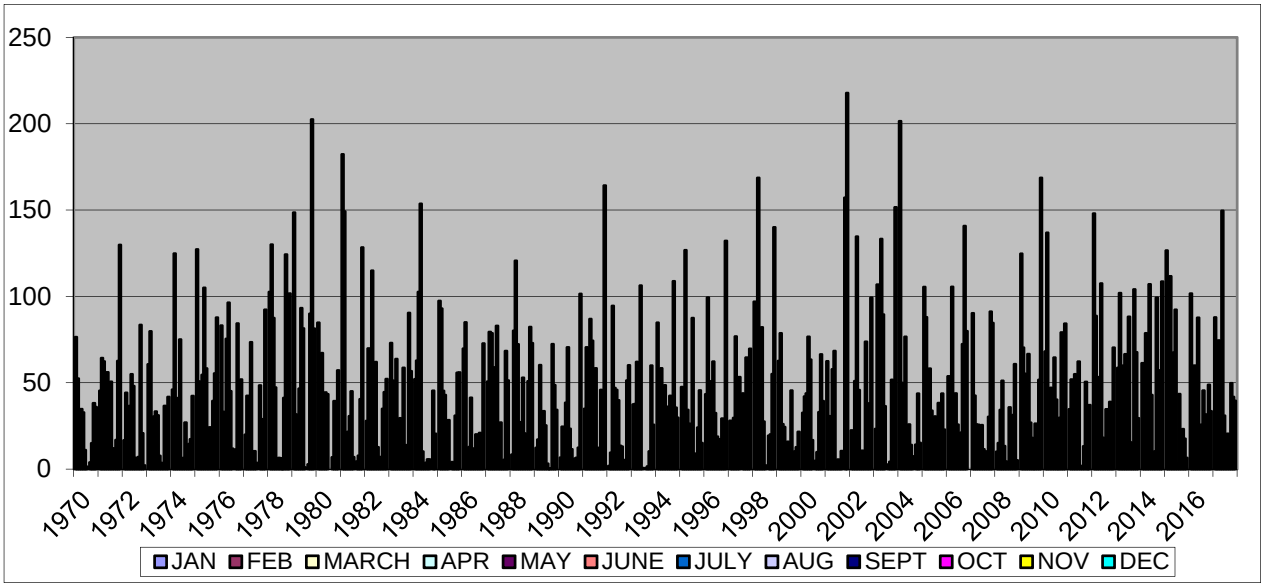

Figure.3. Long-term rainfall data in Isparta of Turkey

We can collect results on the below points as summary:
* Surface temperature shows increasing in Isparta and Mediterranean Region of Turkey.
*Time variation of evapotranspiration level temperature shows increasing depend on agricultural cultivation and management of irrigation in Mediterranean and Isparta region of Turkey.
* Equivalent potential temperature increases depend on climate changes in agricultural area.
* Using of modern irrigation methods should support for agricultural areas.
* Main open irrigation channels should be converted to closed channels in a short time due to high evaporation.
* Furrow irrigation (wild irrigation) must not use for agricultural region and also cultivation due to high evapotranspiration.
* Using of drip irrigation and subsoil irrigation systems proper to agricultural activities.
* Selection is governed by season of the year, crop, and farming techniques.
* Colour and texture best determine suitability. It may help to have an order of preference during field selection.

* Avoid fields with high crops, such as rape, sunflowers and root crops. These are usually either bright or dark colored.

Conclusion

This study is related with the utilisation and interpretation of some surface measurements together with the variations of meteorological data to explain and have some solutions of agricultural regions, climate changing, high evapotranspirasyon and also humidity on gliding and aviation.

The type of vegetative cover is not as important in the evapotranspiration process as is solar radiation if the vegetative cover is dense and sufficient soil moisture is available.[9] The reflective characteristics of the land surface also have an effect on the magnitude of evapotranspiration. The average annual evapotranspiration for irrigated lands varies is dependent on the grass or crop type, quantity of water applied, and length of the growing season. Evaporation is one of the main variables in the humidity budget equations which govern heat fluxes.

Unfortunately, not all flying is at high levels and a significant proportion of flight may take place at low altitudes in a demanding regime of high temperature and low humidity, and also evaporations resultant rapid dehydration if not controlled by fluid intake.[10]

Role of agricultural areas, effects of changing climate on weather and human activities are important points for aviation's, gliding and also outlandings.

References

[1]Brutsaert, W., 1982: Evaporation into the atmosphere. Theory, History, and Applications, Kluwer Academic Publisher, Dordrecht, Boston, London.

[2]Jensen, M.E., Burman, R.D. and R.G. Allen, 1990: Evapotranspiration and irrigation water requirement, NewYork.

[3]Brutsaert, W., 1982: Evaporation into the atmosphere. Theory, History, and Applications, Kluwer Academic Publisher, Dordrecth, Boston, London.

[4]Allen, R.G., Pereira, L.S., Raes, D., and M. Smith, 1998: Crop evapotranspiration, Guidelines for computing crop water requirements, FAO, Rome.

[5]Wright, J.l., 1981: Crop coefficients for estimates of daily crop evapotranspiration, irrigation scheduling for water and energy conservation in the 80's, Am. Soc. of Agric. Engrs. Dec.

[6]Hanson, R.l., 1991: Evapotranspiration and Droughts, U.S. Geological Survey, Water-Supply Paper 2375, pp:99-104.

[7]Thornthwaite, C.W., 1948: An approach toward a rational classification of climate," geographical review, Vol. 38, pp. 55-94.

[8]Thornthwaite, C.W., and J.R. Mather, 1957: Instructions and tables for computing potential evapotranspiration and the water balance: Center on, N.J., Laboratory of Climatology, Publication in Climatology, Vol. 10, no. 3, pp. 185-311.

[9]Kozlowski, T.T., 1964: Water metabolism in plants: New York, Harper and Row, Biological Monographs, p: 227.

[10]Garlick, G., 2014: Outlanding, Module Three, pp. 20-36, Online website date: June, 2014.

Urban Heat Island; In Ankara-İzmir-Karapınar (Turkey)

Kamile Yasdiman [1], Ahmet Tokgozlu [2], E. Tuncay Özdemir[3], Zafer Aslan[4]

[1] İstanbul University, Istanbul, Turkey
[2] Suleyman Demirel University, Isparta, Turkey
[3] Turkish State Meteorological Service, Ataturk Airport Meteorology Office, Istanbul, Turkey
[4] Istanbul Aydın University, Faculty of Engineeirng, Istanbul, Turkey, zaferaslan@aydin.edu.tr

Abstract: In contemporary metropolitan cities, because of lessening green areas and evaporation surfaces, increasing asphalted surfaces and built areas meteorological parameters change and cause local and regional climate changes, which makes the cities unhealthy places that have their own climatic properties. This differentiation between urban areas and surrounding semi-rural and rural areas is determined as 'urban heat island'. In order to understand whether there is an urban heat island effect in Ankara-İzmir, we selected Karapınar, a neighbour rural area that shares similar geographical features with Ankara-İzmir and used its data. The data of averages of monthly maximum temperature, monthly minimum temperature and monthly average temperature between 1963-2015 were received from the Turkish State Meteorological Services.
Keywords: Urban Heat Island, Urban Climate, Local Climate Zone, Heating Rates

Introduction

Temperature tends to be higher in cities than in its natural surroundings, especially during the night (Landsberg, 1981; Oke, 1987; Arnfield, 2003). This is known as the Urban heat Island. Urban surfaces distinguish themselves from their natural surroundings by particular urban surface characteristics like increased thermal inertia (Cai et al., 2008), a lowered vegetation cover and impervious land cover which reduces the evapotranspiration (Grimmond and Oke, 1999), a different albedo, emissivity and aerodynamical characteristics due to presence of streets and buildings. Together with the release of anthropogenic heat, this leads to the UHI effect reaching its maximum during the night. It is especially favoured by high solar irradiation (clear-sky), no precipitation, low wind speeds and stable stratification. Under these conditions, a large amount of solar radiation reaches the surface, which is better transformed to heat, and subsequently retained as storage heat (Grimmond et al., 1999) for a longer time in urban areas compared to rural areas.

The UHI has a considerable impact on human environmental health. It can increase the mortality rate during summer, but especially during heat waves. Indeed, a considerable UHI can also develop during the heat wave, e.g. over Oklahoma city during summer 2008 (Basara et al., 2010). Furthermore, Smargiassi et al. (2009) found that the risk of death on warm summer days in areas with higher surface temperatures was greater than in areas with lower surface temperatures. Moreover, the death rate during the heat waves is significantly associated with the increased minimum temperature during the night (Laaidi et al., 2011; Nicholls, 2009). In addition, the UHI also deteriorates air quality due to an increase of pollutants such as ozone.

While the situation in the world progresses in this direction, these studies gain importance in our developing and rapidly urbanized country. The aim of this study is to evaluate the effect of temperature on Turkey's biggest cities.

Material and Method

The main material of the study are the cities Ankara and İzmir cities and in terms of comparison, the rural district Karapinar. The study centres are located in the west part of Turkey. Ankara's coordinates are latitude: 39° N, longitude: 32 °E and İzmir's coordinates are latitude: 38° N, longitude: 27° E. In addition, the rural district Karapınar's geographical coordinates are latitude: 37 ° 42 '53' N longitude: 33° 33' 8° E. The locations of the study areas are shown in Figure 1, 2 and 3.

Figure 1: Location of Ankara within the country

Figure 2: Location of İzmir within the country

Figure 3: Location of the rural area within the country

The meteorological data which are averages of monthly maximum temperature, monthly minimum temperature and monthly average temperature used this study were received from the Turkish State Meteorological Services. In addition, academic work on urban heat island has been utilized as auxiliary material from relevant domestic and foreign books, magazines, articles and internet media. Two different methods are followed in the studies carried out in order to determine the effect of urbanization on the temperature conditions. First, the changes in the temperature values of the stations over time are examined. In the second approach, the temperature observations of two stations are compared by selecting urban and rural settlements close to each other (Temuçin, 1995).

These two stations are similar in terms of latitude, altitude, altitude and location, which is an important factor for the health of the results. However, this method is thought to be unaffected by urbanization of rural areas. In our study Ankara, İzmir and the rural area Karapınar stations were evaluated from 1963 based on the urbanization and the continuity of the data. In your data analysis, Sen's Trend Slope Method is used and the results are transferred to the graphs. This method, called your tilt estimator (estimator) in the presence of a linear trend in time series, is a non-parametric test method that allows us to detect the change in unit time at the same time and to allow the presence of missing data at the same time. In other words, in the observation series, the trend size is calculated by Sen's Trend slope method with the formulas given below.

$$Q_i = \frac{x_j - x_k}{j - k} \quad (1)$$

(Q_i) represents the data between x_j and x_k.(x_j) is the value calculated at time j, (x_k) is the value calculated at time k, (j) is the time after the time k.The value of N is also calculated by the formula "N = n (n-1) / 2". The median of N and Q_i values is used to estimate Sen's trend slope parameter. The N values of Qi are sorted from smallest to largest, and your trend trend estimate is determined by the following formula (Demirci et al., 2009).

In order to be used in future studies, Delphi 7 (Borland, 2002) has developed a software to detect the trending component with the programming language. The main factor in selecting the Delphi software language specifically is that it has a faster and more flexible structure in graphics work. This software, called "Trend Analysis for Windows", applies Sen's Trend Gradient method to the data and gives it as a result graphic and text. Software has been designed and developed as a very useful interface (Gümüş, 2006)

Results

It is observed that there is a significant increasing trend in the direction of the analysed time series. While Sen test results are being calculated, the total number of years is multiplied by the Sen value and the result is found in degrees. So according to the results of Sen tests ($Q_{med=}$ 0.027 & 0.024 & 0.019) taken from the program, Ankara is 0,5 °C warmer than Karapınar. Also İzmir is 0,3 °C warmer than Karapınar.

It is observed that there is a significant increasing trend in the direction of the analysed time series. According to the results of Sen test ($Q_{med=}$ 0.028 & 0.034 & 0.031) taken from the program, for maximum monthly temperature Karapınar is 0,2 °C warmer than Ankara and İzmir.

The parameter that best shows the presence of urban heat island is the comparison of monthly minimum temperatures. It is observed that there is a significant increasing trend in the direction of the analysed time series. In this context according to the results of Sen tests ($Q_{med=}$0.052 & 0.034 & 0.032) taken from the program, Ankara is 1,1 °C warmer than Karapınar. Also İzmir is 0,1 °C warmer than Karapınar.

References

1. Landsberg, H. E.: International Geophysics Series, Vol. 28: The Urban Climate, Academic Press, Londen, 1981.
2. Oke, T. R.: Boundary Layer Climates, 2nd edn., Methuen and Co. Ltd, London, 1987. 25942 Oleson, K. W., Bonan, G. B., Feddema, J., and Jackson, T.: An examination of urban heat island characteristics in a global climate model, Int. J. Climatol., 31, 1848–1865, doi:10.1002/joc.2201, 2011.
3. Arnfield, A. J.: 5 Two decades of urban climate research: a review of turbulence, exchanges of energy and water, and the urban heat island, Int. J. Climatol., 23, 1–26, doi:10.1002/joc.859, 2003.
4. Cai, G., Du, M., Xue, Y., and Li, S.: Analysis of an Urban Heat Sink using Ther25 mal Inertia Model from ASTER Data in Beijing, China, in: Geoscience and Remote Sensing Symposium, 2008, IGARSS 2008, Boston, Massachusetts, USA, IEEE International, doi:10.1109/IGARSS.2008.4779609, III-1346–III-1349, ISBN:978-1-4244-2807-6, 2008.
5. Grimmond, C. S. B. and Oke, T. R.: Evapotranspiration rates in urban areas, AHS Publ., 259, 235–243, 1999.
6. Grimmond, C. S. B., Oke, T. R., and Timothy, R.: Heat storage in urban areas: local-scale observations and evaluation of a simple model, J. Appl. Meteor., 38, 922–940, doi:10.1175/1520 0450(1999)038<0922:HSIUAL>2.0.CO;2, 1999
7. Basara, J. B., Basara, H. G., Illston, B. G., and Crawford, K. C.: The impact of the urban heat island during an intense heat wave in Oklahoma City, Adv. Meteorol., 2010, 1–10, doi:10.1155/2010/230365, 2010.
8. Smargiassi, A., Goldberg, M. S., Plante, C., Fournier, M., Baudouin, Y., and Kosatsky, T.: Varia15 tion of daily warm season mortality as a function of micro-urban heat islands., J. Epidemiol. Commun. Health, 63, 659–64, doi:10.1136/jech.2008.078147, 2009
9. Laaidi, K., Zeghnoun, A., Dousset, B., Bretin, P., and Vandentorren, S.: The impact of heat 15 islands on mortality in Paris during the August 2003 Heatwave, Environ. Health Perspect., 120, 254–259, doi:10.1289/ehp.1103532, 2011.
10. TEMUÇİN, E. (1995), Türkiye'de Kentleşmenin Sıcaklı Koşulları Üzerine Etkisi, Ege Coğrafya Dergisi, 8, ss. 75–92, İzmir.
11. DEMİRCİ, A.- KARABURUN, A.- KARA, F., (2009), Uzun Dönem Sıcaklık Verilerinde Thiessen Ve Mann-Kendall Metotları İle Trend Analizlerinin Yapılması: İstanbul Örneği, 3. DEÜ CBS Sempozyumu, İstanbul.
12. GÜMÜŞ, V., (2006), Fırat Havzası Akımlarının Trend Analizi ile Değerlendirilmesi, Yüksek Lisans Tezi Şanlıurfa: Harran Üniversitesi, Fen Bilimleri Enstitüsü.

Safety as an additional Subject in Pilot Training

Alfred Ultsch[1,2]
[1]*Databionics, Philipps University Marburg, Marburg, Germany, ultsch@Mathematik.Uni-Marburg.de*
[2]*Akademische Fliegergruppe (Akaflieg) Frankfurt, Frankfurt, Germany*

Abstract: There is an unbearable high risk in glider flying to encounter severe injuries or even death. Over the last 25 years no progress has been made for a reduction in risk in Germany, which hosts one of the largest population of glider pilots. The same holds for several other countries. In the 1980 years the commercial airlines faced the same problem: stagnation of accident rates. The ailines have since developed and implemented a new paradigm for accident prevention subsumed under the term dynamic (proactive) safety. The dramatic improvement by a factor of 10 to 100 in safety in the commercial sector of flying resulted from the introduction of dynamic safety based on trainings of personnel in crew resource management (CRM), line oriented flight training (LOFT), threat and error management (TEM), non-technical Skills (NOTECH), and similar system-oriented methods.
Here it is proposed, that a similar training and instruction programm could and should be implemented in the non commercial, non complex aircraft and non complex organization sector of aviation. A syllabus and time requirements for such training programs are presented.

***Keywords*:** safety, accident prevention, risk, human factors.

Introduction

With ca 20.000 pilots Germany hosts one of the largest populations of glider pilots in the world. However, there is an unbearable high probability to suffer from a severe accident or even get killed in this sport. In a typical German club with ca. 800 to 1200 starts per year each member must be prepared to attend at least one funeral of a fellow club member during his active flying lifetime. If commercial airlines would have this risk level, each month 3 planes would crash with at least one fatality. Figure 1 shows the risk measured as deaths per one million starts for the last 25 years in gliding.

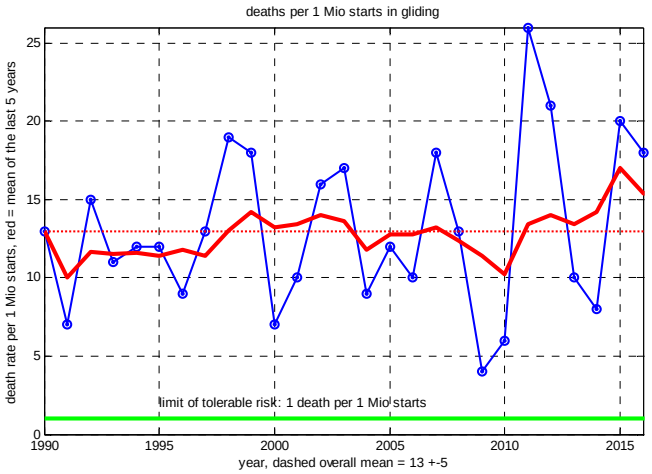

Figure 1: Rate of fatalities (deaths) per 1 million starts in Germany during the last decades

The sad side of the story is that there is no reduction in risk over the last 25 years. Before that time, i.e. up to ca 1990, big progress in safety has been made. With an experience of almost 100 years and the pioneering efforts of brave pilots and glider constructing engineers the largest risk have been eliminated.

Methodology

Thanks to the ongoing effort to improve these rules and regulations the accident rates could be dramatically reduced. Actual numbers from Switzerland (ca 2000 glider pilots) show a reduction from more than 200 deaths per 1 Mio starts in 1980 to 34 in the year 2000. (See Figure 2)

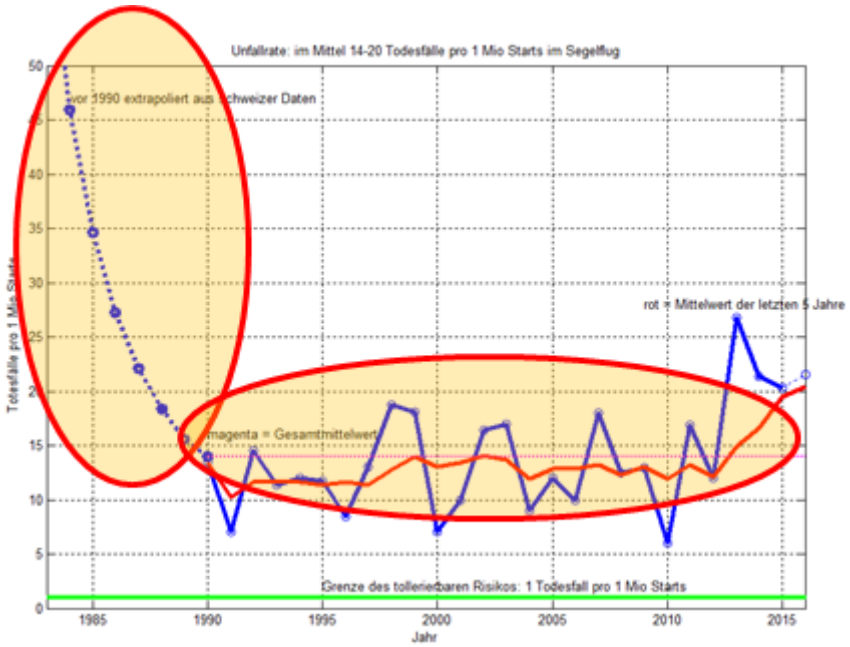

Figure 2: Rate of fatalities for glider flying extrapolated to the years before 1990

However, since ca 1990, i.e. for almost three decades, there is no reduction in risk in glider flying. The probability of a severe accident in glider flying stagnates on an unbearable high level. One death per 1 million starts would be acceptable.
On the other hand, in commercial aviation a 0.1 to 0.001 death per 1 million starts risk level is observed following a new approach to safety.

Proposal

The distinct improvement in safety in the airlines resulted from the introduction of dynamic (proactive) safety methods. Other terms for the methods of dynamic safety are: Crew Resource Management (CRM), Line Oriented Flight training (LOFT), Threat and Error Management (TEM), Non-technical Skills (NOTECH), etc. The static method aims at the reduction of the number of pilot errors and/or deliberate rule violations. The dynamic method acknowledges the fact that humans can never act, in particular never fly, without making an error at some time.
An essential prerequisite of the dynamic method is education in flight safety. Not really in first line on the level of the pilot but in particular on le level of the instructors, the club's officers and the club as a whole. To improve safety in gliding by a factor of two or more can be achieved by teaching and learning dynamic safety methods. These methods operate on the level of the system, i.e. the club or flight school. Therefore the club resp. the flight school must be thought as a whole and in particular to leaders i.e. club officers, flight instructions and the safety officer.
Safety can be taught and learned. This subject should have an equal importance as meteorology of flight rules in pilot and oganization training. For glider flying the teaching requirements for the different groups have been empirically determined. The two programs, FLYTOP in Germany and FLYSAFE in Sweden use more or less these time requirements for the necessary training:

Club as a whole:	2 days including ca. 10 hours of theory
Leaders and Flight instructors:	3 days
Safety Officer:	all of the above plus 4 extra intensive days of instruction

An overview on the syllabus for these teachings is shown in the flight safety „building "used in the FLYTOP course system.

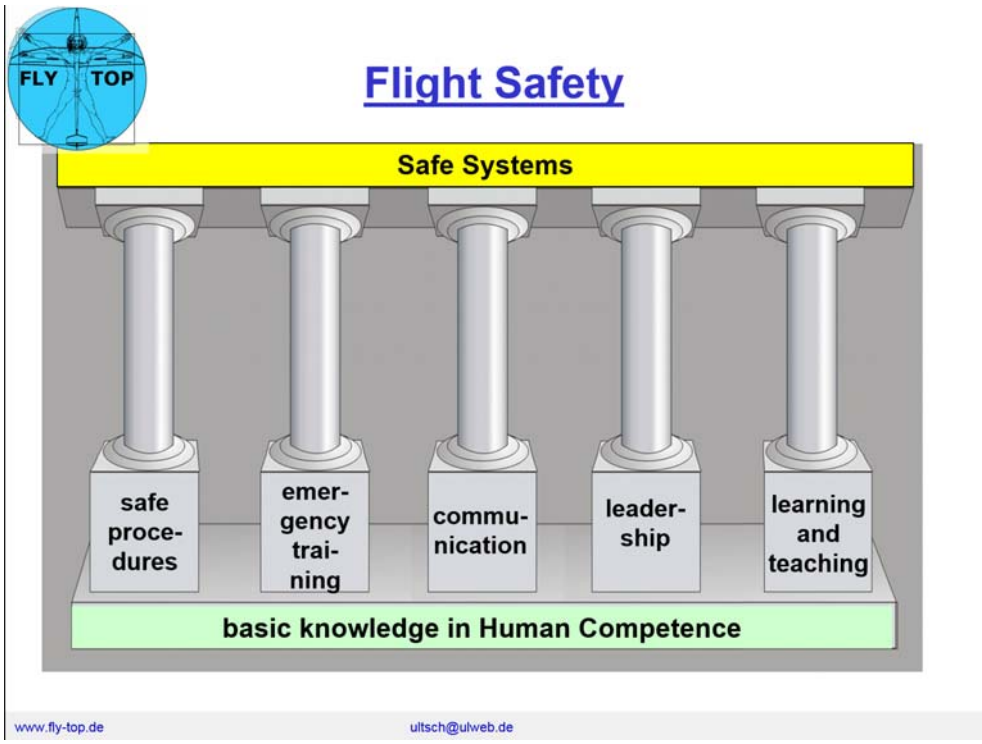

Figure 3 Overview of the main chapters of a syllabus in dynamic safety

References

[1] ICAO: Safety Management Manual (SMM),Doc 9859, ISBN 978-92-9249-214-4, Third edition 2013.
[2] ICAO: Accident Prevention Programme, 2005.
[3] Dörner, D., Kimber,R,:The logic of failure: Recognizing and avoiding error in complex situations. Cambridge, MA: Perseus Books, 1996.
[4] Badke-Schaub, Hofinger, Lauche: Human Factors, Springer, Berlin, Heidelberg, 2nd Edition, 2012.

Time to Escape! A survey of time required for glider pilots to escape a ground based cockpit simulator.

Stu Smith[1]
[1] *Gliding Club of Victoria, Australia*

Abstract: With widespread use of emergency parachutes in gliders now common for all flights, pilots should understand the typical time required to egress the cockpit of the glider in a 'bail-out'. A simulator was built form a cockpit section of Mosquito glider and trials conducted to measure times to egress and activate a parachute ripcord and data was collected about each candidate included age, weight, height and gender. The results show a mean time of 19 seconds, with a standard deviation of 8.3 seconds. There was no correlation between time to egress and the factors noted above. Variability was large. The long average time raises the question about survivability. The results provide useful insight into which factors could be important in improving chance of survival, and give direction for future initiatives.

Keywords: egress, ripcord, mid-air, parachute, ballistic recovery chute, NOAH, Cirrus

Introduction

The project stems from an idea by Vern Rosenfeldt of the Gliding Club of Victoria, who built the simulator in 2009 and along with Alan Patching collected all the data analysed here. He was inspired by the death of a friend resulting from a mid-air collision at 3000'. This shocked many pilots as it was considered to be a height from which egress and parachute deployment should be possible. The building of the simulator was to inspire pilots to practise emergency egress from glider cockpits, to gather data, and to consider how to improve opportunities for successful escape. Some of the questions asked were whether any of the factors, size, weight, age or experience in gliding make a difference to time taken for pilots to escape a simulated glider cockpit at 1 G. It was intended to ballast the pilot to simulate escape at higher G loading, but to date this has not been conducted.

Methodology

A ground-based simulator was built out of the cockpit of a Mosquito glider, a typical 1970s 15m glider representing a very common seating configuration. A sample of active pilots ranging in age from teenage to some in their 70's were tested to see how long it took them to exit to the point of pulling their parachute ripcord. Some candidates did multiple trials. Candidates wore a parachute with a dummy ripcord and fastened a four-point harness and closed and locked the canopy. They were asked to mentally picture themselves flying normally, hand on the stick, and upon a signal (a firm whack on the panel behind them) they were to exit to glider cockpit, and pull the dummy ripcord as fast as possible. There was energy absorbing foam placed outside the cockpit to encourage a realistically urgent egress. These simulated trials and data is only for the case representing a pilot at 1G.

Figure 1. Escape modüle simulator

Figure 2. Escape modüle simulator

Results

Fifty-four candidates completed trial. Only four of these repeated the exercise with additional trials.

The best time recorded was 8 seconds and the worst time was 55 seconds.
The average time recorded was 19 seconds with a standard deviation of 8.3 seconds.

Only eight other candidates (15%) recorded 12 seconds or less. The time of 12 seconds representing 150% of the best time. If the four slowest times (all 30 seconds or greater) are discarded, the average time is still 17.1 seconds with a standard deviation of 4.9 seconds

Table 1: Average, Stand Deviation, R value with respect to time for Age, Height, Weight, BMI

	Time (sec)	Age (years)	Weight (kg)	BMI	Height (m)
Average	18.95	47.5	80.3	25.5	176.7
Standard Deviation	8.35	18.1	13.1	3.1	7.4
R= ,against time	Not applicable	0.02334	0.08016	0.00093	-0.01283

There were four candidates whose time exceeded 350% of the best time and although they might be considered outliers, because there was no specific failure that led to these slow times they were not discarded. Their impact on calculated results was not large and as such did not change the conclusions.

Only four females completed a trial and the spread of their results did not give useful information, so all results were combined and are not gender specific.

Ages ranged from 13 to 79 years and each decade in this range had at least four candidates. A least squares regression analysis of results showed no correlation between age and time recorded with R=0.02334. The age of the candidate with the best time was 54 years. Poorer results were spread across all age groups and also many candidates in their sixties achieved results near the average. However all of the candidates over sixty–nine years were in the 20 to 30 second range, see Table 2 and 4.

Table 2: Age in decades vs average time

Age by decades (years)	Average Time (sec)	Number in group
10-19	15.0	7
20-29	17.6	4
30-39	13.9	4
40-49	13.8	8
50-59	19.3	15
60-69	16.2	10
70-79	24.8	4
Not recorded	27.5	2

Table 3: BMI range vs Average time

Body Mass Index	BMI	Number of candidates	Average Time (sec)
Normal	18-25	17	18.3
Overweight	25.1-30	34	19.0
Obese	Over 30	3	14.8

Weight ranged from 48 to 105 kg with an even spread across this range. A least squares regression analysis of results showed no correlation between weight and time recorded with R=0.08016. As such, Body Mass Index (height over mass squared kg/m2) was calculated. Seventeen candidates were in the normal range (18-25), thirty-three were in the overweight range (25.1-30) and three candidates were in the obese range (over 30) with the highest BMI being 31.7, see table 3 and 4. A least squares regression analysis of results showed no correlation between BMI and time recorded with R=0.00093.

Heights ranged from 150 to 190cm with an even spread across the range. Only ten of the candidates were outside the range 170-185cm. See table 4. A least squares regression analysis of results showed no correlation between height and time recorded with R=0.01283.

Experience of the candidates was considered only after this data was gathered. Candidates were invited from a full range of general gliding experience from complete novice to very high experience in all fields of gliding. Candidates were ranked by the author, categorized as: very high; high; medium; low; very low; and unknown. Because this was considered subjective no statistical analysis was performed, however when the results were grouped into three lots (very high, high, medium), (low, very low) and (unknown) it was apparent that the spread of times over the full range was evident in each lot, showing no better performance in any one lot.

Only four candidates attempted more than one trial in the simulator and this was not enough to investigate if emergency egress practise makes a useful improvement in pilot performance. Whilst it might be expected to help improve performance, without detailed study and follow-up it is not possible to know whether limited events like this trial will have any lasting benefit on the pilot in a real emergency.

Figure 4, below, shows four tables of times recorded in order the parameters of interest. Colour coding is Bright green=best result, light green up to 150% of best result. Yellow to 250%. Orange to 360%. Red over 360%. The average represents 240% of the best time of 8 seconds. Anything yellow, orange or red is not a good time.

Table 4: a) Time vs Age, b) Time vs Weight, c) Time vs BMI, d) Time vs Height

I.D. number	AGE	Time
	yrs	1st
45	13	11
12	15	17
47	15	17
54	15	14
46	16	11
43	17	41
42	18	20
8	21	12
24	21	19
2	26	13.5
44	26	26
18	36	13.5
1	37	15
32	37	16
10	38	11
28	40	15
5	41	15
22	43	10.5
20	44	14
36	44	12
29	47	15
7	48	17
15	48	12
21	50	23
16	51	16.5
27	52	25
39	53	8
30	54	26
48	55	17
3	56	55
41	56	16
6	57	40
11	57	25
14	57	28
17	57	21.5
23	58	16.5
37	58	14
40	59	14
13	61	18
53	61	20
49	62	14
50	62	12
26	63	16.5
33	63	15
4	64	15
25	64	14
35	65	17
38	69	20
31	71	24
9	75	25
19	76	25
34	79	20
51	x	25
52	x	30

I.D. number	Weight	Time
	kg	1st
51	48	25
10	52	11
45	54	11
12	55	17
47	55	17
11	56	25
46	65	11
52	66	30
48	67	17
24	70	19
23	72	16.5
34	72	20
54	73	14
5	74	15
1	75	15
19	75	25
21	75	23
35	75	17
27	78	25
9	80	25
18	80	13.5
44	80	26
13	81	18
37	81	14
4	82	15
6	82	40
28	82	15
39	83	8
29	85	15
30	85	26
36	85	12
38	85	20
49	85	14
50	85	12
33	86	15
7	87	17
32	87	16
17	88	21.5
26	88	16.5
2	90	13.5
8	90	12
22	90	10.5
40	90	14
3	92	55
31	93	24
53	94	20
14	95	28
15	95	12
42	95	20
16	96	16.5
41	97	16
25	100	14
20	105	14
43	unknown	41

I.D. number	BMI	Time
	kg per m2	1st
11	18.5	25
51	18.8	25
47	19.0	17
45	19.8	11
10	20.8	11
24	20.9	19
48	21.1	17
23	22.2	16.5
34	22.2	20
46	22.8	11
12	22.9	17
1	23.1	15
21	23.1	23
19	23.4	25
5	23.9	15
13	24.2	18
52	24.2	30
54	24.4	14
39	24.9	8
8	24.9	12
35	25.1	17
6	25.3	40
28	25.3	15
49	25.4	14
50	25.4	12
37	25.7	14
40	26.0	14
29	26.2	15
36	26.2	12
27	26.4	25
44	26.7	26
32	26.9	16
9	27.0	25
26	27.2	16.5
18	27.4	13.5
33	27.5	15
4	27.7	15
41	27.7	16
38	27.8	20
14	27.8	28
15	27.8	12
42	27.8	20
53	27.8	20
3	27.8	55
22	27.8	10.5
17	27.9	21.5
2	28.4	13.5
31	28.7	24
30	28.7	26
7	29.4	17
16	31.3	16.5
25	31.6	14
20	31.7	14
43	unknown	41

I.D. number	Height	Time
	cm	1st
12	155	17
10	158	11
51	160	25
43	162	41
45	165	11
52	165	30
46	169	11
47	170	17
18	171	13.5
7	172	17
27	172	25
30	172	26
4	172	15
9	172	25
54	173	14
44	173	26
35	173	17
11	174	25
16	175	16.5
38	175	20
5	176	15
33	177	15
17	177.5	21.5
37	177.5	14
2	178	13.5
48	178	17
25	178	14
19	179	25
1	180	15
32	180	16
28	180	15
22	180	10.5
36	180	12
29	180	15
21	180	23
6	180	40
23	180	16.5
26	180	16.5
31	180	24
34	180	20
20	182	14
3	182	55
39	182.5	8
24	183	19
13	183	18
49	183	14
50	183	12
53	184	20
42	185	20
15	185	12
14	185	28
40	186	14
41	187	16
8	190	12

Discussion

Whilst this trial at 1 G shows no correlation between the factors analysed and time to egress, this does not mean that any of these factors may not be significant at higher G loading.
No assessment of candidate fitness, technique, strength or experience in parachuting or practicing emergency egress was conducted and further trials with assessment of these factors may be useful.

In a real emergency, the pilot will have to comprehend the circumstances and respond. Classical terminology for this is an OODA loop where the pilot must: Observe what has occurred; Orientate their mind; Decide what to do; then Act. In this trial, the first three stages are not tested as the candidate knows they are about to practise an emergency egress, they only have to act. As such, the first three stages could add many seconds to the time elapsed. Indeed, road safety research has shown that some people just fail to decide what to do and so, do not act. Also it is not known to what extent the adrenaline rush accompanying the immediate aftermath of something like a mid-air collision motivates and accelerates the pilots egress to a worthwhile extent or whether it actually clouds decision making, might increase fumbling and slow the egress. Such is the variation of human behaviour

Also not considered in this study is the time elapsed from pulling the ripcord until the pilot slows to a survivable speed under the inflated canopy.

Real emergencies would likely fall into one of four following categories:
a) near 1G loading, where presumably the glider is in roughly horizontal trajectory. This being akin to this study situation;
b) Higher positive G loading, likely due to wing failure where ejecting canopy and exiting from the seated position could be much more difficult;
c) Negative G loading, possibly due to loss of tail structure, where forces on the harness could make releasing it much more difficult, though canopy discard and exiting seating position may be enabled;
d) Beak-up of cockpit where pilot is thrown clear. This is rarely reported.
In addition, a wide range of pilot injury may be present as a result of a mid-air collision. All these above conditions may likely increase time to deploy parachute, except possibly item d).

As forty-five of the fifty-four candidates exceeded 150% of the best time and the
average was 19 seconds, the question arises, "how often will a pilot have 12 or more seconds available to make a successful emergency egress?"

Conclusions

This study has shown that there is measured to be a considerable time for a pilot to egress from the point at which they commence action, to the time they have pulled a ripcord, and that other factors add to this time before a parachute can slow them to a survivable speed.

It is noted that the person recording the best time of 8 seconds is both a highly ranked competition pilot and therefore takes a very competitive approach to many things, and also had previously used a parachute to save themselves after a mid-air collision and so had greater insight and motivation to score well. As such it may not be realistic to think there is much that most pilots can do themselves to approach the best times seen here.

Stages before deciding to act, dynamic behavior of the glider, injury and finally time for parachute to deploy will add additional seconds to the time required.
This study gives some insight into why pilots may fail to make successful egress in an emergency.

In contradiction to the substantial times reported here, there are a large number of successful parachute escapes from gliding emergencies and future study should attempt to understand and characterise the circumstances that lead to success.

It may be useful to consider options to improve chance of survival. Amongst the options are:
a) Ballistic Recovery Chute (BRC)
b) NOAH, glider pilot egress system offered in some gliders
c) Static-line for parachute deployment
d) Pilot training

I have listed these in order that I consider offering most benefit. But starting from the bottom, d) Pilot training, has been discussed above and c) Static-line, offers some time reduction to good deployment, but mostly offers increased likelihood of a good, clean deployment. b) NOAH, offers potentially many seconds saved as it simultaneously ejects canopy, releases harness and lifts pilot to the canopy rails to make egress a simple matter of rolling over the side. Unfortunately this option rarely specified by customers.
Option a) Ballistic Recovery Chute, must offer the greatest opportunity as, after a single action of pulling the BRC handle, the rest of the sequence is taken care of, regardless of the pilot attributes that causes performance variation recorded in this study. BRC may offer chance of survival at altitudes too low for successful egress.

Published videos of Cirrus Aircraft SR20 show full canopy deployment in 5 seconds and stabilised decent in 10 seconds after pilot pulls the emergency handle. This time of 10 seconds includes actual canopy deployment and stabilisation and therefore would beat the best times recorded in the glider simulator study, and would have high reliability of deployment.

Recommendations

It is recommended pilots note these results and that glider manufacturers, OSTIV members and leaders of national gliding organisations revisit the benefits of BRC systems particularly in light of the BRC fitment options afforded by new nose mounted electric propulsion systems. In general aviation these BRC systems are being retro-fitment to legacy types such as Cessna170 & 180.

Acknowledgements

I would like to greatly acknowledge the leadership and insight of Vern Rosenfeldt and Alan Patching for creating this project, and also acknowledge Murray Stimson, Jenne Goldsmith, David Goldsmith and Jim Barton for their contributions to the project and the material in this presentation.

Sailplane wing integrated with a motor – propeller system

Jaroslaw Pytka[1], Ernest Gnapowski[2], Andrzej Rypulak[3], Piotr Kasprzak[3], Jan Pytka[3]
[1]*Technical University of Lublin, Faculty of Mechanical Engineering, Poland, j.pytka@pollub.pl*
[2]*University College of Enterprise and Administration, Lublin, Poland*
[3]*Polish Air Force Academy, Dęblin, Poland*

Abstract: The paper presents an idea of integrating a sailplane wing with a single or multiple motor – propeller systems, which consist of an electric brushless motor and a non-folding propeller. The ideas assumes a number of such propelling systems for each wing, right and left. A complete propelling system is located inside the wing, thanks to its small dimensions and cubature. Some additional equipment is required for this design to be practically useful: a mechanism of openings in the skin of a wing; a motor brake and a mechanism for positioning the propeller horizontally. The wing with several propelling units is expected to be a good alternative to a classic retractable propeller, emplaced in the fuselage, mainly because of higher efficiency, better maneuverability and much faster deployment during the flight.

***Keywords*:** motorized sailplane, distributed electric propulsion, wing design

Introduction

Motor gliders are very polupar mainly because of their self – launch capability and a possibility of horizontal flight in case of no thermals. One design type of motor glider uses retractable propeller, usually mounted on a mast that rotates up and forward out of the fuselage, aft of the cockpit and wing carry-through structure. One problem that arises during starting a propelling system, is altitude loss in the flight. There was a tragic accident in Poland, April 2017, when a sailplane went down too much during extending the engine, the pilot died. Therefore, alternative solutions and designs are reasonable.

Figure 1 shows two solutions for the wing integrated with propellers with a function of in – flight start and stop. Both inventions were made when electric propulsion wan premature for aviation applications and they utilize combustion engines. Some drawbacks of these designs are that only 2 propellers or one propeller per wing, a combustion engine inside the fuselage may cause problems with cooling, they are heavy with complicated drive chain. These inventions have never been practically applied.

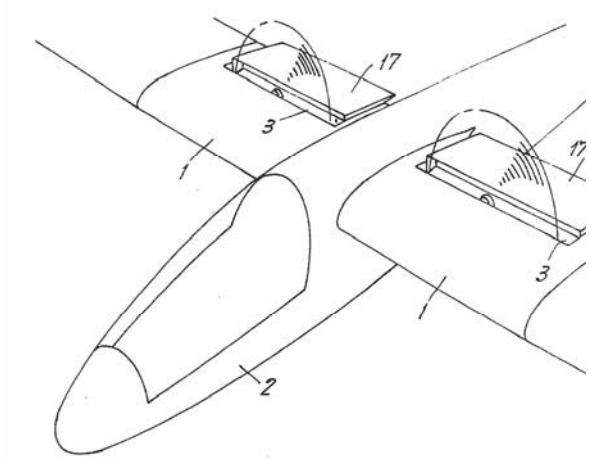

Figure 1. Sailplane design with two in-wing propellers. For details please refer to [1]

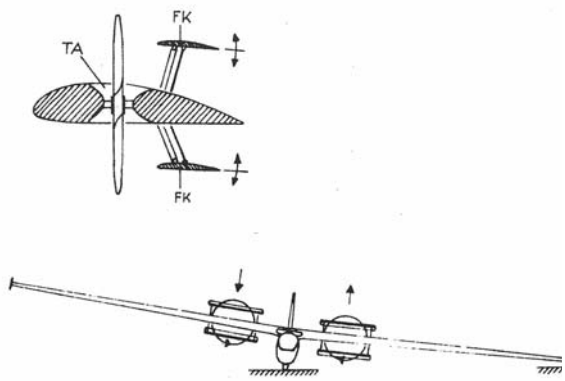

Figure 2. Sailplane with a wing integrated with a propeller [2].

Modern electric propulsion technology enables that sailplanes or light airplanes can be powered with electric motors, reaching reasonable altitudes and flight duration. The Leading Edge Asynchronous Propeller Technology (LEAPTech) by NASA[3] utilizes several small electric motors installed in separate nacelles on the leading edge of a wing (fig. 3). Each motor can be operated independently at different speeds for optimized performance. Potential benefits of LEAPTech include improved aircraft performance through higher propulsion efficiency and ride quality, better maneuverability thanks to possible thrust control along the wing span as well as noise reduction.

Figure 3. Distributed electric propulsion on NASA test wing [3]

The aim of this study was an idea of a sailplane wing integrated with electric propulsion motors, but in such manner that the motors are fully hidden in the wing structure so that they do not affect wing aerodynamics when not in use.

An idea of the wing integrated with motor – propeller system

Figure 4 shows a wing section in a point of one electric motor installation. Today's electric motors are small enough that can be emplaced inside a typical sailplane wing, even if we consider a motor of 3 – 4kW power. The design utilizes a longer motor shaft, since a propeller should be placed in the aft part of the wing profile in order to minimize of air flow disturbances. As note above, the motors are fully hidden in the wing structure so that they do not affect wing aerodynamics in a still stand mode, while in the propulsion mode, wing skin slots are opened so the propeller can rotate loosely. In order to stop the propulsion, the motor stops, then the propeller is adjusted in a horizontal position and the slots are closed. Changing the modes can be made repeatedly during the flight.

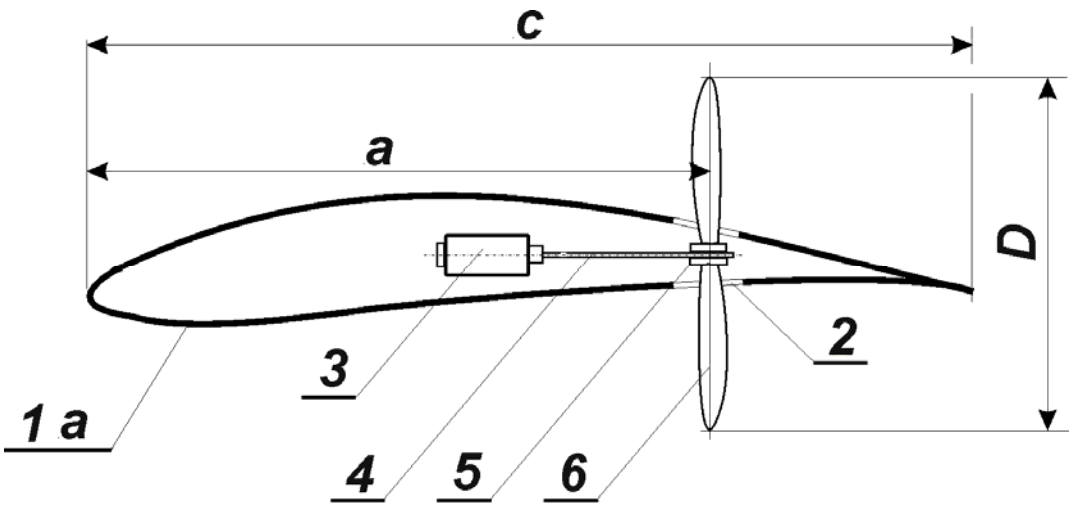

Figure 4. A schematic of the sailplane wing integrated with motor – propeller system. 1a – wing skin, 2 – opening slots in the wing skin, 3 – electric motor, 4 – propeller shaft, 5 – propeller hub, 6 – propeller, D – propeller diameter, a – longitudinal location of the propeller, c – wing chord

Figure 4. A sailplane with wings integrated with motor-propeller units. Three propellers per wing, shown here in open position.

Methodology and expected results

The presented idea of the wing integrated with motor – propeller systems require experimental and numerical verification. An influence of the wing slots and the propeller on airflow and the resulting wing characteristics should be investigated. Moreover, effects of propeller slipstream should also be identified and analyzed. At the present stage of the work, we are planning to continue with the following research:

- building a scale wing section with one propelling system for wind tunnel measurements;
- building a scale model of a sailplane with 10 propelling systems (5 for each wing) and performing flight tests;
- CFD simulations of a sailplane with the subject propelling systems.

Figure 5 shows a model wing section for wind tunnel measurements. This model is 25cm in wing chord and 22cm in width and is fitted with an electric motor and propeller, RC equipment for motor speed control. Additionally, the RC system has the telemetry function and is fitted with a temperature sensor, which will provide motor's temperature during wind tunnel tests.

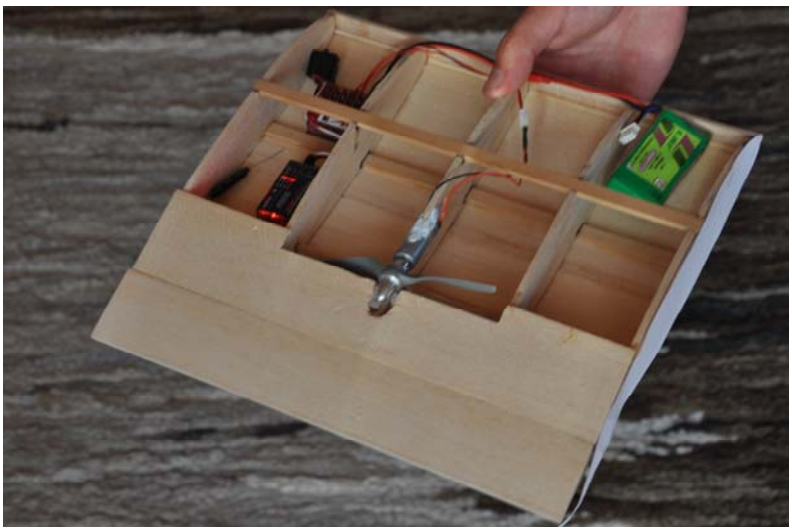

Figure 4. Model wing section with integrated motor – propeller system developed for wind tunnel measurements

References

[1]Somogyi, M., 1974: Planeur a moteur auxiliaire, French patent 72.18437, No. of publication 2.185.538
[2]Schall H., 1970: Motorsegler, Deutsches Patentamt, Offenlegungsschrift 1581069
[3]Moore M., 2015: Distributed Electric Propulsion Aircraft, Lecture on the Universita Degli Studi Di Napoli, 16. Oct 2015

Safety management of battery electric propulsion in Gliders

Rainer Klein
Duale Hochschule Baden Würtemberg-Mosbach, Department of Mechatronics/Elektromobility
rainer.klein@mosbach.dhbw.de

Abstract: The presentation focus on different safety aspects of an electric propulsion especially the risk of thermal runaway within the battery, trigger factors of thermal runawy, avoidance aspects and damage limitation.

***Keywords*:** electric propulsion, battery, thermal runaway, nail penetration test, battery safety

Introduction/Motivation

Every energy, energy source or energy storage has a potential risc of failure and danger. In connection with combustion drives and liquid fuels such as gasoline or diesel (jet fuel), users have come to terms with the residual risk of a fire or explosion. Due to the fact I do not have statistical data on aircraft fires, I use the corresponding data from the automotive sector.

Every year, GDV (Gesamtverband der Deutschen Versicherungswirtschaft eV) registers around 40,000 vehicle fires in Germany [1]. Martin Winter (Forschungszentrum Jülich, Helmholz Institut Münster) calculated for combustion cars 90 fires/ 10^9km whereas electric cars have only 2 fires/10^9km which means the risk of fire in a electric propulsion is a factor of 45 lower[2]. Nevertheless, public perception in the media stands in contrast to these facts. Nobody talks about vehicle fires when it comes to combustion engines, but when an electric car burns; it is on the front page of the media. Unfortunately, with the increasing share of electric drives in aviation, we will observe the same effects.

Compared to the combustion engine, the electric drive is not only much more ecological, it also offers significantly higher reliability and safety. But for most aerospace engineers, it's a new technology, and as mentioned earlier, every energy store, every energy source, is a potential source of risk. We have to identify these potential risks within the electric propulsion, analyse them and develop measures for reduction and/or avoidance.

A combustion propulsion has a high degree of mechanical complexity and nearly no component is negligible! Compared to this, an electric propulsion looks much more less complex, but the complexity in this case is hidden in electronics and software. But once developed and fabricated, electronics and software have the potential to be much more reliable. Reliability and safety result from an analysis of possible errors and measures to avoid them. Figure 1. shows a mind map of key components of an battery electric propulsion and possible failure- / problem sources. Due to the complexity and limited time for the presentation I will focus on some aspects of the hv-battery system. Figure 2. Show a set of possible failures and suggested preventive measures in a mind map

Methodology

Thermal runaway

The most feared incident in a battery electric drive is a thermal runaway. The thermal runaway is a series of exothermic self-reinforcing reactions initiated and propagated throughout the cell. A lot of heat and combustible gases will be produced within this exothermic ractions[3,4]. The worst case is a chain reaction in which the thermal runaway spreads over neighboring cells on the entire battery pack.

Mechanical abuse is the most common method to simulate in-field failures. The most common technique to induce thermal runaway by mechanical abuse of cells or battery packs is penetration of a cell by a nail so called "nail penetration test"

Figure 1. Key Components of a battery electric propulsion and possible failures- /problem sources

A thermal runaway can be triggered by various events

- Overcharging
- Charging at low temperatures
- Deep discharging
- External heat (> 120°C)
- External short circuit
- Internal short circiut
- Mechanical abuse: Damage, crush, or penetration of a cell can cause a short circuit,
- Foreign debris that enters the cell during manufacturing can also cause an internal short circiut

However, the thermal runaway does not have to occur immediately, it can occur hours, days, or weeks after the primary trigger event.

To investigate the consequences of a thermal runaway in a cell or propagation within a battery pack we built up an experimental set up, which enables a safe and remote controlled procedure of the nail penetration test. Data acquisition takes place via 10ch digital data logging for cell temperatures and cell voltages. An infrared camera enables the temperature measurement of the surfaces within the measuring setup. A video camera allows additional visual recordings in slow motion and real time

Figure 2. HV-Battery possible failures/problems and preventive measures

Results

Figure 3 shows the experimental set up for nail penetration test. The cell/battery pack is placed on a heat resistant electric non conductive ceramic plate, a linear actuator penetrates a nail to a predefined depth into the cell.
Figure 4 shows the voltage and temperature during the thermal runaway of an 18650 cell. The surface temperature rises in the maximum up to 580 ° C.
The presentation will show how the occurrence of possible trigger events can be prevented, how possible trigger events can be detected and how the probabylity of occurence and consequences of a possible thermal runaway can be minimized.

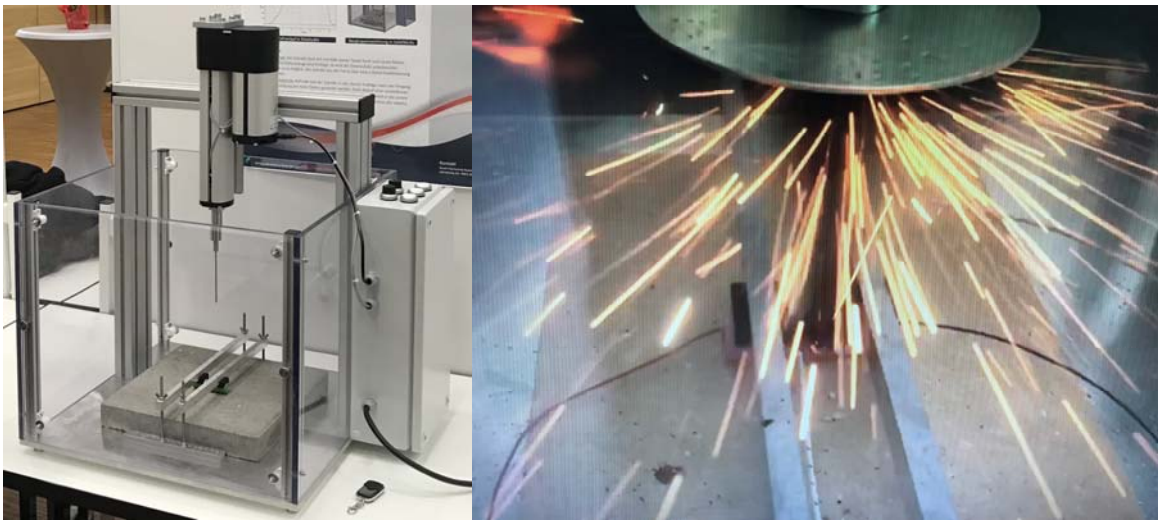

Figure 3. experimental set up and nail penetration test

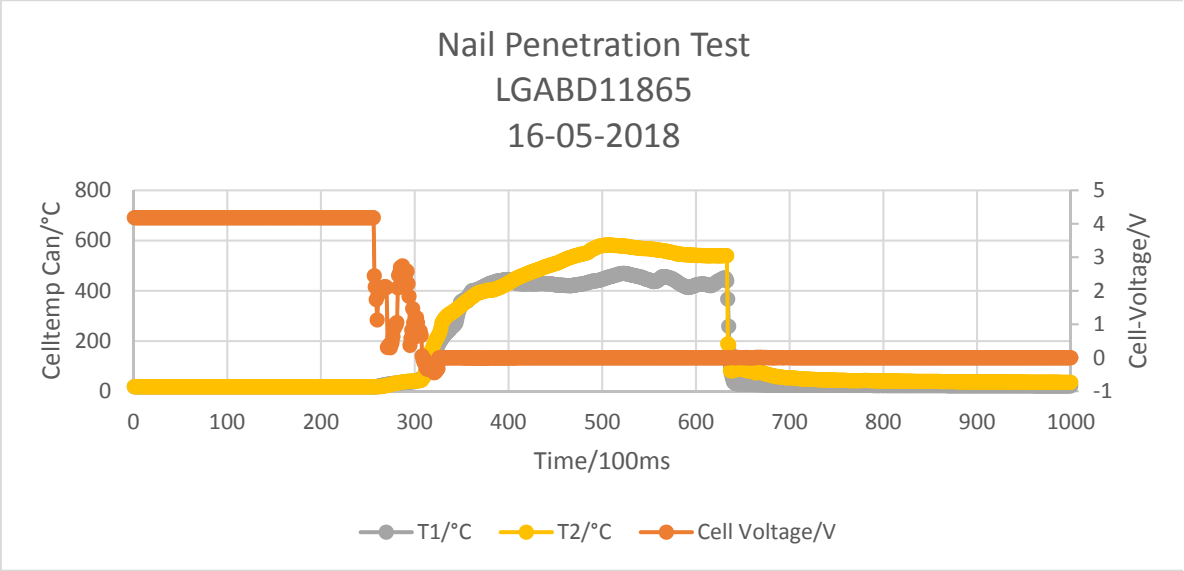

Figure 4. can temperature and voltage of an 18650 cell during nail penetration induced thermal runaway

References

[1] https://www.ruv.de/ratgeber/auto/sicher-unterwegs/autobrand (2017-11-21

[2] https://autorevue.at/ratgeber/statistik-brennen-elektroautos

[3] Thermal-runaway experiments on consumer Li-ion batteries with metal-oxide and olivin-type cathodes
Andrey W. Golubkov,*a David Fuchs,a Julian Wagner,b Helmar Wiltsche,c Christoph Stangl,d Gisela Fauler,d Gernot Voitic,e Alexander Thaleraand Viktor Hackere, RSC Adv., 2014, 4, 3633

[4] "Lithium Battery Thermal Runaway Vent Gas Analysis", Thomas Maloney, Final Report DOT/FAA/TC-15/59, Nov. 2016, Federal Aviation Administration, William J. Hughes Technical Center Aviation Research Division Atlantic City International Airport, New Jersey 08405

Pusher-flap or Coandajet

Georg Emanuel Koppenwallner[1],
[1]*Flugwissenschaftliche Fachgruppe Göttingen, FFG, Germany,* plotter@ploland.de

Abstract: This article describes and estimates a new realizable concept of motor-glider propulsion. The idea is to replace the traditional Schempp-Hirth air brake by a line of small electric impeller units. The airbrake becomes a pusher-flap. The propulsion flow of the thin jet created by a line of impellers over the curved wing surface is strongly connected with the Coandaeffect and the possible increase of lift. Therefore this kind of motor-glider with pusher-flap propulsion ist designated „Coandajet“, (CJ). The estimation shows the feasibility of a selflaunching glider with 16 impellers .

***Keywords*:** Coandajet, pusher-flap, motor-glider, electric impeller units, distributed propulsion, selflaunching glider.

Introduction

The idea of a motor-glider was 1934 described by J.V. Carden [1]. Wolf Hirth improved this idea 1937 [2]. This was the beginning of the retractable engine. Challenge of this type of motor-glider propulsion is the contradiction that the propeller shall be as big as possible and the fuselages cross-section shall be as small as possible. In the 1930ies the Schempp-Hirth airbrake (SHA) was invented, an airbrake that extends spoilers out of the wing. The concept of distributed propulsion is known for a long time [3]. Outside of the General Aviation (GA) electric propulsion was developed for model airplanes, especially impellers for jet models [4]. The recent development of electric drives also in GA enabled the realistic thinking of distributed electrical propulsion (DEP) . Synthesis of this concepts led to the idea of the pusher-flap that is composed of a line of electrical impellers.

Idea

The Froude-efficiency of impuls propulsion depends on the surface that can be used to create the propulsive flow. But this “propulsive” surface is also related to drag during soaring. The classical motor-glider hides or shrinks this surface - normally the propeller disc. The propulsion necessary for sustaining flight of modern gliders can be created with relative small propulsion surfaces and reasonable efficiencies, Figure 1. The idea of this article is to replace the spoilers of the SHA by lines of electrical impellers, Figure 2 , creating a kind of pusher-flap. With a basic estimation the feasibility of this motor-glider shall be calculated. The propulsion flow is a relatively thin jet over wings surface that resembles to a typical Coandaflow for high lift configurations. Therefore this kind of glider can be called Coandajet.

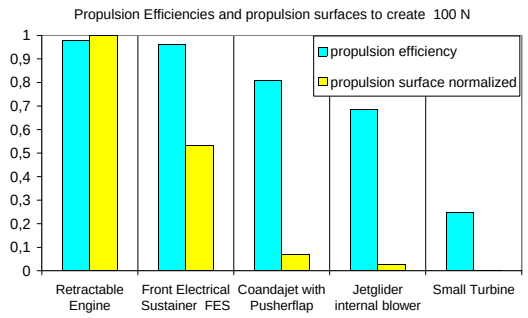

Figure 6: Propulsive efficiencies and surfaces

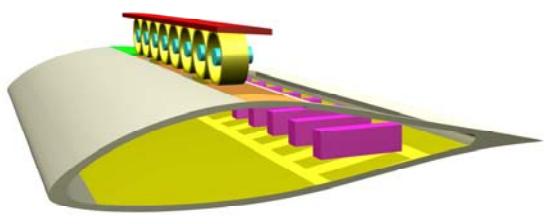

Figure 7: Line of electrical impellers – pusher-flap

Estimation of feasibility

A very simple estimation of thrust ***F***, required power ***P*** and number of revolutions ***n*** is as follows.

$$(1) \qquad F \sim n^2 \text{ and } P \sim n^2 \;\Rightarrow\; \frac{n_1^2}{n_2^2} = \frac{F_1}{F_2} \text{ and } \frac{n_1^3}{n_2^3} = \frac{P_1}{P_2} \;\Leftrightarrow\; F_1 = P_1^{2/3} \cdot \frac{F_2}{P_2^{2/3}} =: P_1^{2/3} \cdot T_2, \text{ with } T_2 =: \frac{F_2}{P_2^{2/3}}$$

This requires that the efficiencies of the engines and the fans are independent of ***n*** .The right hand side of formula (1) shows the calculation of thrust F_1 for a given power P_1 - using the reference value T_2 of thrust F_2 and power P_2. Two reference values were chosen from the measurements of typical model impellers. This estimation is based on the Schübeler DS 86-AXI HDS impeller in combination with a TP5660 engine. The two reference values were calculated with typical thrust/power ratios of 18 N/kW ≈ (58 N/3,92 kW) at 29000 rpm and 14 N/kW ≈ (85 N/6,05 kW) at 34000 rpm. The value pairs of thrust F_1 and power P_1 can be used to calculate the specific thrust and the

energy consumption or battery discharge for different phases of an idealized flight profile. Figure 3 shows the increase of specific thrust and therewith efficiency with decreasing power. Using the value 18 N/kW (solid blue line) the running times for different thrusts were calculated, Figure 4. These thrusts can be connected to different flight phases: rolling and start, climbing and sustaining flight, table 1 .

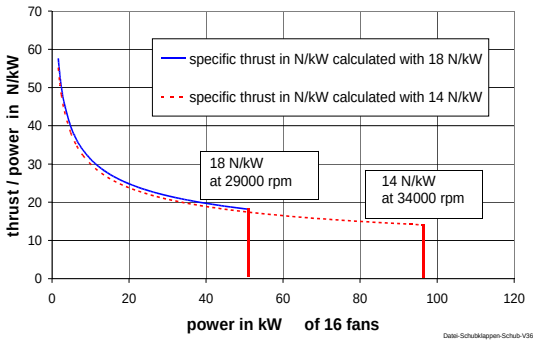

Figure 8: Specific thrust

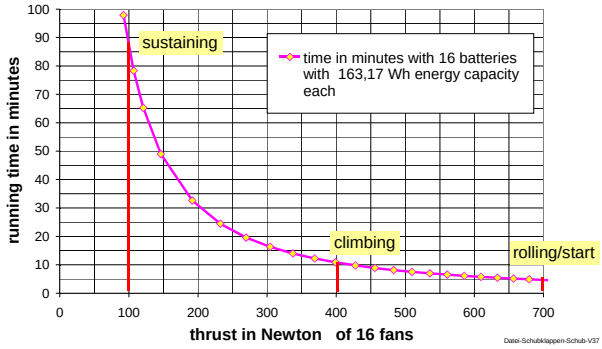

Figure 9: Running times for different thrusts

This flight profile is compared with the polar data of a St. Cirrus with a total mass of 400kg. A thrust of 400 N is sufficient for a climb rate > 2,0 m/s or a gain of 600 m height after 5 minutes. The flight profile is based on 16 fans and 16 batteries with 163 Wh . The mass of these 16 batteries with 2,6 kWh is approximately 17 kg . The mass of one fan with motor, electrical lines and controller is about 1,5 kg. The total mass of the system (without mechanic of the airbrake) is about 40 kg. The maximum thrust of 700 N for the flight profile equals not the possible maximum thrust of 16 fans , 1360 N . Use of the impellers with partial load increases efficiency especially for sustaining flight.

flight profile	thrust in N	time in seconds	time in minutes	consumed energy kWh	% consumed energy	% of remaining energy
rolling	700	60	1	0,59	22,47	77,53
climbing	400	300	5	1,33	51,07	26,46
sustaining flight	105	600	10	0,33	12,77	13,69

Table 1: Flight profile, thrusts, consumed energy, remaining energy

Two battery types shall be considered $LiFePo_4$ batteries and LiPo batteries with typical energy densities of 90 Wh/kg respectively 150 Wh/kg . With these energy densities a battery-mass of 33,3 kg respectively 20 kg is necessary to store 3 kWh of electric energy. The use of more battery capacity will increase the duration of sustaining flight significantly. Assuming that the additional mechanical parts will have a mass of 10 kg the total mass of a pusher-flap-system for a Coandajet glider will be in the order of 50-70 kg. This mass is in the same order as the mass of retractable engines for self launch.

Advantages

A pusher-flap as a kind of DEP especially implemented into an existing glider design shows these advantages: possible self launch, lift increase by the Coandajet, short take off and landing abilities (STOL), potentially high thrusts, operation of the engines with partial load and high efficiencies, no endangered propeller, no change of the landing gear or the fuselage necessary, use of the existing airbrakes, high redundancy, uncritical change between soaring and powered flight, energy recuperation during descent, solar powered recharging during flight possible.

Results

The results of the estimation show the feasability and the potential for this new kind of glider propulsion. Main advantage is the use of existing components, the modified use of the common Schempp-Hirt airbrakes and thereby the safe change between soaring and powered flight. Proof of this concept of the Coandajet with pusher-flap propulsion is necessary and with relatively low effort possible.

References

[1]Carden, J.V., 1934, Improvements in or relating to Aircrafts, GB - 432 301
[2]Hirth, W., 1937, Segelflugzeug mit Hilfsmotor, DE - 698 201
[3]Kim, H. D., 2010: Distributed propulsion vehicles, 27th International Congress of the Aeronautical Sciences; 19-24 Sep. 2010; Nice; France , 11p, https://ntrs.nasa.gov/archive/nasa/casi.ntrs.nasa.gov/20100036222.pdf
[4]Retzbach, L., 1997: Elektro Impeller, Neckar Verlag, Villingen.Schwenningen

Gliding Training in the EU – Past & Future

Patrick PAUWELS
Association of Flemish Gliding Clubs / Belgium
Member OSTIV-Training & Safety Panel / Hon. President European Gliding Union

Abstract: All gliding clubs and glider pilots are confronted with a change from national rules and procedures towards a EU set of rules as the EU decided in 2002 to bring the majority of all aviation related activities under EU-law.

***Keywords*:** EU, EASA

Introduction

With the publication of "Regulation (EC) No 1592/2002 of the European Parliament and of the Council of 15 July 2002 on common rules in the field of civil aviation and establishing a European Aviation Safety Agency" (the so-called 'Basis Regulation') a conversion operation at large was started. Implementing Rules were published in 2003 about 'Initial Airworthiness' (Part 21 - Design and production) and 'Continuing Airworthiness' (Part M – maintenance and airworthiness). With the 'New Basic Regulation' No 216/2008 the scope was enlarged towards flight crew licensing (FCL), medical requirements (MED), operations (OPS) and other domains. As from 2011 Implementing Rules were published for licensing and medical requirements and followed by other rules for training, operations and other domains. The whole EU-gliding community was confronted with this conversion.

Gliding Licensing and Medical Requirements

For many years, the gliding training and examination, medical assessments and the issuing of the licences were based and organized on national rules and procedures. In nearly all countries the requirements of ICAO Annex I 'Personnel Licensing' were applied, sometimes some variations were filed. In the early nineties a EU Directive made bilateral recognition possible of PPL licences. (e.g. a pilot with glider licence issued in France could fly a glider that was registered in Germany).

In 2008/2009 the European Gliding Union and Europe Air Sports were heavily involved in the drafting parties for Part FCL. A fundamental change was the opening towards differentiation with the introduction of the 'Light Aircraft Pilot's Licence' (LAPL) and the LAPL-medical. Rulemaking is not that easy a many parties are involved (the authority side, the users, EASA, the Commission, the legal departments, … and the final result is always a compromise…

With Reg. No 1178/2011 the package of rules was published with the requirements for licensing (Part FCL) and medicals (Part MED). These rules were applicable as from 8 April 2012 with a transfer period until 8 April 2014. Member States could decide to make use of an extra opt-out for gliding until 2018.

With the publication of Reg. No 290/2012, the Reg. 1178/2011 was amended with the requirements for training organisations (Part ORA – Approved Training Organisations (ATO's)).

In 2014 the EU Reg. 965/2012 was amended with operational requirements (Part NCO – Non-Commercial Air Operations with other than Complex Motor Powered Aircraft)

A few member states made the full conversion to the new EU-rules; the most member states have chosen to use the extra opt-out periods where possible.

Future

As from the publication of the first regulation, EAS and the EGU have been sending appeals towards the EU-Commission and EASA to respect the basics of rulemaking: "Appropriate rules to the size and the kind of the activity", and making a difference between "air-transport" and "air-sport".

Finally in 2012, the EU-Commission and EASA published the so-called "GA Road Map". An action plan to simplify the rules on several domains for the lower end of aviation. Here we must thank Mr Patrick KY, the new Executive Director of EASA who was willing to listen to EAS and the EGU and clearly understood the problems that the air sports were faced with.

Task forces were set up to review

- Part M and to have a "Light Part M" for the GA
- the training requirements – which will bring us the option of the 'Declared Training Organisation' (a simplified ATO)
- the operational requirements – to produce specific rules for gliding (Part OPS Gliding)
- the licensing requirements – to produce specific rules for gliding (Part FCL Gliding)

The goal for gliding is to have an appropriate and dedicated 'Rulebook for Gliding' in 2020 for all domains.

The necessary extra opt-out time will be for seen to assure a correct transfer and implementation.

Fatal Accident Rates Involving Spinning for Selected Single-seat Gliders

Murray Stimson[1], Stu Smith[2]

[1]*Melbourne Glidng Club, Bacchus Marsh, Australia* murray.stimson@gmail.com
[2]*Gliding Club of Victoria, Benalla, Australia,*

Abstract: Accidents involving loss of control remain a significant fraction of the total number of fatal accidents in the sport of gliding. The Aviation Safety Network (ASN) online wikibase provided by the Flight Safety Foundation appears to be the only available and searchable global database of aircraft accidents and incidents. Aircraft Service Years (ASY) was a new method proposed in 2017 to act as a proxy for risk exposure, since no data on risk factors such as hours or flights flown were available globally. ASN data was used to compare the fatal and non-fatal accident rates for several single-seat gliders against ASY. The results show a wide variation in accident rates that is difficult to explain only with the shortcomings of the ASN wikibase.

***Keywords*:** Accidents, fatal accidents, loss of control, spinning.

Introduction

All gliders can display spinning behaviour under certain conditions, but some appear to enter and/or remain in a spin more readily than others. Some gliders seemed easy to spin deliberately, while others were spin resistant or required specific techniques to enter a spin. Design philosophies for more modern training sailplanes have arguably diverged into two categories: spin-resistant and easily-spinnable. Would it be possible to also categorise single seat gliders using data on accident rates involving spinning?

Knowledge of the relative safety performance of gliders appears to be limited among clubs, syndicates and individuals engaged in buying, owning and operating new and used gliders. Whilst there are some national accident databases and a smaller set that are available to all, the sample sizes appeared too small for statistical validity. There was no international safety rating for gliders such as the Australasian New Car Assessment Program (ANCAP) safety rating system for automobiles, or the equivalent Euro NCAP.

Methodology

The ASN Wikibase search function was used with Aircraft Category set to "Glider" and Type set to the possible designations of each glider. Resulting lists of glider incidents and accidents were then examined to discover any indication of whether each event primarily involved out of control behavior, specifically spinning. Accident narratives that mentioned spinning behavior were categorized as "Definite", along with those where other categorical evidence was confirmed, such as an investigation report from the national accident investigation service or clear photographs of ground impacts with low translational velocity, steep impact angles or high yaw attitudes. Accidents with descriptions or other evidence suggesting a stall or other hard landing were categorized as "Probable". Where significant doubt existed but the cause was not classifiable as "Unknown" a category of "Doubtful' was created, but attracted few entries. All other accidents were categorized as "Not" involving spinning. For example, mid-air collisions were placed in the "Not" category even if spinning behavior resulted because the initiating event was not loss of control. In many cases the entries also included data on pilot injuries (fatal, serious, minor, unknown) and glider damage (write-off, substantial, minimal, unknown).

A significant shortcoming is that ASN Wikibase relies on available data reaching the contributors and remaining available at the time of search. Especially in the earlier decades (1970's, etc) many entries do not contain sufficient information to categorise as described above. Accident investigation reports from many countries were also found in many cases to be inadequate for the purposes of determining event sequences or causal relationships. Many of the links or report references included in ASN Wikibase entries were no longer active, but where they were available local news reports could provide valuable evidence such as photos, videos or witness reports.

For some glider types, the ASN collection of data appears to be skewed towards accident reports from particular countries. For the ASW-15 for example, 12 of the first 32 ASN Wikibase accident reports from 1971-1985 were from New Zealand, whereas no further reports out of 23 from 1985 to 2017 were from New Zealand. All of these entries originated from NZ government archives website, but other than the date, glider registration, location and pilot name no further details were found. Consequently the presence of spinning behaviour was classified as "unknown". Our method partially allows for these uncertainties by using a categorization scheme with graded certainty and only ascribing the "Definite" category where the evidence is clear.

Our method is unable to account for the uncertainties caused by accident and incident entries not being included in ASN Wikibase.

Some countries appear to generate no or insufficient reports of accidents, especially compared to the size of their resident glider fleets. Although uniform rates of accidents would not be expected for all countries, some countries with substantial gliding activity and hence risk exposure seemed substantially underreported or absent in ASN

Wikibase for the gliders so far examined. Further, Australia, Canada, UK, France, Germany and the USA are notable in that comprehensive accident investigation reports have been available for most serious accidents, with excerpts included in the ASN Wikibase narratives. Some countries have in the past written and continue to write many official accident investigation reports that may attribute causes with descriptions such as "loss of lift", indicating poor understanding of gliding as well as accident investigation techniques and standards. Where ASN Wikibase contributors have paraphrased official accident reports we almost always found the essence of the findings had been correctly explained.

As with our presentation at the 2017 OSTIV Congress on fatal accidents involving spinning for several two-seat gliders, we have used Aircraft Service Years (ASY) as a proxy for risk exposure for a each type of glider. ASY was calculated by determining a build rate that matched reported cumulative build totals from manufacturer's websites between the years of first flight and ceasing production. After subtracting those aircraft reported as written off (ASN[1] and R. Cawsey[2]), a cumulative sum (ASY) of the number remaining in-service each year was derived. Whilst some aircraft may undoubtedly have been rebuilt and returned to flying status, that number could well have been more than overshadowed by those aircraft that were seldom or not flown during any particular year. At best, ASY was an approximate measure of the amount of flying done for each type around the world.

Results

Numbers of fatal accidents for each type are shown in Table 1, along with the rate per 1000 ASY for both the categories where spinning behaviour was definite and probable, and the consequent total.

Table 1. Fatal accident rates and raw accidents for selected single-seat glider types where the accident was catgorised as either definitely or probably involving spinning behaviour, over the period from first flight to 2017.

Type	Number Built to 2017 (Est.)	Aircraft Service Years	Reported Fatal Accidents (Aviation Safety Network)					
			Definite Spin		Probable Spin		Total	
		(1000 ASY)	No.	Rate	No.	Rate	No.	Rate
ASW-15 a, b	447	19.468	0	0.00	1	0.05	1	0.05
LS-4, a, b	1048	28.094	5	0.18	1	0.04	6	0.21
Cirrus Standard a, b, 75	838	32.833	7	0.21	3	0.09	10	0.30
DG-300/303	511	12.682	2	0.16	2	0.16	4	0.32
SZD-48 Jantar Std 2, 3	677	22.565	4	0.18	5	0.22	9	0.40
Discus a, b, CS	1102	21.566	9	0.42	0	0.00	9	0.42

Note: Accident Rate given as: Fatal Accidents per 1000 ASY

Although Table 1 ranked the glider types on the total rate of fatal accidents involving spinning, the data shows no appreciable differences between the most popular types of single seat glider so far examined. The ASW-15 data is potentially suspect due to the preponderance of data from incidents in New Zealand and also the substantial number where the category was "unknown" due to the lack of any substantive incident report.

Limitations in applicability of ASY as a risk exposure measure may also have played a role in skewing these results. ASY takes no account of the higher flying hours and number of flights that might differentiate higher performance single seat gliders because more pilots in more countries wish to fly them more often and either longer or further. For example, pilots seeking to maximize their achievements may more likely choose a Discus rather than a Cirrus if that choice was otherwise equal in cost and risk.

Table 2 shows a comparison of fatal and non-fatal accidents and rates for the same period and set of glider types. The ranking has been maintained from Table 1, but the total number and rate of reported incidents in ASN Wikibase no longer supports that ranking. SZD-48 Jantar Standard 2/3 now shows the lowest rate of incident reports, but this may well be due to a significant dearth of reports in ASN Wikibase involving those gliders. For the Cirrus, the total number of incident reports was dominated by the number with unknown causes (49 out of 103), indicating that data on the nature of these incidents has not been readily available. This was to a lesser extent true for both ASW-15 (23 out of 55) and Discus (20 out of 80).

Table 2. Comparison of fatal vs total reported incident numbers for each category of certainty regarding the presence of Loss of Control or spinning as a primary initiating event in the ASN Wikibase.

Type	Definite spin		Probable spin		Doubtful spin		Not Spin		Unknown cause		Total	
	Fatal	Total	Fatal	Total	Fatal	Total	Fatal	Total	Fatal	Total	No.	Rate
ASW-15, a, b	0	1	1	2	0	0	5	29	3	23	55	2.83
LS-4, a, b	5	5	1	4	0	1	3	39	0	2	51	1.82
Cirrus Standard a, b, 75	7	11	3	5	2	5	9	33	4	49	103	3.14
DG-300/303	2	3	2	4	1	4	2	13	2	3	27	2.13
SZD-48 Jantar Std 2, 3	4	7	5	5	0	1	2	9	0	8	30	1.33
Discus a, b, CS	9	10	0	5	1	5	6	40	5	20	80	3.71

Note: Rate shown as per 1000 ASY

Conclusions

Substantive conclusions aimed at classifying the relative safety of different glider types were not possible from this examination of fatal accident rates and total reported incidents for selected single-seat gliders. Lack of reliable data was the primary confounding factor, exemplified by the high rate of incidents with unknown causes for some of the gliders chosen to date. Limitations in the utility of ASY as a risk exposure proxy reinforce previous recommendations that real data must be collected and curated regarding global flight hours, number of flights and other valid exposure metrics.

This report also highlights several improvements to the ASN Wikibase that would benefit future safety studies. ASN should ensure that incident and accident reports are continually upgraded with causal data when and if it becomes available, ensuring that a copy of any official investigation report will be available in perpetuity for future research. The international network of contributors from all gliding nations could be expanded to include each national operations manager or staff in the national administrating body of gliding. The primary objective would be to address the geographic "black spots" emerging where insufficient or no data has been uploaded to this valuable safety resource.

References

[1]Aviation Safety Network Wikibase, a service of the Flight Safety Foundation. https://aviation-safety.net/wikibase/wikisearch.php accessed May-Jun 2018.

[2]R Cawsey, Glider production and status lists. http://www.rcawsey.co.uk/index.htm accessed May-Jun 2018

A static line system designed to be retrofitted to typical emergency parachutes for use by glider pilots: - Buying the pilot time in a critical situation.

Stu Smith
Gliding Club of Victoria, Australia

Abstract: A very large number of modern era gliders, post 1965, have structural anchorage(s) for attachment of a parachute static line. The author noted that use of static lines in gliding is rare in many countries and typical emergency parachutes used today do not offer a static line option. A versatile retrofitted static line has been designed by a qualified parachute harness maker and has been in service in Australia for several years by both a club operation and by individual cross-country rated pilots. This presentation discusses the design attributes of the particular static line assembly and its operational performance. The aims and benefits of adopting a static line system of this type are discussed.

***Keywords*:** static line, emergency parachute.

Introduction

This project arose in the aftermath of a tragic mid-air collision of two gliders with the author interested in what options were available for increasing the probability of successful escape to a fully deployed emergency parachute. Discussions with a senior Australian parachuting expert involved in Coronial Inquests, indicated that once free of the glider, correct identification of the D-Ring, pilot posture and rotation, pilot hesitations, and time taken to commence a deployment were all important issues in quickly achieving a full canopy free of any tangling. In the urgent haste that the pilots find themselves between exiting the cockpit and pulling the ripcord they suddenly face several concerns such as being clear of the glider, are they speeding up or slowing down, to delay or not to delay pulling ripcord, what position is best and what time remains available?

When we consider the situation of a novice pilot or first time passenger taking a scenic flight, it is reasonable to consider whether they are well equipped to deal with deploying a parachute in an emergency, even if they have fully absorbed a pre-flight briefing on its use. As such, the use of a static line for passengers and novice pilots takes care of one step of the process. They need to clear the canopy and release the harness, (two actions for which they have at least some familiarity with, being akin to getting out of a car) and then upon getting out of the glider the static line takes care of the last required action.

Anecdotal evidence of use of emergency parachutes includes stories of pilots who's feet touch down very soon after the opening of the canopy, leading to thinking that any seconds saved may make a considerable difference to outcomes. Reviewing sources such as GFA accident summaries and Aviation Safety Network wikibase for cases where glider pilots completed egress from cockpit but failed to deploy a parachute does not yield cases, though they must have occurred. Frequently the outcomes fall into two categories of pilot failed to clear the cockpit, or they parachuted successfully. So evidence that potentially saving small amounts of time provides a significant safety benefit is not forthcoming. Another paper presented by this author at this congress indicates that time to egress glider cockpits is more than most pilots realise and any time saving in any step in the process may be critical.

Methodology

The aims of the static line design presented here was to be available to add-on to almost any existing emergency parachute, to be low cost, to be dependable, durable and low maintenance, to be fitted by pilots not parachute packers, to be optional so that the parachute with one fitted retains all its normal operations and serviceability, in its use it should reduce time to fully deploy the canopy, and to increase the probability that no tangle or malfunction occurs due to pilot circumstances during deployment, to provide extra confidence for the pilot in command that if their passenger or student was to need to make an emergency escape that the parachute would deploy.

In consultation with Jo Chitty of Skywerx, Melbourne, Australia, the requirements of such a system were clarified and Jo built a prototype static line kit that attaches to the outside of the parachute. After some minor adjustment to the size of the module, this unit is now available for purchase. The author would like to advise that he is not connected with the sale of this item, not with any part of the Sywerx business and derives no benefit from its sale. The author has been using this system for more than 4 years and several other pilots in Australia have bought one. A large Melbourne gliding club has purchased multiple units and has adopted its regular use for flying passengers.



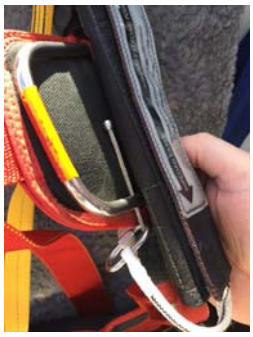
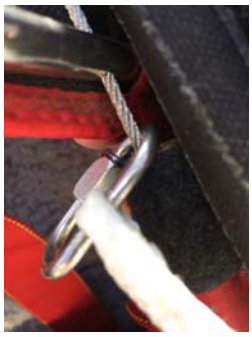


Figure 1. **Figure 2.** **Figure 3.** **Figure 4.** **Figure 5.**

The Skywerx static line module attaches to webbing with Velcro tabs above and below the area of the D-ring (Figure 1). The snap-shackle on the end of the yellow line connects to an anchor or anchor strap on the glider (Figure 2). The other end attaches to the cable just below the D-ring with a threaded shackle that will fit over the cable but not the D-ring (Figures 3&4). After exiting the glider, the separation will pull white Spectra rope from the yellow end of the black module, which is only held closed with Velcro. A small tie prevents this being pulled out on the ground inadvertently. When the white spectra is at full stretch it pulls on the ripcord cable and pulls the whole D-ring out of the parachute for canopy deployment.

If pilot forgets to attach the static line before flight, the D-ring is still there for normal deployment technique.
If pilot is flying above 7000m and would not want an immediate deployment at high altitude, the connector at the D-Ring end can be disconnected in flight (Figure 4) to enable only manual D-Ring deployment. Upon descent to lower altitude, the static line can be re-connected. If pilot forgets this step, D-ring is still operational.

If after landing, the pilot or passenger forgets to release the static line from the anchorage, the weak tie (at top of Figure 5) will resist as they walk away. If they manage to break the tie, they would have to walk to the wing tip to actually deploy the parachute inadvertently. This system does not require a parachute packer to assemble if the line is pulled out. The white Spectra is sized to be approximately 9 metres to put escaping pilot clear of tail or wingtip.

The design requirements were: that this add-on module must not impede any of the standard design functions of the parachute; that all possible errors in operation be designed out of it from the beginning; that it is able to be retro-fitted to almost any modern emergency parachute without modification; and that it is low price. The cost of this unit is believed to be around 5-7% of the cost of a parachute

Discussion

There are two parameters of interest here: time to full deployment; and quality of deployment, meaning no tangling, line-over canopy or figure 8 canopies. These are not independent. For novice parachutists such as glider pilots exiting their glider, parachute instructors advise that early deployment, before the pilot has time to tumble or accelerate, increases chance of safe full deployment.

Successful escape via parachute in an emergency is not unlike the reverse of the traditional Swiss Cheese Model, where the path to success is to line up the outcomes that step towards a fully deployed parachute.
This could be quantified by assigning a probability to each step in the process.

<u>An event occurs</u>, (mid-air collision, bird-strike, control jam or disconnection)
Is glider controllable?
If "yes", continue to next decision; such as decide if safe return is possible. Is it wiser to stay or go?
If "no", egress to a parachute descent.
A Probability distribution will exist for time before first action.
Then there is:

Probability canopy is ejected	probability = 1-a, where a is the chance of not ejecting canopy
Probability canopy is misses striking pilot	probability = 1-b, b is probability pilot is struck
Probability harness is released,	probability = 1-c
Probability pilot exits cockpit,	probability = 1-d

Note: -Static line only operates here between this and the next item
Probability of deploy is assumed very closer to 1 for static line, and time is reduced by some amount.

Probability pilot pulls ripcord fully,	probability = 1-e

Probability canopy successfully deploys,	probability = 1-f
Probability time left is enough to slow down,	probability = 1-g
Probability of a good landing,	probability = 1-h
Probability pilot is found,	probability = 1-j

It can be seen from this sequence that a static line offers extra safety margin in only one item from this list. But to achieve survival, all items must be completed in remaining time and time saved using a static line, particularly for novices may make the crucial difference.

Other systems such as NOAH offer very useful improvements in the first four actions in the above list (a to d). A static line supports improvements in the next item (e). Fast exit to a deployed canopy supports the next three items that are also dependant upon initial time available (f, g, h). And the last item, (j) regarding pilot location is now covered by many GPS solutions. As such improvements are available for each step, should pilots choose to take these options.

It should be noted that Ballistic Recovery Chutes (BRC) are showing potential to supersede all the complexity discussed here with systems both fast and reliable and serious consideration should be given to the gliding movement adopting those systems. This presentation has aimed to discuss one system improvement in the context of the overall system and highlight that complexity, in comparison to newer BRC systems.

Recommendations

If parachutes are to be worn, as they now usually are, then an assessment of the capability of the person wearing the parachute could dictate if it is desirable for a static line to be used to reduce complexity in the escape process for them.

Acknowledgements

The author would like to acknowledge the contributions provided by Murray Stimson and Joe Chitty OAM

Validating mountain-wave updraft speeds predictions from the High-Resolution, Rapid-Refresh (HRRR) numerical weather prediction (NWP) model

Edward (Ward) Hindman
Em. Prof. Dr., Earth and Atmospheric Sciences Department
The City College of New York, New York, NY US10031, ehindman@ccny.cuny.edu
from XXXIV OSTIV Congress Program and Proceedings, 28 July-3 August 2018

Abstract: The United States has developed the HRRR NWP model and made the predictions available, free-of-charge, at *rapidrefresh.noaa.gov/hrrr/*. The model is sufficiently high-resolution to predict mountain waves. The waves appear in the 'max updraft' maps as linear and quasi-linear regions. In this study, glider flight recorder data from eastern US wave flights are compared with these regions. The regions, indeed, contained mountain waves. A number of the flights achieved the 5-km Diamond Altitude climb. The predicted updraft speeds were consistent with the updraft speeds calculated from the flight recorder data.

Keywords: Mountain wave predictions, numerical weather prediction models, HRRR model validation

Introduction

Climbs to achieve the altitude requirement for FAI soaring badges are often made in mountain waves. Thus, forecasts of these conditions are essential. The first report in the OSTIV literature about detecting and forecasting their occurrence is described in [1]. Since that report, there has been tremendous progress. Probably the most up-to-date system is described in [2] and a remarkable wave flight using the system is described in [3]. In the winter of 2016, I was asked by northeast US wave pilot Timothy Chow to help interpret the HRRR NWP model 'max updraft' forecasts. The forecasts depicted linear updraft regions resembling waves in mountainous regions. Thus, I compared his flight recorder data, and that of other northeast US wave pilots, with the corresponding HRRR model forecasts as follows.

Methods

The locations of the high-points of wave flights and the maximum rate-of-climb to those points were determined from glider flight records (*.igc files). Then, those locations were identified on the 'max updraft' prediction charts (*.png files) and the magnitude of the updrafts were recorded. The measured and predicted updraft values were compared. Eight recent eastern US wave flights were investigated.

On 20160204 (Flight 1), Timothy Chow made a wave flight in the Green Mountains of Vermont. The high-point of the flight was determined from his *.igc file *(www.onlinecontest.org/olc-2.0/gliding/flightinfo.html?dsId=4835311*). In SeeYou (*www.naviter.com/products/seeyou*), the barogram trace was animated to the high-point and the time, altitude and latitude/longitude at that point were recorded.

The high-point was located on the corresponding HRRR model 'max updraft' *.png file using the image analysis software ArcSoft (*www.arcsoft.com*):

1. The file was expanded to extract x, y values of unique ground-points. Latitude and longitude values for the points were determined using the *skyvector.com* aeronautical chart.
2. An x-y grid with superimposed latitude and longitude values of the ground-points was constructed. The pixel corresponding to the latitude and longitude of the high point was determined by interpolation and recorded.
3. The Red Green Blue (RGB) values of the pixel were compared to the RGB values of the updraft speed scale. The closest match was defined as the predicted updraft speed; for the Chow flight the speed was 0 - 0.5 m/s. The predicted updraft was recorded (see the table).
4. The pixel in the *.png file that corresponded to the high point was colored red.
5. The pixel in the *.png file that corresponded to the summit upwind of Chow's high-point was colored green. Similarly, the pixels corresponding to locations of mountain summits where the other wave flights reported here were made were colored green: Mt. Washington in the White Mountains of NH, Sugarbush Peak in the Green Mountains of VT and Slide Mountain in the Catskill Mountains of NY.

The high-point for Chow's flight and the mountain summits are illustrated in Figure 1 (left).

The HRRR model atmospheric profiles for the location, date and time of the high-points were retrieved from *ready.arl.noaa.gov/READYamet.php*. The atmospheric conditions were determined from the profiles. The profile

for Figure 1 (left) is given in Figure 1 (right). The '+1h' profile was the closest in the archive to the desired initialization profile (0h) which was not available in the archive.

The maximum climb rate achieved in the region of the wave at which the high-point was reached was determined from the *.igc file as illustrated for Flight 1 in the Table: 'Time' is the time the maximum rate-of-climb was achieved (steepest barogram slope) in the region of wave that led to the high-point, 'Altitude' is the altitude at the steepest slope, '+ alt' is the altitude at the top of the steepest slope, '– alt' is the altitude at the bottom of the steepest slope, 'del t' is the interval to climb from below to above the altitude with steepest slope, 'Climb rate' is equal to the difference between +alt and -alt divided by del t, 'Sink rate' is from the glider's polar, 'Measured' is the climb rate plus the sink speed, 'Predicted' is the HRRR model updraft prediction.

Table
Measured and predicted updraft speeds

Flight	Date	Time	Altitude	+ alt	t	- alt	t	del t	Climb rate	Sink-rate	Measured	Predicted
		UTC	m AMSL	m AMSL	hhmmss	m AMSL	hhmmss	s	m/s	m/s	m/s	m/s
1	20160204	165844	2520	3020	170204	2020	165548	376	2.7	0.9	3.6	0.5
2	20160206	185700	4274	4522	185940	4094	185340	360	1.2	0.7	1.9	0.75
3	20161010	163629	4250	4750	164054	3750	163150	536	1.9	0.6	2.4	2.3
4	20161014	193614	3500	3750	194102	3250	193118	584	0.9	0.5	1.3	0.75
5	20171117	180901	3000	3250	181259	2750	180450	469	1.1	0.6	1.7	1.8
6	20171126	153712	3500	3750	154010	3250	153438	332	1.5	0.6	2.1	3.8
7	20180127	154536	4500	4750	154848	4250	154243	366	1.4	0.8	2.1	2.25
8	20180205	143000	3250	3500	143158	3000	142812	226	2.2	0.8	3.0	3.8
	AVERAGE								1.6		2.3	2.0

The climb rate was adjusted to account for the headwind as follows. From the PIK-20D polar (Chow's aircraft), the minimum sink rate is 0.58 m/s at 40 knots (73 km/h). Using a indicated airspeed (IAS) - to - true airspeed (TAS) calculator (*indoavis.co.id/main/tas.html*) and atmospheric conditions from Figure 1 (right), the IAS was 68 knots (124 km/h) for Chow to remain stationary in the wave and the TAS was 69 knots (126 km/h). The sink rate of the ship in still-air at 126 kph from the polar is 0.9 m/s. So, the measured maximum updraft was 2.7 + 0.9 m/s = 3.6 m/s. The value was recorded (see the Table).

Seven additional flights were analyzed: Timothy Chow's 20160206 flight (Flight 2) in the Sugarbush wave, Paul Villinski's 20161010 flight (Flight 3) and Roy Bourgeois's 20161014 flight (Flight 4) in the Mt. Washington wave and Daniel Sazhin's 20171117, 20171126, 20180127 and 20180205 flights (Flights 5 – 8) in the Slide Mountain wave (all flight logs were found at *www.onlinecontest.org*). The high-points and profiles for the Villinski and 20171117 Sazhin flights are given in Figures 2 and 3 (the results from the remaining flights are in [4]). The updraft values for all the flights are listed in the Table.

Results

It can be seen from Figure 1 (left) that Chow's high-point pixel was 4240 m AMSL (altitude gain 2597 m, Silver Badge) in a linear updraft region just downwind of Okemo Peak. The maximum predicted updraft speed for that pixel was 0 - 0.5 m/s and the maximum climb rate was 3.6 m/s passing through 2520 m AMSL (Table). This altitude corresponds to approximately the 750 mb level where, from Figure 1 (right), the winds were from 205 degrees-true at 68 knots.

It can be seen from Figure 2 (left), that Villinski's high-point pixel was 6412 m AMSL in a quasi-linear updraft region just downwind of Mt. Washington (altitude gain 4818 m, Gold Badge). The maximum predicted updraft speed for that pixel was 2 – 2.5 m/s and the maximum climb rate was 2.4 m/s passing through 4250 m AMSL (Table). This altitude corresponds to approximately the 600 mb level where, from Figure 2 (right), the winds were from 360 degrees-true at 45 knots.
It can be seen from Figure 3 (left), that Shazin's high-point pixel was 5435 m AMSL in a linear updraft region just downwind of the SW-NE oriented ridge of Slide Mt. (altitude gain 5095 m, Diamond Badge). The maximum predicted updraft for that pixel corresponded to 1.5 - 2 m/s and the maximum climb rate was 1.7 m/s passing through 3000 m AMSL (Table). The 3000 m altitude corresponds to approximately the 700 mb level where, from Figure 3 (right), the winds were from 350 degrees-true at 40 knots. Reference [3] details this extraordinary flight.

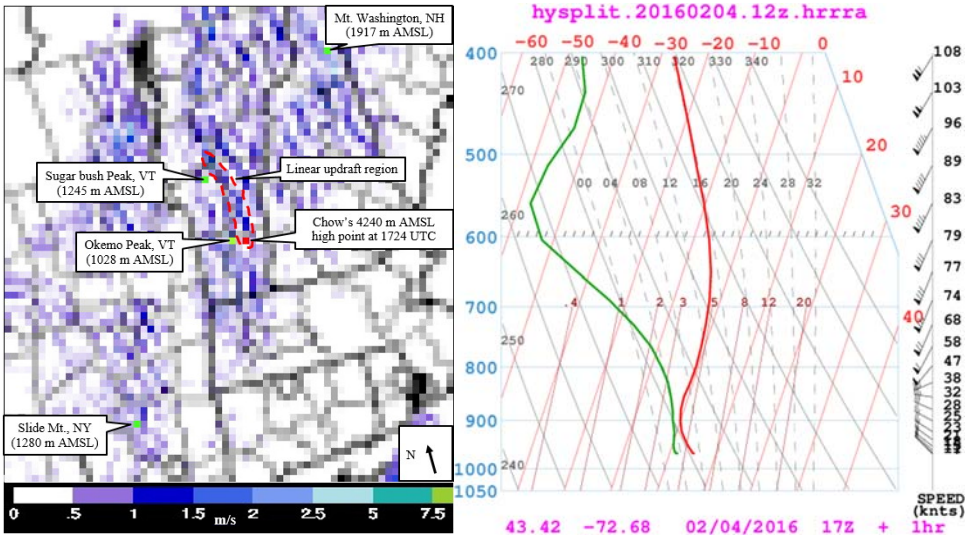

Figure 1: Left, 20160204, HRRR model 7h forecast valid at 1700UTC (1200LT) for the maximum updraft speed (m/s) surface to 100 mb over the previous hour. Labeled is the high-point of Tim Chow's flight (red pixel), the linear updraft region (dashed red line) and the location of mountains (green pixels) that produced the wave flights described herein. Right, the atmospheric profile for the location, date and time of the high-point.

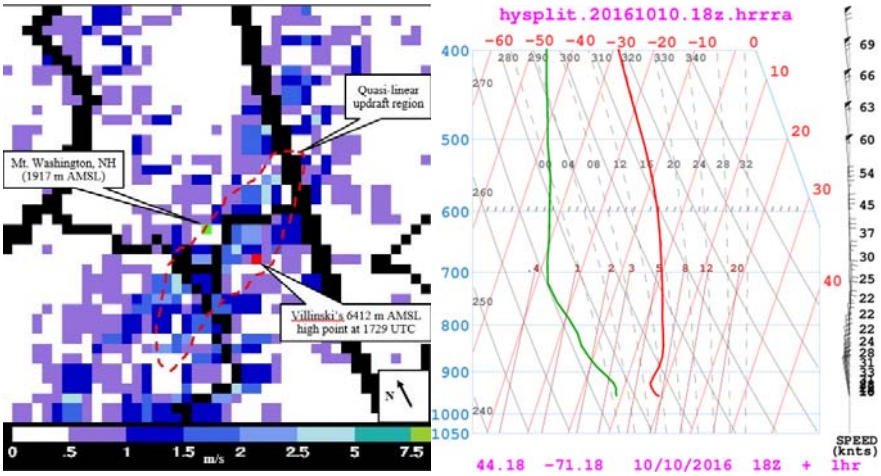

Figure 2: Left, 20161010, HRRR model 6h forecast valid at 1800UTC (1300LT) for the maximum updraft speed (m/s) surface to 100 mb over the previous hour. Labeled is the high-point of Paul Villinski's flight (red pixel), the quasi-linear updraft region (dashed red line) and the location of the mountain summit (green pixel) on the ridge that triggered the wave. Right, the atmospheric profile for the location, date and time of the high-point.

Discussion

The HRRR model is a real-time, 3-km resolution, hourly-updated, cloud-resolving, convection-allowing model, initialized by 3-km grids with 3-km radar assimilation. The model covers the contiguous US. The model predicts hourly for an 18h period the major meteorological parameters. Hence, predictions made in the evening should be useful for next-morning flight decisions.

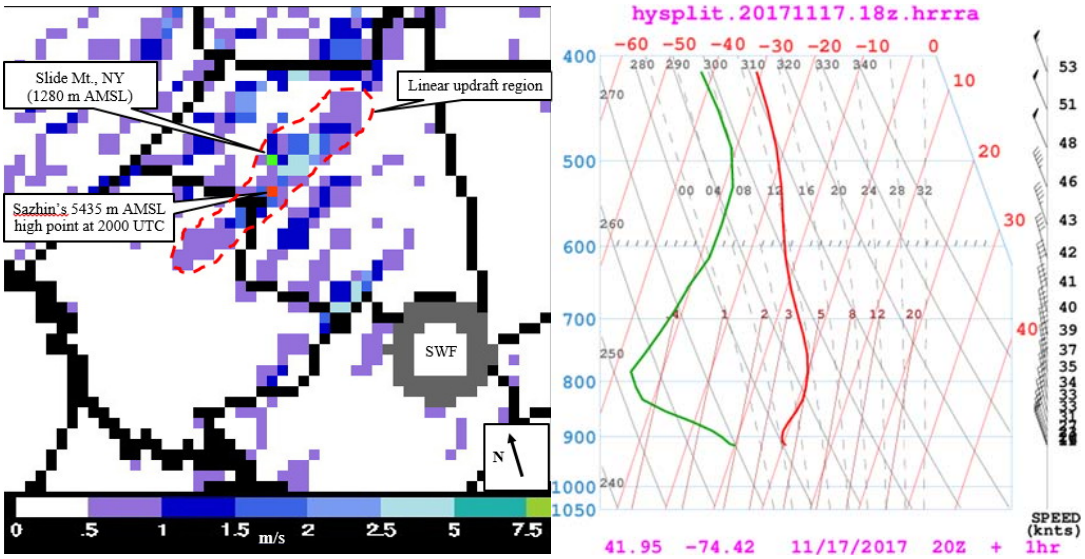

Figure 3: Left, 20171117, HRRR model 10h forecast valid at 2000UTC (1500LT) for the maximum updraft speed (m/s) surface to 100 mb over the previous hour. Labeled is the high-point of Daniel Sazhin's flight (red pixel), the linear updraft region (dashed red line), the location of the mountain summit (green pixel) on the ridge that triggered the wave and Steward Field (SWF). Right, the atmospheric profile for the location, date and time of the high-point.

Of the eight flights, five of the high-points were in linear updraft regions (Figures. 1 and 3, the remainder are in [4]) while three were in quasi-linear regions (Figure 2, the remainder are in [4]). These coincidences prove the predicted updraft regions, indeed, were mountain waves.

On 9 February 2016, I e-mailed a HRRR model developer, Dr. John Brown of the NOAA-ESRL in Boulder CO, and asked how to interpret the 'maximum updraft/downdraft' predictions. Here is his helpful response: "*In the case of mountain waves, the vertical velocity in vertically propagating mountain waves is fairly well represented, but trapped lee waves in general will not be well described because these waves are typically too small in horizontal wavelength to be well represented by a model with 3km grid spacing*." Brown's statement is supported by the results in the Table. The average of the measured updraft speeds was 2.3 m/s and the average of the predicted updraft speeds was 2.0 m/s. But, there is no correlation between the individual speeds. When higher resolution predictions are available, the correlation should improve. Nevertheless, the HRRR model 'max updraft' predictions are consistent with the measurements. Hence, the prediction can be used to estimate whether a wave will be 'weak' or 'strong'.

Conclusions

The freely available HRRR NWP model predictions (*rapidrefresh.noaa.gov/hrrr/*) of 'max updraft' have been shown to identify regions and strengths of mountain waves. Hourly predictions are available for an 18-hour period. Hence, predictions of the location and strengths of mountain waves made in the evening should be useful for next-morning flight decisions.

References

[1]Lindsay, C., 1965, "Satellite wave observations used as an aid to wave soaring." *OSTIV Publication VIII*, 5 pg. (*journals.sfu.ca/ts/index.php/op/article/view/1692*).
[2]Sazhin, D., Chidekel, P. and Bird, J., 2018, "Catskill Mountain wave project: Exploration, mapping, and forecasting of wave conditions in southern New York." *XXXIV OSTIV Congress Program and Proceedings*, in press.
[3]Sazhin, D., 2018, "You gotta believe!", *Soaring*, 82(5), 16-19.
[4]Hindman, E., 2018, "Validating mountain-wave predictions from the United States High-Resolution, Rapid-Refresh (HRRR) numerical weather prediction (NWP) model", *Technical Soaring*, to be submitted after the XXXIV OSTIV Congress, 6 pp.

Lee waves without mountains
Extensive wave induced cloud streets over Germany on 14th April 2015

Julian M. West MA, D.Phil.
westjulian1@gmail.com

Abstract: In the afternoon of 14th April 2015 between 1400 and 1500 UTC a spectacular set of cloud streets having the form of convective wave bars with (foehn) fingers was observed over Haag an der Amper, which is located 40km NNW of Munich. One of a series of satellite pictures for this time period reveals an extensive area of uniform cloud streets with an ENE alignment covering most of Germany from north of Bremen to south of Munich a distance of over 600km. The longest cloud streets ran from north of Stuttgart to east of Pilzen in the Czech Republic, a distance of over 300km.

Radiosonde soundings from the affected areas of Germany, Poland and the Czech Republic are all rather similar, and typically comprise a bottom layer of very low stability (9.5 deg/km) capped at around 2,000 m NN by very thin sharp inversion. Above that is a layer of moderate stability (5 deg/km) capped at about 3,500 m NN by another very thin inversion, above which there is a very deep layer of low stability (8 deg/km).

The forecast surface chart for 1200 UTC shows Germany covered by an extensive area of front free high pressure centred over the Black Forest with a warm front located just to the east of Denmark.

The formation of extensive lee wave trains does not require the presence of a topographical barrier. A meteorological barrier, such as a vertical density discontinuity in combination with a warm front crossing it, can be more effective in generating lee waves marked by uniform cloud streets that cover a very large area.

Keywords**:** *lee waves,* cloud streets, convective wave clouds, centrifugal waves, coastal alignment, warm front

Fig. 1

Introduction

In the afternoon of 14th April 2015, between 4 and 5 pm, a spectacular set of cloud streets having the form of cumulus wave bars with (foehn) fingers (Fig. 1) was observed above Haag an der Amper, which is located 40km NNW of Munich. They stretched as far as the eye could see in all directions and they were stationary. The surface wind had a northerly component.

One of a series of satellite pictures (Fig. 2) for this time period, 1400 to 1500 UTC, reveals an extensive area of stationary uniform cloud streets with an ENE alignment covering most of Germany from north of Bremen to south of Munich a distance of over 600km. The longest cloud streets ran from just north of Stuttgart to slightly east of Pilzen in the Czech Republic, a distance of over 300km. The satellite picture for 1200 UTC also shows a set of rather higher wave bars with a longer wavelength over eastern Poland.

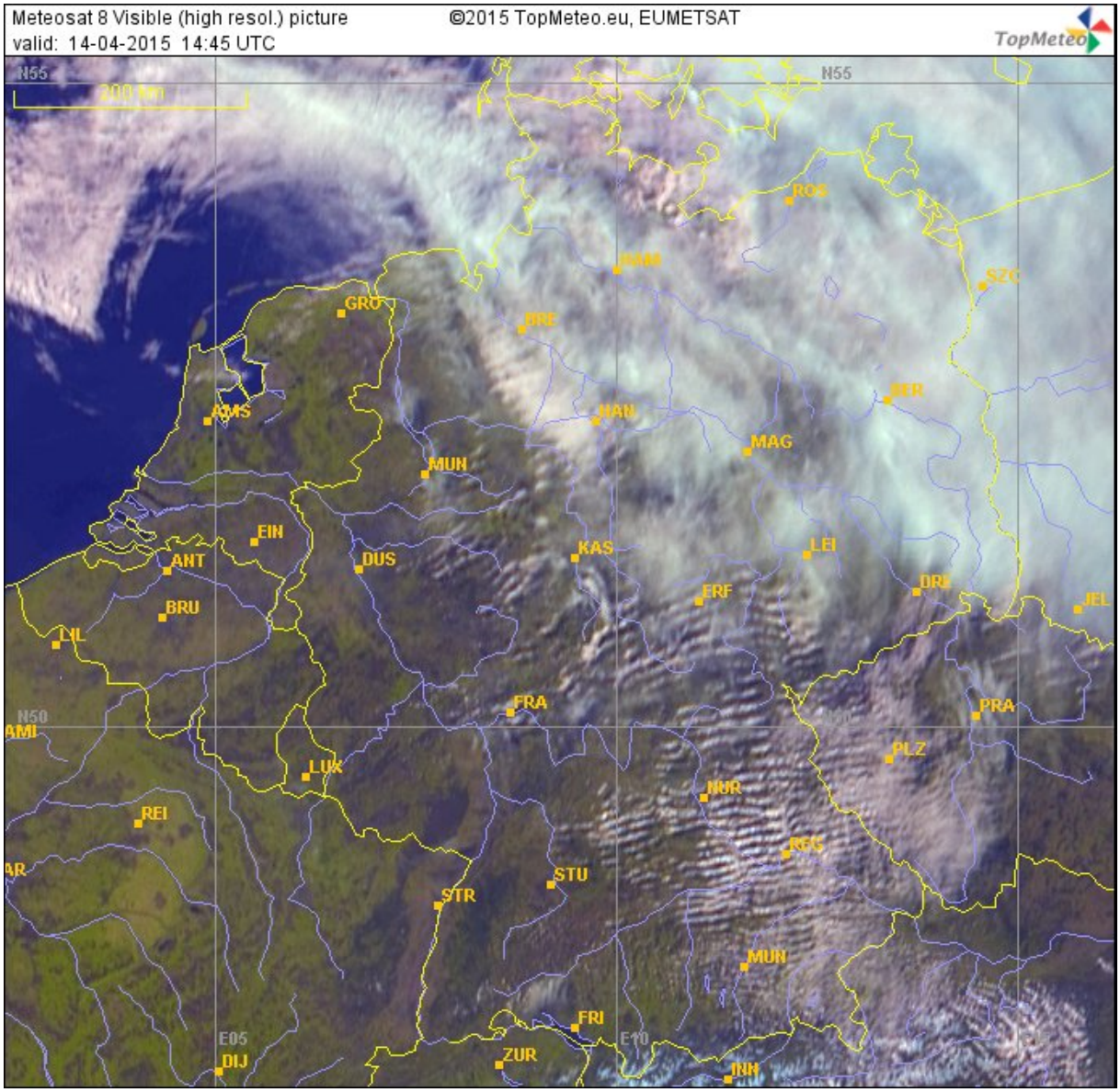

Fig. 2

The forecast surface chart for 1200 UTC (Fig. 3) shows Germany covered by an extensive area of front free high pressure centred over the Black Forest with a warm front located just to the east of Denmark. The COSMO vertical wind forecasting model for 1900 UTC does not show any up- or down-draft alignments corresponding with these cloud streets. Unfortunately, for this day no record of any sailplane flights exploiting the cross-country potential of these cloud streets has been found.

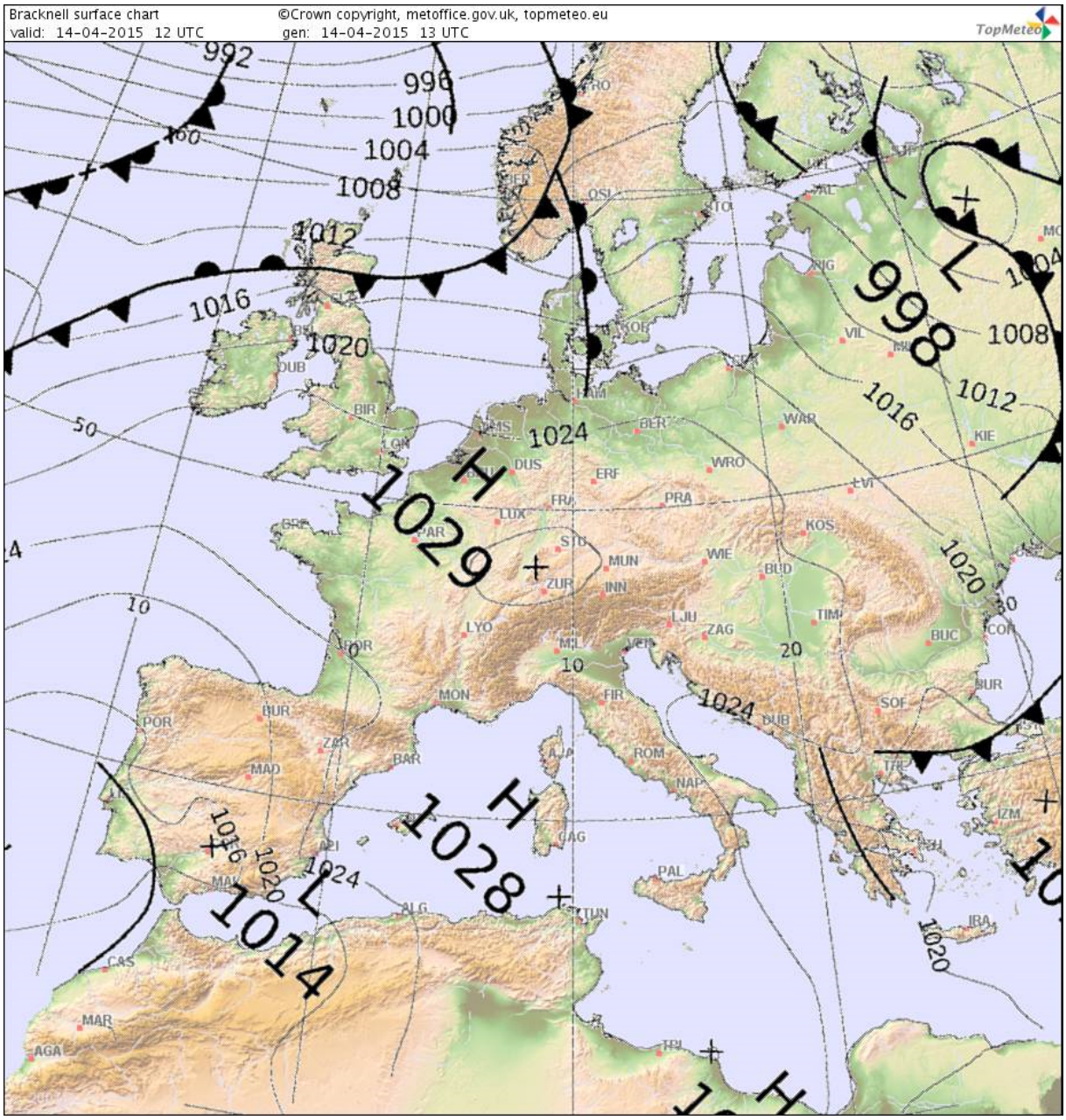

Fig. 3

Data Analysis

Radiosonde soundings from the affected areas of Germany, Poland and the Czech Republic have been collected and are described in some detail. They are all rather similar, typically comprising a bottom layer with extremely low stability (9.5 deg/km) capped at around 2,000 m NN by very thin inversion. Above that is a layer with significant stability (5 deg/km) capped at about 3,500 m NN by another very thin inversion, above which there is a very deep layer with low stability (8 deg/km). A more detailed description of the sounding nearest to the clouds of the photographs taken by the author is given below.

The 1200 UTC radiosonde sounding for Kuemmersbruck (Amberg) in Bavaria displays an initially dry adiabatic ELR up to 1,250m NN followed by a wet adiabatic ELR up to 1,900 m NN topped by a thin 30 m inversion, above which is a stable ELR topped by second thin 50 m inversion at around 2,300m NN, with a 250 m deep isothermal layer above that. At 3,800 m NN there was a third 100 m thick inversion. At the surface there was an 8 knot westerly airflow which then gradually increased and veered to a north westerly flow at 2,300 m NN, above which the wind speed (30 +/- 3 kts) and direction (324 +/- 12 deg) remained sensibly constant right up to 6,400 m NN. The spacing between the cloud streets in this central area indicates a wavelength of about 11 km, almost twice that expected for lee waves from the rule of thumb, Lambda = (0.6 U m/s – 3) km. From the above data, a rough estimate for the maximum vertical wind component of the airflow gives a value of 3.5 m/s. The relative humidity peaked at 2,300 m NN (82%), and was very low immediately above that.

Lee Wave Theory

In a three layer model the wavelength increases with a decrease in the thickness of the lower and the middle layers, being more sensitive to changes in the middle layer, and the wavelength also increases with a decrease in the value of l2 in every layer, being most sensitive to its value in the upper layer, Zang, Zhang & Huang (2007). As the value of the Scorer parameter in the uppermost layer is very low, the waves are trapped and have a longer than expected wavelength. A concise summary of linear and non-linear lee wave theory is to be found in Durran (2003).

Convective Wave Clouds

The low static stability at cloud formation level results in wave clouds having a convective cumulus form rather than a stable smooth appearance, and the criteria for this difference are discussed.

Centrifugal Waves

The formation of cloud fingers, which may extending into the gaps between wave bars, by laterally propagating centrifugal waves is also favoured by low static stability in the lowermost layer, and the conditions required for these are explained by Scorer (1967).

Thin inversions

The small depth of the lower inversion could be responsible for the downwind extent of these wave bars. According to Cruette (1976), the horizontal extent of lee waves downwind of a topographical barrier is inversely proportional to the thickness of the stable layer, and suggests that the stable layer traps the energy of the perturbation acting as a “wave guide”.

Wave reinforcement by convection

Convective clouds do not normally form a significant barrier to airflow unless they contain thermals, Hauf & Clark (2007), but in this case the internal convection might be sufficiently vigorous for them to act as a perfectly placed series of sinusoidal barriers.

Coastal Alignment

As their orientation appears to correspond that of the coasts of the North and Baltic Seas, their origin might be due to the passage of a warm front from east to west during the previous 12 hours creating a perturbation in the upper air that was parallel to the coast . A possible mechanism for this could be the development overnight of a density discontinuity between the land and sea air. The buoyancy of the warmer air rising at the front would differ on the land and sea air sides of the discontinuity creating a vertical kink in the warmer air running parallel to the coastline. The upper air, flowing more or less at right angles to the line of this kink, would then be perturbed by flowing over a virtual escarpment at the same level, thereby setting off a train of lee waves having the same alignment as the coast. The warm front would also have the effect of increasing humidity at the level of the perturbation, thereby facilitating cloud formation in the wave crests.

Conclusion

The formation of extensive lee wave trains does not require the presence of a topographical barrier. A meteorological barrier, such as a vertical density discontinuity in combination with a warm front crossing it , can be more effective in generating a very large area of lee waves that are marked by uniform cloud streets.

References

Cruette D. “Experimental study of mountain lee waves ..” Tellus 28, pp 499-523
Durran D.R. “Lee Waves and Mountain Waves” Elsevier Science Ltd. (2003)
Hauf & Clark “Convective Waves and Cumulus Growth,”XXth OSTIV (1987)
Scorer R.S. “Clouds of the World” David & Charles (1972)
Zang Z., Zhang M. & Huang H. “Influence of the Scorer parameter profile on the wavelength of trapped lee waves” Journal of Hydrodynamics, Ser. B, Vol, 19, Issue 2, April 2007, pp. 165-172

Ongoing Developments in Mountain Wave Forecasting at the Hungarian Meteorological Service

Peter Salavec
Hungarian Meteorological Service, Department of Forecasting, Unit of Aviation Meteorology, 1. Kitaibel Pál st. Budapest, Hungary, H-1024, salavec.p@met.hu

Abstract: The website *aviation.met.hu* is on which all the products of the Unit of Aviation Meteorology of the Hungarian Meteorological Service are available. Among these, model forecast outputs from the AROME mesoscale meteorological model are presented for the different branches of flight traffic, including mountain wave gliding. For them, however, only a wind time-height section is presented for four sport airfields, and a surface precipitation and wind gust map. As mountain wave formation is determined by more complex features, this information is less useful, it is thus important to improve mountain wave forecasts by new products which is planned to finish this year. This paper presents design plans of the planned products through a case study. Further plan is theoretical and technical work for forecasting mountain wave turbulence.
Keywords: mountain wave, Scorer-parameter, wave forecasting, wave turbulence

Introduction

In the Hungarian airspace, low level flight traffic is mainly in the lower 3 km where ultralight planes, sailplanes, gliders, para-gliders, hang-gliders, balloons etc. operate. As mountain waves develop several times in the airspace of Carpathian Basin, pilots may like to know the conditions for mountain wave forming because they can use mountain waves for soaring and accompanying secondary turbulent flows, especially when they don't have a visual appearance (mountain wave CAT), are dangerous.

At the Unit of Aviation Meteorology in the Hungarian Meteorological Service, some products are created routinely to help low level flight operations. Mountain wave forecasting, however, is a poorly covered field. Until the spring of 2010, a mountain wave forecast existed (Fövényi, 1997) containing a description of the synoptic situation including statements on possibility of mountain wave development, preferable areas, sometimes the risk of severe turbulence (rotors, etc.) for the next 36 hours and a short outlook for the next 4–5 days.

On 1st November 2016, a web page http://aviation.met.hu has started where aviation meteorological bulletins (METARs, TAFs, GAMET, SIGMETs, AIRMETs), measurement data (QNH, visibility, cloud base, 2 m temperature and dew point, actual weather, relative humidity, wind/gusts, rain radar), a regional area forecast for VFR flights (textual description and graphical map of hazardous phenomena), low level significant weather chart (LLSIGWX SFC/FL100 for 6, 12 and 18 UTC), and some AROME model outputs are provided.

Model outputs contain wind/gust and temperature forecast maps for several heights in the lower 3 km, the predicted height of 0 °C, thermal conditions (average and maximum lifting, thermal top, CCL, LCL, cumulus probability and amount, average lapse rates in different layers and temperature deficits for different minimum thermal heights), lability indices (SSI, K, TT), products for hot air ballooning (0–3 km wind time-height sections for several sport airfields, 10 m gust and surface precipitation maps) and mountain wave gliding (similar but wind profiles are shown for lowest 12 km, for four cities).

Because mountain waves can develop in quite restricted circumstances, these products are not suitable for their prediction. The profile of Scorer-parameter is very much useful as it indicates if some modes of mountain waves are periodic or evanescent in a given height range. It also indicates if there is a layer in which some modes are trapped which causes its amplitude to increase and the upper air to also undulate. These trapped waves are often accompanied with secondary turbulent flows (rotors, wave breaking, etc.).

The AROME NWP model (Horányi, Kertész, Kullmann, & Radnóti, 2006; Szintai, Szűcs, Randriamampianina, & Kullmann, 2015) is a limited area mesoscale model with a horizontal resolution of 30" running at every 3 hours for the next 2 days. This model can describe mountain waves with a wavelength $\gtrsim$4 km. This is often not suitable for weaker wind conditions in which the mountain ranges inside the Carpathian Basin (e.g. Börzsöny, Buda mts, Sopron mts, Bakony, Mecsek etc.) produces shorter waves (with wavelength of 0.2–5 km) in the lower troposphere but it can describe the waves of the Western Carpathians and the Alps in a strong (15–40 m/s in lower troposphere) NW wind situation which have a wavelength of 2–50 km.

A research has begun in 2017 (and is in an early state yet) to provide new mountain wave forecast products. Horizontal and vertical wind, relative humidity, potential and equipotential temperature and Scorer-parameter time-height cross-sections will be provided for more places, spatial profile sections are also planned. The calculation of Scorer-parameter is not complete yet. Due to an interpolation problem, an oscillating noise arises which causes the shear term to grow unrealistically in the boundary layer. This noise has to be filtered.

A case study of 13th October 2017 is used to generate the products for testing and establishing they main design plans. On this day, strong NW wind has blown in the whole troposphere on the foreside of an anticyclone mainly before early afternoon, causing widespread mountain wave forming mainly in the Eastern Carpathian Basin due

to Western Carpathians. The test products will be presented to our users. The implementation in operative use is planned in 2018 for users and forecasters to verify their usefulness. Later, according to the feedbacks, necessary changes can be made. A future plan is to work on methods for the prediction of mountain wave turbulence.

Background

As Hungary lies in the Carpathian Basin, there is an ideal geographic environment for mountain wave development. Mountain waves can develop several times when the synoptic conditions are valuable. However, the waves often cannot be used because other features of the weather (e.g. thick cloudiness, severe turbulence etc.) make it dangerous and thus impossible.

As the wind speed is generally not strong because of the climate, mountain wave formation happens not so often in the Carpathian Basin. In some synoptic situations, however, they are more common. Mostly in a situation when strong NW wind regime sets up, the chance of mountain wave formation increases well. In these cases, mountain waves can form in the lee of the Western Carpathians and/or the Alps. Moreover, profiles of the temperature gradient and the wind can create ideal conditions for mountain wave formation in the lee of the mountain ranges inside the Carpathian Basin for which weaker winds can be enough. In the former case, mountain waves usually occupy the whole troposphere vertically and extend over a larger area horizontally (sometimes the whole Carpathian Basin). Their wavelength is longer than the latter which is restricted to be in a thinner layer of a strong inversion. As the wind speed is generally not strong because of the climate, mountain wave formation happens not so often in the Carpathian Basin. In some synoptic situations, however, they are more common. Mostly in a situation when strong NW wind regime sets up, the chance of mountain wave formation increases well. In these cases, mountain waves can form in the lee of the Western Carpathians and/or the Alps. Moreover, profiles of the temperature gradient and the wind can create ideal conditions for mountain wave formation in the lee of the mountain ranges inside the Carpathian Basin for which weaker winds can be enough. In the former case, mountain waves usually occupy the whole troposphere vertically and extend over a larger area horizontally (sometimes the whole Carpathian Basin). Their wavelength is longer than the latter which is restricted to be in a thinner layer of a strong inversion.

As the wind speed is generally not strong because of the climate, mountain wave formation happens not so often in the Carpathian Basin. In some synoptic situations, however, they are more common. Mostly in a situation when strong NW wind regime sets up, the probability of mountain wave formation increases. In these cases, mountain waves can form in the lee of the Western Carpathians and/or the Alps. Moreover, profiles of the temperature gradient and the wind can create ideal conditions for mountain wave formation in the lee of the mountain ranges inside the Carpathian Basin for which weaker winds can be enough. In the former case, mountain waves usually occupy the whole troposphere vertically and extend over a larger area horizontally (sometimes the whole Carpathian Basin). Their wavelength is longer than that of the latter which is restricted to be in a thinner layer of a strong inversion.

For the pilots, probability of mountain wave development is essential information not only because it can be used for soaring but accompanying turbulent secondary phenomena are dangerous. Mountain waves are useful for long distance flights with sailplanes, as well as lifting to higher levels can be earned using mountain waves than using thermals. The streaming in the mountain waves are usually smooth but there are often secondary turbulent phenomena present.

Mountain waves can be categorized considering whether moisture causes cloud formation or not. Dry waves form in an environment dry enough not to reach saturation at the wave peak. In this case, cloud formation doesn't happen and the associated turbulence has to be considered as CAT. These are referred to as *dry mountain waves*. If the moisture is enough for cloud formation at the wave peaks, the type of stability gives us another two types of mountain waves. In an absolute stable environment, waves named *moist reversible mountain waves* and Ac len clouds will form. If the air is moist unstable, deep convection can set up and Cb cloud will develop over the mountain, this is the so called *moist irreversible mountain wave*. This also destroys the waves in the lee side, so it is not even a wave in the common sense. As moisture is not constant with height, there can form even mixed type waves the type of which can be different at different heights. Examples for these are the multi-layered lenticular clouds of the pileus over a cumulus. In the most cases, streaming suitable for wave forming is on such a synoptic situation in which thick cloudiness also forms making flights impossible.

As mountain waves are a type of inner gravity waves, they can also be categorized by a feature called trapping. Essentially, the equations describing the mountain waves contains a parameter ℓ^2 (Scorer, 1949) which can be represented as the group velocity length of the mountain waves. Waves form with all horizontal wavelengths but the components of which it is greater than the Scorer-parameter will be evanescent vertically. Because the Scorer-parameter depends on height, there can be layers in which a particular wave is periodic in vertical while in others not. In the latter, the group velocity is horizontal, i.e. their energy doesn't radiate vertically. This means that the boundary between such two layers behaves as a mirror: a wave which is periodic in the one layer will be reflected back on this boundary and thus trapped in that layer. Reflection happens formally infinitely many times enhancing the amplitude. From these trapped waves, the depth of the trapper layer selects some particular waves by quantization. These waves will constitute those which will be the most useful for soaring.

Developments in wave forecasting

At the Hungarian Meteorological Service, a mountain wave forecast was issued daily until 11th March 2010. This contained a description of synoptic situation for the next 36 hours including statements on possibility of mountain wave development and a short outlook for the next 4–5 days. Tables for Budapest, Pécs, Miskolc and Szombathely were also attached with wind, temperature, lapse rate and Scorer-parameter profiles for the lower 8 km.

6.5 years of pause followed until the new aviation meteorology website https://aviation.met.hu started. The AROME model outputs published on this site contain useful information mostly for low level flight traffic. For mountain wave gliding, however, the only output is a wind time-height cross-section for Dunakeszi, Kőszeg, Pécs and Pipishegy. In some circumstances, the possibility of mountain wave forming can be estimated but wind profile is not the main determining factor. Thus, we decided to create new products to give the glider pilots more useful information for mountain wave gliding.

Time-height cross sections are planned for several places in the Carpathian Basin, not only in the lee of the mountain ranges inside as better waves can form on the Carpathians and the Alps and can extend horizontally over larger areas. Spatial cross-sections are also planned from the Alps and the Western Carpathians to the E, SE and S directions according to the common wind regimes, intersecting other mountain ranges inside the Carpathian Basin. On these products, forecasts of more parameters are planned to show. Some wind profiles are more favorable for mountain wave forming despite that wind profile is not the primary determining factor. The duration in both time and space of these conditions can be checked on the time-height and the spatial cross sections respectively. However, the wind direction relative to the mountain range also determines the probability of wave forming because wind direction perpendicular to mountain range helps mountain waves more to develop. Another spatial cross-section thus will show the wind component magnitude parallel to the section. Another important information is the relative humidity which can be an indicator of the cloudiness. Users can estimate the probability of a cloud cover making wave gliding impossible. Potential and equipotential temperature is for estimating stability and determining its type. This helps to identify the type of the waves at different heights. Time-height and space-height cross-sections of these parameters will be created as well, being useful for checking that for how much time and how far away the favorable conditions will help mountain waves to develop. Given from its horizontal resolution, the dynamics of the model can describe mountain waves with a wavelength $\gtrsim$4 km. This makes a spatial cross-section showing the vertical velocity useful, as the waves on their own can be seen on it. However, this parameter contains higher relative uncertainty as the vertical velocity can be susceptible to little changes of the determining factors (stability, waving layer depth, etc.).

According to the theory of mountain waves (Scorer, 1949), the most useful information is contained in the Scorer-parameter profile. Higher values of it can reveal if some layers in the atmosphere are trappers, i.e. behave like a wave tunnel, in which the amplitude of some wave modes enhance. The height until which the wave amplitude doesn't decrease much over the trapper layer can also be estimated. The Scorer-parameter was not calculated from the AROME model until recently. A collaboration between the units of Aviation Meteorology and Methodology Development in the HMS is in progress for this aim.

Case study and further plans

On 13th October 2017, widespread mountain wave formation happened over the E, SE parts of Hungary and the Carpathian Basin. Satellite imagery revealed long wavelength pattern on mid and high level clouds in late morning. We decided to check the AROME output and, using our HAWK-3 visualization system (Bozó, 2011), we generated a space-height cross-section of vertical velocity and relative humidity from Orava Magura ('Árvai-Magura') mountain range towards the NE part of Great Plain, intersecting also the Lower Tatras ('Alacsony-Tátra') and Bükk mountain ranges. Around local noon (11 UTC), the vertical velocity field showed impressive waving in the troposphere in the AROME model output (init: 6 UTC). Even the relative humidity followed this pattern as local maxima appeared after the wave updrafts, i.e. the maxima were on the peaks (**Figure 10.**). A short newsletter was written on the website of the HMS (Salavec, 2017).

As the development of the new products for mountain wave gliding began, we decided to use this case study for creating the products which resulted in design plans. These will be presented through a detailed description of this case in the full article. We plan the products to be operative in the autumn or winter this year. The next step will be the work on getting the communication between the Unit and the pilots active. Frequent feedbacks are needed to help us improve our new products in a way which makes them more useful for the pilots. A plan for the more distant future is to model mountain wave turbulence which needs improvements in the theory as well as the numerical models.

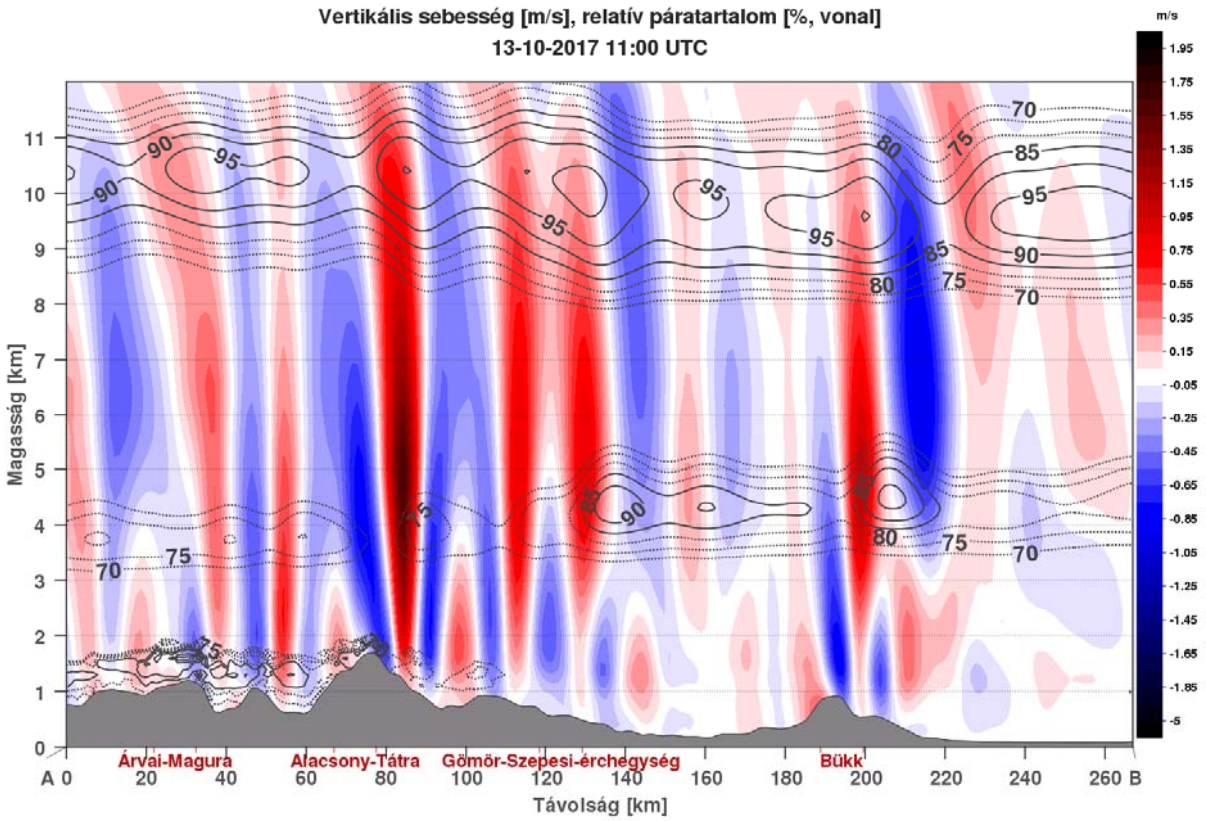

Figure 10. Vertical velocity (shade, red=upstream) and relative humidity (line) on 13th October 2017, at 11 UTC from the AROME NWP model (init: 06 UTC).

References

Bozó, L. (2011). Hungarian National Report on IAMAS 2007-2010: Activities at the Hungarian Meteorological Service. *Acta Geodaetica et Geophysica Hungarica, 79*(2), 215-231. doi:10.1556/AGeod.46.2011.2.5

Fövényi, A. (1997). Making forecasts for sport aviation using ALADIN data. *RC LACE Bulletin, 3*, 5.

Horányi, A., Kertész, S., Kullmann, L., & Radnóti, G. (2006). The ARPEGE/ALADIN mesoscale numerical mdoeling. *Időjárás, Quarterly Journal of the Hungarian Meteorological Service, 110*(3-4), 203-227.

Salavec, P. (2017). *Hullámképződés a Kárpát-medencében október 13-án.* Retrieved from http://www.met.hu/ismeret-tar/meteorologiai_hirek/index.php?id=2221&m=2

Scorer, R. S. (1949). Theory of waves in the lee of mountains. *Quarterly Journal of the Royal Meteorological Society, 75*(323), 41-56. doi:10.1002/qj.49707532308

Szintai, B., Szűcs, M., Randriamampianina, R., & Kullmann, L. (2015). Application of the AROME non-hydrostatic model at the Hungarian Meteorological Service: physical parameterizations and ensemble forecasting. *Időjárás, Quarterly Journal of the Hungarian Meteorological Service, 119*(2), 241-265.

On the way to glide ratio 100:1

L.M.M. Boermans
Delft University of Technology, Faculty of Aerospace Engineering, The Netherlands
l.m.m.boermans@tudelft.nl

Abstract: The lecture consists of 3 parts:
1. development of the Concordia, the best sailplane in the world,
2. development of sailplane airfoils with flaps since 1962,
3. development of boundary layer suction.

Keywords: sailplane design, sailplane airfoil design, boundary layers, transition, boundary layer suction.

Introduction

The description of the Concordia, the best sailplane in the world, gives an idea of the present status of sailplane development. The description of airfoil development over the last 55 years shows that further drag reduction by conventional means is hampered by physical limits and that unorthodox measures are necessary in order to improve performance. The most promising of such measures is boundary layer suction. This technology is not new, but large use of it has stayed away mainly due to lack of a suitable porous material. With new production technologies as making holes in a carbon fiber laminate with a strong laser, the application of boundary layer suction has a good chance.

Development of the Concordia

The design of the Concordia was the master thesis work of Johannes Dillinger, supervised by Loek Boermans (aerodynamics, TU Delft, Faculty of Aerospace Engineering) and Gerhard Waibel (structures, Alexander Schleicher Segelflugzeugbau). The project was initiated and financed by Dick Butler. The main design parameters were determined by Waibel and Butler: span 28m, mass 550kg - 850kg (prescribed) and wing area 13.7m², which give a wide wing loading range of 40–62kg/m² and very high aspect ratio of 57.4.

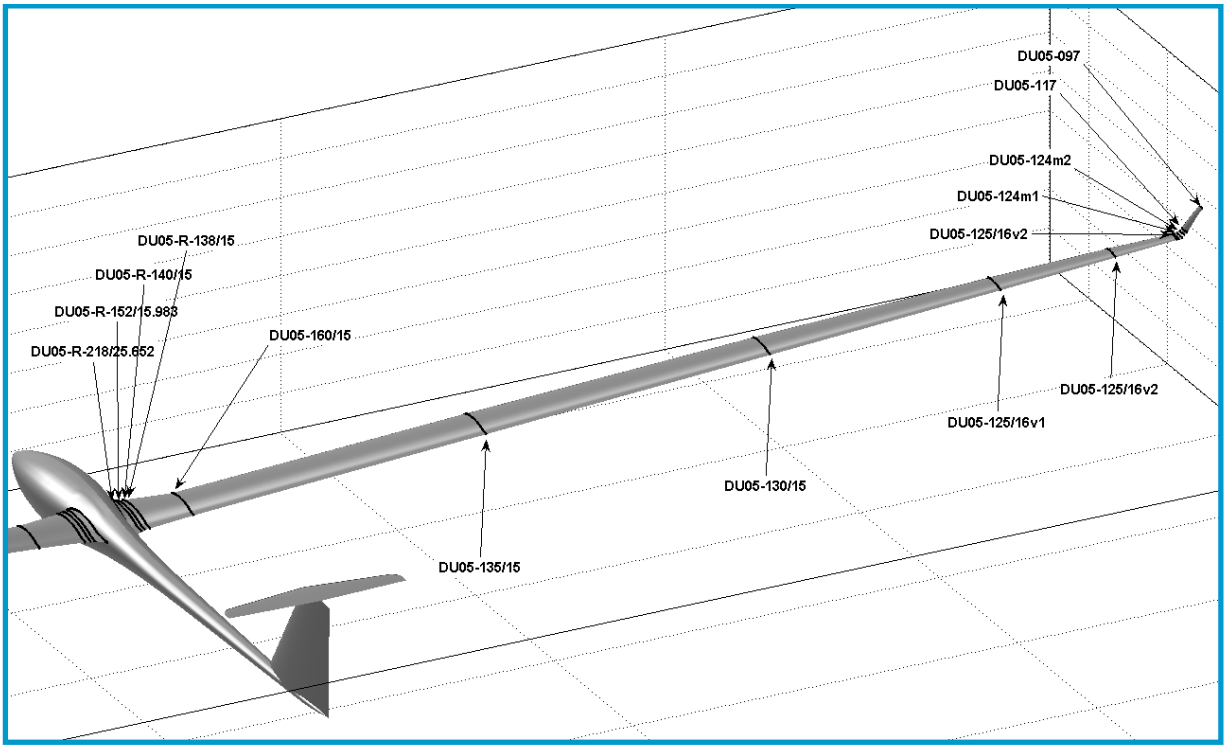

Figure 1. Airfoil sections and positions in the Concordia wing

The wing planform with winglets and wing-fuselage junction has been optimized for minimum induced drag according to Munk's 3rd theorem, and fourteen airfoils (of the DU89 type, see next chapter) were optimized for low drag considering the local Reynolds numbers. The forward part of the fuselage with wing connection pins is equal to the ASW-27. The chord of the wing root was enlarged and twist was applied in the widened section next

to the fuselage in order to fit the wing to the pins at the right angle of incidence. For compensation the flap was twisted as well to realize the proper lift distribution. The airfoils in the junction region were designed to cope with the local turbulent flow. The tailboom has been fitted to the streamlines at 200km/h, the vertical tailplane has been adjusted to the large span, and the horizontal tailplane is equal to the ASW-27.
Structurally, special carbon fiber material has been applied in the wing. Using software suitable for aero-elastic tailoring, the position of the spar and orientation of the fibers in the skin of the sandwich structure have been determined such that no wing twist occurs at 200km/h, thus guaranteeing minimum profile drag. At low speed a linear twist to 0.5° at the wing tip is present.
All in all, at wing loading of 62kg/m² , a best glide ratio of 76:1 is calculated at 135km/h, and the sink rate is just 1m/s at 200km/h.
It took Johannes Dillinger about 3 years to do the design work for the Concordia; he received his master thesis with epitheton Cum Laude and was honored as the best student of the Faculty of Aerospace Engineering in 2006.
It took Dick Butler, assisted by Hans-Jorg and Christian Streifeneder, several years to build this best sailplane in the world; the first flight was in 2012.

Development of sailplane airfoils with flaps since 1962

Key factors for low profile drag are a small thickness (low pressure drag) and large laminar flow extents on both sides (low friction drag). However, key factor for a wide low drag bucket is a large thickness.
Two typical well-known airfoils with flaps of the previous generation are FX62-K-131 (applied in ASW-12, ASW-17, ASW20) and FX67-K-150 (Nimbus, Janus, LS-3, DG-200, DG-400) designed by F.X. Wortmann. Both airfoils are smooth at zero flap deflection and have kinks in the upper- and lower surface at other flap deflections. The FX67 type of airfoil turned out to be very sensitive for rain and bugs, and their typical pressure distributions were not further developed.
The FX62 airfoil had 75% laminar flow on upper surface and 70% on the lower surface and was further developed into HQ17 (ASW-22, ASH-25) by K.H. Horstmann and A. Quast in 1980 primarily by extending the laminar flow on the lower surface to 80% and using blowing holes as transition device.

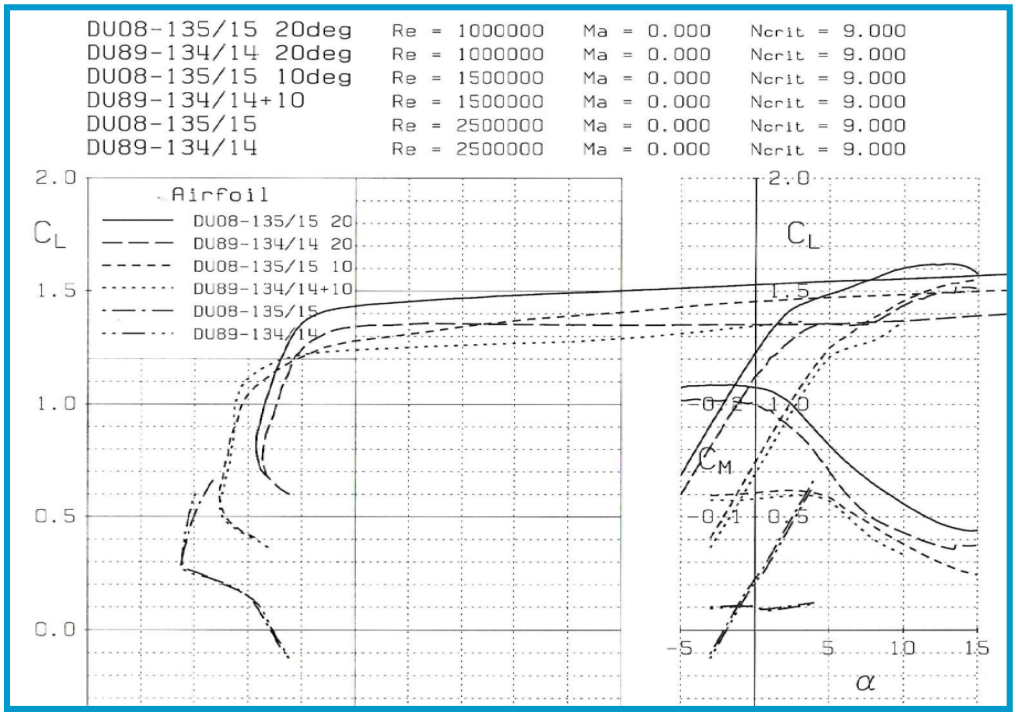

Figure 2.Comparison of calculated characteristics of DU89-134/14 and DU08-135/15

The first airfoil with flaps designed in Delft was DU89-134/14, Figure 2 (applied in the ASH-26, ASW-27, ASG-29, ASH31). The flap has been integrated in the design right from the beginning, consequently the upper and lower surface can be better squeezed out and are smooth at different flap deflections. The upper surface has laminar flow up to 75% and the lower surface up to 95% (on the flap) where blowing holes acts as turbulator. A similar but thinner airfoil with zigzag tape turbulator on the flap lower surface is DU97-127/15M (Antares) and a variant with a turbulator on the lower surface just in front of the flap has been used in the DG-800 and Ventus-2. All these airfoils have as design criterion a step in the lift curve at the flap deflection for climbing; this was considered the be a limit because a dip in the lift curve appeared to cause bad handling characteristics in thermals.

An extensive study revealed, however, that a positive gradient instead of a step improves the climb performance in turbulent thermals. DU08-130/15 is such an airfoil, see Figure 2. Secondary effect of this design is a lower sensitivity for rain and bugs. This type of airfoil has been applied successfully in the Diana 2 (designed by K. Kubrynski), ASH-30, ASG-32, EB-29R and Nimeta, and will be applied in the Nixus.
The final conclusion of this chapter on airfoil development is that further drag reduction by extending the laminar flow on the upper or lower surface is hampered by the physical limit of early separation. Boundary layer suction is a very beckoning perspective for further drag reduction.

Development of boundary layer suction

The goal of boundary layer suction is to lower the drag by keeping the flow laminar and attached and/or to increase the lift by keeping the turbulent flow attached. The first option is preferable in many cases. The latter option requires much more power than the first one.
Figure 3 shows the drag contributions of an airfoil with boundary layer suction.

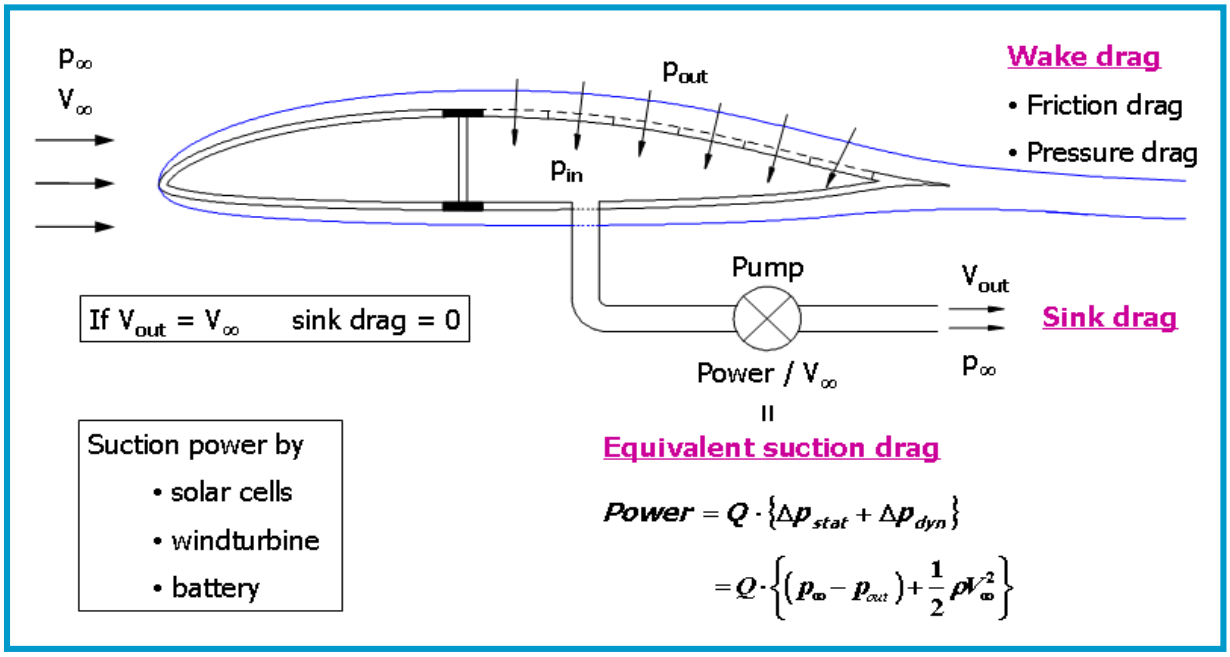

Figure 3. Drag contributions of an airfoil with boundary layer suction

The friction and pressure drag of the airfoil is found in the continuation of the boundary layers i.e. the wake. The momentum loss of the air sucked through the porous surface and brought to standstill in the wing, called sink drag, can be nullified by blowing this air out backwards with flight speed. The equivalent suction drag implies the power required to bring the suction air back from internal pressure to ambient pressure and from zero internal velocity to flight speed.
The well-known code XFOIL has been extended for the design of airfoils with boundary layer suction. With this code an airfoil has been designed where suction is applied between 35% and 90% chord on the upper surface followed by artificial transition by zigzag tape at 90% chord. Artificial transition on the lower surface is at 80% chord. For the design of the 6mm thick suction sandwich on top of the structural sandwich another code has been developed: DUXS. Figures 4 and 5 illustrate that the suction sandwich consists of a carbon fiber top layer with many tiny holes of about 0.1mm diameter every 1mm, glued on a folded core (named foldcore, developed at the TU Stuttgart, Institut für Flugzeugbau) with holes of diameter varying between 1 and 4mm. All holes can be made by specific laser equipment. The suction air goes through the tiny holes, then forward through the holes in the foldcore and finally through throttling holes to the inner room of the wing. The chordwise suction distribution is controlled by the low pressure inside the airfoil, produced by a pump, and the varying diameter of the holes in the foldcore.

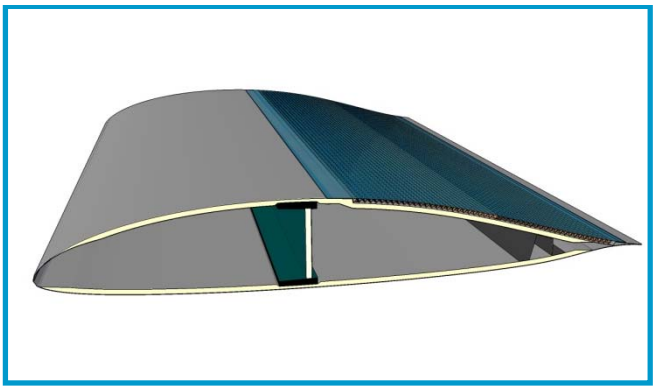

Figure 4. Airfoil with boundary layer suction

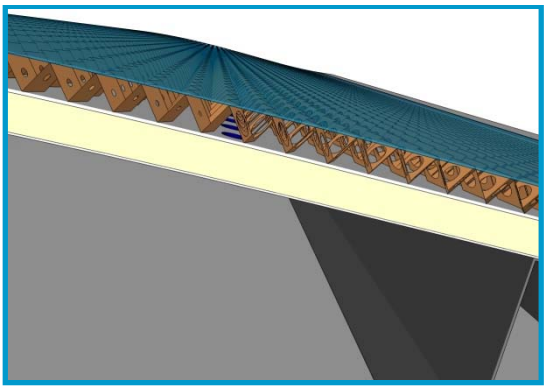

Figure 5. Suction sandwich structure

Suction reduces the profile drag by 50% at high speed to 70% at low speed, figure 6. In case of turbulent flow (due to rain or bugs) the drag is about twice the drag without suction, as usual.
The minimum sink rate of a Standard Class glider provided with this airfoil would be reduced by 20%, the sink rate at high speed would be reduced by 30%, and the best glide ratio would be improved by 35%, figure 7.
The suction power required is between 150W at low speed and 300W at high speed.

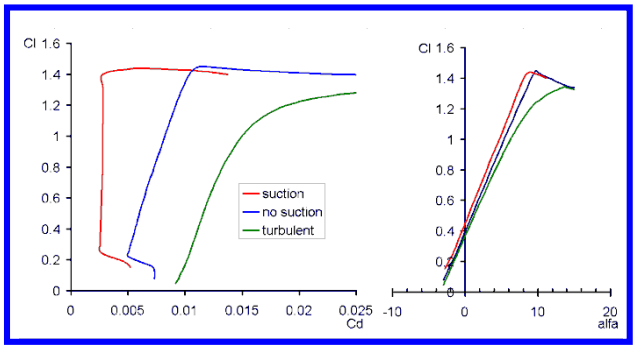

Figure 6. Characteristics with/without suction

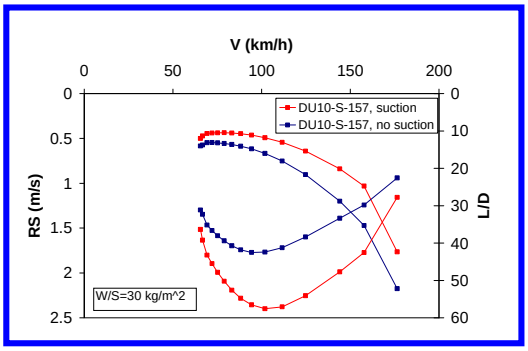

Figure 7. Speedploar with/without suction

For validation of the computer codes and verification of the performance, a wind tunnel model of this airfoil is being built at Glasfaser Flugzeug-Service (H. Streifeneder) at the moment, and calculations are performed with sophisticated CFD codes.

Conclusions

- Improvements in aerodynamic and structural design of the Concordia have been described.
- Improvement of airfoil performance over the last 55 years has been described. Further improvement is hindered by the physical limitation of early separation.
- Boundary layer suction for laminarization is a very beckoning perspective for further drag reduction.
- If the improvement in glide ratio of 35% shown for the Standard Class glider can be realized with boundary layer suction at an Open Class glider like the Concordia, the glide ratio of 100:1 comes into sight.

An Ultra-Long Endurance Solar-Powered Unmanned Airplane

Bill Bissonnette[1], Travis Krebs[1], Michael Melville[1], Götz Bramesfeld
[1]*Ryerson Unviersity, Department of Aerospace Engineering, Toronto, Canada, michael.melville@ryerson.ca*

Abstract: The goal of the Clean Renewable Energy Aerial Test Vehicle (CREATeV) project is to create a solar-powered ultra-long endurance unmanned aerial vehicle, for the purpose of setting an endurance world record. The current world record is 336 hours, 22 minutes and 8 seconds. The CREATeV test vehicle is a comparatively small aircraft, at approximately 12 kg and a 6m wingspan. Designing and building the aircraft is a unique challenge which spans several disciplines that all equally vital in order to achieve the record.

***Keywords*:** Long endurance, Unmanned Aerial Vehicle, solar power.

Meteorology and Flight Location

As CREATeV is solar-powered, finding a suitable flight location is of principal importance in the early stages of design, as the available solar energy will drive the aircraft sizing. To determine optimal locations, land regions in Canada and the USA were examined in a 0.5x0.5 degree grid using NASA MERRA satellite data. An important metric is the mean daily global insolation (kWh/m^2), which is a measure of the amount of solar energy to reach the ground in a day. As a reference point, direct sunlight is typically 1 kW/m^2. Thus, a daily global insolation of 5 kWh/m^2 would be equivalent to 5 hours of direct sunlight in a day. In reality, the amount of solar irradiance reaching the ground is distributed unevenly throughout the day, with the most intense energy arriving with the sun at its apex. Cloud cover will also affect solar irradiance and insolation.

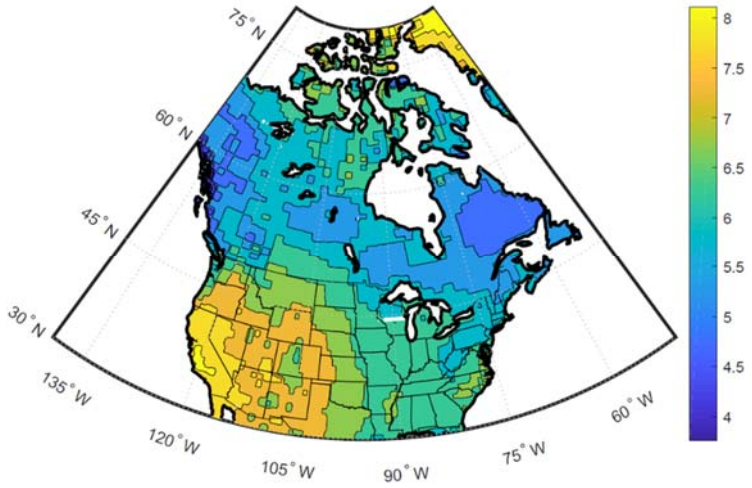

Figure 11. Daily insolation across North America, averaged over the summer months. Scale is kWh/m^2.

Figure 1 shows the daily insolation across Canada and the USA, averaged over the months of June and July from 2008 through 2016. The insolation changes drastically, due mostly to local weather patterns. Ideal locations with daily insolation levels of 8 kWh/m^2 are isolated to the high arctic in Greenland, and the Central Valley in California. These two locations have effective, though different, combinations of daylight hour length and predictably thin cloud cover in the summer months. Other countries were looked at, and flight locations around the world with ideal solar insolation include Perth, Australia and the Atacama Desert in Chile, both in the months of December and January. For logistical reasons, California was chosen as the primary flight location, with Perth chosen as an off-season backup location.

Powertrain Testing

Estimating and predicting the power consumption of the aircraft is essential in determining the probability of success of a record flight. The largest power draw is the powertrain, which includes the motor, propeller, and electronic speed controller. These three components must work together in an efficient way in order to maximize the probability of success. To gain an accurate understanding of the powertrain draw, various motor/propeller/esc combinations were analyzed in the Ryerson Large Subsonic Wind Tunnel, at the predicted flight conditions as well as off-design conditions. With the most efficient combination selected, the power draw and thrust output of the system at various RPMs and flight speeds was recorded, which was then in turn used to design the aircraft in an optimization process, using predictions on flight durations from the weather model simulations.

Structural Design

Designing the wing structure for CREATeV posed some unique challenges as the design requirements varied from those of conventional aircraft. The addition of solar cells to the upper surface of the wing required the skin to be especially stiff. Significant amounts of bend/twist coupling would prove to be detrimental to the cells since their range of acceptable deformation is minimal, thus maximizing torsional stiffness was crucial. Additionally, the main wing spar needed to be able to support the wing loading with minimal deformation; while internal components placed within the wing helps to alleviate some of the loading, making a spar that is both adequately stiff and light is a challenge.

A combination of both fibreglass and carbon fibre was selected to manufacture the wing using a female mold; the carbon fibre provides excellent structural properties with small weight penalties. A lightweight fibreglass cloth was used to both insulate the solar cells on the upper surface of the wing as well as provide a lightweight lower surface. Lightweight core materials were used in both the spar and wing skin to provide a greater area moment of inertia, thus increasing the stiffness of each section.

Avionics & Flight Controls

Critical to the success of long-endurance missions is a reliable and robust avionics suite. The CREATeV test vehicle uses an open source autopilot firmware running on an advanced flight controller board. These were selected due to years of experience and active development within their respective communities. The selected firmware allows for extensive real-time telemetry as well as on-board data logging for post-flight analysis. CREATeV's flight controller board includes many failsafe features, redundant power sources and redundant sensor options.

The autopilot can be operated within both Software-in-the-Loop (SITL) and Hardware-in-the-Loop (HIL) simulations. This allows for the autopilot and its subsystems to be thoroughly tested through various levels before being installed on a flight test vehicle. Having HIL simulation capabilities also enables the avionics and charging system to be physically endurance/stress tested before attempting a long-endurance flight with a flight test vehicle.

Efficient and robust control surface actuators are also necessary for long endurance missions. Several servo motors have been analyzed to determine their power draw as a function of torque generated. This, in combination with the results of a multi-week endurance test under predicted flight loads, allowed for the selection of an optimum servo motor to drive the control surfaces.

Power System and Solar Charging

Mounting solar cells to the upper surface of CREATeV's wing presents unique challenges. A few of the challenges include: ensuring the cells remain fixed in place and do not exceeding bending limits, ensuring the cells stay clean in flight, and minimizing the potential efficiency losses due to any covering materials used. To solve these problems, a solar test rig is used that can simulate various loads on the solar cells and monitor their performance under varying weather conditions using different mounting methods.

Using the available energy from the solar cells to charge batteries requires a solar charge controller. With CREATeV's HIL simulation tools, the solar charge system can be thoroughly tested before being installed on a flight test vehicle. To test under various solar conditions, a programmable power supply is used to simulate the power available from a solar cell array.

Conclusions

To set a new endurance record, the CREATeV test vehicle must be extremely efficient and reliable. To achieve the efficiency targets, accurate weather and solar irradiance models, hardware testing and flight performance simulations were used in an optimization process to design the vehicle. Having a reliable design requires not only each of the subsystems to be thoroughly tested independently, but also the subsystems must be carefully and properly integrated.

Dilemma resolved: Airbrakes tamed

Michael Greiner, Galih Bangga
University of Stuttgart, Institute for Aerodynamics and Gas Dynamics, Germany, greiner@iag.uni-stuttgart.de

Abstract: Aerodynamic forces upon Schempp-Hirth airbrakes make it difficult to fulfill all certification requirements simultaneously, especially with respect to pilot's control force. A certain design of the airbrake allows to reduce the aerodynamic source of this force considerably. This also reduces the risk of self extention of unlocked airbrakes at take-off.

***Keywords*:** Sailplane design, Airbrakes, Pilot control force

Introduction

"Schempp-Hirth"-type airbrakes (Fig. 1) are state of the art for sailplanes. This type of airbrakes are efficient in controlling the glide path, because they not only create pressure drag, but also induced drag. Handling is usually considered good-natured, since the ensuing decrease of wing lift coefficient is compensated by an increase of trim speed. Available literature on the topic of these airbrakes concentrate on the effect upon lift, drag and aerodynamic moment of different 2D- and 3D-configurations [1,2,6,7,9,13,14,15].

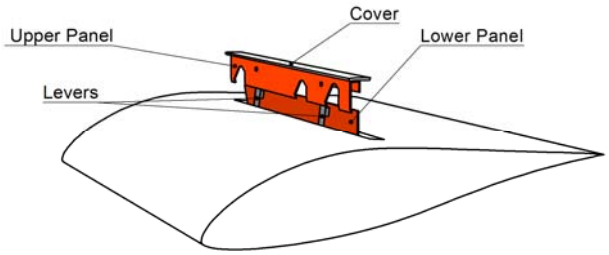

Figure 1: Components of an Schempp-Hirth airbrake

But for the designer of modern sailplanes "Schempp-Hirth"-type airbrakes have constituted a problem in a different respect. All common airworthiness codes from obsolete LFSM [11] to CS22 [5] require not only a glide slope not flatter than 1:7 during approach and certain speed limiting capabilities at high speed. It is also required, that the pilot control force does not exceed 20daN at certain speeds. With increasing wing loadings and glide ratios, this becomes increasingly difficult to fulfill simultaneously. The involved requirements have continuously been mollified since the introduction of LFSM in 1975, which proofs the ongoing existence of this dilemma. Adding to the problem is, that none of these properties can be predicted in advance with simple methods and necessary precision.

The unwanted pilot control force originates from the vertical aerodynamic force upon the airbrake, pulling the latter out of the wing. This force is also responsible for the vicious characteristic, that unlocked airbrakes extend themselves during launch, preventing the normal climb to safe altitude. To avoid this risk, additional measures have to be stacked upon the control system.

The goal of the present investigation is to strike at the root of the problem, and to reduce the aerodynamic force F_y, which acts in direction of airbrake extension. Ideas, possibly improving the situation, were proposed in [15]. In [8] it was reported for a configuration comparable to V1 of figure 3, that the control force of the airbrakes is neutral at all speeds flown at that time, and that the airbrakes would remain at their position when released during approach. It was assumed, that this is due to the slant forward airbrakes.

Methodology

The variables in the design of the airbrake are identified in figure 2. Basic considerations lead to the approximation, that the pilot control force is proportional the product of cover length, airbrake width w and maximum height h. This leads to two tasks:

1. For a required drag increase effect, make the airbrake as efficient as possible, to allow a small as possible $h \cdot w$.
2. For a given $h \cdot w$, design the airbrake in a way to reduce the aerodynamic force in direction of extension F_y.

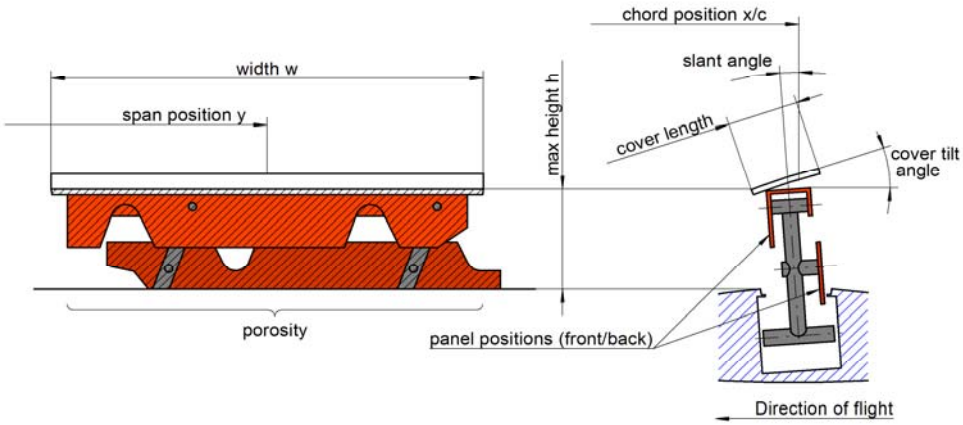

Figure 2: Degrees of freedom in the design of the airbrake. Porosity describes, how tight the airbrake is (compare hatched area with area *h·w*, and consider gap between upper and lower panel)

For the first task literature indicates advantages of a high aspect ratio *w*/*h*, a low porosity, and a slant forward [9]. A low porosity requires that all airbrake panels are installed on the same side of the levers, either in front or at the rear.

For the second task a number of parameters may be relevant. The cover length can only be reduced to a limited degree, due to structural constraints and maintenance needs. With the ASW 27 glider Gerhard Waibel introduced a cover, which turns a few degrees upon extension (cover tilt angle), but this measure is limited due to the kinematics needed for this. Therefore two parameters remain, first the position of the panels, i.e. behind or in front of the levers, and second the slant angle of the whole airbrake.

To investigate both parameters, three 2D-configurations were defined (Fig 3), which were investigated with CFD. The airbrakes of configurations V1 and V2 are slanted forward 12°. In the first, the panels are in the front, leaving only little forward protrusion of the cover. The second configuration V2 has the panels at the rear. The third configuration V3 differs from V1 in that the airbrake extends vertically.

A common configuration is the one depicted in Fig 1 and 2, with the upper panel located in front of the levers, and the lower panel(s) located behind. It has the advantage that the rear edge of the cut-out in the wing skin supports the lower panel(s). Nevertheless this configuration was not included, because it has a large porosity (reduced drag) and due to the deflections of the air flowing through, it is not very promising with respect of pilot control force.

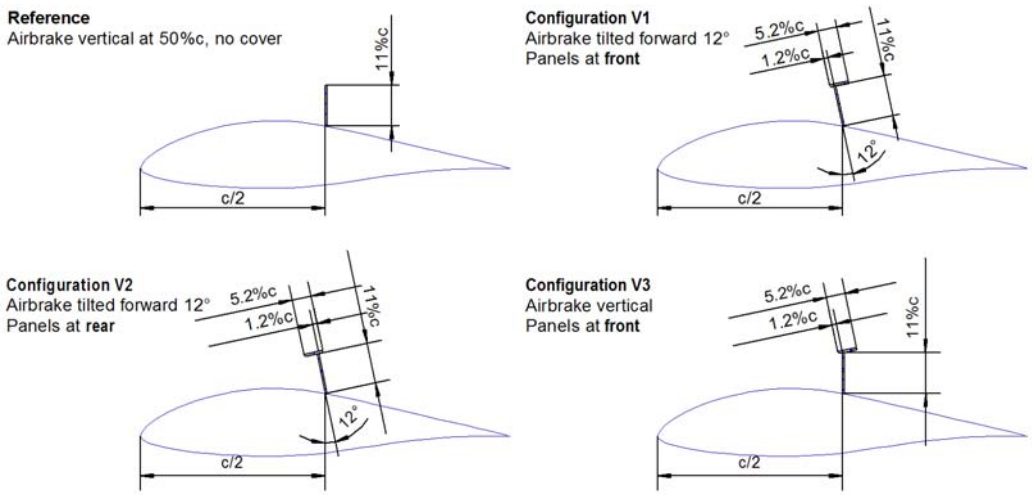

Figure 3: Configurations examined in CFD. Airfoil FX 66-17AII-182, Re=1.5e6. The reference case is comparable to measurements performed in [1] for $c_a(\alpha)$. Configurations V1 to V3 are calculated for $\alpha=0°$

The 2D simulations were carried out using the CFD code FLOWer developed by the German Aerospace Center (DLR) [10]. The code has been extended in the recent years for aircraft and wind turbine simulations at IAG [3,17]. The turbulence closure was modeled using the Shear-Stress-Transport (SST) k-ω model according to Menter [12]. The model was shown in previous studies to be able to model flow separation on airfoils and 3D rotors accurately for reasonable angle of attack operations [3,4,12]. The time dependent solution of the URANS model was

integrated using the dual-time-stepping approach, allowing a second order accuracy on smooth meshes. The hybrid 5-stages Runge-Kutta scheme was employed for this purpose. The time step size was set to be less than 0.01 of the convective time required for a fluid particle to pass the airfoil. The spatial discretization uses a central discretization approach. Convergence was accelerated by means of the multigrid level 3 scheme. The grid was generated using the software Pointwise employing a Chimera (overset) method. By doing so, high quality meshes can be built separately, simplifying the generation of the meshes significantly. The airfoil is resolved by 281 x 129 grid points on the airfoil surface and in normal direction, respectively. The boundary layer is discretized by 32 cells with the growth rate of 1.1 and a non-dimensional wall distance of $y^+ < 1$. The latter is required to resolve the boundary layer as no wall model is used. The simulations were performed on the High Performance Computing Center Stuttgart (HLRS) on the LAKI cluster employing 24 CPUs for each simulation.

Results

Figure 4 shows the pressure distribution and streamlines of the three configurations.

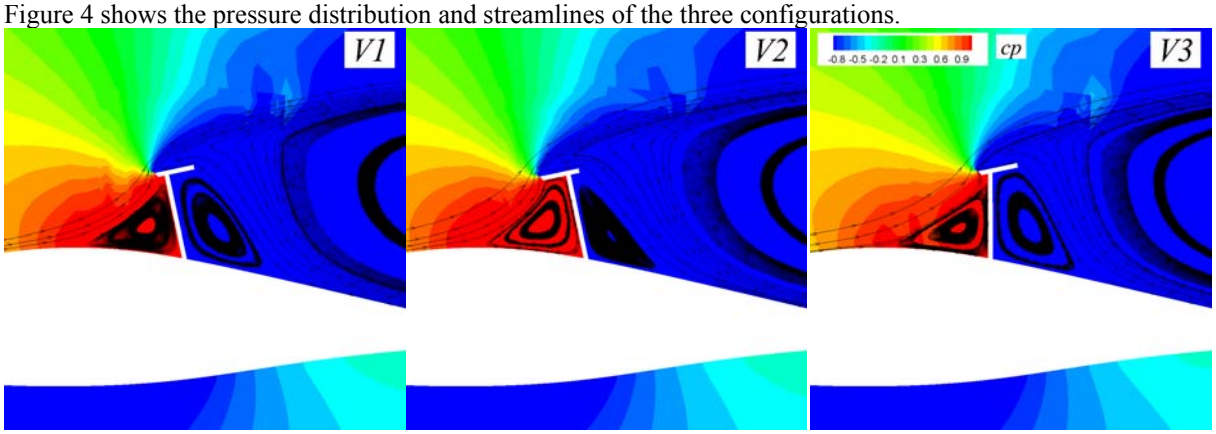

Figure 4. Pressure distributions and streamlines at Re = 1.5e6, α = 0°, h/c = 11%, x/c = 50%

The force was calculated only for the airbrake parts alone, separated in a component normal to the airbrake panel (F_x/dz) and in direction of extension (F_y/dz). The pressure and skin friction distributions were integrated for this purpose over the cover and the panel. The calculated forces are normalized by the freestream conditions as:

$$C_{x,y}=F_{x,y} / (\tfrac{1}{2} \rho_\infty V_\infty^2 c\, dz)$$

Figure 5 and 6 show C_x and C_y over time. The fluctuations result from the shedding of vortices. The values are plausible, but cannot be used for direct design purposes, because the relative cover length l/c is smaller than typical values, and on real wings additional 3D effects occur.

The position of the airbrake panels in front or behind the levers has a strong influence on the extension force F_y. With the panels installed in the front, the force F_y is reduced to the half compared to case V2. With the panels mounted on the front side, slanting the airbrake forward has indeed a favorable influence on F_y and F_x but only a small one.

For low pilot control force and high efficiency, the panels should be mounted on the front of the airbrake, and the cover should protrude as little forward as possible. The panels should be tight, to maintain the low pressure on the rear. In this configuration, slanting the airbrake forward is favorable, but less important.

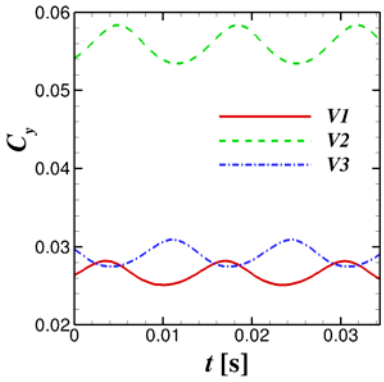

Figure 5: Force coefficient in direction of extension

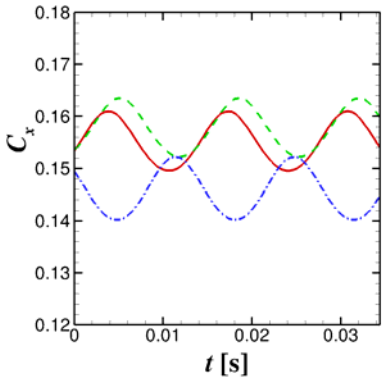

Figure 6: Force coefficient normal to panel

References

[1] Althaus, D., Wortmann, F. X., 1981: Stuttgarter Profilkatalog I, Friedrich Vieweg & Sohn, Braunschweig, pp. 260 – 286.

[2] Arnold, K. O., 1966: Aerodynamische Untersuchungen an Flügeln mit Bremsklappen, Z. Flugwiss. 14, Heft 6, pp. 276 – 281.

[3] Bangga, G., Weihing, P., Lutz, T. and Krämer, E., 2017: Effect of computational grid on accurate prediction of a wind turbine rotor using delayed detached-eddy simulations. Journal of Mechanical Science and Technology, 31(5), pp.2359-2364.

[4] Bangga, G., Hutomo, G., Wiranegara, R. and Sasongko, H., 2017: Numerical study on a single bladed vertical axis wind turbine under dynamic stall. Journal of Mechanical Science and Technology, 31(1), pp.261-267.

[5] EASA, 2004: Certification Specifications for SAILPLANES AND POWERED SAILPLANES CS22, European Aviation Safety Agency, Köln

[6] Flower, J.W., 1999: Lift and rolling moment due to spoilers on wings with flaps undeflected at subsonic speeds, ESDU 90030, Royal Aeronautical Society, London

[7] Green, M.J., 1999: Drag and yawing moment due to spoilers, ESDU 96026, Royal Aeronautical Society, London

[8] Greiner, M., 2014: Schleichers neuer 20m Doppelsitzer: Was die ASG 32 ausmacht, presentation at the symposium for sailplane development, Braunschweig

[9] Hoerner, S. F., 1965: Fluid Dynamic Drag, Hoerner Fluid Dynamics, Bakersfield, pp. 3-14 – 3-17 and 13-11 – 13-12

[10] Kroll, N., Rossow, C.C., Becker, K. and Thiele, F., 2000: The MEGAFLOW project. Aerospace Science and Technology, 4(4), pp. 223-237.

[11] LFSM, 1975: Lufttüchtigkeitsforderungen für Segelflugzeuge und Motorsegler, Anlage zur 1. DV LuftBauO-LFSM, Bundesanzeiger Nr. 204 vom 31. Oktober 1975

[12] Menter, F.R., 1994: Two-equation eddy-viscosity turbulence models for engineering applications. AIAA journal, 32(8), pp.1598-1605.

[13] Merklein, H. J., 1963: Bestimmung aerodynamischer Beiwerte durch Flugmessungen an 12 Segelflugzeugen mit Brems- und Landeklappen, FFM-Bericht Nr. 63, Flugwissenschaftliche Forschungsanstalt e.V., München

[14] Pátek, Z. , Cervinka, J., Vrchota, P., 2012: Wind tunnel and CFD study of airfoil with airbrake, 28th International Congress of the Aeronautical Sciences

[15] Schaum, A., 2011: Konstruktion von Bremsklappen für Segelflugzeuge und Motorsegler mit dem Ziel der Erreichbarkeit niedriger Bedienkräfte, Diploma Thesis, Technische Hochschule Mittelhessen, Fachbereich Maschinenbau, Mechatronik, Materialtechnologie

[16] Straub, J., 2009: Experimentelle Untersuchungen zur Wirksamkeit von Störklappen bei Segelflugzeugen, Studienarbeit, Institut für Aerodynamik und Gasdynamik, Stuttgart

[17] Weihing, P., Letzgus, J., Bangga, G., Lutz, T. and Krämer, E., 2016: September. Hybrid RANS/LES Capabilities of the Flow Solver FLOWer—Application to Flow Around Wind Turbines. In Symposium on Hybrid RANS-LES Methods (pp. 369-380). Springer, Cham.

Airfoil optimization with CST-parameterization for (un-)conventional demands

Johannes Achleitner[1], Kai Rohde-Brandenburger[2], Mirko Hornung[1]
[1] *Technical University of Munich, Institute of Aircraft Design, Germany, johannes.achleitner@tum.de*
[2]*DLR, Institute of Aerodynamics and Flow Technology, Braunschweig, Germany, kai.rohde-brandenburger@dlr.de*

Abstract: For the development of modern airplanes new and "better" airfoils are needed. The design of a new airfoil is mostly done for a number of fixed design points by the inverse method and optimized by manual iteration. When changing the preliminary design of the airplane, the airfoil design parameters are changing continuously in the design process. Therefore a tool chain was created, which allows the parametric optimization of the airfoil and the connection with a 2D panel method with fully coupled boundary layer calculation (XFOIL) with an optimizer. This paper will show an approach for airfoil optimization using an enhanced parameterization method of the airfoil coordinates. It explains the tool chain and the influence of the parameters used. The validation results for optimizing typical main wing airfoils with and without camber changing flap are shown. Based on that validation for conventional airfoils, more complex airfoils for unconventional geometries can be optimized. First results for a high lift system on a morphing wing system for a sailplane are shown and discussed.

***Keywords*:** airfoil design, airfoil optimization, CST shape parametrization, morphing, variable geometry, XFOIL.

Introduction

Numerical airfoil optimization has been widely employed in aerodynamic design of airfoils for aircraft and in the wind energy sector. For instance the airfoils for the Diana 3 [1] sailplane are designed with this method by Kubrynski. For the parametrization of the airfoil the "shape function / class function" methodology (CST) proposed by Kulfan and Bussoletti [2] has been used in the presented work. It has some advantages over other parametrization methods, e.g. infinite leading edge slope, i.e. the airfoil has a round edge radius and a finite trailing edge angle

Airfoil optimization methodology

The airfoil optimization methodology is shown in Figure 1. A set of design variables defines a start airfoil which is translated to airfoil coordinates by the parametrization tool. The airfoil coordinates are imported into a modified XFOIL [3]. The derivatives, i.e. drag coefficients at different lift coefficients are calculated. The objective function is a weighted sum of the drag coefficients with physically motivated weights. An optimization algorithm changes the design variables in order to obtain a better airfoil. For an airfoil with a variable leading edge geometry a subset of extra design variables is used for the parametrization of the nose droop. After convergence an optimized airfoil is obtained.

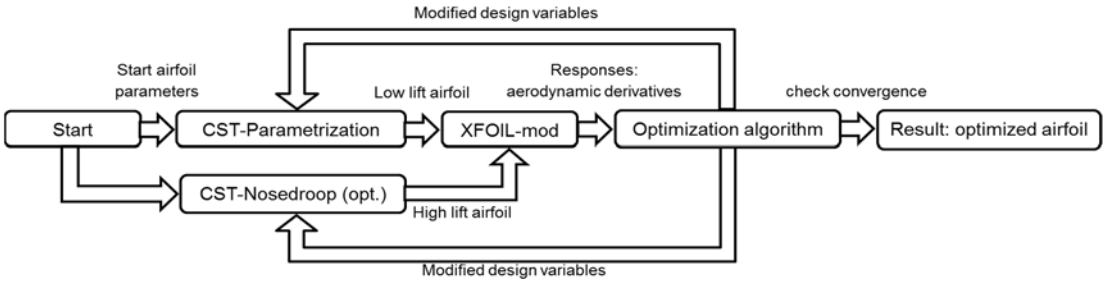

Figure 1. Airfoil optimization methodology

As optimization algorithm the Subplex algorithm is used, developed by Rowan [4]. It is a subspace line search method using a gradient free Nelder-Mead-Simplex [5] algorithm for optimization on the subdomains. A minimum thickness distribution for ensuring a minimum airfoil and flap thickness has been implemented. A minimum y/c coordinate at $x/c = 1.25$ % was implemented to ensure that leading edge stall occurs beyond the normal angle of attack range with sufficient margin. Both constraints were added as penalty functions on the objective function. Some modifications have been made to the used XFOIL version, motivated by the observations of Timmer and van Rooij [6]. An improved post stall prediction is achieved by the adaptions proposed by van Rooij [7] and Hansen [8]. The drag prediction has been improved by implementation of the adaptions proposed by Ramanujam [9].

CST Parametrization of airfoils with and without camber changing flap

The contour line of the airfoil is expressed by two separate curves for top and bottom side, which are parametrized independently. The top and bottom contour lines, i.e. their z-coordinates as a function of its x-coordinates, are obtained by multiplication of a class function C(ψ) with a shape function S(ψ):

$$\zeta(\psi) = C(\psi)\, S(\psi) \qquad where: \qquad \psi = \frac{x}{c} \quad and \quad \zeta = \frac{z}{c} \tag{1}$$

The class function for the airfoil's top and bottom coordinates is defined as:

$$C(\psi) = \psi^{N_1}(\psi - 1)^{N_2} \qquad with \quad N_1 = 0.5 \quad and \quad N_2 = 1.0 \tag{2}$$

$N_1 = 0.5$ ensures a round leading edge with infinite slope at $\psi = 0$. For the trailing edge angle to be finite at $\psi = 1$, N_2 is set as $N_2 = 1.0$. Bernstein polynomials are used as weighted shape functions. The weighting factors x_i are the design variables for the optimization problem.

$$S(\psi) = \sum_{i=0}^{n} x_i\, B_i(\psi) \qquad where: \qquad B_i(\psi) = K_i\, \psi^i (1-\psi)^{n-i} \quad and \quad K_i = \binom{n}{i} = \frac{n!}{i!\,(n-i)!} \tag{3}$$

Figure 2 shows the CST parametrization of an airfoil with 5 CST parameters each on bottom and top side. The Bernstein polynomials are shown in the middle graphs. They are already weighted. The resulting shape function is shown as a colored line each.

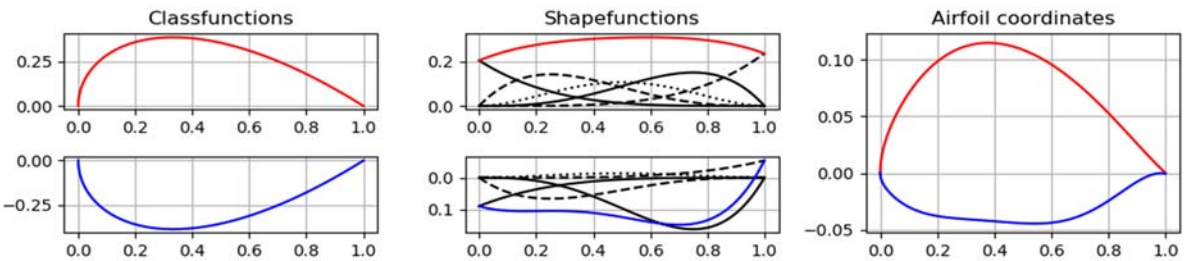

Figure 2. CST Parametrization of airfoil with fixed geometry

For airfoils with camber changing flaps, Boermans and van Garrel [10] proposed an airfoil design methodology with two distinct flap settings where either the top surface or the bottom surface is kink free. The resulting airfoil DU89-134-14, used on the ASH 26 and ASW 27 sailplanes marked the beginning of a new generation of flapped airfoils with long laminar flow regions on the bottom side up to 95%. In order to correctly parametrize this design methodology, a modification to the CST method is proposed here, shown in Figure 3. In addition to the parametrization of fixed geometry airfoils, a quadratic parabola is added to the top side coordinates. The parabola is scaled accordingly, so that the parabola crosses the trailing edge of the airfoil when the flap is deflected with the angle where the top side is kink free. Then the top side of the coordinates behind the flap axis are re-rotated so that the trailing edge ends at (1,0), shown as a dashed line in the right graph of Figure 3.

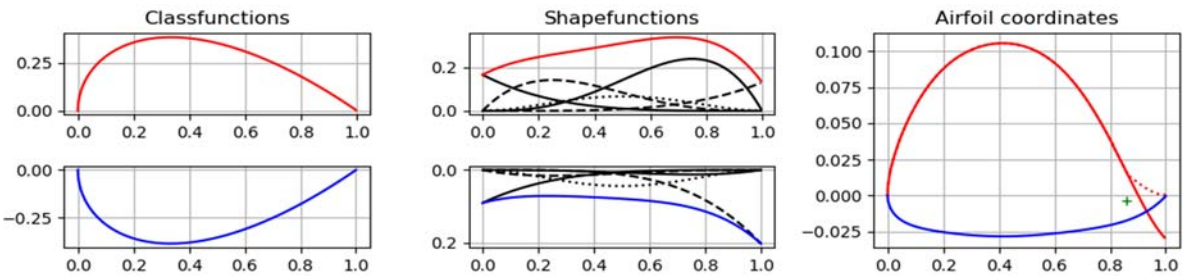

Figure 3. CST Parametrization of airfoil with camber changing flap

Optimization results of airfoils with fixed geometry and with camber changing flap

Figure 4 shows the calculated polars of the optimized airfoils as well as the polars of the reference airfoils. In the left two graphs the calculated (dashed) and the measured (solid) polars of the DU84-158 [11] airfoil are shown. Good agreement of measurements with calculations can be observed, although the lift in post stall is still overpredicted, but less than with default XFOIL 6.99. The preliminary design optimized airfoil (dotted) shows superior performance at high lift, but the lower corner of the laminar low drag bucket is at a higher $\boldsymbol{c_l}$ value. A redesign is recommended in order to obtain similar $\boldsymbol{c_l}$ values for the lower corner of the laminar low drag bucket. For the flapped optimized airfoil lower drag values were achieved compared to the DU89-134-14. Again, the laminar low drag bucket width of the optimized airfoil is smaller than of the reference airfoil. The lift curve of the optimized airfoil shows a drop of lift coefficient beyond the laminar low drag bucket, which is detrimental for

thermalling in turbulent conditions. Furthermore, a good airfoil performance can be reached by numerical optimization. This preliminary results suggest another optimization iteration by adaption of the design lift coefficients and postprocessing by inverse design.

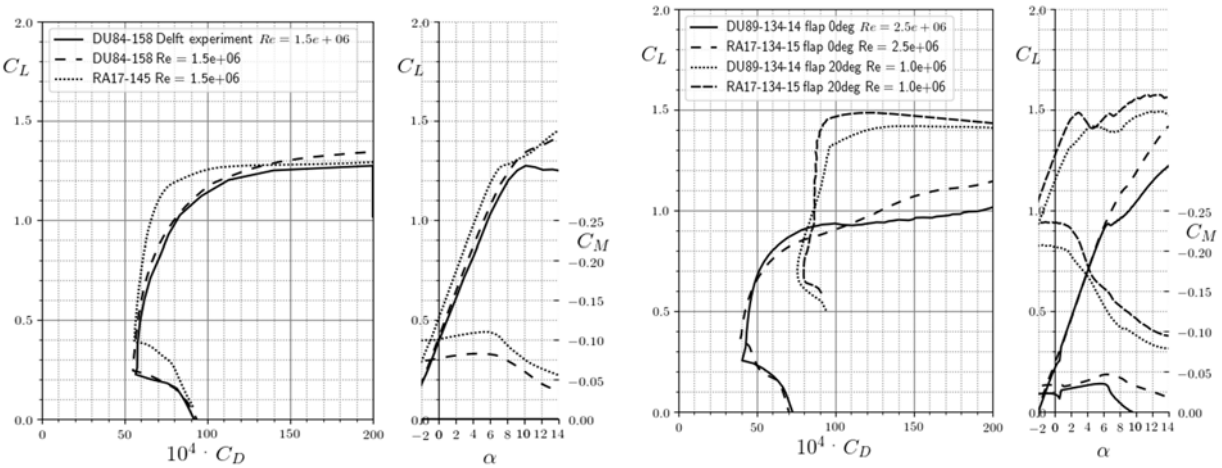

Figure 4. Polars of fixed geometry airfoils (left) and airfoils with camber changing flap (right)

CST parametrization of a variable leading edge geometry

A concept for a shape variable leading edge for sailplane design has been proposed by Weinzierl et al [12]. They also presented an aifoil reaching lift coefficients of $c_l = 1.8$. Thus enabling to increase the aspect ratio of the wing and the wing loading up to 70 kg/m^2, leading to a superior high speed performance. However, the presented airfoil suffered from separated turbulent flow on the flap top side, leading to high drag values and probably weak aileron effectiveness. The design of a morphing airfoil with conventional inverse and mixed-inverse methods seems to be complex because a geometrical match of unmorphed and morphed nose as well as the rigid center section is necessary. Therefore an extension of the CST method is presented which allows the parametrization of a variable leading edge geometry for numerical optimization. The upper and lower contour lines of the airfoil are decomposed into the camber line and the thickness distribution.

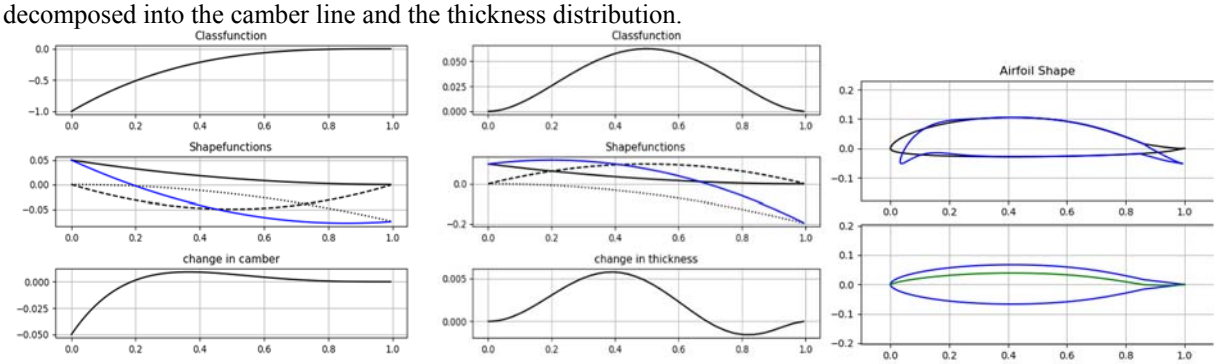

Figure 5. Class & shape functions for camberline(left), thickness distribution (middle), resulting airfoil (right)

Then, morphing is performed by adding additional functions to both curves. Compared to the undeformed airfoil parametrization, different class functions are used. For morphing of the thickness distribution, the class function from Eq. 2 is used, but with different exponents $N_1 = N_2 = 2.0$. The ψ coordinates are transformed to the area, where morphing is applied (Eq.4). ψ_e denominates the end of the morphing section. In this case, it was decided to morph the front 40% portion of the airfoil. Therefore, $\psi_e = 0.4$. In order to ensure a precise leading edge shape, which is important for a gentle stall behavior and good performance, the thickness of the leading edge part remains fixed. Consequently, the leading edge is supposed to undergo a rigid body motion only. At position ψ_s is the beginning of the section where the thickness distribution is changed. ψ_s is set equal to the leading edge radius.

$$\psi_t = \frac{\psi - \psi_s}{\psi_e - \psi_s} \quad and \quad \psi_c = \frac{\psi}{\psi_e} \tag{4}$$

The camber line morphing begins right at the leading edge, thus the coordinate transformation according to right part of Eq.4 is utilized. As class function, a parabola is utilized:

$$C_c = (\psi_c - 1)^{N_1} \quad with: \quad N_1 = 2.0 \tag{5}$$

A generic example of morphing an airfoil with the CST method is shown in Figure 5. The class functions are shown in the topmost figures. The resulting shape function is shown as a blue line in the centered figures, which is a sum of the weighted Bernstein polynomials (black lines). The resulting change in camber (left) or thickness (middle) is shown in the bottom diagram. The recomposed undeformed (black) and morphed airfoil (blue) is shown in the right image.

Optimization results of an airfoil with variable leading edge geometry

Figure 6 shows the airfoil shape of the optimized morphing wing airfoil. The airfoil is 11.6% thick, with a conventional camber changing flap of 16% length and 3.4% nose droop. In the bottom right picture the thickness distribution and the camber line in low lift configuration are shown. The minimum thickness curve is shown as the red dashed line. On the left half of the picture the calculated polars of the morphing airfoil compared to the DU89-134-14 with 0° and 20° flap deflection are shown. The morphing airfoil shows lower drag values in low lift configuration than the DU89-134-14. In high lift configuration similar drag values than the DU89-134-14 in 20° flap setting can be achieved, but at higher lift coefficients. It seems to be possible, that a lift coefficient of $c_l = 1.8$ can be reached with low drag values. This would enable to design a sailplane with a wing loading of 70 kg/m^2 with the same stall and thermalling speed of a conventional camber changing flap sailplane at wing loadings up to 60 kg/m^2, but with a large benefit for high speed performance. This demonstrates the performance potential of the variable leading edge geometry concept.

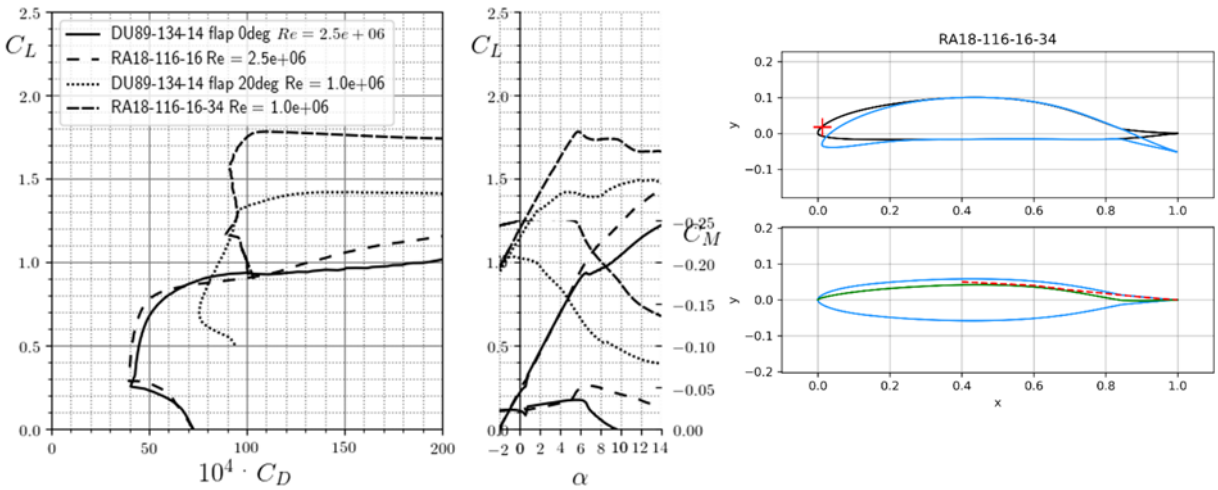

Figure 6. Calculated polars of DU89-134-14 and morphing airfoil (left), morphing airfoil shape (right)

References

[1]Kubrynski, K., 2012: Design of a Flapped Laminar Airfoil for High Performance Sailplane, 30th AIAA Appl. Aerodynamics Conf.

[2]Kulfan B.M., Bussoletti J.E. , 2006: “"Fundamental" Parametric Geometry Representations for Aircraft Component Shapes”, Int. 11th AIAA/ISSMO Multidisciplinary Analysis and Optimization Conference

[3]Drela, M., 1989: XFOIL: An Analysis and Design System for Low Reynolds Number Airfoils, Low Reynolds Number Aerodynamics. Lecture Notes in Engineering, Vol 54: 1-12.

[4]Rowan, T.H. 1990: Functional Stability Analysis of Numerical Algorithms, Dissertation, University of Texas, Austin.

[5]Nelder, J.A., Mead, R., 1965: A simplex method for function minimization. Computer Journal, Vol. 7: 308–313.

[6]Timmer, W.A., van Rooij, R.P.J.O.M, 2003: Summary of the Delft University Wind Turbine Dedicated Airfoils, Journal of Solar Energy Engineering, Vol 125 No 4: 488-496

[7]van Rooij, R.P.J.O.M., 1996: Modification of the boundary layer calculation in RFOIL for improved airfoil stall prediction. Report IW-96087R, Institute for Wind Energy, Delft University of Technology.

[8]Hansen, T.H., 2018: Airfoil optimization for wind turbine application, Wind Energy Journal, Online Version

[9]Ramanujam, G et al., 2016: Improving Airfoil Drag Prediction, Journal of Aircraft, Vol 53, No 6, pp 1844-1852

[10]Boermans, L.M.M., van Garrel, Design and Windtunnel Test Results of a Flapped Laminar Flow Airfoil for High-Performance Sailplane Applications ICAS-Paper 94-5.4.3

[11]Boermans, L.M.M., Waibel, G.: Aerodynamic and Structural Design of the Std. Class Sailplane ASW-24 ICAS-Paper 88-2.7.2

[12]Weinzierl, M., Achleitner, J., Baier, H., 2015: Highly Extensible Skin of a Variable Geometry Wing Leading Edge of a High-Performance Sailplane, Technical Soaring Vol 39 No 1: 4-9

Gefördert durch:
Bundesministerium für Wirtschaft und Energie
aufgrund eines Beschlusses des Deutschen Bundestages

Modern sailplane wing design

Mark D. Maughmer
Department of Aerospace Engineering, Penn State University, University Park, PA, mdm@psu.edu

Abstract: The performance of sailplanes has improved dramatically over the past fifty years. While much of this performance increase can be attributed to remarkable advances in materials, better weather prediction, and developments in onboard avionics, a great deal of this improvement is the result of significant gains in aerodynamics. These gains are the consequence of better design tools that result in airfoils having remarkably low drag due to ever increasing amounts of laminar flow along with a better understanding and utilization of wing planform geometries that result in lower induced drag. The many trade-offs that are necessary result in the wings of our sailplanes looking the way they do.

Introduction

The design of a modern sailplane is an iterative process that trades off a great many design variables in order to achieve the performance goals sought. Unlike most aircraft, which are most often designed to achieve their best performance around a cruising point, the design of a sailplane is complicated by the very conflicting goals of being able to climb efficiently at low speeds in thermals against that of being able to glide efficiently at high speed between them. This challenging trade-off is exacerbated for the designer fact that both the climb and the glide are fully dependent on the weather of any particular day: the size, strength, and structure of thermals, the wind on course, the length of the soarable day, and so forth [1-3].

Profile Drag

As wing profile drag is such a large portion of the overall drag, it is important to design and use the best airfoils possible. To accomplish this, the designer must know exactly the aerodynamic requirements and operating environment over which these airfoils must perform. Ultimately, the drag and moment data for these airfoils over the operational ranges of lift coefficient, Reynolds number, and flap deflections must be included in the performance predictions of the glider for both climb and glide. For the design and analysis of airfoils in the flight regime of sailplanes, both the PROFIL [4] and XFOIL [5] codes have been well validated, as is shown in Fig. 1, and the predicted aerodynamic characteristics are more than sufficient for design and performance calculations.

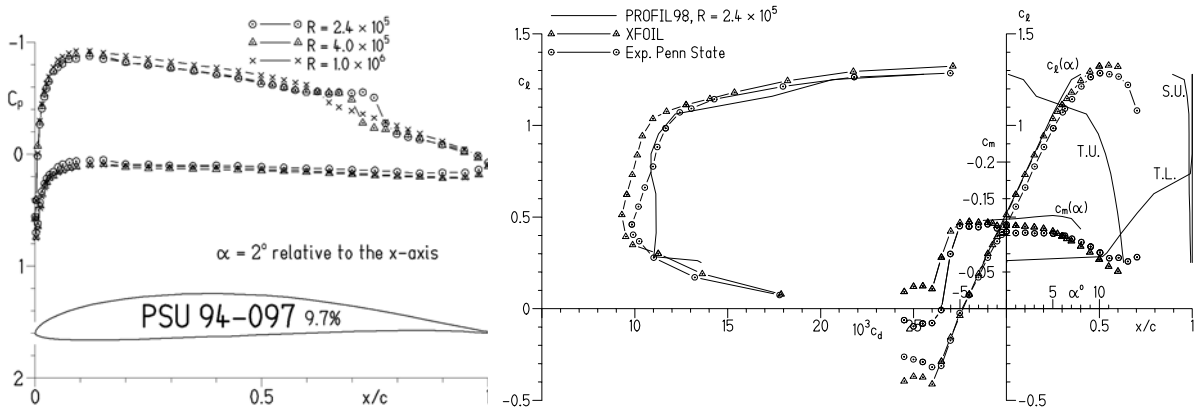

Figure 1. The theoretical and experimental pressure distributions and section characteristics for the PSU94-097 winglet airfoil [6].

Induced Drag

The other essential component for predicting the aerodynamics of a sailplane wing is the determination of its span efficiency and spanwise lift distributions. The lift distribution directly affects the wing profile drag, and the planform efficiency dictates the induced drag of the wing. Currently, use is made of a multiple lifting-line method for the prediction of the finite wing aerodynamics. This method has several chordwise lifting lines, each having a second-order vorticity distribution [7], which produces a continuous sheet of vorticity that is shed into the wake. The method allows the spanwise lift distributions, examples of which are presented in Fig. 2, and the induced drag of non-planar wing geometries to be predicted with reasonable accuracy and less computational effort than is required by a three-dimensional panel method. Although not accounting for the consequences of thickness and a free wake, the multiple lifting-line procedure has been found to be of sufficient accuracy for final design purposes. The use of the multiple lifting-line program along with the inclusion of measured or predicted airfoil characteristics

allows the performance to be accurately predicted for both straight- and turning-flight [8]. An example comparison of a predicted straight flight polar with Idaflieg flight-test results is presented in Fig. 3.

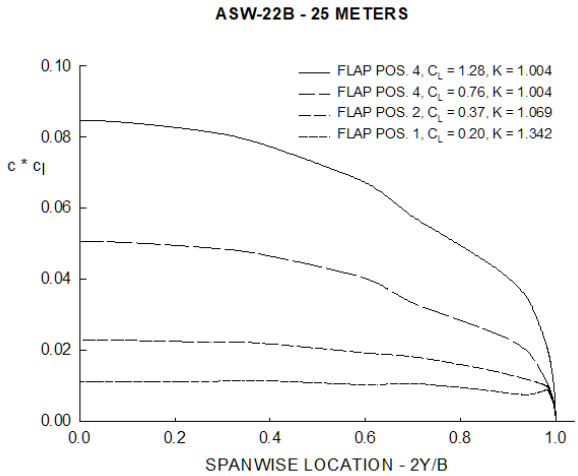

Figure 2. Example of span loadings for the ASW-22B at different flap settings as calculated using the multiple lifting-line method [7].

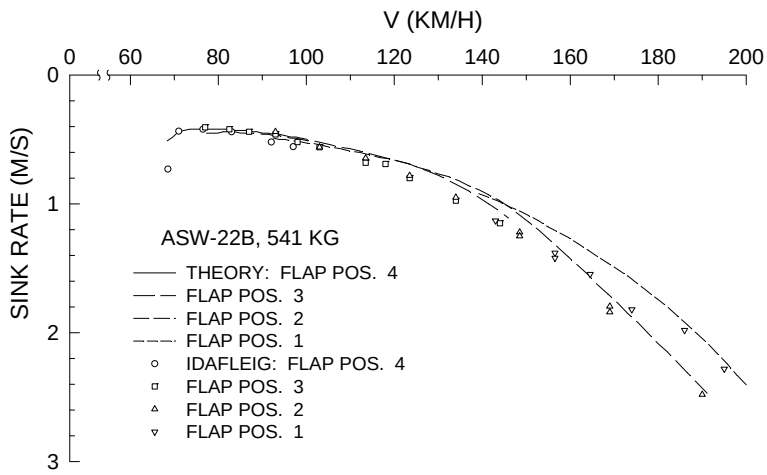

Figure 3. Comparison of predicted [8] and experimental flight-test data for the ASW-22B at different flap settings.

Putting It All Together

Once the straight flight and turning performance of the glider have been predicted, the iterative process of determining the optimum cross-country performance over a wide range of different weather situations can begin [1-3, 8-10]. This process has evolved over the years as better analyses tools and weather models have been developed. This process continues, as demonstrated in Fig. 4, in which recent developments in computational fluid dynamics allow such methods to better deal with transitional aerodynamics that are so important in sailplane operating regimes. Likewise, the availability of actual in-flight logger data has significantly improved the understanding of the weather in which gliders are flown, as well as how they are used. An example of the the iteration process in which the performance prediction is blended with the weather modeling is demonstrated in Fig. 5, in which a new weather model based on logger data is used to predict the performance of different design configurations of a new sailplane [10].

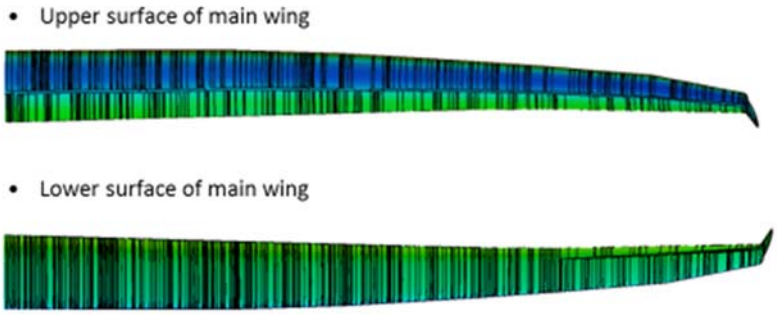

Figure 4. Computational fluid dynamic predictions of the surface streamlines of a modern sailplane wing demonstrating transition prediction at C_L = 0.3 and R_{root} = 2.45 × 10^6.

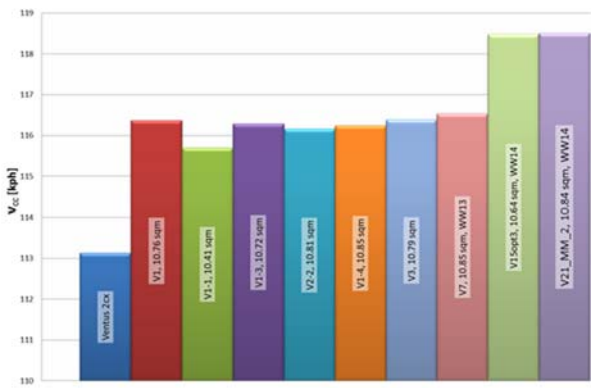

Figure 5. Example of the average cross-country speed prediction of several design configurations using a new weather model [10].

Conclusions

The design of a modern sailplane wing remain strongly dependent on the classical assumptions regarding two-dimensional airfoil aerodynamics and lifting-line approaches to three-dimensional wing aerodynamics. Although modern developments in computational fluid dynamics are proving to be beneficial, these classical methods have stood the test of time and will remain important and reliable tools in sailplane design for years to come.

References

[1]Reichmann, H., *Cross-Country Soaring*, Seventh Edition, Soaring Society of America, Inc., 1993.
[2]Thomas F., *Fundamentals of Sailplane Design,* Judah Milgram, translator and contributor, College Park Press, College Park, MD, 1999
[3]Carmichael, B.H., "What Price Performance," *Soaring*, May/June, 1954, pp.6-10.
[4]Eppler, R., Airfoil Program System "PROFIL07," User's Guide, Richard Eppler, c. 2007.
[5]Drela, M. and Youngren, H., "XFOIL 6.9 User Primer," Massachusetts Institute of Technology, Cambridge, MA, 2001.
[6] Maughmer, M.D., Swan, T.J., and Willits, S.M., "The Design and Testing of a Winglet Airfoil for Low-Speed Aircraft," *Journal of Aircraft*, Vol. 39, No. 4, July-Aug. 2002, pp 654-661.
[7]Horstmann, K.H., "Ein Mehrfach-Traglinienverfahren und seine Verwendung für Entwurf und Nachrechnung nichtplanarer Flügelanordnungen," DFVLR, Institut für Entwurfsaerodynamik, Braunschweig, DFVLR-FB 87- 51, 1987.
[8] Kunz, P.J. and Maughmer, M.D., "Sailplane Winglet Design," XXV OSTIV Congress, Saint Auban sur Durance, France, July 3-11, 1997.
[9]Maughmer, M.D., "The Design of Winglets for High-Performance Sailplanes," *Journal of Aircraft*, Vol. 40, No. 6, Nov.-Dec. 2003, pp. 1099-1106.
[10]Maughmer, M.D., Coder, J.G., Wannenmacher, C., and Würz, W., "The Design of a New Racing Sailplane: A New Thermal Mix Model and the Role of Transitional CFD," AIAA 2017- 4091, 2017 AIAA Aviation Forum, Denver, CO, June 5-9, 2017.

Fine structure of thermals in arid climate: results of glider-based in flight measurements

Alfred Ultsch[1,3] and Christof Maul[2,3]
[1]*Data Bionics, Philipps University Marburg, Marburg, Germany,ultsch@Mathematik.Uni-Marburg.de*
[2]*Institute of Physical and Theoretical Chemistry, Technische Universität Braunschweig, Braunschweig, Germany*
[3]*Akademische Fliegergruppe (Akaflieg) Frankfurt, Frankfurt, Germany*

Abstract: Current developments in small single-board computers together with the low prices of high precision sensors, originally developed for smart-phones or automotive applications allow the realization of low cost equipment for measuring and data logging of meteorological and flight related parameters such as ambient temperature, pressure, and GPS data. Using a low cost, public domain available equipment of this kind, two measuring campaigns were performed in the arid climate of Namibia, Africa. The automatic classification using rule-bases and neural network techniques coincided with a manual classification. Regarding the distribution of temperature the measurements seem to suggest that there is only a small gradient between the interior and the exterior of the thermal. The immediate surrounding of a thermal plume appears to be denser than the inside and the more distant parts of a thermal plume.

***Keywords*:** thermals, turbulence, fine structure, boundary layer

Introduction

Recently the fine structure of the driving force of the atmospheric has been intensively discussed. One question is whether the main driving force of the buoyancy are differences in humidity or differences in temperature with respect to the immediate and larger surrounding of the thermal. Doubtlessly both differences deliver density differences: more humid air is less dense than dryer air of the same temperature as is warmer air compared to colder air of identival humidity[1]: This has been reported before for in-flight measurements [2]. However very few in-flight measurements have been published so far.

Current developments in small single-board computers together with the low prices of high precision sensors, originally developed for smart-phones or automotive applications allow the realization of low cost equipment for measuring and data logging of meteorological and flight related parameters such as ambient temperature, pressure, and GPS data.

Using low cost (< 100EUR) equipment of this type two measuring campaigns were performed in central and south Namibia, Africa. Namibia has a subtropical desert climate characterized by large differences in day and night time temperatures, low rainfall and overall low humidity (arid climate). Here, we report some results of these measurements.

Methodology

Temperature, relative humidity and air pressure were measured with a time resolution of 1Hz (1 per second) and recorded together with longitude, latitude, time, and GPS altitude. Measurements were performed on three days with cloud base up to 5000m for 3 flights starting from Kiripotib, Namibia, in November 2017. These resulted in 71.000 data points covering ca. 20 hours of in-flight measuring time. A second campaign was performed at Bitterwasser in January 2018 . Measurements were performed on 4 days with pure (blue) thermals with convection height up to 3000 m giving 17.5h of measurement time corresponding to 65.000 points.

Temperature was reduced to a standard height using dry adiabatic lapse rate. Dew Point, absolute humidity, virtual and potential temperature, and the partial pressures of air and water were calculated using the standard meteorological equations [3].

A classification of flight time into inside thermal and non-thermal was performed using rule based enhanced with an artificial neural network [4]

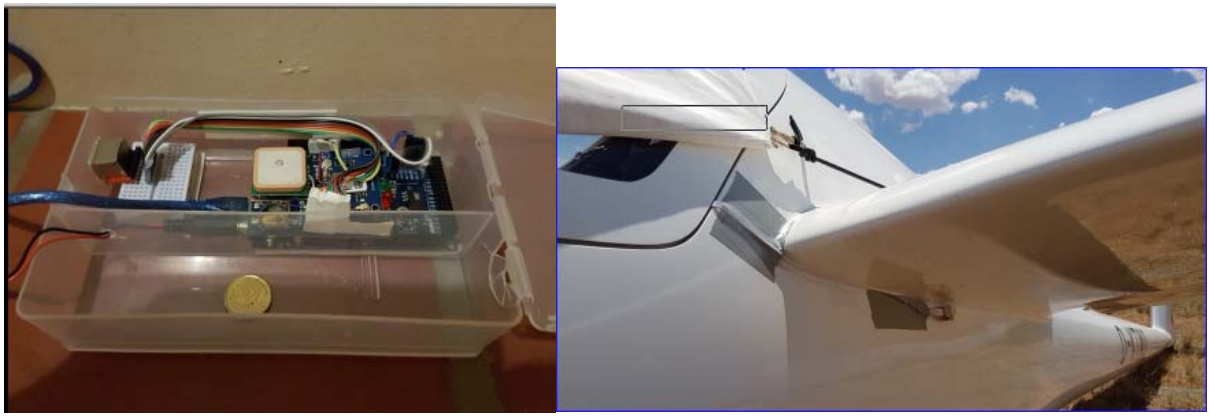

Figure 1. Left: Arduino with GPS and DS logger ; right: Position of the sensors underneath the glider's wing

Results

The results of the automatic classification were found to be in sufficiently good agreement with a manual classification. With respect to the distribution of temperature the measurements seem to suggest that there is only a small gradient between the interior an the exterior of the thermal (see Figure 2).
The immediate surrounding of a thermal plume appears to be denser than the inside and the more exterior parts of a thermal plume. This needs to be explained.

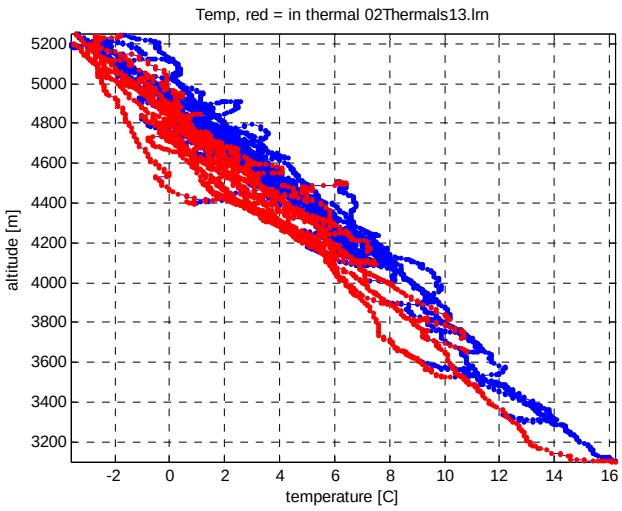

Figure 2. Temperature vs altitude inside (red) and outside (blue) thermals for one flight

References

[1] D. Müller and C. Kottmeier: Meteorologische Aspekte des Streckensegelflugs, Universität Hannover, 1985
[2] A.G. Williams and J.M. Hacker: Inside Thermals, Technical Soaring 16, 57, 1992.
[3] J.R. Holton and G.J. Hakim: An introduction to dynamic meteorology. 5th ed., Academic Press, 2013.
[4] R. Heise and A. Ultsch: Data Mining to Distinguish Wave from Thermal Climbs in Flight Data, in: W. Gaul et al (Eds.) Advances in Data Analysis, Data Handling and Business Intelligence (Proc. of the 34th Annual Conference of the Gesellschaft für Klassifikation e.V., Karlsruhe), Springer, 2010.

Measurement Results from Warm Air Thermals over the Namibian Steppe

Albert Kießling
Akademische Fliegergruppe am Karlsruher Institut für Technologie e. V, Germany, albert.kiessling@t-online.de

Abstract: An Open class glider was used as a test carrier for humidity, temperature and barometric pressure measurements in the Namibian thermals. The data were collected during several long distance flights from the gliding center Bitterwasser and plotted by means of 2 battery powered dataloggers mounted on 2 different locations near the fuselage of the glider. The main goal of the measurements was to detect the influence of temperature and humidity on the thermal strength dependent on the cloud base, paired with the challenge to confirm or not to confirm the humidity theory of Henry Blum, published in his book "Meteorology for glider pilots"[2]. The measurements show clearly, that the temperature difference is the dominant buoyancy source especially in the case of high cloud/convection bases, whereas the humidity only plays a role in the early thermals respectively at low convection bases.

***Keywords*:** Buoyancy factor, warm air thermals, temperature difference, humiditiy difference.

Introduction

Already in the year 1977 Carsten Lindemann [1] has carried out some measuring flights with his motor glider D-KAME of the University of Berlin which was equipped with a humidity, temperature and pressure recorder. He documented the values inside and outside of thermals by flying horizontally through the thermals at different altitude layers and in different phases of the thermal development. Unfortunately he published the results only for a cloud base of about 1300m and considered only the temperature differences between inside and outside the thermal, the humidity difference was not in his focus at that time. His measurements showed that there was no temperature difference at all above an altitude of 1000m. This fact led Henry Blum to the conclusion that the temperature difference of thermals will in general disappear above an altitude of 1000m above ground level. As a consequence he concluded that thermals with high cloud bases must be driven by another buoyancy factor, namely the humidity difference. Knowing that high cloud bases cause per se low humidity values, he addressed with his theory especially the warm air masses whose humidity values are nevertheless big enough to eventually cause reasonable buoyancy. Therefore the Namibian steppe seemed to be the ideal surrounding to check the theory by measurements.

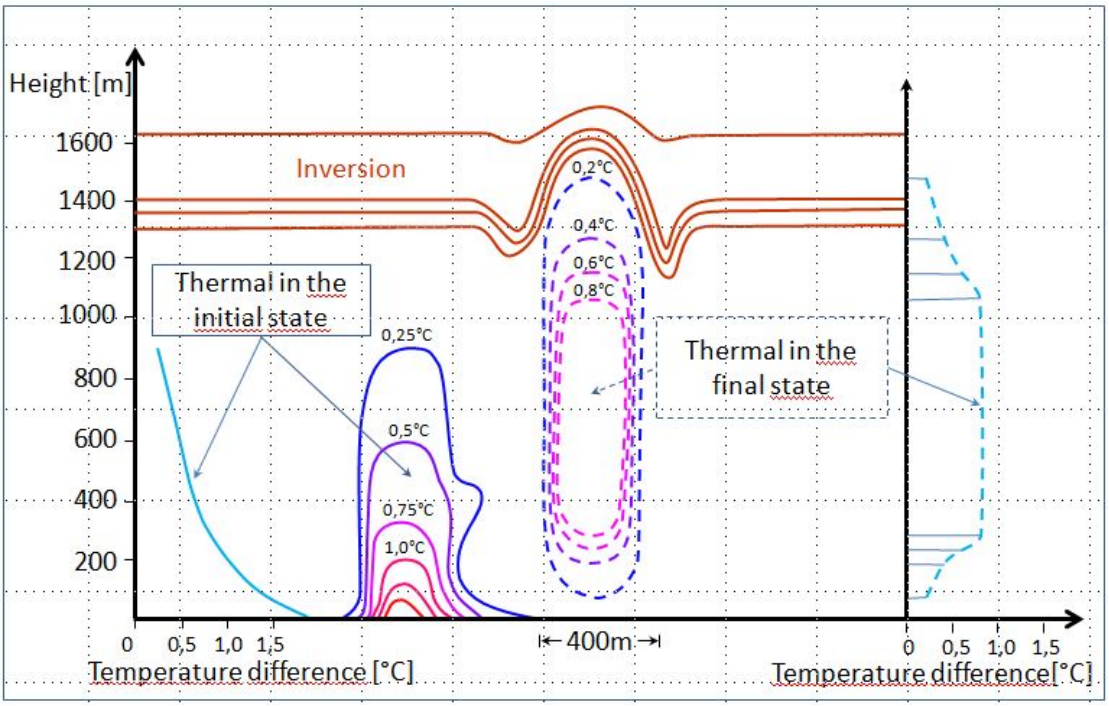

Figure 12: Measuring results of Carsten Lindemann 1977 [1], combined with the interpretation of Müller/Kottmeier 1978 [3]

Methodology

The measuring method of Carsten Lindemann is especially in Namibia too expensive for me as a private person. Therefore the measurements were done during the normal cross country flights over distances of up to 1100 km by two different methods.

The first method measures the temperature and humidity difference between inside and outside the thermal only twice, first at flying in the thermal and secondly at leaving of the thermal. The altitude difference, which the glider has to climb or to fall in order to get the same temperature as before entering or leaving the thermal, is a direct measure for the temperature difference between the thermal and the surrounding air because of the adiabatic lapse rate 1°/100m (see Figure 2).

The second method assumes that the surrounding air shows an adiabatic respectively "neutral" stratification during the thermal convection period. In this case, it is possible to relate all temperatures to the ground level and to compare these so called potential temperatures directly at different heights. By means of the potential temperature the temperature differences between the thermal air mass and the surrounding air mass can easily be read out of the diagrams.

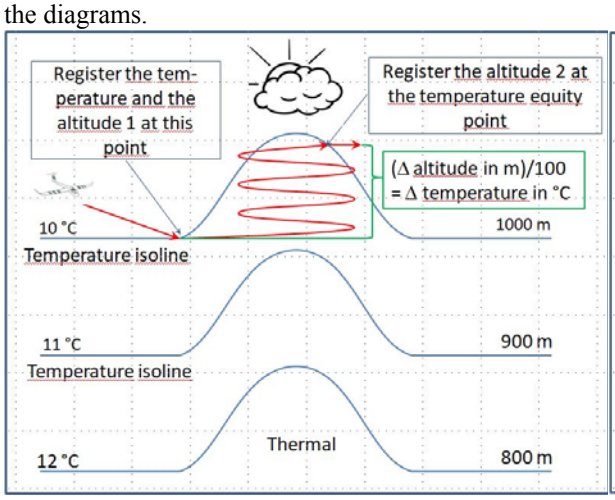

Figure 2: Measuring method 1

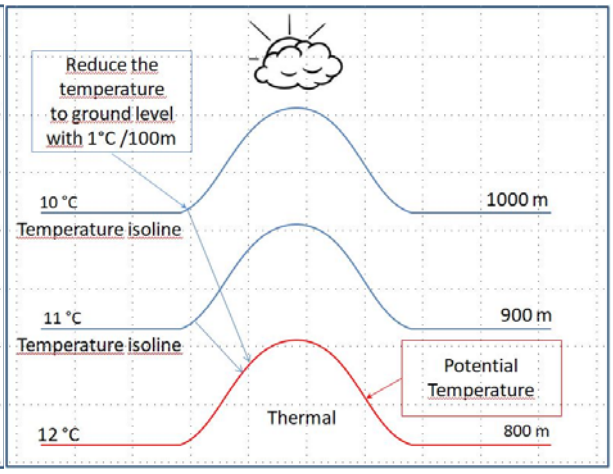

Figure 3: Measuring method 2

One of the used data loggers was mounted on the fuselage of the glider at a location, where we usually find a turbulent air flow and from where the altimeter of the glider get's its static pressure. This logger recorded synchronously the barometric pressure, the temperature and the dewpoint of the surrounding air with a sampling rate of 2 s. The time constant of the humidity sensor had a value of 8 s, that of the temperature sensor 20 s and of the pressure sensor 2 ms (milliseconds). The temperature sensor of this logger was too slow for method 1, because of the high vertical velocities of the Namibian thermals. Therefore a second logger with a thermo element based sensor and a time constant of about 0.5 s was mounted further ahead at a point, where the airflow changes from laminar to turbulent and where the temperature is also not influenced by the speed of the glider. The values of this sensor are called "temperature fast" in the following diagrams. Furthermore the diagrams contain heights above ground calculated out of the measured temperature and pressure values, the potential temperature calculated out of the measured temperature and altitude values, and the mixing ratio respectively water vapor content calculated out of the measured dew point and pressure values.

Results

A total of 4 cross country flights were documented in the described manner. Only one of them showed some influence of the humidity on the thermals. Therefore I prefer to present especially the measuring results of this flight from 06.12.2017, which started very early in the morning, as usual with blue thermals, but initially quite unusual with very low convection heights between 500 and 1300m above groundlevel. This first phase of the day is documented in the following figure 4. It shows with the proceeding daytime the increased level of the potential temperature together with relatively high temperature differences between the thermal and the surrounding air (up to 2.2 °C) as well as relatively high humidity variations of up to 3g/kg, which corresponds to virtual temperature differences of about 0.5 °C. Compared with the potential temperature variations it's still small but not negligible. Easy to see is, that the temperature inside the thermal after leaving it is about 1°C lower than outside. Obviously the thermals penetrate – driven by the humidity and the inertia of the thermal mass – into the inversion despite some negative thermal drive. At leaving the thermal within the inversion layer the humidity drop is especially high, obviously because dry air masses are flowing down from the dry air layers in and around the inversion.

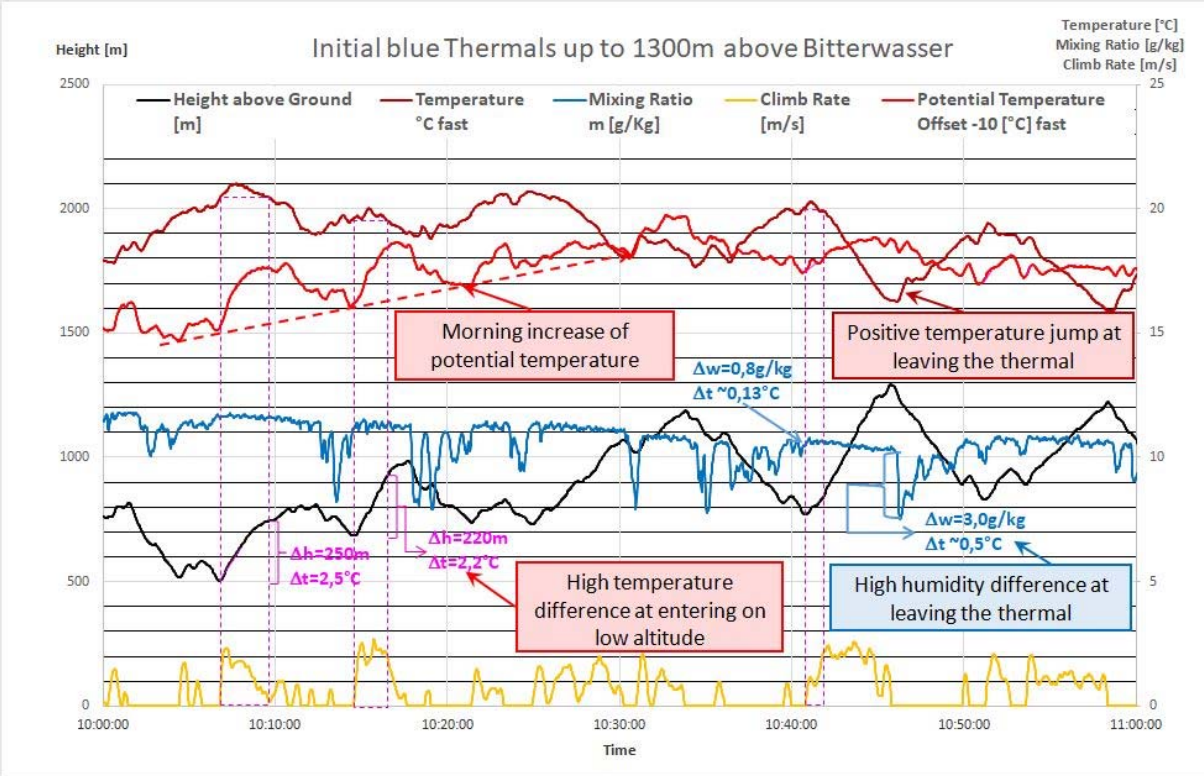

Figure 4: Flight documentation from 06.12.2017 in the morning

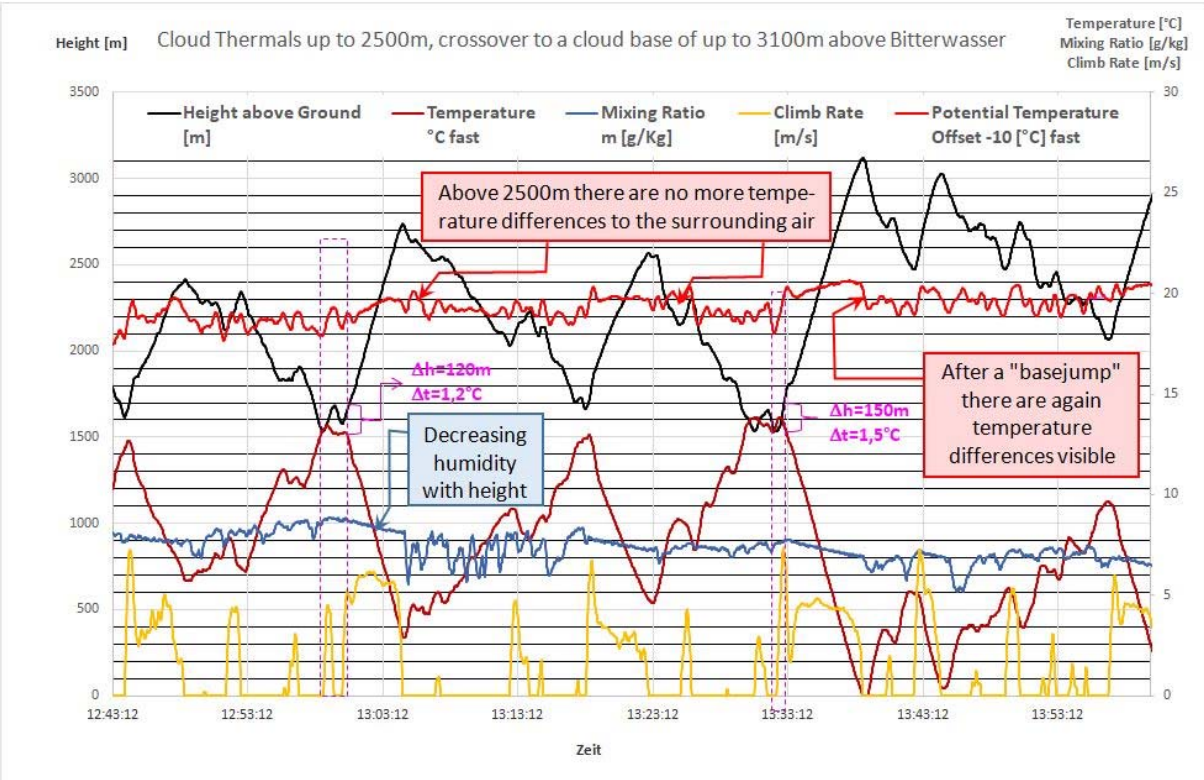

Figure 5: Flight documentation from 06.12.2017 in the early afternoon

The measurements up to this point nearly completely correspond to the measurements of Carsten Lindemann from the year 1977 [1] at a cloud base of 1300m.

Later in the day, the convection heigths of the thermals climb in steps to higher levels whereby the humidity is going down, and the humidity differences between thermals and their surrounding air mass decrease as well from step to step (see figure 5 and 6). Temperature differences disappear in the temporarily existing inversions and revive after braking the inversion. In the later afternoon, the humidity differences disappear nearly completely,

while the temperature differences remain up to high altitudes. In the vicinity of an inversion or stable stratification they reduce according to the theory, and in absence of humidity differences only inertia forces let the thermals proceed, but slow down (see figure 5).

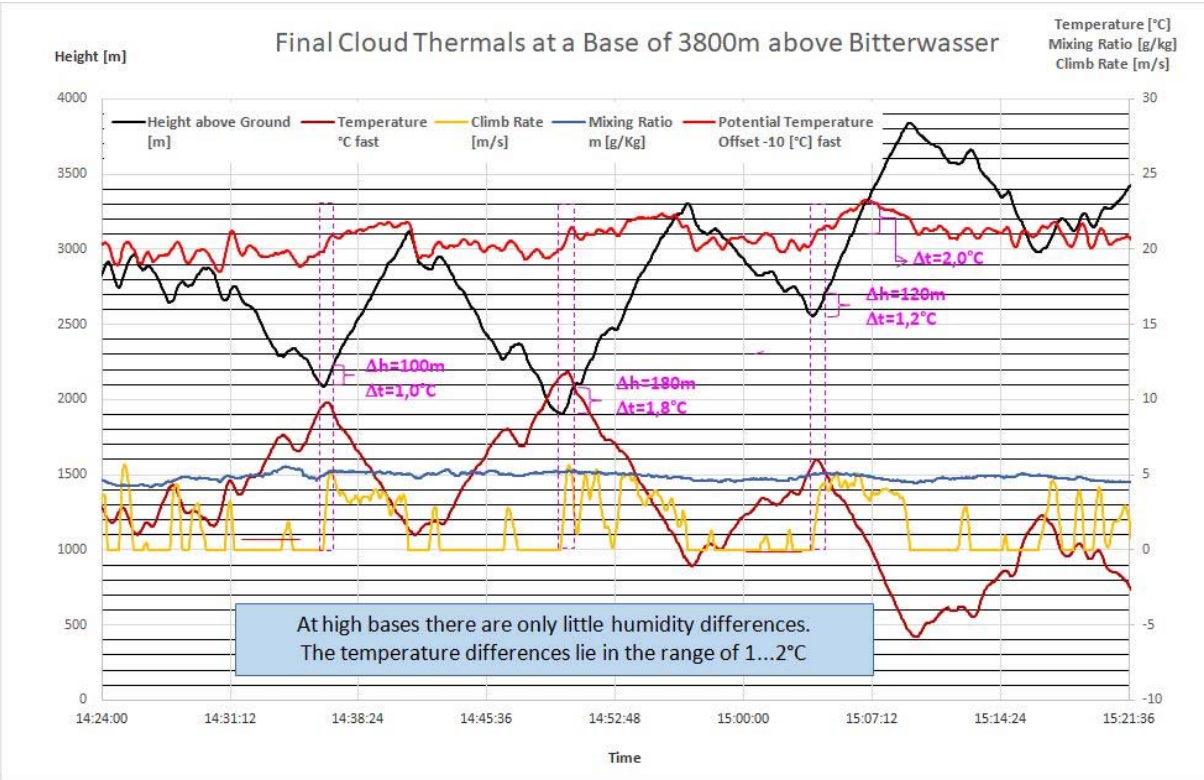

Figure 6: Flight documentation from 06.12.2017 in the later afternoon

As a conclusion I can determine, that the measurements of Carsten Lindemann can be extrapolated and scaled to higher convection layers by simply relating the thermal parameters to the height of the convection layer. Higher convection layers obviously distribute the limited humidity coming from the surface much faster into the bigger volumes of dry air, so that the influence of the humidity is drastically reduced with the convection height.

Acknowledgement

I would like to thank to Olivier Liechti for the precious inputs and the active support in the preparation of the data.

References

[1]Carsten Lindemann, Erleichterte Aufwindsuche, Aerokurier 5/1987, Bild mittlere Verhältnisse der europäischen Thermik
[2]Henry Blum, Meteorologie für Segelflieger, 1. Auflage 2014, Motorbuchverlag Stuttgart
[3]Detlef Müller und Christoph Kottmeier, Meteorologische Aspekte des Segelflugs, Institut für Meteorologie und Klimatologie der Universität Hannover 1985

Modeling Bounded Rationality and Risk Strategy in Thermal Soaring

John J. Bird*, Daniel Sazhin+, Jack W. Langelaan*

*Department of Aerospace Engineering, Pennsylvania State University
+General Psychology, New York University

Abstract: Awareness and management of the risk of failing to encounter lift is fundamental to thermal soaring. When the weather or aircraft condition changes substantially, the pilot may be exposed to a greater risk of landing out. In these situations the pilot may need to alter strategies in order to minimize risk exposure at the expense of speed, often referred to as "gear-shifting." In this work, we explore several models to explain why small changes in the environment can cause large changes in risk exposure, requiring this shifting. We also examine several flight strategies in simulation to define the relative risk and reward for adopting various levels of risk tolerance and for failing to "shift gears" when the risk of landing out increases.

Keywords: bounded rationality, psychology, risk assessment, flight planning, competition strategy

Introduction

Thermal soaring is a cognitively taxing task. Decisions trees branch from each possible thermal source and mulitply rapidly. The net effect is that much like a chess game, it is impossible to examine all possibilities to find the optimal outcome. Attempting to do so would simply overwhelm a pilot[1]. To make the task more manageable, pilots employ heuristics -- mental shortcuts that minimize cognitive workload by excluding strategies likely to be suboptimal[2]. Pilots employ different heuristics, "shifting gears" depending on the situation.

Classic heuristics are "racing" and "survival". These strategies emerge as the pilot experiences losses and gains differently depending on how they process their situation[2]. For instance, when in an optimization (racing) mindset, alternatives that reduce speed are experienced as a loss. On the other hand, when the pilot is in a risk-minimization mindset (survival), options that increase risk exposure are felt as a loss.

Inevitably, this brings several questions: What is an appropriate amount of risk one can accept and succeed over the long run? When should a pilot reframe their situation and shift gears? To answer these questions, we modeled the risk of landing out as a function of the likelihood of finding a thermal on each glide and computed the long-term impact of certain risk preferences. This simple model is reinforced by Monte Carlo simulations which quantify how much risk a pilot should accept and when it is appropriate to switch strategies. Finally, we use these statistical baselines to provide insights into the decision-making process and examine how to apply these insights in the cockpit.

Strategic Risk

Considering the risk of landing out, one can think of each glide as an independent event, a gamble with two outcomes: finding a climb (success) or landing out (failure). Looking at a contest day as a whole, we can consider the sequence of glides and compute the cumulative probability of success. A contest is defined as several such sequences, in order to complete a contest without landing out, the pilot must win the glide gamble many times in a row. The question then is, "what is the strategic baseline of risk that is acceptable in a contest?"

We first compute the likelihood of completing a contest given the risk accepted on each glide. To do this, we calculated and graphed the probability of completing a contest day without landing out given a range of landout risk tolerance for each glide. It is apparent that the probability of completing the task is very sensitive to risk tolerance -- on a day with 15 glides the pilot with a 1% risk tolerance has only an 80% chance of completing the task.

For each additional contest day left, the risk compounds. As a result, one must consider the cumulative probability of landing out over the *entire* contest. Assuming pilots maintain consistent risk preferences and flies 15 glides per day, the probability of completing the contest without landing out can be computed. This relationship is depicted in Figure 1a, in a five day competition a pilot flying at Ptolerance=0.01 would have less than a 50% chance of completing the contest without landing out. To be confident in completing a nationals, a pilot should maintain a risk tolerance of Ptolerance=0.001 or less.

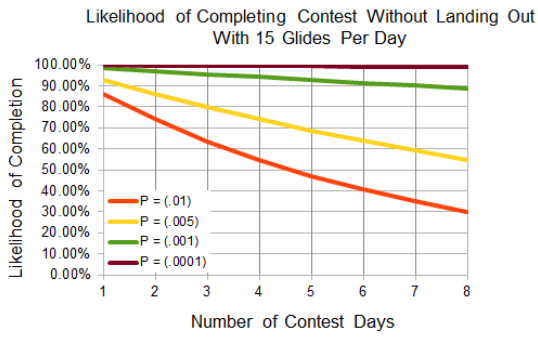

a) **Probability of completing a contest without landing out assuming each contest day requires 15 glides to complete.**

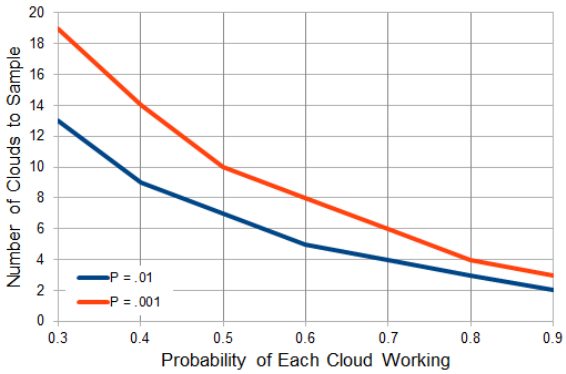

b) **Number of clouds required to maintain a desired risk tolerance as a function of the probability that each potential thermal works.**

Figure 1: To be confident in completing a contest, the pilot must fly with a very low risk threshold. Achieving this threshold can require a surprising number of climb options in unpredictable conditions.

Tactical Risk

How can we measure how much risk we are accepting while in the cockpit? Let us consider a pilot leaving a thermal and assessing the lift options ahead. Each possible sequence of lift options offers the opportunity to sample a certain number of thermal sources (clouds or ground featres) as the pilot trades altitude for distance. One way to think about each thermal sampled as either a success or failure at finding lift at each thermal source. This is akin to flipping a coin and landing heads each time a pilot find a thermal and tails whenever he misses. If the pilot is unlucky enough to flip tails on each cloud, he will land out. Ultimately, we can calculate the probability of a completely failed sequence, such as flipping five tails in a row, and then compare it against the strategic baseline of Ptolerance =0.001.

A naive approach to assessing options is to assume a cloud is just like a fair coin flip -- it will either work or it won't. In this case, the pilot needs *at least* ten clouds in reach to maintain the strategic baseline of Ptolerance≤0.001. Once again, the probability of landing out is very sensitive to this risk level: maintaining 7 instead of 10 options over an eight day competition with 15 glides each day *quadruples* the risk of landing out over the course of a competition.

Experienced pilots know that the likelihood of finding a thermal under a cloud can be better than a tossup. This can be treated like a weighted coin and the number of options required to maintain a desired risk tolerance can be computed for a known probability that each thermal fails. The number of clouds required to maintain a safe strategic risk profile is depicted in Figure 1b. Once the probability of contacting a thermal under a cloud is less than 50%, it is very difficult to maintain a low risk tolerance. Examined another way, unless the clouds are reliably predicting lift, in situations where only a few options are available, aggressive action should be taken in order to regain and maintain the strategic baseline risk.

Monte Carlo Simulations

The coin toss shows the sensitivity of success to risk level and demonstrates that uncertain and option limited situations are high risk. This motivates the need for behavioral frames, but does not lend itself to analysing the complexity of flights to turnpoints with limited altitude bands. To enable deeper exploration of risk strategy in thermal soaring, we used a Monte Carlo approach. This is conceptually similar to work done by previous authors[3,4] except that we explicitly explore the pilot's risk tolerance rather than using MacCready setting as a proxy.

A simple triangle task of approximately 220 km length is located in a 100 km square environment with unreliable thermals scattered throughout. The pilot can locate any thermal within gliding range, but is unable to determine if a thermal is working before reaching it. The probability that each thermal works is uniform within a single run and set to either 0.7 or 0.4. A range of pilot risk tolerances is simulated. For each risk tolerance and thermal consistency, 350 tasks are flown both by a pilot who gear shifts and a pilot who only optimizes. Figure 2 summarizes the effect of risk tolerance and gear shifting on average speed and probability of landing out under two different soaring conditions.

Effect of Risk Tolerance on Speed and Landing out

In consistent conditions similar speeds are maintained for a range of risk tolerances, but the risk of landing out increases with risk tolerance. There seems to be a reasonable tradeoff point of small risk of landing out with high average speeds for a purely optimizing pilot in predictable conditions. Unpredictable conditions require many thermals to maintain a strategic baseline, sometimes driving large deviations to lift, reducing average speed. In unpredictable conditions it is difficult to keep enough options to maintain an appropriate baseline, and landouts occur about 30% of the time when the pilot remains in an optimization frame, regardless of the strategic baseline.

Impact of Gear Shifting Strategy

Gear shifting can reduce the risk of landing out considerably for every risk tolerance and across environmental conditions. In unpredictable conditions the improvement is profound, shifting into a survival frame in high risk situations reduces the probability of landing out by approximately a factor of 10, from greater than 30% to less than 3%.

The risk reduction from gear shifting comes at the expense of speed, reducing the speed on task by more than 5 kmh^{-1} across a range of risk tolerance. In fact depending on the acceptable risk of landing out on a contest day it may be advantageous to abandon gear shifting. For example if the acceptable risk of landing out on a given day is 5% (perhaps on the last day of a close contest), it is faster to adopt a risk 1% chance of landing out on each glide but press on without gear shifting than it is to fly even very aggressively (risk tolerance of 0.1) with gear shifting.

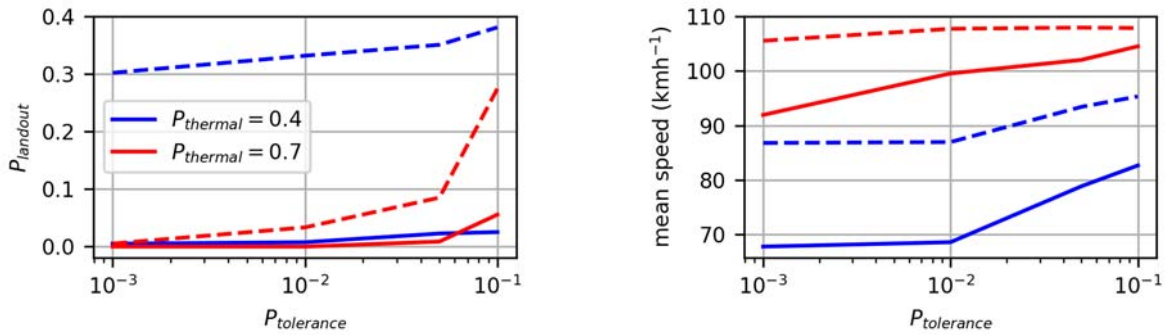

b) Probability of failing to complete the task. **a) Cross-country speed averaged over completed**

Figure 2: Performance as a function of risk tolerance under two environmental conditions. Pthermal represents the probability that a thermal will work. Solid lines indicate a gear shifting pilot while dashed lines indicate pilot who purely optimizes.

Summary

Succesfully completing contests, especially at the national and world level requires a very low risk tolerance. In uncertain situations many climb options must be available to maintain a low risk, this sensitivity motivates the existence of racing and survival heuristics. We demonstrate the effect that shifting frames has on success in a contest in Monte Carlo simulations. From these calculations and simulations the authors suggest several heuristics for use in the cockpit and decision criteria for engaging one strategy over the other.

- If more than half of the clouds are working, a pilot can become more selective about his choices.
- If fewer than half of the clouds work, conservatism is required to avoid a landout.
- Tactically, having strong confidence in at least one lift source/cloud ahead greatly diminishes risk exposure.
- Improvements in thermal "hit" probability can dramatically improve speed and reduce risk.

References

[1]Janis, I. L., and Mann, L., Decision making: A psychological analysis of conflict, choice, and commitment, Free Press, New York, NY, 1977.
[2]Kahneman, D., and Tversky, A., "Choices, values, and frames," American psychologist, Vol. 39, No. 4, 1984.
[3]Cochrane, J., "MacCready Theory with Uncertain Lift and Limited Altitude," Technical Soaring, Vol. 23, No. 3, 1999, pp. 88–96.
[4]Teter, M. P., "A Monte Carlo Approach to Competition Strategy," Science and Technology of Low Speed and Motorless Flight, 1979, pp. 389–397.

List of Authors

Join us!

How to become an OSTIV Member ...

Visit us online at **http://www.ostiv.org** and click on **Join us!** in the menu bar.

Just load down the Application Form, fill it in and send it to the OSTIV Secretariat.

What you get ...

1. TECHNICAL SOARING, published quarterly, containing papers presented at OSTIV Congresses, reports of other OSTIV meetings and other articles dealing with the scientific and technical aspects of soaring. Digital copies of TECHNICAL SOARING are immediately available to all OSTIV members.
2. Active and Scientific/Technical members each receive a free copy of any OSTIV publication published.
3. Organizing OSTIV Congresses for the reading of scientific and technical papers during and on the World Gliding Championships.
4. Organizing and assisting training courses devoted to scientific and technical aspects of soaring.
5. Distribution of OSTV-Letters, informing members, institutions, organisations and all interested persons about the ongoing activities and matters regarding OSTIV's constitutional objectives.

... and what you give

Students under 25 years of age	free
Individual Membership	EUR 25,-- per year
Scientific/Technical Membership	EUR 80,-- per year
Active Membership	EUR 250,-- per year